

Diese Dissertation haben begutachtet:

.....



**TECHNISCHE  
UNIVERSITÄT  
WIEN**  
Vienna University of Technology

DISSERTATION

# Physical properties of the anisotropic Kondo insulator $\text{CeRu}_4\text{Sn}_6$

Ausgeführt zum Zwecke der Erlangung des akademischen Grades eines  
Doktors der technischen Wissenschaften unter der Leitung von

Univ. Prof. Dr.rer.nat. Silke Bühler-Paschen

E138

Institut für Festkörperphysik

eingereicht an der Technischen Universität Wien

Fakultät für Physik

von

Dipl.-Ing. Hannes Heinrich Winkler

Matrikelnummer: 0426106

Hermesberg 1, 9531 Nötsch im Gailtal

Villach, am 09. September 2013

---

*Gutachter:*

Univ. Prof. Dr.rer.nat. Silke Bühler-Paschen  
Prof. Dr. Cornelius Krellner

*Eingereicht am:* 09. September 2013

*Tag der Verteidigung:* 27. September 2013

# Abstract

Kondo insulators/semiconductors are a small group of materials showing unusual temperature-dependence of physical properties. Due to interaction effects between the magnetic moments of localized electrons and conduction electrons (Kondo effect), a narrow energy gap opens at low temperatures. Although simplified models based on Kondo physics can explain some features found in these materials, a correct theoretical description is still missing.

Most Kondo insulators known to date exhibit a cubic crystal structure. In addition, a few orthorhombic and tetragonal systems with semiconducting behaviour have been found. The orthorhombic compound CeNiSn for instance exhibits strongly anisotropic behaviour that has been ascribed to the opening of an anisotropic hybridization gap. Previous physical property measurements on polycrystalline CeRu<sub>4</sub>Sn<sub>6</sub> as well as preliminary magnetization measurements on single crystalline CeRu<sub>4</sub>Sn<sub>6</sub> suggested similar physics in this tetragonal compound. To advance the understanding of the underlying mechanisms, detailed investigations of single crystalline CeRu<sub>4</sub>Sn<sub>6</sub> were performed.

Within this thesis, high-quality single crystalline CeRu<sub>4</sub>Sn<sub>6</sub> was successfully grown. Due to the sensitivity of low-temperature properties on impurities, single crystals of high quality are essential for the investigation of Kondo insulators. Electrical transport and optical spectroscopy measurements (in collaboration with V. Guritanu, J. Sichelschmidt, T. Weig and M. Scheffler) were made to determine the anisotropic transport behaviour and deduce the anisotropy of the energy gap and its consequences. Direct magnetization, torque magnetometry and resonant X-ray absorption spectroscopy (in collaboration with F. Strigari and A. Severing) measurements were performed to determine the crystalline electric field split level scheme and, as a result, the ground state of the localized 4*f* electron state. This information is of great interest for the visualizing orbital overlaps and for theoretical calculations done by P. Wissgott in parallel to this experimental investigation. Finally, cleaving tests and preliminary scanning tunneling spectroscopy measurements were performed by S. Wirth, resulting in the direct detection of a pseudo gap feature and in the clarification that angle-resolved photoemission spectroscopy (ARPES) measurements on CeRu<sub>4</sub>Sn<sub>6</sub> should be possible.

All physical properties investigated within this thesis revealed a strong anisotropy between the [001] axis and the (001) plane directions ([100] and [110]) while anisotropy between the [100] and [110] directions turned out to be minimal. Together with theoretical calculations these were interpreted as evidence for the presence of a hybridization gap within the tetragonal

---

(001) plane, but the absence of such a gap for the [001] direction. The ground state and crystalline electric field split level scheme could not yet be consistently determined from all available experiments: Further experiments are needed and under way. In addition, a number of  $\text{CeRu}_4\text{Sn}_6$  single crystals for future ongoing measurements (muon spin rotation, thermal transport measurements and non-resonant inelastic X-ray spectroscopy) were grown.

In addition to the investigations on  $\text{CeRu}_4\text{Sn}_6$ , service measurements on  $\text{Ce}_{3-x}\text{La}_x\text{Pd}_{20}\text{Si}_6$  and on the type-I clathrate  $\text{Ba}_8\text{Au}_6\text{Si}_{40}$  substituted with Ce and La were performed within other projects. These measurements are shown and briefly discussed in the appendix.



# Kurzfassung

Kondo Isolatoren, welche auch als Kondo Halbleiter bezeichnet werden, bilden eine kleine Gruppe an Materialien mit ungewöhnlichem temperaturabhängigen Verhalten der physikalischen Eigenschaften. Aufgrund der Wechselwirkung zwischen den magnetischen Momenten der lokalisierten Elektronen und den Leitungselektronen (Kondo-Effekt) öffnet sich eine Energielücke in der elektronischen Zustandsdichte an der Fermi-Energie bei tiefen Temperaturen. Trotz der Tatsache, dass das gezeigte Verhalten teilweise mit vereinfachten Modellen basierend auf dem Kondo-Effekt beschrieben werden kann, existieren bislang keine theoretischen Modelle zur exakten Beschreibung von Kondo Isolatoren.

Die meisten bekannten Kondo Isolatoren besitzen eine kubische Kristallstruktur, gefolgt von wenigen Verbindungen mit orthorhombischer und schlussendlich tetragonaler Kristallstruktur. Ein Vertreter ist die orthorhombische Verbindung  $\text{CeNiSn}$ , welche stark anisotropes Verhalten zeigt. Der Grund dafür liegt in einer richtungsabhängigen Ausbildung der Energielücke in der elektrischen Zustandsdichte. Vorangegangene Messungen physikalischer Eigenschaften an  $\text{CeRu}_4\text{Sn}_6$  Polykristallen und Magnetisierungsmessungen an Einkristallen zeigten ähnliches Verhalten zu jenem von  $\text{CeNiSn}$ . Aufgrund dieser Tatsache, wurden umfangreiche Untersuchungen an  $\text{CeRu}_4\text{Sn}_6$  Einkristallen in dieser Arbeit durchgeführt. Eine Bestimmung der zugrundeliegenden Physik für das anisotrope Verhalten könnte zu einem weitreichenden Verständnis über die Ausbildung der Energielücke im Allgemeinen führen.  $\text{CeRu}_4\text{Sn}_6$  bildet ein tetragonales Kristallgitter aus, welches im Vergleich zum orthorhombischen  $\text{CeNiSn}$  eine höhere Symmetrie besitzt und daher die Voraussetzungen für eine einfachere Untersuchung der anisotropen physikalischen Eigenschaften erfüllt.

In dieser Arbeit wurden hochwertige  $\text{CeRu}_4\text{Sn}_6$  Einkristalle erfolgreich gezüchtet. Die hohe Qualität der gezüchteten Einkristalle ist eine Grundvoraussetzung für die Untersuchung physikalischer Eigenschaften von Kondo Isolatoren, da die Ausbildung der Energielücke und daher das Tieftemperaturverhalten sehr stark durch extrinsischen Effekte (Verunreinigungen) beeinflusst wird. Neben der Herstellung von Einkristallen höchster Qualität, wurde der Fokus der weiteren physikalischen Untersuchungen auf zwei Kernpunkte gelegt. Zum Ersten wurde mittels Messungen diverser physikalischer Eigenschaften die elektronische Bandstruktur untersucht, um eine anisotrope Bandstruktur und Anzeichen auf eine Energielücke festzustellen und darauffolgend im Detail zu untersuchen. Diese richtungsabhängigen Eigenschaften der elektrischen Bandstruktur wurden mit optischen Leitfähigkeitsmessungen (durchgeführt von

---

V. Guritanu, J. Sichelschmidt, T. Weig und M. Scheffler) und elektrischen Transportmessungen untersucht. Zusätzlich wurde mittels Rastertunnelspektroskopie (STS) (Messung ausgeführt von S. Wirth) eine nicht vollständig ausgeprägte Energielücke an der Fermi-Energie bei tiefen Temperaturen gemessen. Dieses Ergebnis ist ein weiteres Indiz für die Ausbildung einer anisotropen Energielücke und unterstützt die Schlussfolgerungen aus den Ergebnissen der Transportmessungen und Bandstrukturberechnungen, die parallel zur experimentellen Untersuchung von P. Wissgott durchgeführt wurden. Zum Zweiten wurde mit Magnetisierungsmessungen, Torque Magnetometrie und Röntgenabsorptionsspektroskopie (durchgeführt von F. Strigari und A. Severing) versucht, die Kristallfeldaufspaltung und das Grundzustandsmultiplett des lokalisierten  $4f$  Elektrons zu bestimmen. Diese Information ist von entscheidender Bedeutung für die Berechnung der Bandstruktur mit theoretischen Modellen. Neben diesen zwei Kernpunkten, wurden "Cleaving"-Tests an  $\text{CeRu}_4\text{Sn}_6$  Einkristallen von S. Wirth durchgeführt, um die Möglichkeit von winkelaufgelöster Photoelektronenspektroskopie (ARPES) an  $\text{CeRu}_4\text{Sn}_6$  Proben zu testen. Diese Tests verliefen positiv und ARPES Messungen sind in Planung.

Alle physikalischen Eigenschaften, die in dieser Arbeit untersucht wurden, zeigen stark anisotropes Verhalten zwischen der  $[001]$  Achse und den Achsen in der  $(001)$  Ebene. Innerhalb der  $(001)$  Ebene ist nur ein gering unterschiedliches Verhalten zwischen der  $[100]$  und  $[110]$  Achse festzustellen. Unter Einbeziehung der theoretischen Berechnung der elektronischen Bandstruktur durch P. Wissgott kann das gemessene Verhalten auf eine anisotrope Hybridisierungsstärke in  $\text{CeRu}_4\text{Sn}_6$  zurückgeführt werden. Diese anisotrope Hybridisierungsstärke führt zur Entstehung einer Energielücke an der Fermi-Energie in der tetragonalen  $(001)$  Ebene im Gegensatz lückenlosen Bandstruktur im Bereich der Fermi-Energie entlang der  $[001]$  Achse. Aufgrund widersprüchlicher Messergebnisse konnte die Kristallfeldaufspaltung der lokalisierten  $4f$  Elektronen nicht bestimmt werden. Um diese Widersprüche zu untersuchen sind weitere Messungen notwendig und bereits geplant. In dieser Arbeit wurden  $\text{CeRu}_4\text{Sn}_6$  Einkristalle für weitere Messungen hergestellt, die für geplante bzw. bereits durchgeführte Myonen-Spin Rotationsmessungen ( $\mu\text{SR}$ ), thermische Transportmessungen und inelastische Röntgenspektroskopie (NIXS) Messungen verwendet wurden bzw. werden.

Zusätzlich zur Untersuchung von  $\text{CeRu}_4\text{Sn}_6$  wurden im Rahmen weiterer Projekte Messungen an  $\text{Ce}_{3-x}\text{La}_x\text{Pd}_{20}\text{Si}_6$  und mit Ce und La substituierten  $\text{Ba}_8\text{Au}_6\text{Si}_{40}$  Typ-I Klathraten durchgeführt. Die Messergebnisse sind im Anhang gezeigt.

# Contents

<b>List of figures</b>	<b>iii</b>
<b>List of tables</b>	<b>vii</b>
<b>Symbols and abbreviations</b>	<b>xi</b>
<b>1 Introduction</b>	<b>1</b>
<b>2 Theory</b>	<b>7</b>
2.1 Single-ion Kondo effect . . . . .	7
2.2 Kondo lattice . . . . .	8
2.3 Kondo insulator . . . . .	10
2.4 Landau-Fermi liquid theory . . . . .	12
2.5 The Coqblin-Schrieffer model . . . . .	13
2.6 Thermopower . . . . .	16
2.7 Hall effect . . . . .	19
2.8 Crystalline electric field effects . . . . .	21
2.8.1 Crystalline electric field effects in $\text{CeRu}_4\text{Sn}_6$ . . . . .	22
2.9 Magnetic anisotropy . . . . .	23
<b>3 Experimental techniques</b>	<b>25</b>
3.1 Electrical transport . . . . .	25
3.2 Magnetization . . . . .	28
3.3 Torque magnetometry . . . . .	29
3.4 Thermopower . . . . .	31
3.5 Optical spectroscopy . . . . .	32
3.6 X-ray absorption spectroscopy (XAS) measurements . . . . .	33
<b>4 Crystallography and single crystal growth</b>	<b>37</b>
4.1 Crystal structure . . . . .	37
4.2 Single crystal growth and orientation procedure . . . . .	49
4.2.1 Single crystal growth . . . . .	49
4.2.2 Phase and domain purity analyses . . . . .	50
4.2.3 Orientation procedure . . . . .	52

---

4.2.4	Finalizing sample preparation . . . . .	55
<b>5</b>	<b>Theoretical calculations for <math>\text{CeRu}_4\text{Sn}_6</math></b>	<b>57</b>
<b>6</b>	<b>Experimental investigations</b>	<b>61</b>
6.1	Magnetic properties . . . . .	61
6.1.1	Direct magnetization measurements . . . . .	62
6.1.2	Torque magnetometry . . . . .	79
6.2	Electrical resistivity . . . . .	99
6.3	Hall effect measurements . . . . .	110
6.4	Magnetoresistance . . . . .	117
6.5	Thermopower . . . . .	146
6.6	Measurements with grown/prepared $\text{CeRu}_4\text{Sn}_6$ single crystals by cooperating groups . . . . .	151
6.6.1	X-ray absorption spectroscopy . . . . .	151
6.6.2	Optical reflectivity measurements . . . . .	152
6.6.3	Cleaving tests, scanning tunneling microscopy and preliminary scanning tunneling spectroscopy analysis . . . . .	155
<b>7</b>	<b>Summary and outlook</b>	<b>161</b>
<b>A</b>	<b>Contributions to other projects</b>	<b>163</b>
A.1	$\text{Ce}_{3-x}\text{La}_x\text{Pd}_{20}\text{Si}_6$ . . . . .	163
A.2	Physical properties measurements on type-I clathrates including La and Ce . . .	165
	<b>Bibliography</b>	<b>169</b>
	<b>Acknowledgments</b>	<b>175</b>

# List of Figures

1.1	Electrical resistivity measurements on $\text{CeRu}_4\text{Sn}_6$ by Das and Sampathkumaran [1]	2
1.2	Electrical resistivity, thermopower, thermal conductivity and Hall constant measurements on $\text{CeRu}_4\text{Sn}_6$ by Strydom et al. [2]	4
2.1	Schematic temperature dependence of the magnetic contribution to the electrical resistivity and the evolution of the density of states for Kondo lattices and Kondo impurity systems	9
2.2	Doniach phase diagram	10
2.3	Schematic electronic bandstructure and density of states of a Kondo insulator [3,4]	11
2.4	Theoretically calculated density of states in anisotropic Kondo insulators [5,6]	12
2.5	Magnetic contribution to the electrical resistivity calculated by Coqblin and Cornut in 1972 [7]	15
2.6	Thermopower of $\text{Ce}(\text{Cu,Au})_6$ and calculated thermopower curves for Ce-containing compounds with different hybridization strengths [8]	19
2.7	Schematic illustration of the Hall effect	20
2.8	Schematic illustration of the anomalous Hall effect contribution and the Hall coefficient as a function of temperature of polycrystalline $\text{Ce}_3\text{Pd}_{20}\text{Si}_6$	21
2.9	Schematic illustration of the tetragonal magnetic anisotropy energy with different anisotropy constants	24
3.1	Schematic drawing of the sample contacts for the electrical resistivity, magnetoresistance and Hall effect measurements and photograph of a contacted sample	26
3.2	Photograph of the different sample holders which were used for magnetization measurements within this work	29
3.3	Schematic drawings of the torque-lever chip of the PPMS (Quantum Design) and of the used sample shape	31
3.4	Schematic drawing of the thermopower measurement set-up	33
3.5	Photographs of a separated $\text{CeRu}_4\text{Sn}_6$ sample (batch G3) for optical spectroscopy measurements	34
3.6	Photographs of a separated $\text{CeRu}_4\text{Sn}_6$ sample for XAS measurements	35
3.7	Energy level schemes included in the $M_4$ and $M_5$ transitions used by XAS measurements	35
4.1	Unit cell and cage structure of $\text{CeRu}_4\text{Sn}_6$	38

---

4.2	Atomic environment of Ce sites and the layered structure in $\text{CeRu}_4\text{Sn}_6$ . . . . .	38
4.3	Schematic illustration of the tetragonal and quasi-cubic unit cell of $\text{CeRu}_4\text{Sn}_6$ and notation of crystalline directions used in this thesis . . . . .	39
4.4	Crystal structure of $\text{CeRu}_4\text{Sn}_6$ displayed along different lattice directions . . . .	40
4.5	Atomic chains along $[100]$ for $\text{CeRu}_4\text{Sn}_6$ . . . . .	43
4.6	3-dimensional representations of straight and indirect Ce-containing atomic chains along $[100]$ for $\text{CeRu}_4\text{Sn}_6$ . . . . .	44
4.7	Atomic chains along $[001]$ and their directional dependent presentation for $\text{CeRu}_4\text{Sn}_6$ . . . . .	45
4.8	Atomic chains along $[110]$ for $\text{CeRu}_4\text{Sn}_6$ . . . . .	46
4.9	3-dimensional representations of the direct and indirect Ce-containing atomic chains along $[110]$ for $\text{CeRu}_4\text{Sn}_6$ . . . . .	47
4.10	Ce-4 <i>f</i> -electron orbitals and Wannier orbitals calculated by P. Wissgott [9] for $\text{CeRu}_4\text{Sn}_6$ in the $(J, m_j)$ -base . . . . .	48
4.11	DTA measurements made by T. Nezu [10] and derived growth length dependence of the atomic composition . . . . .	50
4.12	Schematic drawing of the floating zone technique and grown $\text{CeRu}_4\text{Sn}_6$ batch G6	52
4.13	Photographs and representative SEM images of $\text{CeRu}_4\text{Sn}_6$ batch G6 . . . . .	53
4.14	Photograph of $\text{CeRu}_4\text{Sn}_6$ batch G7 . . . . .	53
4.15	Analyzed powder diffraction pattern of $\text{CeRu}_4\text{Sn}_6$ batches G3 and G7 . . . . .	54
4.16	Orientation scheme of $\text{CeRu}_4\text{Sn}_6$ . . . . .	55
5.1	Partial density of states for $\text{CeRu}_4\text{Sn}_6$ , calculated with LDA by P. Wissgott [9] .	58
5.2	Orbital spectrum for $\text{CeRu}_4\text{Sn}_6$ , calculated at 290 K with LDA+DMFT by P. Wissgott [9] . . . . .	59
5.3	Temperature-dependent orbital spectrum for $\text{CeRu}_4\text{Sn}_6$ , calculated with LDA+DMFT by P. Wissgott [9] . . . . .	59
5.4	Band structure of $\text{CeRu}_4\text{Sn}_6$ , calculated with LDA+DMFT by P. Wissgott [9] .	60
6.1	Magnetic susceptibility of $\text{CeRu}_4\text{Sn}_6$ along the $a$ , $c$ and $c'$ direction . . . . .	63
6.2	Inverse magnetic susceptibility including Curie-Weiss fits for $\text{CeRu}_4\text{Sn}_6$ . . . . .	65
6.3	Results of crystalline electric field calculations with a simple point-charge model for $\text{CeRu}_4\text{Sn}_6$ . . . . .	68
6.4	Calculated energy splitting and ground state properties by setting the CEF pa- rameter $B_2^0$ to 6 meV and changing $B_4^0$ and $B_4^4$ for $\text{CeRu}_4\text{Sn}_6$ . . . . .	71
6.5	Inverse magnetic susceptibility as a function of temperature for $\text{CeRu}_4\text{Sn}_6$ , in- cluding CEF calculations with McPhase 4.8 ( $m_j = \pm 3/2$ ground state) . . . . .	72
6.6	Magnetic susceptibility and its inverse as a function of temperature for $\text{CeRu}_4\text{Sn}_6$ , including CEF calculations with McPhase 4.8 ( $m_j = \pm 1/2$ ground state) . . . . .	73

---

6.7	Low-temperature (inverse) susceptibility as a function of temperature for $\text{CeRu}_4\text{Sn}_6$ . . . . .	76
6.8	Magnetization along different crystallographic directions for $\text{CeRu}_4\text{Sn}_6$ at low temperatures . . . . .	77
6.9	Inverse magnetic susceptibility, magnetic susceptibility and magnetization at low temperatures for different samples of $\text{CeRu}_4\text{Sn}_6$ . . . . .	78
6.10	Schematic drawings of the $\text{CeRu}_4\text{Sn}_6$ samples used for torque magnetometry measurements . . . . .	79
6.11	Schematic drawing of nomination used for torque magnetometry measurements and of the directional dependencies within a standard torque measurement . . .	80
6.12	Magnetic anisotropy energy terms and the contributions of the anisotropy constants $K_1$ and $K_2$ . . . . .	82
6.13	Torque measurement of $\text{CeRu}_4\text{Sn}_6$ within the (110) plane at 100 K . . . . .	84
6.14	Torque measurement of $\text{CeRu}_4\text{Sn}_6$ within the (100) and (110) plane between 15 and 300 K . . . . .	84
6.15	Torque measurement of $\text{CeRu}_4\text{Sn}_6$ within the (100) and (110) plane between 3 and 10 K . . . . .	85
6.16	Torque measurement of $\text{CeRu}_4\text{Sn}_6$ in the (001) plane . . . . .	86
6.17	Magnetic susceptibility derived by torque magnetometry and direct magnetization measurements on $\text{CeRu}_4\text{Sn}_6$ between the easy plane and hard $c$ axis . . . .	87
6.18	Comparison of the magnetic anisotropy in the (001) plane of $\text{CeRu}_4\text{Sn}_6$ derived by torque and direct magnetization measurements . . . . .	88
6.19	Field dependence of the magnetic susceptibility formula in $\text{CeRu}_4\text{Sn}_6$ at 3 K . .	94
6.20	Investigations of misalignment effects in magnetization measurements on $\text{CeRu}_4\text{Sn}_6$	95
6.21	Determination of the crystalline electric field parameter $B_2^0$ with torque magnetometry measurements . . . . .	97
6.22	Electrical resistivity as a function of temperature along the three main directions	100
6.23	Energy gaps using a semiconductor picture for the electrical resistivity along the three main directions in $\text{CeRu}_4\text{Sn}_6$ . . . . .	102
6.24	Electrical resistivity of $\text{CeRu}_4\text{Sn}_6$ along the $a$ direction in a semilogarithmic plot	103
6.25	Electrical resistivity of $\text{CeRu}_4\text{Sn}_6$ along the $c$ and $c'$ direction in semilogarithmic plots . . . . .	104
6.26	Relative electrical resistivity of $\text{CeRu}_4\text{Sn}_6$ samples along the $c'$ direction . . . .	107
6.27	Electrical resistivity of $\text{CeRu}_4\text{Sn}_6$ measured and calculated [9] along the main directions . . . . .	109
6.28	Hall coefficient $R_H$ for $\text{CeRu}_4\text{Sn}_6$ as a function of temperature . . . . .	111
6.29	Hall coefficient $R_H$ for $\text{CeRu}_4\text{Sn}_6$ as a function of temperature at high temperatures	112
6.30	Hall resistivity as a function of magnetic field along the three main directions of $\text{CeRu}_4\text{Sn}_6$ samples . . . . .	113
6.31	Charge carrier concentration and Hall mobility of $\text{CeRu}_4\text{Sn}_6$ along the $a$ , $c$ and $c'$ direction . . . . .	115

---

6.32	Hall coefficient and Hall mobility of the Kondo insulators (semimetals) CeNiSn and CeRhSb [11]	116
6.33	Schematic drawing of the notations used for magnetoresistance measurements	118
6.34	Magnetoresistance of CeRu <sub>4</sub> Sn <sub>6</sub> (sample G2_A_1) with the electrical current applied along $c$ above 2 K	119
6.35	Angle dependent transverse magnetoresistance for CeRu <sub>4</sub> Sn <sub>6</sub> along the $c$ direction at several temperatures with an applied magnetic field of 9 T	120
6.36	Magnetoresistance of CeRu <sub>4</sub> Sn <sub>6</sub> along the $c$ axis as a function of the magnetic field direction at several temperatures with several different applied magnetic fields	121
6.37	Magnetoresistance of CeRu <sub>4</sub> Sn <sub>6</sub> along the $c'$ axis as a function of the magnetic field direction at several temperatures with differing applied magnetic fields in the (110) plane	122
6.38	Magnetoresistance of CeRu <sub>4</sub> Sn <sub>6</sub> along the $c'$ axis as a function of the magnetic field direction at several temperatures with differing applied magnetic fields in the (001) plane	124
6.39	Magnetoresistance of CeRu <sub>4</sub> Sn <sub>6</sub> along the $a$ direction at 2 K as a function of the magnetic field direction and strength	125
6.40	Comparison of longitudinal magnetoresistance along the $c'$ axis of CeRu <sub>4</sub> Sn <sub>6</sub> samples separated from batches B and G2	127
6.41	Comparison of the relative transverse magnetoresistance along the $a$ axis with an applied magnetic field along the perpendicular $a$ axis	128
6.42	Longitudinal magnetoresistance and its derivative along the $a$ and $c'$ axis for CeRu <sub>4</sub> Sn <sub>6</sub> samples with an applied magnetic field up to about 60 T	130
6.43	Longitudinal magnetoresistance and its derivative along the $c$ direction for CeRu <sub>4</sub> Sn <sub>6</sub> samples with an applied magnetic field up to about 60 T	131
6.44	Longitudinal magnetoresistance of CeRu <sub>4</sub> Sn <sub>6</sub> samples along the three investigated directions at the lowest temperatures	133
6.45	Derivative of the longitudinal magnetoresistance of CeRu <sub>4</sub> Sn <sub>6</sub> samples along the three investigated directions at the lowest temperatures	134
6.46	Transverse magnetoresistance of CeRu <sub>4</sub> Sn <sub>6</sub> samples along the three investigated directions at the lowest temperatures	135
6.47	Derivative of the transverse magnetoresistance of CeRu <sub>4</sub> Sn <sub>6</sub> samples along the three investigated directions at lowest temperatures	136
6.48	Temperature dependence of the minima of magnetoresistance measurements on CeRu <sub>4</sub> Sn <sub>6</sub> for different orientations of the magnetic field and electrical current	137
6.49	Comparison of longitudinal and transverse magnetoresistance of CeRu <sub>4</sub> Sn <sub>6</sub> focused on the applied magnetic field direction	139
6.50	Comparison of the derivative of the longitudinal and transverse magnetoresistance of CeRu <sub>4</sub> Sn <sub>6</sub> focused on the applied magnetic field direction	140
6.51	Magnetoresistance of CeNiSn [12]	141
6.52	Comparison of the magnetoresistance of different CeNiSn samples [13]	142



---

6.53	Magnetoresistance of $\text{Ce}_3\text{Bi}_4\text{Pt}_3$ [14] . . . . .	143
6.54	Magnetoresistance of $\text{SmB}_6$ [14] . . . . .	143
6.55	Thermopower measurements of $\text{CeRu}_4\text{Sn}_6$ . . . . .	148
6.56	Thermopower calculated by [9], measured thermopower and its temperature derivative along the main directions of $\text{CeRu}_4\text{Sn}_6$ . . . . .	148
6.57	Thermopower measurements of the anisotropic Kondo insulator $\text{CeNiSn}$ [4] . . .	149
6.58	XAS measurements on $\text{CeRu}_4\text{Sn}_6$ and simulations by F. Strigari [15] . . . . .	153
6.59	L-edge XAS-PFY measurements on $\text{CeRu}_4\text{Sn}_6$ by F. Strigari in the group of A. Severing . . . . .	153
6.60	Optical reflectivity spectra and optical resistivity on $\text{CeRu}_4\text{Sn}_6$ [16] . . . . .	155
6.61	Results of cleaving tests on $\text{CeRu}_4\text{Sn}_6$ at 300 K by S. Wirth . . . . .	157
6.62	Results of cleaving tests on $\text{CeRu}_4\text{Sn}_6$ at 2 K by S. Wirth . . . . .	158
6.63	Preliminary scanning tunneling spectroscopy measurements on $\text{CeRu}_4\text{Sn}_6$ performed by S. Wirth . . . . .	159
A.1	Electrical resistivity measured on $\text{Ce}_{3-x}\text{La}_x\text{Pd}_{20}\text{Si}_6$ samples as a function of temperature . . . . .	164
A.2	Heat capacity measured on $\text{Ce}_{3-x}\text{La}_x\text{Pd}_{20}\text{Si}_6$ samples as a function of temperature and site-selective occupation of the Ce sites in $\text{Ce}_{3-x}\text{La}_x\text{Pd}_{20}\text{Si}_6$ . . . . .	165
A.3	Electrical resistivity and magnetic susceptibility measured on type-I clathrate $\text{Ba}_8\text{Au}_6\text{Si}_{40}$ substituted with La and Ce as a function of temperature . . . . .	166



# List of Tables

4.1	Atomic coordinates of $\text{CeRu}_4\text{Sn}_6$ . . . . .	37
4.2	Table of grown and measured $\text{CeRu}_4\text{Sn}_6$ single crystals . . . . .	51
6.1	Results of a Curie Weiss fit on $\text{CeRu}_4\text{Sn}_6$ single crystals at high temperatures . .	64
6.2	Relevant data of corrections to calculate the magnetic susceptibility along the hard $c$ axis by combining torque magnetometry in the (100) plane and direct magnetization measurements . . . . .	90
6.3	Relevant data of corrections to calculate the magnetic susceptibility along the hard $c$ axis by combining torque magnetometry in the (110) plane and direct magnetization measurements . . . . .	91
6.4	Enhancement of the magnetic susceptibility along the $c'$ direction on sample G2_B_3 used to calculate the susceptibility along the $c$ direction . . . . .	93
6.5	Electrical resistivity, magnetoresistance and Hall effect measurement overview of $\text{CeRu}_4\text{Sn}_6$ single crystals . . . . .	99
6.6	Table of minima and maxima revealed by electrical resistivity measurements . .	100
6.7	Maxima of the electrical resistivity and characteristic temperatures for several $\text{CeRu}_4\text{Sn}_6$ samples . . . . .	106
6.8	Temperature of the maxima revealed by electrical resistivity and Hall effect investigations for $\text{CeRu}_4\text{Sn}_6$ . . . . .	112
6.9	Relations between different $\rho_{mag}(T) \cdot \chi(T)$ values used for the analysis of the anomalous Hall effect in $\text{CeRu}_4\text{Sn}_6$ . . . . .	114
6.10	Table of extrema in $\rho_{B,long}(H)$ measurements in high magnetic fields at different temperatures . . . . .	131
6.11	Table of minima and maxima revealed by thermopower measurements . . . . .	146



# Symbols and abbreviations

Below, the symbols and abbreviations used within this PhD thesis are listed. Notations, which were introduced in isolated passages are not included. Symbols with suffix have been considered only when their meaning is relevant and/or not unambiguous.

$A$	coefficient of the quadratic temperature dependent term of the resistivity
ARPES	angle-resolved photoemission spectroscopy
$a$	lattice constant, tetragonal axis in the basal plane
ac	alternating current
$\alpha$	mixing coefficient, angle, exponent
$B_l^m$	crystalline electric field parameters
$\beta$	angle
$C$	Curie constant
CEF	crystalline electric field
CS	Coqblin-Schrieffer
CW	Curie-Weiss
$C_p$	heat capacity
$c$	lattice constant, tetragonal axis perpendicular to the basal plane
$c'$	lattice constant, diagonal crystallographic axis in the tetragonal plane
$\chi$	magnetic susceptibility
$\Delta\chi_{xy}$	difference of the magnetic susceptibility along the $x$ and $y$ axis measured by torque magnetometry
$\chi_{c,calc,cx}$	magnetic susceptibility along the $c$ axis calculated with direct magnetic measurements along $x$ and torque magnetometry measurements with rotating magnetic field in the plane including the $c$ and $x$ axis
$D$	bandwidth of conduction electrons
DM	direct magnetization

---

DMFT	dynamic mean-field theory
DOS	density of states
dc	direct current
$\Delta$	energy gap
$\delta$	angle
EDX	energy dispersive X-ray spectroscopy
$E_F$	Fermi energy
$E_{aniso}$	magnetic anisotropy energy
$e$	electrical charge $1.60219 \cdot 10^{-19}$ C
$\epsilon$	energy
$F_l^{s(a)}$	Landau parameters
$g$	Landé factor
$\Gamma$	crystalline electric field state
$\gamma$	linear specific heat coefficient, angle
$H$	Hamilton operator, magnitude of magnetic field $\vec{H}$
HF	heavy fermion
$\hbar$	reduced Planck constant $1.054571726 \cdot 10^{-34}$ Js
$I$	magnitude of the electrical current $\vec{I}$
INS	inelastic neutron scattering
$J$	exchange integral, total angular quantum number
$j$	total angular quantum number, magnitude of the electrical current density $\vec{j}$
KI	Kondo insulator
KIMP	Kondo impurity
KL	Kondo lattice
$K_i$	anisotropy constant
$k$	magnitude of the electron wave vector $\vec{k}$ , i.e., wave number
$\vec{k}$	electron wave vector

---

$k_B$	Boltzmann constant $1.3807 \cdot 10^{-23} \text{ JK}^{-1}$
LDA	local density approximation
LFL	Landau-Fermi liquid
$M$	magnetization
$m$	multiplicity
$m^*$	effective electron mass
$m_e$	free electron mass $9.1095 \cdot 10^{-31} \text{ kg}$
$m_j$	projected total angular momentum quantum number
$\mu_0$	vacuum permeability $4\pi \cdot 10^{-7} \text{ Vs/(Am)}$
$\mu_B$	Bohr magneton $9.2741 \cdot 10^{-24} \text{ JT}^{-1}$
$\mu_{eff}$	effective magnetic moment
NMR	nuclear magneto resistance
$N(E_F)$	density of states of conduction electrons at the Fermi level
$N_A$	Avogadro constant $6.02214129 \cdot 10^{23} \text{ mol}^{-1}$
$n$	charge carrier concentration
$O_l^m$	Stevens operator
$\omega$	angular frequency
PCM	point-charge model
PFY	partial fluorescence yield
$P_i$	fit parameters (magnetoresistance measurements)
$\phi$	azimuthal angle
$q$	electrical charge $1.60219 \cdot 10^{-19} \text{ C}$
$R$	optical reflectivity
RE	rare earth
RKKY	Ruderman-Kittel-Kasuya-Yosida
$R_H^A$	anomalous Hall coefficient
$R_H$	Hall coefficient

---

$\bar{\rho}$	relative electrical resistivity
$\rho$	electrical resistivity
$\rho_0$	residual electrical resistivity
$\rho_B$	magnetoresistivity
$\rho_{B,long}$	longitudinal magnetoresistivity
$\rho_{B,trans}$	transverse magnetoresistivity
$\rho_{Hall}$	Hall resistivity
$\rho_{mag}$	magnetic contribution to the electrical resistivity
$\rho_{ph}$	phonon contribution to the electrical resistivity
$\rho_{rel0}$	fit parameter (magnetoresistance measurements)
$S$	thermopower
SEM	scanning electron microscopy
SO	spin-orbit
STM	scanning tunneling microscopy
STS	scanning tunneling spectroscopy
SWR	Sommerfeld-Wilson ratio
$\vec{S}$	spin of localized electrons
$\sigma$	electrical conductivity
$\vec{\sigma}$	spin of conduction electrons
$T$	temperature
TM	torque magnetometry
$T_{coh}$	characteristic temperature for coherence effect on the Kondo lattice
$T_K$	Kondo temperature
$\Theta$	paramagnetic Weiss temperature
$\tau$	relaxation time, magnitude of the magnetic torque $\vec{\tau}$
$1/\tau$	scattering rate
$\theta$	polar angle
$U$	Coloumb interaction strength, voltage
UHV	ultra-high vacuum
$V$	volume in real space (e. g. , sample volume), hybridization matrix element



---

$V_{sf}, V_{kd}$  hybridization matrix element

XAS resonant X-ray absorption spectroscopy



# Chapter 1

## Introduction

In 1964, Kondo [17] succeed to describe a phenomenon which had been unexplained for three decades. Experiments in 1934 by de Haas et al. revealed a minimum in the electrical resistivity of Au including Fe impurities at low temperatures and an increasing electrical resistivity with further decreasing temperature [18]. Kondo described this phenomenon by including second-order scattering processes in the calculations of the interaction between the localized magnetic moments of the impurity elements with the conduction electrons. This effect was later named Kondo effect. Together with the RKKY (Ruderman-Kittel-Kasuya-Yosida) interaction it governs the physical properties of heavy-fermion (HF) compounds, which were discovered in 1975 (CeAl<sub>3</sub> [19]). Away from quantum critical points [20–22], these materials exhibit Landau-Fermi liquid behaviour at low temperatures with quasiparticles of very heavy mass. Thus, this material class is named HF compounds. In a small number of HF compounds, namely Kondo insulators/semiconductors, a narrow gap opens at low temperatures, leading to an insulating or semiconducting ground state.

Most Kondo insulators known to date exhibit a cubic crystal structure, e.g., SmB<sub>6</sub> [23, 24], YB<sub>12</sub> [25], Ce<sub>3</sub>Sb<sub>4</sub>Au<sub>3</sub> [26], CeFe<sub>4</sub>P<sub>12</sub> [27, 28], CeOs<sub>4</sub>Sb<sub>12</sub> [29], FeSi [30], URhSn [31], URhSb [31] and U<sub>3</sub>Sb<sub>4</sub>Pt<sub>3</sub> [32]. Only a few Kondo insulating materials with an orthorhombic crystal structure were found, e.g., CeNiSn [33], CeRhSb [34] and CeRhAs [35]. The compound CeRu<sub>4</sub>Sn<sub>6</sub> studied here crystallizes in a tetragonal crystal structure (space group:  $I\bar{4}2m$ ) and is thus situated between these two material classes. Only one other Ce-based compound, CeCuAs<sub>2</sub> [36], and one U-based compound, U<sub>2</sub>Ru<sub>2</sub>Sn [37, 38], form in a tetragonal structure and have been classified as Kondo insulators. The tetragonal crystal structure of CeRu<sub>4</sub>Sn<sub>6</sub> yields a more anisotropic environment for the Ce atom than in cubic systems but a higher symmetry than in the orthorhombic compound CeNiSn [33]. Thus, results on CeRu<sub>4</sub>Sn<sub>6</sub> may be simpler and easier to interpret than the complex behaviour of CeNiSn.

Polycrystalline CeRu<sub>4</sub>Sn<sub>6</sub> was first synthesized and characterized by electrical resistivity and magnetic susceptibility measurements from 2 K to room temperature by Das and Sampathkumar in 1992 [1]. In that work, the same physical properties of several other RRu<sub>4</sub>Sn<sub>6</sub> compounds (R = La, Gd and Y) were also investigated. The electrical resistivity of CeRu<sub>4</sub>Sn<sub>6</sub>

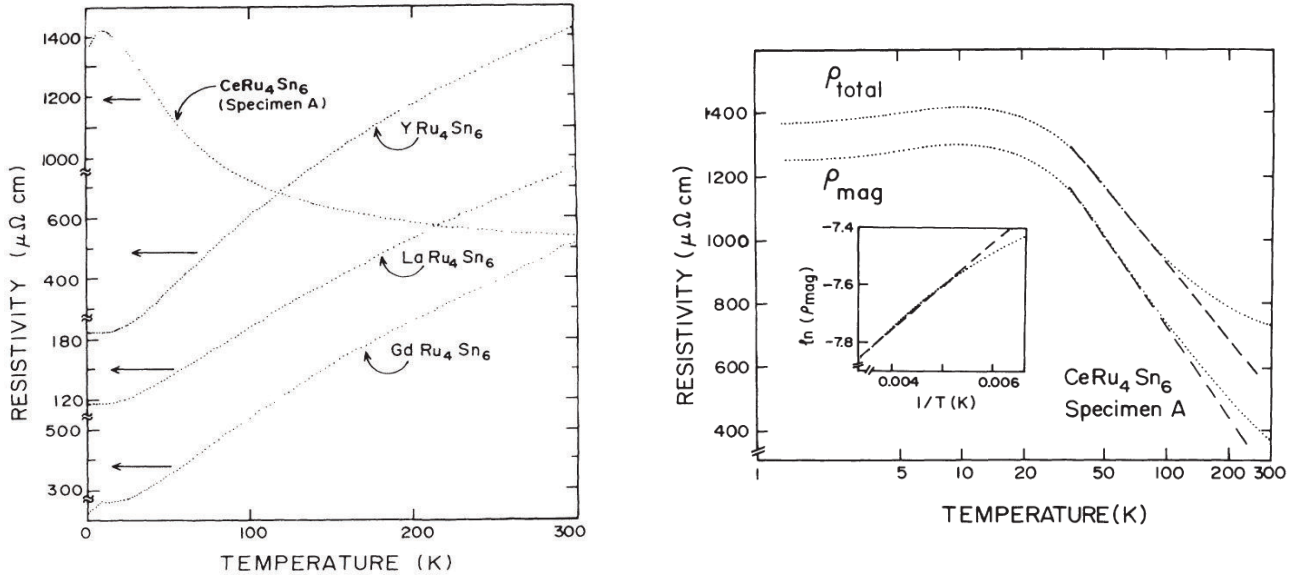


Figure 1.1: The left panel displays the electrical resistivity as a function of temperature for several  $\text{RRu}_4\text{Sn}_6$  compounds ( $R = \text{Ce}, \text{La}, \text{Gd}$  and  $\text{Y}$ ) measured by Das and Samarthkumaran [1]. In the right panel a semilogarithmic plot of the total electrical resistivity  $\rho_{\text{total}}$  and its magnetic contribution  $\rho_{\text{mag}}$  as a function of temperature is shown [1]. Within this plot, the  $-\ln T$  behaviour is marked with dashed lines. The inset displays the semiconducting behaviour at highest measured temperatures.

shows unique behaviour within this series, namely increasing electrical resistivity with decreasing temperature (Fig. 1.1, left panel). A maximum in the electrical resistivity at about 10 K was observed for one of three investigated  $\text{CeRu}_4\text{Sn}_6$  specimens, which was expected for a Kondo lattice. The other two investigated specimens of  $\text{CeRu}_4\text{Sn}_6$  showed either a maximum at lower temperatures or no maximum at all. The absence of a maximum was attributed to an excess of Ce in that sample. This spread in properties at low temperatures is characteristic for Kondo insulators; it is frequently difficult to distinguish between intrinsic and extrinsic effects, as seen for instance in  $\text{CeNiSn}$  [33, 39]. Interestingly,  $-\ln T$  behaviour, which is characteristic of incoherent Kondo scattering, was found only between 35 and 100 K (Fig. 1.1, right panel) [1]. The deviation from this law above 100 K persists even when the phonon contribution derived from  $\rho(T)$  measurements of  $\text{LaRu}_4\text{Sn}_6$  is subtracted (Fig. 1.1, right panel). This was attributed to the thermal activation of carriers across an energy gap of about 30 K (160 K) for the full (magnetic contribution to the) electrical resistivity. The magnetic measurements on  $\text{CeRu}_4\text{Sn}_6$  showed Curie-Weiss behaviour above 100 K, with a moment of  $\approx 2.7 \mu_B$  per Ce and a Weiss temperature of about -150 K. No magnetic ordering was detected down to 2 K.

In 1997, Pöttgen et al. published a detailed analysis of the crystal structure of  $\text{CeRu}_4\text{Sn}_6$  and several related compounds [40]. Additionally, heat capacity  $C_p$  and Mössbauer spectroscopy measurements of  $\text{CeRu}_4\text{Sn}_6$  were performed. In the temperature range between 10 and 20 K,  $C_p$  can be fitted with  $C_p = \gamma T + \beta T^3$ . This analysis yields  $\gamma \approx 40 \text{ mJ/mol K}^2$ . Furthermore, a strong

---

increase of  $C_p/T$  with decreasing temperature was observed at the lowest temperatures ( $> 2$  K). After an only weak  $T$ -dependent region of  $C_p/T$  between 4 and 10 K at about 275 mJ/mol K<sup>2</sup>,  $C_p/T$  increased rapidly with lowering temperature and reached a value of about 600 mJ/mol K<sup>2</sup> at 2 K.

In 2005, Guo investigated electronic transport properties of CeRu<sub>4</sub>Sn<sub>6</sub> and Ce<sub>1-x</sub>La<sub>x</sub>Ru<sub>4</sub>Sn<sub>6</sub> in his master thesis at the University of Johannesburg [41].

Also in 2005, an article by Strydom et al. [2] was published which shows results of electrical resistivity, magnetoresistivity, thermopower, thermal conductivity and Hall resistivity measurements on polycrystalline CeRu<sub>4</sub>Sn<sub>6</sub>. Within that work, electrical resistivity and magnetoresistance were measured from 0.4 K to room temperature (Fig. 1.2, left panel) and results similar to the ones of Das and Sampathkumaran [1] were observed. The electrical resistivity shows a maximum at about 10 K which is followed by a  $-\ln T$  behaviour to higher temperatures. The deviation of the magnetic contribution of the electrical resistivity from the  $-\ln T$  behaviour (indicated as line in Fig. 1.2, left panel) at temperatures above 100 K is less pronounced than in the measurements of Das and Sampathkumaran [1]. A weak decrease of the electrical resistivity with decreasing temperature is seen below 10 K. It is followed by a reincrease below 3 K. An applied magnetic field leads to a drastic suppression of this low-temperature resistivity upturn (inset Fig. 1.2, left panel). This behaviour was attributed to a field-induced stabilization of a metallic state [2] or, alternatively, to the negative magnetoresistance effect of a Kondo lattice at temperatures considerably larger than the coherence temperature [2]. The right panel of Fig. 1.2 shows the temperature dependences of the thermopower, thermal conductivity and Hall coefficient. Semiconductor-like behaviour was found in the thermopower (fit marked as line in Fig. 1.2, right panel, top), with an energy gap of 36 K. This value is close to the one found by Das and Sampathkumaran who derived a gap value of 30 K by fitting an Arrhenius expression to the electrical resistivity [1]. Thermopower and thermal conductivity show extrema at about 20 K, which is slightly larger than the temperature of the maximum in electrical resistivity (Fig. 1.2). The maximum in the thermal conductivity was related to a strongly reduced charge carrier concentration, which is also confirmed by the steady increase of the Hall coefficient with decreasing temperature (Fig. 1.2, right panel). It was concluded that a ground state of strongly correlated quasiparticles forms out of a state with low charge carrier concentration.

One year later, results of low-temperature muon spin relaxation ( $\mu$ SR) measurements on polycrystalline CeRu<sub>4</sub>Sn<sub>6</sub> were published by Strydom et al. [42]. Neither spontaneous nor magnetic field induced magnetic ordering was observed down to 50 mK. The data were interpreted as non-Fermi liquid (NFL) behaviour with a spin gap [42].

Also in 2006, nuclear magnetic resonance (NMR) investigations on CeRu<sub>4</sub>Sn<sub>6</sub> were published by Brüning et al. [43, 44]. The temperature dependence of the spin-lattice relaxation rate was shown to follow semiconductor-like behaviour down to 20 K, with an energy gap value of about 33 K, in overall agreement with the values found in [1] (30 K) and [2] (36 K). Below 20 K, an upturn is seen which was interpreted as the formation of a strong correlated state.

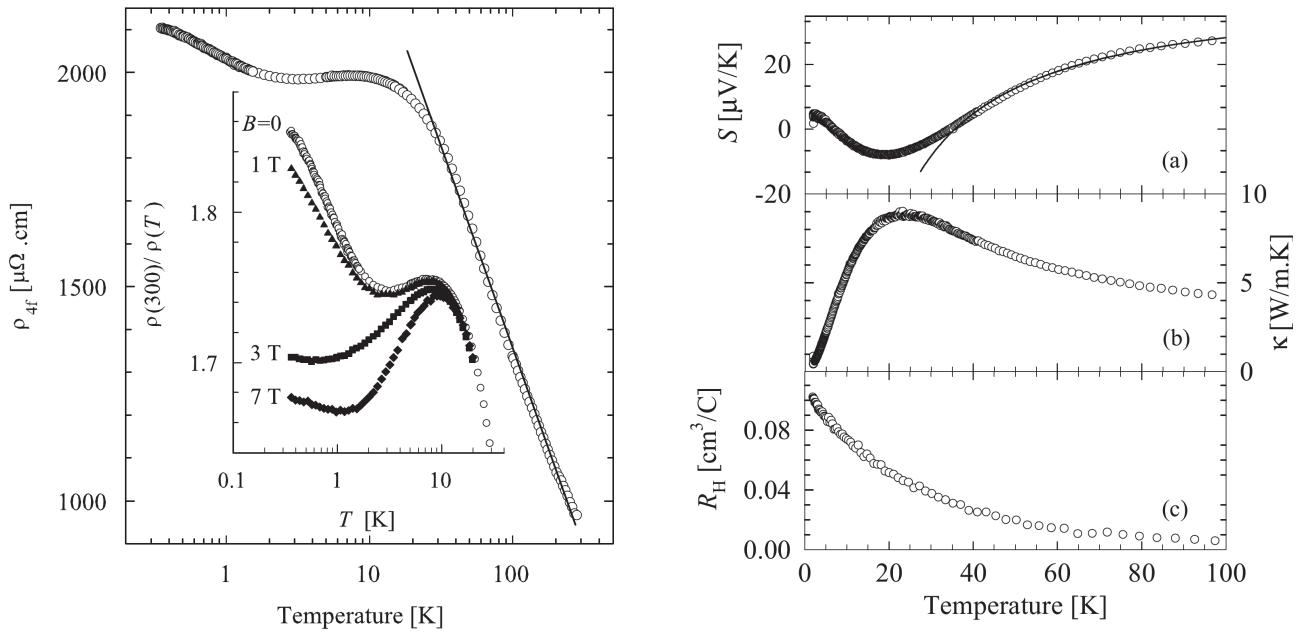


Figure 1.2: The left panel displays the magnetic contribution of the electrical resistivity  $\rho_{4f}$  as a function of temperature of polycrystalline  $\text{CeRu}_4\text{Sn}_6$  published by Strydom et al. [2]. In the right panel the thermopower  $S$ , thermal conductivity  $\kappa$  and the Hall constant  $R_H$  as a function of temperature are shown. These measurements were also published by Strydom et al. in 2005 [2].

High-energy inelastic neutron scattering (INS) measurements were performed on polycrystalline  $\text{CeRu}_4\text{Sn}_6$  by Adroja and Strydom et al. [45]. These measurements revealed a peak in the intensity at about 30 meV.

In 2010, Brüning et al. published thermopower, magnetic susceptibility, magnetization, heat capacity, entropy and  $^{119}\text{Sn}$  nuclear magnetic resonance (NMR) measurements on polycrystalline  $\text{CeRu}_4\text{Sn}_6$  [46]. The zero-field thermopower is consistent with results of [2]. In an applied field of 9 T a peak at around 5 K develops, which was attributed to magnetically sensitive in-gap states. The magnetic-field dependent heat capacity, NMR and magnetization data were modeled with a doubly-gapped electronic density of states (DOS), with a large pseudo-gap of about 30 K and a narrow gap within residual in-gap states of 0.65 K at zero field [46].

The pressure dependence of the electrical resistivity and magnetoresistivity of polycrystalline  $\text{CeRu}_4\text{Sn}_6$  was investigated by Sengupta et al. in 2012 [47]. The electrical resistivity increased with applied pressure up to 15.1 kbar, but shows a slight decrease at higher pressures up to 20.6 kbar at 1.8 K. In addition, shoulder-like features were determined in the temperature dependencies of the electrical resistivity. These features were attributed to the interplay between the effects of Kondo coherence and the hybridization. Magnetoresistivity measurements at 15.1 kbar and 1.8 K revealed a minimum at  $\approx 6$  T. The authors concluded that a non-monotonic response of the gap opening as a function of pressure was the origin of this behaviour, similar

---

to the case of CeRhSb [48].

The first measurements on single crystalline CeRu<sub>4</sub>Sn<sub>6</sub> were made in 2008 within the diploma thesis of Nezu at the Vienna University of Technology [10]. Within that work, electrical resistivity, Hall resistivity and magnetic susceptibility measurements were performed. The electrical resistivity showed behaviour similar to that of polycrystalline CeRu<sub>4</sub>Sn<sub>6</sub> [1, 2], namely a maximum at about 10 K, followed by a  $-\ln T$  behaviour in the range between 30 and 100 K. Another important result was the determination of the anisotropy of the magnetization along three orthogonal directions in CeRu<sub>4</sub>Sn<sub>6</sub>, which were not determined exactly. This uncertainty was caused by the orientation process with the available Laue device, which yields could not discriminate between the [110] and [001] direction. A well defined orientation of CeRu<sub>4</sub>Sn<sub>6</sub> single crystals was achieved later in the master thesis of the present author [49]. Finally, a detailed analysis of the crystal growth procedure by Nezu provided an excellent basis for the single crystal growth within this PhD thesis (Sect. 4.2).

Anisotropies in the magnetization and magnetic field-dependent heat capacity were studied in the master thesis of the present author at the Vienna University of Technology [49]. As already mentioned above, a defined orientation of the CeRu<sub>4</sub>Sn<sub>6</sub> single crystals was achieved. So, the tetragonal (001) plane directions ([100] and [110]) and the perpendicular direction [001] were investigated. A clear anisotropy between the tetragonal (001) plane and the orthogonal [001] direction was found for both investigated physical properties [50].

Below, the status of affairs at the beginning of this PhD thesis is summarized. Electrical resistivity measurements performed by several groups exhibited a maximum at about 10 K, a  $-\ln T$  behaviour between 30 and 100 K, a semiconductor-like exponential behaviour at higher temperatures, and an increase of the electrical resistivity at temperatures below 2 K. Hall effect measurements confirmed the low charge carrier concentration at lowest temperatures. These findings were attributed to a pseudo-gapped electronic structure at lowest temperatures. However, any details about the electronic structure remained unknown. Due to the only small increase of the electrical resistivity at lowest temperatures in comparison to other Kondo insulators, the presence of directional dependent (pseudo-) gaps or extrinsic in-gap states was suggested. To clarify the origin of the observed electrical resistivity behaviour and reveal and understand its anisotropy, detailed investigations of the directional dependent electronic transport were performed within this thesis.

Also the nature of the magnetic ground state remained unclear: Magnetization measurements on polycrystalline CeRu<sub>4</sub>Sn<sub>6</sub> suggested that the 6-fold degenerate  $^2F_{5/2}$  ground state multiplet of the Ce<sup>3+</sup>-4*f* state was essentially degenerate (no crystalline electric field (CEF) splitting) [46]. By contrast, a remarkable CEF splitting was suggested by an analysis of the entropy of polycrystalline CeRu<sub>4</sub>Sn<sub>6</sub> [46], by the anisotropic non-Curie-Weiss like magnetic susceptibility of single crystalline CeRu<sub>4</sub>Sn<sub>6</sub> [10, 49] and by the measured peak at 30 meV in the inelastic neutron scattering measurements [45]. Another result that caused confusion was the absence of a maximum in the temperature dependent magnetic susceptibility, that is usually found

in Kondo insulators like, e.g.,  $\text{Ce}_3\text{Bi}_4\text{Pt}_3$  [51]. Therefore, a detailed analysis of the magnetic behaviour in terms of CEF effects was performed within this thesis.

In conclusion, simple models of the underlying physics failed to describe the overall behaviour of  $\text{CeRu}_4\text{Sn}_6$ . Instead several mechanism were put forward to describe selected aspects of the behaviour of  $\text{CeRu}_4\text{Sn}_6$ . Within this thesis, possible contributing mechanism were investigated in much greater depth, paying special attention to the anisotropy and its origin in a  $k$ -dependent electronic structure.

This PhD thesis is organized as follows. Next, the theoretical concepts (Chap. 2) and the experimental techniques (Chap. 3) used within this thesis were discussed. In the following chapter, the crystallographic properties and the single crystal growth of  $\text{CeRu}_4\text{Sn}_6$  are presented (Chap. 4). Then, the results of theoretical local density approximation and dynamic mean-field theory calculations performed by P. Wissgott within his PhD thesis in parallel to the experimental investigations are briefly discussed [9] (Chap. 5). Next, the physical properties measurements on  $\text{CeRu}_4\text{Sn}_6$  made within this thesis are presented (Chap. 6). Sections 6.1 to 6.5 presents magnetization, torque magnetometry, electrical resistivity, Hall effect, magnetoresistivity and thermopower measurements, respectively. In addition, the results of the X-ray absorption spectroscopy, optical spectroscopy investigations and cleaving tests in combination with STM investigations performed by collaborators on  $\text{CeRu}_4\text{Sn}_6$  samples provided within this thesis are discussed (Sect. 6.6). In Chap. 7 a summarizing discussion of the performed measurements and their conclusion is presented.



# Chapter 2

## Theory

### 2.1 Single-ion Kondo effect

In 1934, de Haas et al. [18] observed a minimum in the electrical resistivity of Au including Fe impurities at low temperatures and an increasing electrical resistivity to the lowest achievable temperatures. This phenomenon was unexplained for about 30 years and several other alloys showing comparable behaviour were found within this period. In 1964, Kondo succeed to describe this phenomenon theoretically [17]. The conduction electrons interact with the magnetic moment of the localized electrons, introduced by the dissolved impurities, via the spin-exchange interaction (so called Zener model or  $s$ - $d$  interaction) [52]. The spin of the conduction electrons in an  $s$ -band interact with the localized spins of the electrons in the  $d$ -shell. The Heisenberg Hamilton operator [53] is given by

$$H = -J(\vec{r})\vec{\sigma}\vec{S} \quad , \quad (2.1)$$

with the exchange integral  $J$ , the conduction electron spin  $\vec{\sigma}$  and the spin of the magnetic impurity  $\vec{S}$ . Kondo found that by considering also second-order scattering processes, a logarithmic temperature dependence of the scattering between the localized and conduction electrons is observed. If  $J$  is negative (antiferromagnetic, conduction electrons screen localized moments) the electrical resistivity increases with decreasing temperature as  $\rho \propto -\ln T$ .

In general, the single-ion Kondo effect is observed in diluted alloys with a small amount of magnetic impurities including electrons in the  $3d$ ,  $4f$  or  $5f$  shell. The large distances between the magnetic impurities prohibit a direct interaction between the magnetic impurities. The single-ion Kondo effect yields a nonmagnetic ground state and an energetically higher lying triplet, which is separated by the characteristic energy scale

$$k_B T_K \approx D e^{-\frac{1}{2|J|N(E_F)}} \quad , \quad (2.2)$$

containing the half band width  $D$  and the density of states (DOS) at the Fermi energy  $N(E_F)$  of the conduction electron band.  $J$  is determined by the hybridization strength or matrix element

of the  $s$ - $f$  mixing  $V_{sf}$  and by the binding energy of the  $4f$  level  $\epsilon_{4f}$  via

$$J = -\frac{V_{sf}^2}{|\epsilon_{4f}|} . \quad (2.3)$$

The hybridization between the localized and conduction electrons leads to a strong enhancement of (sharp peak in) the DOS in the vicinity of the Fermi energy with a width of about  $k_B T_K$ , namely the Kondo or Abrikosov-Suhl resonance. For  $T \gg T_K$ , the physical properties are almost unaffected and show metal-like behaviour. For instance, the localized  $4f$  moments are unscreened and show paramagnetic Curie-Weiss (CW) behaviour. The CW formula (Pierre Curie 1896, Pierre-Ernest Weiss 1907) is given by

$$\chi = \frac{C}{T - \Theta} , \quad (2.4)$$

which contains the Curie constant  $C$ , the temperature  $T$  and the Weiss temperature  $\Theta$ .  $C$  is given by  $C = N_A \mu_{eff}^2 / (3k_B)$  with the Avogadro constant  $N_A$ , the effective moment  $\mu_{eff}$  and the Boltzmann constant  $k_B$ .

For  $T \approx T_K$ , the hybridization effects become important and yield the typical  $-\ln T$  behaviour in the electrical resistivity.

## 2.2 Kondo lattice

If the concentration of the magnetic impurities ( $3d$ ,  $4f$  or  $5f$  ions) is increased, the mutual interaction can no longer be neglected. If the impurities completely occupy at least one lattice site, a so-called Kondo lattice (KL) is developed. The physical properties are qualitatively different from the diluted Kondo systems discussed above. The behaviour of KLs can be phenomenologically described by a model of S. Doniach [54]. At high temperatures ( $T > T_K$ ), all physical properties of KLs can be described properly by single impurity models (Kondo impurity (KIMP) models). Thus, the localized moments behave as independent moments (independent from each other) at high temperatures. At lower temperatures, distinct differences are found between the KIMP and KL model. The differences are seen, e.g., in the electrical resistivity (Fig. 2.1, left panel). The KIMP system shows the characteristic logarithmic increase with decreasing temperature saturating at lowest temperatures. By contrast, the logarithmic increase in KL systems ( $\rho \propto -\ln T$ ) ends in a maximum at  $T_{max} \propto T_K$ . In the following a strong decrease sets in, ending typically in a  $\rho = \rho_0 + AT^2$  ( $A$  = coefficient) behaviour of the electrical resistivity well below  $T_{max}$ . This decrease can be explained by the translation symmetry of the scattering centers enabling the conducting electrons to pass the scattering centers in form of Bloch waves.

Physical property measurements of non-magnetic KLs revealed that the coefficient  $A$  in the  $T^2$ -dependent electrical resistivity term, the linear specific heat coefficient  $\gamma$  and the temperature

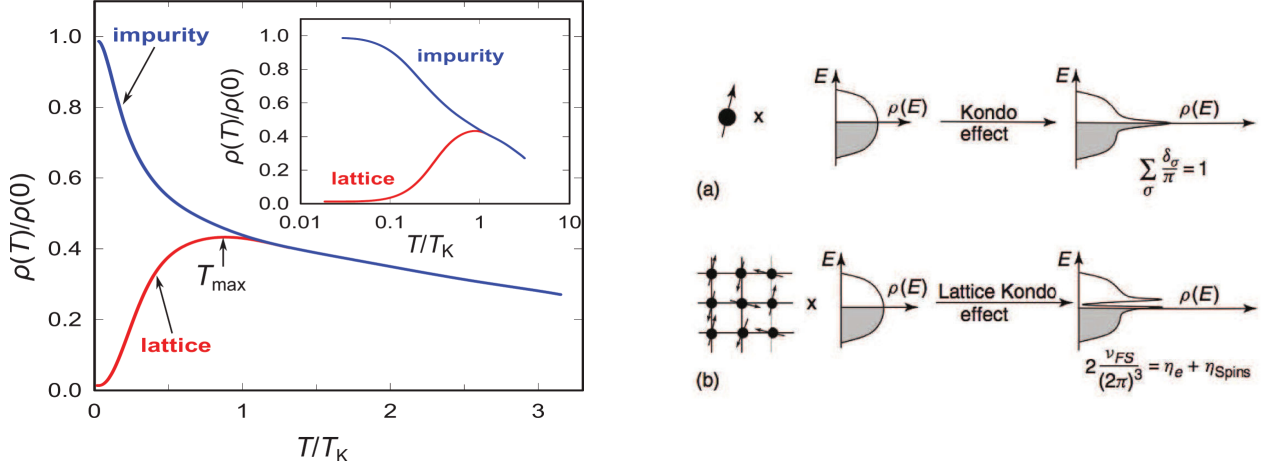


Figure 2.1: Left: Schematic temperature dependence of the magnetic contribution to the electrical resistivity  $\rho(T)/\rho(0)$  [55]. Right: Schematic drawing of the evolution of the density of states for Kondo impurity (top) and Kondo lattice (bottom) systems [56] (extracted from [57]).

independent susceptibility  $\chi$  at low temperatures achieve large values in comparison to the ones found in normal metals. This enhancement is attributed to a strongly enhanced effective electron mass  $m^*$  (about 100-1000  $m_e$ ) within the Landau-Fermi liquid theory. Thus, these compounds are called heavy-fermion (HF) systems.

The differences between KIMP and KL systems in the DOS are schematically displayed in Fig. 2.1, right panel. In KL systems the resonance in the vicinity of the Fermi energy  $E_F$  splits and a small hybridization gap opens [56, 57].

In addition to the changes of the Kondo physics in KL, the magnetic exchange interaction between the localized electrons has to be taken into account. In metallic 4f systems, this interaction arises predominantly from the spin polarization of the conduction electrons (Ruderman-Kittel-Kasuya-Yosida (RKKY) interaction). The spin polarization has a damped oscillatory character and is given by the RKKY exchange

$$J_{RKKY} \propto J^2 N(E_F) \frac{x \cos(x) - \sin(x)}{x^4}, \quad (2.5)$$

with  $x = 2\vec{k}_F \vec{r}_{ij}$  ( $\vec{k}_F$  = Fermi wave vector). Thus, the magnetic ordering at low temperatures due to the RKKY interaction can be either ferromagnetic or antiferromagnetic. Note that the periodicity of the RKKY interaction does not necessarily coincide with the lattice translation symmetry. In fact, compounds with incommensurate propagation vectors are frequently found (e.g.  $\text{CeCu}_{6-x}\text{Au}_x$  [58]).

In conclusion, the competition between two different interactions, namely the RKKY interaction (magnetic ground state) and the Kondo effect (singlet formation, non-magnetic ground

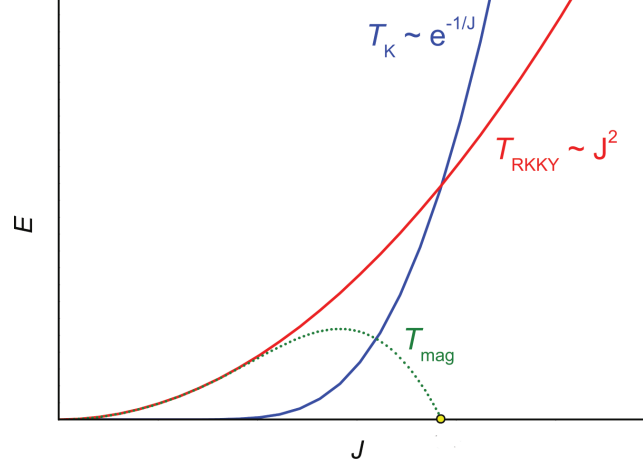


Figure 2.2: Doniach phase diagram [54]. The different  $J$ -dependence (exchange integral-dependence) of the Kondo interaction strength ( $T_K$ ) and RKKY interaction strength ( $T_{RKKY}$ ) yield to a dominance of the RKKY interaction (Kondo effect) at low (high)  $J$ . In the intermediate region, where  $T_K \approx T_{RKKY}$  the magnetic ordering ( $T_{mag}$ ) is suppressed to zero [54].

state), leads to manifold characteristics in KL systems at lowest temperatures. The interplay between the energy scales  $T_{RKKY} \propto J^2 N(E_F)$  and  $T_K \propto \exp(-\frac{1}{2|J|N(E_F)})$  is presented in Fig. 2.2 via the Doniach Phase diagram [54]. For a small exchange integral  $J$ , the RKKY interaction dominates and a magnetically ordered ground state is formed. In contrast, the Kondo interaction dominates at high  $J$  leading to valence fluctuating or intermediate valence compounds. In the intermediate region (HF systems), where  $T_K \approx T_{RKKY}$ , the interplay of the Kondo effect and RKKY interaction leads to an elimination of the magnetic order (indicated by  $T_{mag}$  in Fig. 2.2) [54]. In general,  $J$  may be varied by chemical doping or by applying pressure. In Ce (Yb) compounds, hydrostatic pressure increases (decreases)  $J$ . Note that the Doniach model exhibits very simple assumptions and a quantitative comparison to experimental results may be not reliable, as discussed in [59].

## 2.3 Kondo insulator

A small group of Kondo lattice systems, namely Kondo insulators/semiconductors (KI/KS), show insulating/semiconducting behaviour at low temperatures due to the opening of a narrow energy gap at the Fermi level. At high temperatures, the behaviour of KI systems is reminiscent to that of KIMP systems, which can be properly described by uncorrelated scattering of the conduction electrons from the localized  $f$ -electrons. A simplified model to describe the narrow energy gap at the Fermi level at lowest temperatures is a hybridization-induced energy gap model shown in Fig. 2.3. The insulating gap arises by the hybridization of a flat  $f$ -electron

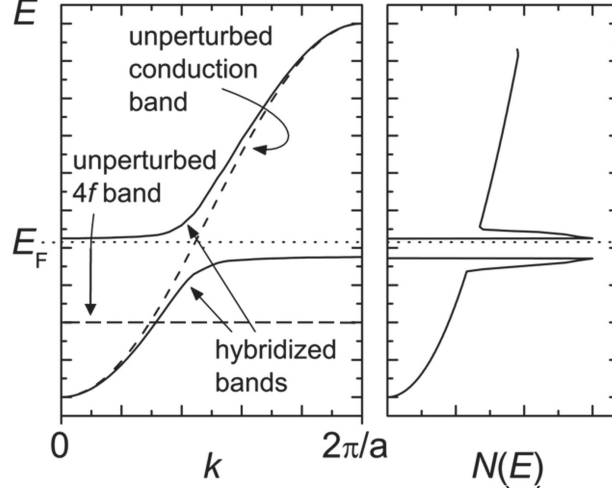


Figure 2.3: Schematic electronic band structure (left) and density of states (right) of a Kondo insulator described by a simplified Anderson lattice model extracted from [4] according to [3].

band with a broad conduction band. A flat  $f$  band crossing only one conduction electron band is essential to obtain a gapped DOS and a half-filling of the hybridized bands ( $E_F$  in the gap, insulating state).

A basic model to describe the behaviour of KI is the Anderson lattice model [3]. The total Hamiltonian is given by

$$H_A = H_f + H_c + H_{cf} \quad , \quad (2.6)$$

where the Hamiltonian  $H_f$  ( $H_c$ ) describes the localized  $f$  (conduction) electrons and  $H_{cf}$  describes the hybridization between  $f$  and conduction electrons.  $H_{cf}$  is given by

$$H_{cf} = N_s^{-1/2} \sum_{i, \vec{k}, \alpha} \left[ V(\vec{k}) \exp(-i\vec{k}\vec{R}_i) f_{i, \alpha}^+ c_{\vec{k}, \alpha} + V^*(\vec{k}) \exp(i\vec{k}\vec{R}_i) f_{i, \alpha} c_{\vec{k}, \alpha}^+ \right] \quad , \quad (2.7)$$

with the total number of lattice sites  $N_s$ , the hybridization matrix element  $V$ , the site denomination  $i$ , the Bloch wave vector  $\vec{k}$ , the space vector to the lattice sites  $R_i$ , the creation (annihilation) operator for localized  $4f$  electrons  $f_{i, \alpha}^+$  ( $f_{i, \alpha}$ ), the creation (annihilation) operator for conduction electrons  $c_{\vec{k}, \alpha}^+$  ( $c_{\vec{k}, \alpha}$ ) and the combined spin-orbit label  $\alpha$ . If the Coulomb repulsion of the  $f$  electrons for a doubly occupied lattice site is neglected,  $H_A$  is exactly solvable. The band structure displayed in Fig. 2.3 (left panel) is achieved with this simplification if the binding energy of the  $f$  levels lies within the bandwidth of the unhybridized conduction electrons. For a half-filling of the resulting band structure, an insulating state develops. Ongoing theoretical approaches including dynamic mean-field theory calculations can be found, e.g., in [60].

The Anderson lattice model (Eqn. 2.6) was used by Ikeda and Miyake [5] to explain the behaviour of the anisotropic Kondo insulator CeNiSn by assuming an anisotropic  $V(\vec{k})$  (Eqn. 2.7).

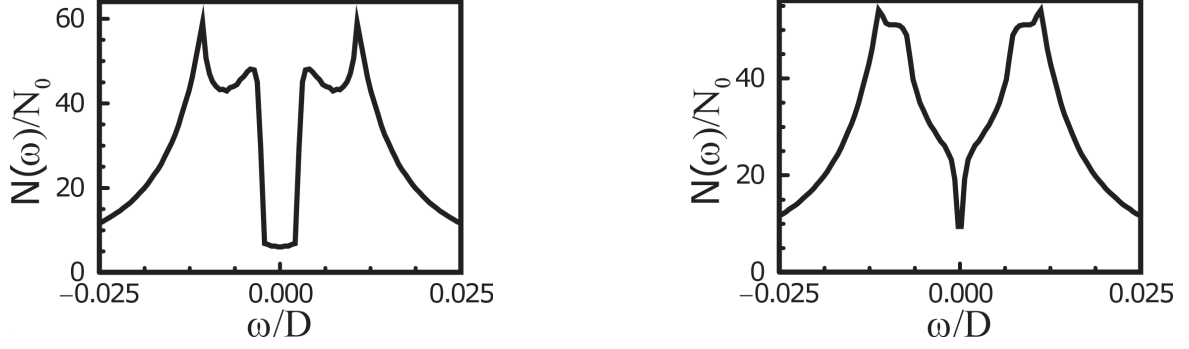


Figure 2.4: Theoretically calculated density of states as a function of the energy in anisotropic Kondo insulators by Ikeda and Miyake [5] (left) and by Moreno and Coleman [6] (right). The density of states was calculated with different theoretical approaches. These plots were extracted from [6].

This approach yield a partially closed energy gap in the  $k$  space (Fig. 2.4, left panel). An alternative approach to described the anisotropic gap formation in CeNiSn was made by Moreno and Coleman [6] yielding comparable results (Fig. 2.4, right panel).

## 2.4 Landau-Fermi liquid theory

One of the most important theories in solid state physics is the Landau-Fermi liquid (LFL) theory, which was presented by Landau [61] (1956) to describe the physical properties of liquid  $^3\text{He}$ .

The low-temperature behaviour of simple metals can be described by the Sommerfeld theory, which assumes an ideal Fermi gas of non-interacting electrons. The success of this theory is surprising because the Coloumb interacting between the electrons is of the same magnitude as their kinetic energy. Landau demonstrated that the derived results describe fermionic quasiparticles and not free electrons. The difference between the quasiparticles and the electrons is only an enhanced effective mass  $m^*$  induced by the Coloumb interaction. This interaction is incorporated in the LFL theory via the Landau parameters  $F_l^{s(a)}$ .  $m^*$  is given by

$$m^* = m_e \left(1 + \frac{1}{3} F_1^s\right) \quad , \quad (2.8)$$

with the electron mass  $m_e$ . The magnetic susceptibility  $\chi_{LFL}$  (including the Bohr magneton  $\mu_B$ ) and the electronic contribution to the electrical resistivity  $\rho_{LFL}$  ( $A$ =coefficient) are given by

$$\chi_{LFL} = 2\mu_B^2 N(E_F) \frac{1}{1 + F_0^a} = 2\mu_B^2 N_0(E_F) \left(1 + \frac{1}{3} F_1^s\right) \frac{1}{1 + F_0^a} \quad \text{and} \quad (2.9)$$

$$\rho_{LFL} = AT^2, \text{ where } A \propto m^{*2} \quad . \quad (2.10)$$

Due to the dependence of the coefficients  $\gamma$  (linear specific heat term),  $\chi$  and  $A$  to the DOS  $N(E_F)$  an almost constant relation between, e.g.,  $\chi / \gamma$  (Sommerfeld-Wilson ratio (SWR)) can be found, although the absolute values of  $\chi$  differ over a few orders of magnitude for different compounds [62]. The SWR ( $\mu_{eff}$  = effective moment) is given by

$$\text{SWR} = \left( \frac{\pi k_B}{\mu_{eff}} \right)^2 \frac{\chi}{3\gamma} = \frac{1}{1 + F_0^a} \quad (2.11)$$

where  $\mu_{eff}$  is the effective moment. Non-interacting systems yield  $\text{SWR} = 1$ . In HF compounds, SWR values of 2-5 are usually found [55].

## 2.5 The Coqblin-Schrieffer model

A KIMP model that takes crystal field effects into account was derived by Coqblin and Schrieffer in 1969 (Coqblin-Schrieffer (CS) model) [63]. Although the CS model is a single-impurity model, the physical properties of concentrated Kondo and Kondo lattices systems are well described in the high-temperature range. Within this thesis, the magnetic contribution to the electrical resistivity  $\rho_{mag}$  and to the thermopower  $S_K$  are discussed within the CS model.  $S_K$  is described in Sect. 2.6. The CS Hamiltonian and  $\rho_{mag}$  are discussed below.

The CS model is a simplified variant of the Anderson model with an almost integer valence of the  $4f$  impurity. Due to the strong spin-orbit coupling in rare earth (RE) ions the total angular quantum number  $j$  is a good quantum number. For Ce, the  $4f$  levels split due to spin-orbit coupling into  $j = 5/2$  and  $j = 7/2$  multiplets. The excited  $7/2$  levels are usually situated more than 100 meV above the ground state level with  $j = 5/2$ . Thus, the  $7/2$  level can usually be neglected. The CS Hamiltonian  $H_{CS}$  is given by

$$H_{CS} = H_0 + H_1 \quad (2.12)$$

with

$$H_0 = \sum_{k,M} \epsilon_k n_{k,M} + \sum_M E_0 n_M + (1/2)U \sum_{M,M'} n_M n_{M'} \quad (2.13)$$

and

$$H_1 = \sum_{k,M} (V_{kf} c_{k,M}^+ f_M + V_{kf}^* f_M^+ c_{k,M}^+) \quad (2.14)$$

These formulas contains the wave vector  $\vec{k}$ , the spin  $M$ , the number operators  $n$ , the energy of the conduction electrons  $\epsilon$ , the unperturbed energy of the  $4f$  electrons  $E_0$ , the Coloumb interaction  $U$ , the hybridization matrix element  $V_{kf}$ , the annihilation (creation) operator for a conduction electron  $c_{k,M}$  ( $c_{k,M}^+$ ) and the annihilation (creation) operator for localized  $4f$  electrons  $f_M$  ( $f_M^+$ ). In the case of Ce impurities  $f_M$  ( $M = m_j$ ) annihilates a localized  $4f$  state with  $j = 5/2$  and  $m_j = 1/2, 3/2$  or  $5/2$ .  $c_{k,M}$  eliminates a conduction electron wave function

with  $l = 3$ ,  $j = 5/2$  and  $M = m_j$ . Using the Schrieffer-Wolff transformation (only valid for almost integer  $4f^1$  configuration of Ce impurities) and including the influence of the crystalline electric field (CEF) (splitting of the 6-fold degenerate ground state) the effective exchange Hamilton  $H_1$  can be written as

$$H_1 = - \sum_{k,k',M,M'} (J_{MM'} c_{k,M}^+ c_{k',M} (f_M^+ f_M' - \delta_{MM'} \langle n_M \rangle)) + \bar{V} \sum_{k,k',M} c_{k',M}^+ c_{k,M}^+ \quad . \quad (2.15)$$

In Eqn. 2.15, the first (second) term describes the exchange interaction (direct interaction  $\bar{V}$  of the impurity moments with the conduction electrons). The occupation number  $\langle n_M \rangle$  is derived by a mean field approximation. In the limit of large values of  $U$  [55],  $J_{MM'}$  can be written as

$$J_{MM'} = 1/2 |V_{kf}|^2 \left( \frac{1}{E_M} + \frac{1}{E_{M'}} \right) \quad , \quad (2.16)$$

with the energy  $E_M$  (relative to  $E_F$ ) of the localized  $4f$  electron created by  $f_M^+$ .

## Electrical resistivity

In 1973 Cornut and Coqblin [7, 59] calculated the electrical resistivity due to the Kondo effect in a CEF-split environment. They used a third order perturbation-type calculation to determine the relaxation time  $\tau_k$ , which is given by

$$1/\tau_k = \frac{m_e k V_0}{\pi \hbar^3 (2j + 1)} (R_k + S_k) \quad . \quad (2.17)$$

This equation contains the electron mass  $m_e$ , the sample volume  $V_0$  and the second (third) order term  $R_k \propto J^2$  ( $S_k \propto J^3$ ). In addition to  $\tau_k$ , the CEF-split energy levels were taken into account by Coqblin and Cornut to obtain the electronic transport equations used within this thesis (Eqns. 2.18 and 2.27).

The magnetic contribution to the electrical resistivity  $\rho_{mag}(T)$  from the direct (Eqn. 2.18, first term, usual spin disorder resistivity, second order perturbation type) and the resonant (Kondo) scattering (Eqn. 2.18, second term, third order perturbation type) is given by

$$\rho_{mag}(T) = A J^2 N(E_F) \left[ \frac{\lambda_n^2 - 1}{\lambda_n (2j + 1)} + 2 J N(E_F) \frac{\lambda_n^2 - 1}{(2j + 1)} \ln \left( \frac{k_B T}{D_n} \right) \right] \quad . \quad (2.18)$$

This formula includes a constant  $A$ , the exchange parameter  $J$ , the DOS  $N(E_F)$ , the effective degeneration level of the  $4f$  levels  $\lambda_n$ , the total angular quantum number  $j$ , the Boltzmann constant  $k_B$  and the bandwidth of the conduction electrons  $D_n$  (acts as cut-off parameter). An exemplary  $\rho_{mag}(T)$  curve calculated with Eqn. 2.18 is shown in Fig. 2.5, left panel [7]. The consequences of different direct scattering strength  $\bar{V}$  and different  $N(E_F)$  are presented in the right panel of Fig. 2.5 [7].



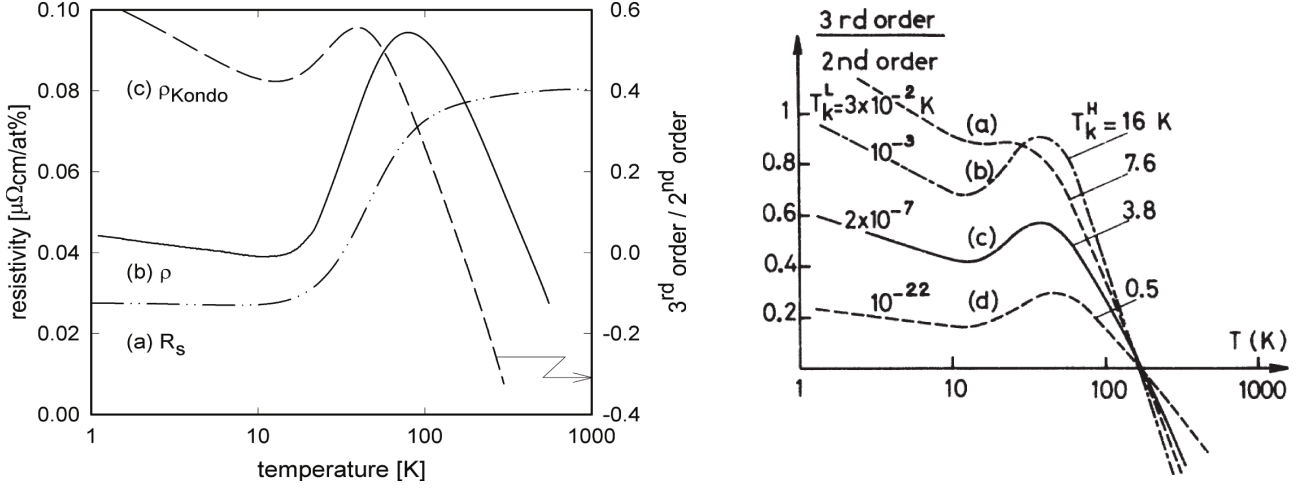


Figure 2.5: Left: Temperature dependence of the (a) spin disorder resistivity (first term in Eqn. 2.18), (b) total magnetic contribution to the electrical resistivity  $\rho_{\text{mag}}$  and (c) weighted Kondo scattering contribution (Eqn. 2.18, (term 2)/(term 1)). This plot was extracted from [7, 55]. Used parameters for calculation: CEF splitting energy  $\Delta_{01} = 100$  K,  $D = 400$  K,  $\bar{V} = 0.05$  eV,  $N(E_F) = 0.5$  eV $^{-1}$ , ground state degeneracy  $\alpha_0 = 2$  and excited CEF state degeneracy  $\alpha_1 = 4$ . Right: Temperature dependence of the weighted Kondo contribution for different  $\bar{V}$  and  $N(E_F)$  on a semilogarithmic scale extracted of [7]. The parameters  $\Delta_{01}$ ,  $D$ ,  $\alpha_0$  and  $\alpha_1$  are listed above. The influence of the direct scattering is compared by  $N(E_F) = 0.5$  eV $^{-1}$  and (a)  $\bar{V} = 0$  eV, (c)  $\bar{V} = 0.05$  eV or (d)  $\bar{V} = 0.1$  eV (dashed lines). In addition, the influence of the DOS is compared with  $\bar{V} = 0.05$  eV and (b)  $N(E_F) = 0.8$  eV $^{-1}$  or (c)  $N(E_F) = 0.5$  eV $^{-1}$ .

## 2.6 Thermopower

A temperature gradient applied across a specimen leads to an electric field between the hot and the cold side. This effect is based on the temperature dependence of the Fermi-Dirac distribution, which leads to a higher average velocity and higher number of mobile charge carriers at the warm end of the sample. Thus, a net diffusion of carriers from the hot to the cold side of the specimen sets in and an internal electric field develops. Due to the major role of the electronic structure and the scattering processes of the involved electrons for this effect, information about the electronic structure of the investigated material can be extracted. In general, the thermopower is given by

$$S = S_e + S_p + S_m \quad , \quad (2.19)$$

including the electron diffusion term  $S_e$ , the phonon-drag term  $S_p$  and the magnon-drag term  $S_m$ .  $S_p$  and  $S_m$  are effects of second order. The electronic diffusion contribution  $S_e$  to  $S$  (without including inelastic scattering processes), calculated with the linearized Boltzmann equation ( $k_B T \ll E_F$ ), is defined by the Mott relation as

$$S_e(T) = \frac{\pi^2 k_B^2}{3e} T \left( \frac{\partial \ln \sigma(\epsilon)}{\partial \epsilon} \right)_{\epsilon=E_F} \quad , \quad (2.20)$$

which includes the Boltzmann constant  $k_B$ , the electron charge  $e$ , the temperature  $T$ , the dc electrical conductivity  $\sigma$ , the energy  $\epsilon$  and the Fermi energy  $E_F$ .  $S_e$  is direct proportional to the temperature  $T$  and to the logarithmic derivative of  $\sigma$  with respect to the charge carrier energy at the Fermi level  $E_F$ . The sign of  $S_e$  thus depends on the sign of the charge carriers (p- or n-type) and on the energy derivative of  $\ln \sigma$ . By contrast, the Hall constant  $R_H$  depends only on the sign of the charge carriers and, if multiple conduction bands exist, on the respective charge carrier mobility of each band (Sect. 2.7). For a spherical Fermi surface and an isotropic relaxation time  $\tau$ ,  $\sigma$  derived via the Bloch-Boltzmann theory is given by

$$\sigma = \frac{e^2}{3} N(\epsilon) v_g^2(\epsilon) \tau(\epsilon) \quad , \quad (2.21)$$

with the elementary charge  $e$ , the density of states (DOS)  $N$ , the group velocity  $v_g$  and the relaxation time  $\tau$ . Combining Eqns. 2.20 and 2.21 yields

$$S_e(T) = \frac{\pi^2 k_B^2}{3e} T \left( \frac{\partial \ln N(\epsilon)}{\partial \epsilon} + \frac{\partial \ln v_g^2(\epsilon)}{\partial \epsilon} + \frac{\partial \ln \tau(\epsilon)}{\partial \epsilon} \right)_{\epsilon=E_F} \quad , \quad (2.22)$$

with three different terms contributing to  $S_e$ . For normal metals (e.g., Na, Al, Au), the second and third term are negligible in comparison to the first term. Therefore, Eqn. 2.22 can be simplified to

$$S_e(T) = \frac{\pi^2 k_B^2}{3e} T \left( \frac{\partial \ln N(\epsilon)}{\partial \epsilon} \right)_{\epsilon=E_F} \quad . \quad (2.23)$$

In a free-electron model with the assumption of an energy-independent  $\tau$ , Eqn. 2.23 simplifies to

$$S_e(T) = \frac{\pi^2 k_B^2}{2 e E_F} T \quad . \quad (2.24)$$

The absolute values of  $S$  for normal metals are of the order of a few  $\mu\text{V}/\text{K}$  at room temperature.

In Kondo systems,  $S_p$  is in general small in comparison to  $S_e$ . In addition,  $S_m$  is not relevant for paramagnetic  $\text{CeRu}_4\text{Sn}_6$ . So, it is assumed that  $S \approx S_e$ . If different independent scattering processes (different  $\tau$ ) occur,  $S_e$  is, according to the Gorter-Nordheim rule, given by

$$S_e \kappa^{-1} = \sum_i S_{e,i} \kappa_i^{-1} \quad , \quad (2.25)$$

with the thermal conductivity  $\kappa$  and the respective contributions  $i$ . If the Wiedemann-Franz law is used, Eqn. 2.25 can be converted into

$$S_e \rho = \sum_i S_{e,i} \rho_i \quad (2.26)$$

with the electrical resistivity  $\rho$ . Hence, if the Wiedemann-Franz law is valid, the different contributions to  $S_e$  can be separated with the help of electrical resistivity measurements. For Kondo systems, the separation between the contributions to  $S_e$  due to light charge carriers and due to Kondo scattering may be separable using Eqn. 2.26.

### Thermopower in heavy-fermion and Kondo systems

In heavy-fermion (HF) systems, the hybridization between the localized  $f$  and itinerant  $s,p$  and/or  $d$  electrons yields a peaked structure (Kondo or Abrikosov-Suhl resonance) in the DOS in the vicinity of the Fermi energy. Therefore, the energy derivative of  $N(E)$  is strongly enhanced in comparison to normal metals. In addition,  $E_F$  of HF systems is reduced in comparison to normal metals due to the enhanced effective mass  $m^*$  of the quasi-particles within LFL theory (Sect. 2.4). The LFL theory describes physical properties of HF compounds at the lowest temperatures ( $E_F \propto 1/m^*$ ) appropriately. Hence, a strongly enhanced  $S(T)$  is expected for HF compounds in comparison to normal metals, if the simplified Eqns. 2.23 and 2.24 are used. In general, a strong temperature dependence of  $S(T)$  is observed for HF compounds with a 10-100 times higher absolute value than measured on normal metals. Therefore, the simple approach with a linear temperature dependence does not hold for HF systems over the entire temperature range, but can only be used in the LFL regime at lowest temperatures.

The Kondo effect may sensitively influence  $S(T)$  due to the energy dependence of the scattering processes. The thermopower  $S_K(T)$  derived by Cornut and Coqblin in 1973 [64] (Sect. 2.5) for

Kondo scattering in a single-impurity model is

$$S_K(T) = \frac{1}{e} \frac{1}{T} \frac{1}{\sigma^{(2)}} \int_{-\infty}^{+\infty} \frac{S_k}{R_k} \left( \frac{df_k}{d\epsilon_k} \right) d\epsilon_k \quad . \quad (2.27)$$

To derive this relation, a perturbation-type calculation in  $JN(\epsilon)$  ( $J$  = exchange integral) was used, taking both the Kondo effect and crystalline electric field (CEF) effects into account. The relaxation time  $\tau_k$  was calculated with a 3rd order perturbation-type calculation, which includes the parameters  $R_k$  and  $S_k$  (Eqn. 2.17).  $R_k$  is a second order term in  $J$  ( $\propto J^2$ ) and  $S_k$  is a third order term (spin-flip processes  $\propto J^3$ ). Additional quantities that enter the expression for  $S_K$  are the characteristic function  $\sigma^{(2)}$  (describes the interaction between itinerant and localized electrons with respect to the temperature dependent occupancy of the CEF-split levels), the Fermi-Dirac distribution function  $f_k$  and the wavenumber  $k$ . If CEF splitting is absent,  $S_K(T)$  exhibits universal behaviour with a maximum for Ce-containing HF compounds in the vicinity of the Kondo temperature  $T_K$  like, e.g., in  $\text{Ce}(\text{Ni}_x\text{Pd}_{1-x})_2\text{Si}_2$  [65]. Additionally, a second peak in  $S(T)$  (maximum for Ce HF compounds) evolves at higher temperatures, if the total CEF energy splitting  $T_{\Delta_{\text{CEF}}} \gg T_K$ , e.g. in  $\text{Ce}(\text{Cu,Au})_6$  [66] (Fig. 2.6, left panel),  $\text{Ce}(\text{Ni}_x\text{Pd}_{1-x})_2\text{Si}_2$  [65],  $\text{CeCu}_2\text{Si}_2$  [67] and  $\text{CeNiSn}$  [4] (Fig. 6.57). This two-peak structure for  $S(T)$  ( $T_{\Delta_{\text{CEF}}} \gg T_K$ ) is confirmed by theoretical calculations (extends the theory by Cornut, Coqblin and Bhattacharjee [64, 68]) using the single-impurity Anderson model with a non-crossing approximation [8, 67, 69] (Fig. 2.6, right panel). A CEF-splitting induced maximum for Ce-containing compounds in  $S(T)$  arises at [4, 8, 55, 68, 70, 71]

$$T_{\text{max}} \approx (0.16 - 0.6) \Delta_{\text{CEF}}/k_B \quad . \quad (2.28)$$

As a result, thermopower measurements are a useful tool to investigate  $T_K$  and  $\Delta_{\text{CEF}}$  in HF compounds. The CEF energy splitting and  $T_K$  respond differently to, e.g., substitution of the rare earth elements or pressure; this can be used to investigate the peaks separately. The left panel in Fig. 2.6 shows  $S(T)$  for different  $\text{Ce}(\text{Cu,Au})_6$  alloys [66]. The CEF splitting increases with increasing Au content (investigated with inelastic neutron measurements [72]), which is in agreement with the shifting of  $T_{\text{max}}$  in  $S(T)$  to higher temperatures.

As already mentioned, the two peaks occur for well separated  $T_{\Delta_{\text{CEF}}}$  and  $T_K$ . The peak at lower  $T$  is shifted to higher temperature with increasing hybridization strength  $V$  (Fig. 2.6, right panel). For  $T_K \gtrsim 0.1 T_{\Delta_{\text{CEF}}}$ , the well separated peaks merge and a single peak is formed. With further increasing  $T_K$ , a single large maximum around  $T_K$  is seen in  $S(T)$  and the CEF contribution is negligible. A detailed description, numerous HF compounds exhibiting the features discussed above and a classification with respect to the relation of  $T_{\Delta_{\text{CEF}}}$  and  $T_K$  is found in [67].

Note that the single-impurity Anderson model is only valid in the incoherent Kondo scattering regime. In dense Kondo systems (Kondo lattices), this model becomes invalid if the coherent scattering regime is reached. Nevertheless, the single-Anderson impurity model describes  $S(T)$

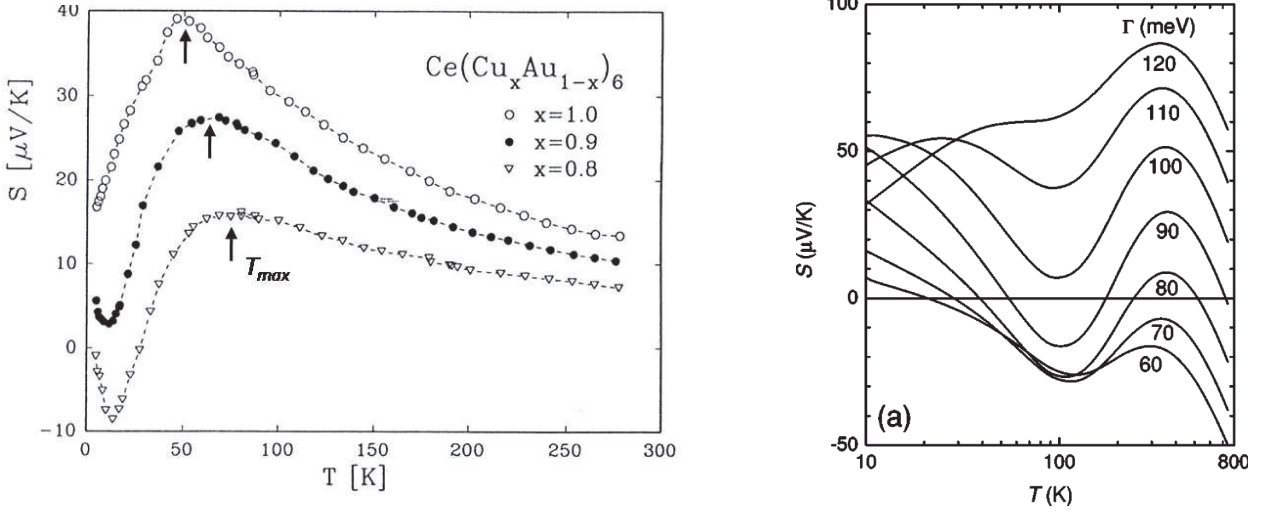


Figure 2.6: The left panel shows the thermopower  $S$  as a function of temperature  $T$  for different  $\text{Ce}(\text{Cu},\text{Au})_6$  alloys [66]. In the right panel,  $S$  calculated with a single-impurity Anderson model (non-crossing approximation) for Ce-containing compounds for several hybridization strengths  $\Gamma$  ( $\equiv V$ ) (CEF energy splitting of  $\Delta_{\text{CEF}} = 0.07$  eV) are shown as a function of temperature  $T$  [8].

in the incoherent Kondo scattering regime of Kondo lattices nicely and revealed the correct tendency of  $S(T)$  at the onset of coherent Kondo scattering. In general, the peak due to  $T_K$  is overestimated within the single-impurity Anderson model for Kondo lattices leading to a too pronounced peak in  $S(T)$  calculations.

Although many HF compounds can be described with the former approaches, a general description of the behaviour of  $S(T)$  of HF compounds has not been made.

## 2.7 Hall effect

The Hall effect describes the development of a voltage difference  $U_H$  in an electrical conductor perpendicular to the direction of the electrical current density  $j$  and perpendicular to an applied magnetic field  $\mu_0 H$  ( $H$  perpendicular to  $j$ ) [73] (Fig. 2.7). The charge carriers are deflected by  $H$  via the Lorentz force  $F_L$ , leading to the development of a transverse electrical field  $E_H$ . The Hall resistivity is given by  $\rho_{\text{Hall}} = E_H / j$  with the geometrical relations shown in Fig. 2.7. The Hall coefficient  $R_H$  is given by (geometrical relations in Fig. 2.7)

$$R_H = \frac{E_H}{j\mu_0 H} = \lim_{H \rightarrow 0} \frac{\partial \rho_{\text{Hall}}(H)}{\partial (\mu_0 H)} \quad . \quad (2.29)$$

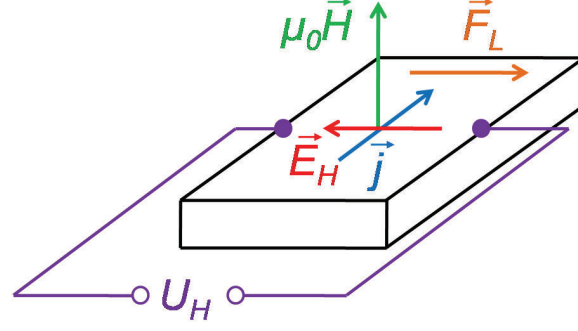


Figure 2.7: Schematic illustration of the Hall effect in a conducting sample (black lines). The sketch shows the directional dependences of the electrical current  $\vec{j}$ , the magnetic field  $\mu_0 \vec{H}$ , the electrical field  $\vec{E}_H$ , the Hall voltage  $U_H$  and the Lorentz force  $\vec{F}_L = \mu_0 q (\vec{v} \times \vec{H})$ . The formula of  $\vec{F}_L$  includes the charge  $q$  and the velocity  $\vec{v}$  of the charge carriers. The direction of  $\vec{F}_L$  is independent of the charge carrier type (electrons or holes). By contrast,  $\vec{E}_H$  is negative for electrons and positive for holes.

For simple metals where only one type of charge carriers (electrons or holes) provided from a single band contributes to  $j$ ,  $R_H$  is given by

$$R_H = \frac{1}{nq} \quad , \quad (2.30)$$

with the charge carrier concentration  $n$  and the charge of the carriers  $q$ . So electrons (holes) yield a negative (positive)  $R_H$ . This simple situation with only one involved band is usually not met in realistic compounds. Instead, several bands contribute to the charge transport which leads to remarkable changes in the behaviour of  $R_H$ . For one electron band and one hole band, with the charge carrier concentration  $n$  ( $p$ ) for electrons (holes) and the respective mobility  $\mu_e$  ( $\mu_h$ ) one gets

$$R_H = \frac{p\mu_h^2 - n\mu_e^2}{q(p\mu_h + n\mu_e)^2} \quad . \quad (2.31)$$

An additional contribution to the Hall effect can come from the anomalous Hall effect (AHE), which is discussed in detail in, e.g., [58]. In the incoherent Kondo regime, the most important contribution to the anomalous Hall coefficient  $R_H^A$  arises from skew scattering (anisotropic scattering of conduction electrons on localized magnetic ions by spin-orbit type interactions) (Fig. 2.8, left panel).  $R_H^A$  is given by [74]

$$R_H^A(T) = \gamma_1 \rho_{mag}(T) \chi(T) \quad (2.32)$$

where  $\rho_{mag}$  is the magnetic contribution to the electrical resistivity,  $\chi$  the magnetic susceptibility and  $\gamma_1$  a coefficient.  $\gamma_1$  is associated with the phase shifts of the scattered electrons. Therefore,  $\gamma_1$  varies between different Kondo scattering regimes (incoherent and coherent Kondo scattering) [74]. The maximal  $R_H^A$  contribution is reached at the transition from incoherent to coherent scattering at about  $T_{coh}$ , where a maximum in the electrical resistivity is seen, too.

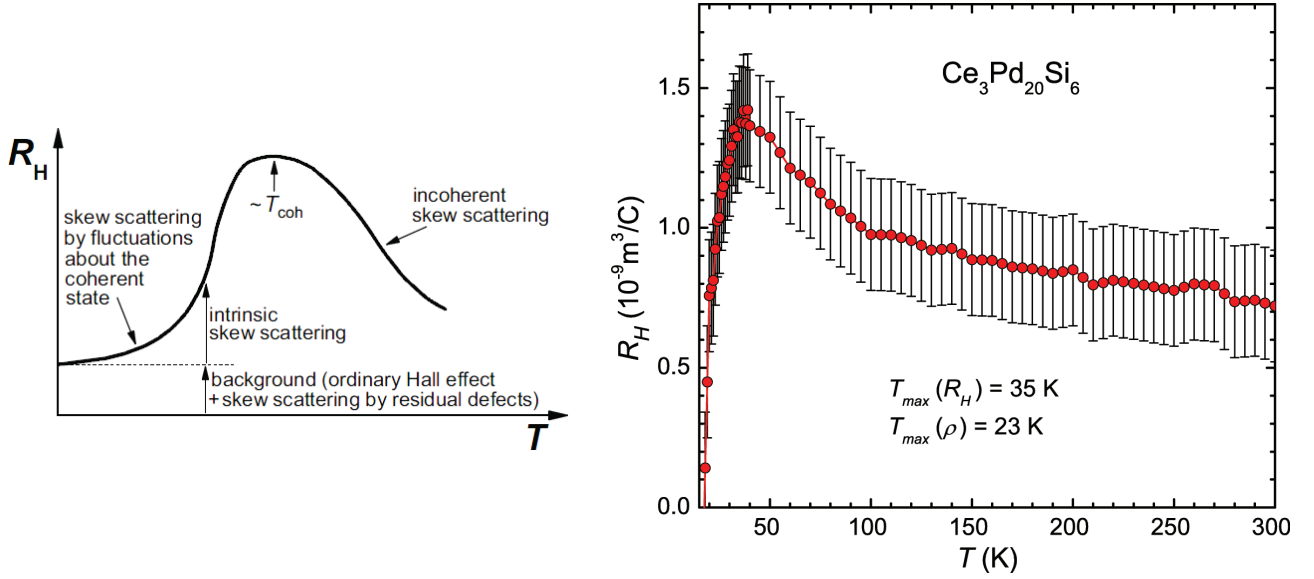


Figure 2.8: (Left): Sketch of the anomalous Hall effect that closely resembles experimental results on, e.g.,  $\text{CeAl}_3$  [74],  $\text{UPt}_3$  [75],  $\text{UAl}_2$  [74] and  $\text{CeRu}_2\text{Si}_2$  [76]. (Right):  $R_H(T)$  of the cubic heavy fermion compound  $\text{Ce}_3\text{Pd}_{20}\text{Si}_6$ . The temperatures of the maxima in  $R_H(T)$  and  $\rho(T)$  are listed in the plot.

$R_H^A$  frequently dominates the temperature dependence of  $R_H$  in heavy fermion compounds (Fig. 2.8) [74]. Exemplarily,  $R_H(T)$  of the cubic heavy fermion compound  $\text{Ce}_3\text{Pd}_{20}\text{Si}_6$  is shown in Fig. 2.8, right panel. Here, the dominating contribution of  $R_H^A$  is seen above about 20 K.

## 2.8 Crystalline electric field effects

Crystalline electric field (CEF) effects are single ion effects and can remarkably influence the physical properties of compounds that include rare earth elements (elements with partially filled  $4f$  shells). In contrast to the free ion treatment of the rare earth (RE) elements, the permanent magnetic moment of RE ions in solids is interacting with the CEF produced by the ions surrounding the RE ion. This interaction leads to a deformation of the charge density of the magnetic ion and changes the energetic level scheme of the  $4f$  electron(s).

For RE ions (except  $\text{Sm}^{3+}$  and  $\text{Eu}^{3+}$ ), the spin-orbit (SO) interaction produces typically a more than one order of magnitude higher energy splitting than the CEF splitting. Therefore, the total angular quantum number  $J$  is a good quantum number and the SO-split states can be derived via Hund's (third) rule(s). The CEF leads to an energy splitting of the  $(2J + 1)$ -fold degenerated SO-split states. According to Kramers theorem the degeneracy of the CEF-split states is restricted by the  $4f$ -electron number due to time inversion symmetry (i.e. the degeneracy is at minimum 2 for Kramers ions with an odd electron number). In addition, a lower point



symmetry of the RE ion causes lower degeneracies of the CEF-split energy levels. In comparison to the free RE ion, an additional energy splitting of the energy levels (different eigenstates) and, importantly, a directional dependence in solids (directional dependent magnetic anisotropy) is established.

The CEF Hamilton operator in Stevens notation is given by

$$H_{CEF} = \sum_{l,m} B_l^m O_l^m \quad , \quad (2.33)$$

with the CEF parameters  $B_l^m$  and the corresponding Stevens operators  $O_l^m$  [77]. The Stevens operators consist of the orbital angular momentum operators  $J_z$ ,  $J^2$  and the respective ladder operators  $J_+$  and  $J_-$ . The CEF parameters depends on the point symmetry of the RE ion and the RE element itself. For symmetry reasons only  $B_l^m$  with  $l = 2, 4$  and  $6$  are non-zero for  $4f$  elements. In addition, the point symmetry limits the number of non-zero CEF parameters for some elements if the coordinates are properly chosen.

### 2.8.1 Crystalline electric field effects in CeRu<sub>4</sub>Sn<sub>6</sub>

The Ce<sup>3+</sup> ions in CeRu<sub>4</sub>Sn<sub>6</sub> are surrounded by Ru and Sn atoms in a tetragonal point symmetry ( $D_{2d}$ , Sect. 4.1). The corresponding  $H_{CEF}$  for a tetragonal point symmetry is given by

$$H_{CEF} = B_2^0 O_2^0 + B_4^0 O_4^0 + B_4^4 O_4^4 + B_6^0 O_6^0 + B_6^4 O_6^4 \quad . \quad (2.34)$$

Equation 2.34 can be simplified for Ce<sup>3+</sup> ions (due to properly chosen coordinates) to

$$H_{CEF} = B_2^0 O_2^0 + B_4^0 O_4^0 + B_4^4 O_4^4 \quad . \quad (2.35)$$

The Ce<sup>3+</sup> ion contains one  $4f$  electron. So the  $4f$ -electron number is odd and Ce<sup>3+</sup> is a Kramers ion. As a result, the CEF-split states are at least doubly degenerate. The energetically lower lying 6-fold degenerated  $J = 5/2$  state (due to SO splitting) splits in the tetragonal environment into three doublets ( $J, m_j$ -basis):

$$\begin{aligned} |0\rangle &= |5/2, \pm 1/2\rangle \quad , \\ |1\rangle &= \alpha^{1/2} |5/2, \pm 3/2\rangle + (1 - \alpha)^{1/2} |5/2, \mp 5/2\rangle \quad \text{and} \\ |2\rangle &= (1 - \alpha)^{1/2} |5/2, \mp 3/2\rangle - \alpha^{1/2} |5/2, \pm 5/2\rangle \quad . \end{aligned} \quad (2.36)$$

The symmetry of the states  $|0\rangle$ ,  $|1\rangle$  and  $|2\rangle$  are  $\Gamma_6$ ,  $\Gamma_7^2$  and  $\Gamma_7^1$ , respectively.  $\alpha$  is the mixing coefficient ( $0 \leq \alpha \leq 1$ ).



## 2.9 Magnetic anisotropy

Magnetic anisotropy is commonly found in rare earth metals and rare earth transition metals. Its origin is based on several different mechanism (list incomplete):

- magneto-crystalline anisotropy
- shape anisotropy
- surface anisotropy
- stress anisotropy

Within this thesis, only the magneto-crystalline anisotropy (MCA) is of importance and discussed below.

The microscopic origin of the MCA is the spin-orbit interaction. Note that the exchange interaction within the Heisenberg model is isotropic (rotational invariant) and does not couple to the crystal symmetry. Due to the spin-orbit coupling, the spins correspond (via the angular momentum) to the atomic orbitals with an anisotropic charge density. A rotation of these orbitals caused by an external magnetic field yield a directional-dependent interaction of this atomic orbitals with the surrounding electronic structure (different overlap of the electronic wavefunctions). Consequently, a magnetic field direction dependent contribution to the free energy of the system is produced. This contribution is called magnetic anisotropy energy contribution and it exhibits the identical symmetry as the point symmetry of the spin-including ion. The anisotropy energy is defined as energy required to rotate the spins from the magnetically “easy” to a magnetically “harder” direction.

The anisotropic energy density  $E_{aniso}$  can be described with a power series of sinusoidal functions ( $\alpha_i$ ) relative to the main crystallographic axis:

$$E_{aniso}(\theta, \phi) = b_0 + \sum_{i=1,2,3} b_i \alpha_i + \sum_{i,j=1,2,3} b_{i,j} \alpha_i \alpha_j + \sum_{i,j,k=1,2,3} b_{i,j,k} \alpha_i \alpha_j \alpha_k + \dots \quad , \quad (2.37)$$

with

$$(\alpha_1, \alpha_2, \alpha_3) = (\sin(\theta)\cos(\phi), \sin(\theta)\sin(\phi), \cos(\theta)) \quad . \quad (2.38)$$

$\theta$  and  $\phi$  are the polar and azimuthal angles, respectively (Fig.6.11, left panel). The matrix elements of the anisotropy tensors  $b$  can be dramatically reduced by symmetry operations corresponding to the underlying point symmetry of the magnetic ion.

For tetragonal systems  $E_{aniso,tetr}$  is given by

$$E_{aniso,tetr}(\theta, \phi) = K_0 + K_1 \cos(\theta)^2 + K_2 \cos(\theta)^4 + K_3 \sin(\theta)^4 \cos(\phi)^2 \sin(\phi)^2 \quad , \quad (2.39)$$

with the anisotropy constants  $K_0$ ,  $K_1$ ,  $K_2$  and  $K_3$  and the rotation angles  $\theta$  and  $\phi$ . The polar axis is positioned along the tetragonal  $c$  direction. The constant  $K_0$  is isotropic and describes

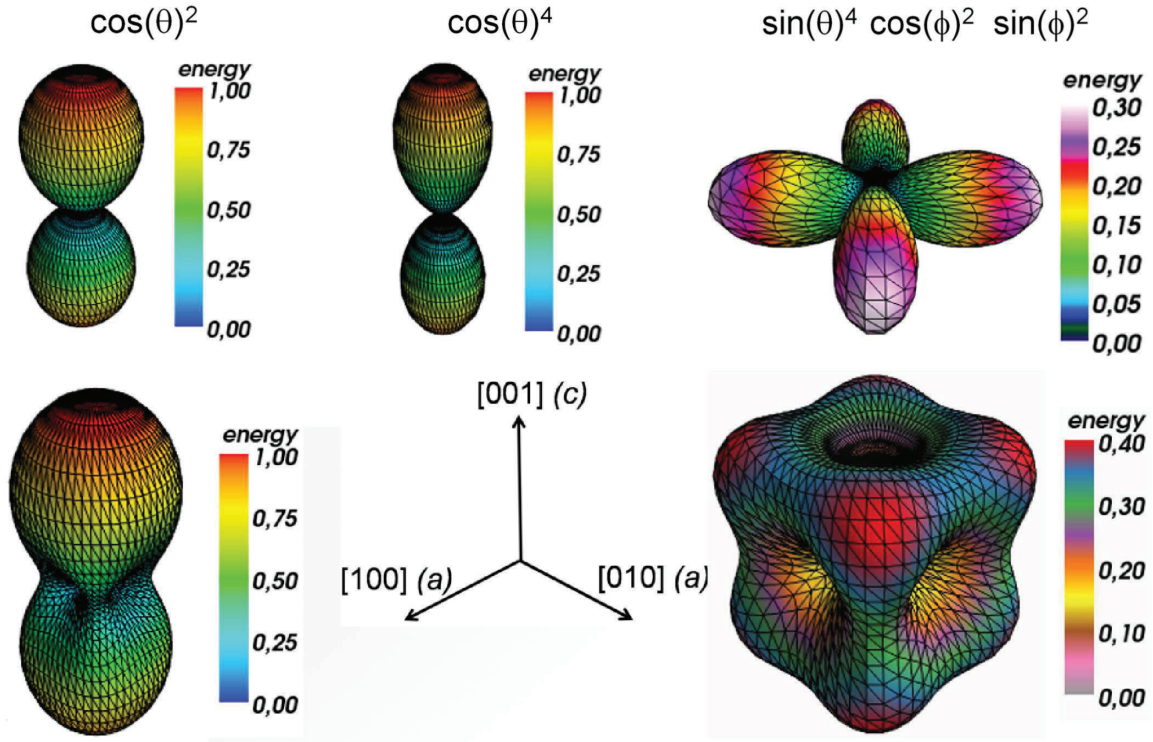


Figure 2.9: In the upper panel the contributions of the different terms to the magnetic anisotropy energy  $E_{aniso,tetr}$  of Eqn. 2.39 with the respective energy scales (next to the figures, on the right) are shown. The anisotropy constant  $K_0$  was set to 0.05.  $K_1$ ,  $K_2$  and  $K_3$  were set to 1 and their respective angular dependencies (Eqn. 2.39) are displayed separately on the left, in the middle and on the right in the upper panel. In the lower panel  $E_{aniso,tetr}$  for  $K_0=0.05$ ,  $K_1=1$ ,  $K_2=0$  and  $K_3=1$  ( $K_0=0.05$ ,  $K_1=1$ ,  $K_2=-0.85$  and  $K_3=1$ ) is shown on the left (right). The crystallographic directions for each figure are displayed in the middle of the lower panel.

the purity and perfection of the investigated single crystal.  $K_1$  and  $K_2$  determine the easy or hard axis behaviour of  $c$  and the constant  $K_3$  describes the anisotropy within the basal plane (Fig. 2.9).

# Chapter 3

## Experimental techniques

Within this thesis, single crystalline  $\text{CeRu}_4\text{Sn}_6$  samples were investigated. Since its synthesis is an important aspect of this thesis, a separate section (Sect. 4.2) is devoted to its discussion. The present chapter only describes measurement techniques. Note that the crystallographic directions are specified with  $a$  ( $\langle 100 \rangle$ ),  $c'$  ( $\langle 110 \rangle$ ) and  $c$  ( $\langle 001 \rangle$ ) within this chapter in accordance to the published data on  $\text{CeRu}_4\text{Sn}_6$ . So,  $a$ ,  $c'$  and  $c$  does not only nominate lattice constants, but also directions.

### 3.1 Electrical transport

Electrical resistivity was measured in the temperature range from approximately 50 mK to approximately 620 K, with three different devices. Magnetoresistance and Hall effect measurements were made between 50 mK and 350 K with two different devices. The maximum applied magnetic field was 9 T between 2 and 350 K and 15 T below 2 K. A standard 4-point (6-point) technique was used for all resistivity (Hall effect) measurements (Fig. 3.1). Typical sample dimensions used in this thesis were 4.0 mm x 1.5 mm x 0.5 mm. The samples were contacted with 25 or 50  $\mu\text{m}$  thick gold wires by spot welding. Only for the first measurements of  $\text{CeRu}_4\text{Sn}_6$  two-component silver epoxy (Epotek H20E, Epoxy Technology Inc.) was used because no suitable spot welding parameters could be identified. Later, these parameters were found and enabled measurements at high temperatures. Furthermore, the measurement accuracy was enhanced by the spot welded contacts, especially at the lowest temperatures.

Due to the non-avoidable small misalignment of the perpendicular Hall contacts, contributions from the longitudinal voltage  $U$  are measured within the signal of the Hall voltage  $U_H$  (Fig. 3.1). Unlike  $U_H$  that changes sign upon magnetic field reversal, this additional voltage is independent of the magnetic field direction and can thus be eliminated by measurements with opposite field direction:  $U_H = \frac{1}{2}(U_H + U) - (-U_H + U)$ . The voltages in the parentheses indicate the values measured for the two opposite  $H$  directions.

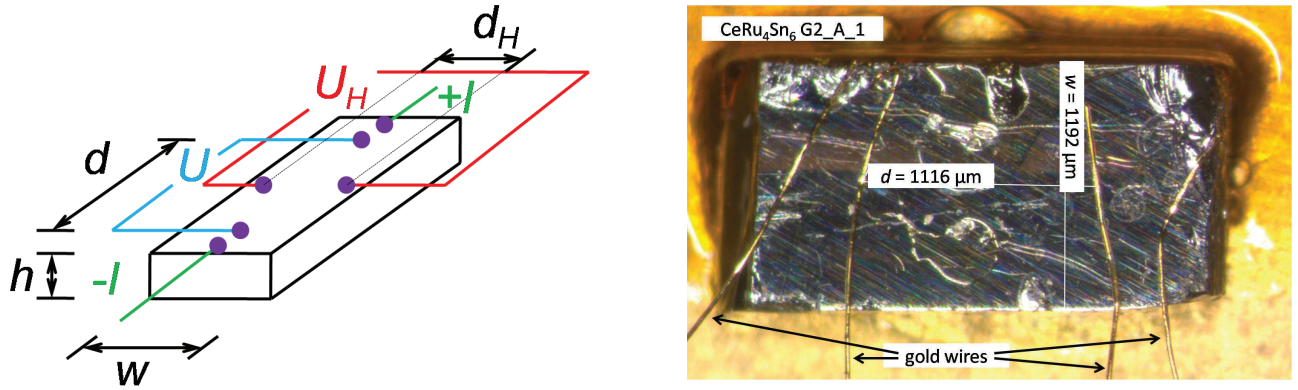


Figure 3.1: The left panel shows a schematic drawing of a sample contacted for electrical resistivity, magnetoresistance and Hall effect measurements. The electrical current  $I$  is applied along the longest direction of the sample ( $-I$  to  $+I$ ). Contacts for the Hall voltage  $U_H$  and the electrical resistivity (magnetoresistivity) measurements  $U$  are situated perpendicular and parallel to the current direction, respectively. The violet dots indicate the contacts between the sample and the gold wires. Also the dimensions relevant for determining the resistivity  $\rho = R \frac{w h}{d}$  and Hall resistance  $\rho_{Hall} = R_H \mu_0 H$  from the resistance  $R = \frac{U}{I}$  and Hall resistance  $R_H = \frac{U_H w h}{I d_H \mu_0 H}$  (Sect. 2.7) are indicated. In the right panel a photograph of a sample contacted for 4-point measurements is shown.

To check for consistency between measurements in different devices, large enough overlapping temperature ranges were studied. No discrepancies were found.

Additionally, longitudinal magnetoresistance measurements on CeRu<sub>4</sub>Sn<sub>6</sub> were performed in high magnetic fields (up to 60 T) along the three crystallographic directions [100], [001] and [110] (Sect. 6.4) by J. Larrea and F. Weickert at the High Field Laboratory at the Helmholtz-Zentrum Dresden-Rossendorf. The sample preparation for these measurements was made within this thesis.

### Low-temperature measurements (50 mK - 5 K)

Electrical resistivity, magnetoresistance and Hall effect were investigated for several CeRu<sub>4</sub>Sn<sub>6</sub> samples in this temperature range. The measurements were done with low-frequency ac current in a <sup>3</sup>He/<sup>4</sup>He dilution refrigerator from Oxford Instruments in collaboration with K.-A. Lorenzer. The cryostat includes a NbSn<sub>3</sub>-NbTi hybrid magnet driven by an IPS120-10 power supply from Oxford Instruments. With this magnet, a magnetic field  $\mu_0 H$  of 15 T can be generated. The samples, mounted in the field center, were fixed with GE varnish 7031 (Cryophysics GmbH) and with thin cigarette paper between the sample and the sample holder. As already mentioned, a considerable enhancement of the measurement accuracy was achieved by using spot welded

contacts. Their lower resistance compared with glued contacts decreases Joule heating and thus allows higher resolutions of the measurement signal at the lowest temperatures in the dilution refrigerator. Further details on the measurements in the dilution refrigerator are given in the PhD thesis of K.-A. Lorenzer [78]. The gold wires, spot welded to the sample, are soldered to the sample platform. Measurements with a constant applied  $H$  and varying temperature  $T$  ( $T$ -sweep measurements) and vice versa ( $H$ -sweep measurements) were done in the entire  $T$  and  $H$  range. As the longitudinal contribution to the Hall effect signal has to be eliminated, the Hall effect at each temperature was measured with an  $H$  sweep from negative to positive values.

### Intermediate temperature measurements (2 K - 350 K)

Within this temperature range, electrical resistivity, magnetoresistivity and Hall effect measurements on several  $\text{CeRu}_4\text{Sn}_6$  and  $\text{Ce}_{3-x}\text{La}_x\text{Pd}_{20}\text{Si}_6$  samples were made. These measurements were done with alternating dc current in a physical property measurement system (PPMS) from Quantum Design. The maximum applied magnetic field in the PPMS was 9 T. All  $\text{CeRu}_4\text{Sn}_6$  samples were measured with the horizontal rotator option of the PPMS device. The samples were glued with GE varnish to the sample platform of the measurement chip. The gold wires from the sample were soldered to the pads on the measurement chip. The spurious longitudinal contributions to the Hall signal were rejected by a rotation of  $180^\circ$  of the sample within the constant applied  $H$ .

The electrical resistivity of polycrystalline  $\text{Ce}_{3-x}\text{La}_x\text{Pd}_{20}\text{Si}_6$  samples was measured with the resistivity sample puck from Quantum Design. The samples were glued with GE Vanish and an intermediate layer of cigarette paper to the resistivity sample puck platform.

### High-temperature measurements (300 K - 620 K)

In the high temperature range electrical resistivity was measured with a homemade device set-up by E. Bauer's group at the Vienna University of Technology (Institute of Solid State Physics (IFP)). The measurements were made with alternating dc current and the voltage was measured with a nanovoltmeter (Keithley Instruments, Inc.). The temperature was measured with a NiCr-NiAl thermocouple. Because of the high temperature reached within these measurements, the  $\text{CeRu}_4\text{Sn}_6$  samples were clamped to the sample holder with thin mica plates. For the same reason, the gold wires were spot welded to the sample and they were clamped to the measurement line clamp contacts of the sample holder.

## 3.2 Magnetization

Magnetization measurements of  $\text{CeRu}_4\text{Sn}_6$  from 2 to 1000 K along the main axes [100], [001], and [110] were carried out within this thesis with two different devices as described below. The measured  $\text{CeRu}_4\text{Sn}_6$  samples had a rectangular shape, with masses between 25 and 60 mg. Their measurements were complicated by two facts. Firstly, due to strong magnetocrystalline anisotropy the orientation of the investigated axis with respect to the magnetic field had to be done with great care, in particular for  $H \parallel c$ . Secondly, the absolute value of the magnetization along the magnetic hard [001] axis was very small. Therefore, a very low and/or well known background signal was required for reliable magnetization measurements. The latter made in particular high temperature magnetization measurements challenging.

### Low-temperature magnetization measurements (2 K - 300 K)

Low-temperature magnetization measurements were made with a superconducting quantum interference device (SQUID) magnetometer from Cryogenic Ltd. in collaboration with A. Sidorenko (IFP, Vienna University of Technology). The  $\text{CeRu}_4\text{Sn}_6$  samples were attached with super glue (Loctite gel and/or liquid) to the sample holder, as shown in Fig. 3.2, left panel. The background signal from the glue is  $H$  dependent (almost linearly above 3 T), but almost temperature independent above 10 K. Exemplary values are about  $-3.5 \cdot 10^{-8}$  and  $-1.3 \cdot 10^{-7} \text{ Am}^2$  at 3 and 7 T, respectively. In the data analysis, the respective background signal at each  $H$  was subtracted.

### High-temperature magnetization measurements (200 K - 1000 K)

High-temperature magnetization measurements from 200 to 1000 K were made with two different inserts of the Vibrating Sample Magnetometer (VSM) in a PPMS from Quantum Design. A quartz sample holder was used for measurements between 200 and 400 K. The sample was glued with Loctite 4204 glue to the sample holder. The signal from this high-temperature glue is slightly higher than the one used in the SQUID. Again, this contribution was determined separately and subtracted in the data analysis. A schematic picture of this sample holder is shown in Fig. 3.2 (right panel, top) [79].

For the highest temperatures (300 - 1000 K) the VSM oven option was used. The sample was fixed with Zircar cement to the sample holder and surrounded with a copper foil to avoid thermal radiation during the measurements. A picture of the VSM oven sample holder is shown in Fig 3.2 (right panel, bottom) [80]. Again, great care had to be taken to obtain reliable results. The measurement signal of  $\text{CeRu}_4\text{Sn}_6$  decreases with increasing temperature. Since the sample space is limited and the maximal possible sample is about 50 mg for  $\text{CeRu}_4\text{Sn}_6$  samples, the signal amplitude is relatively small. Additionally, high temperature glue (Zircar





Figure 3.2: The left panel shows a photograph of a mounted  $\text{CeRu}_4\text{Sn}_6$  sample on the sample holder for SQUID measurements. The right panel displays the two sample holders used in the PPMS. On top the low temperature quartz sample holder with a mounted sample is shown [79]. Below the high temperature VSM oven sample holder is displayed [80].

cement from Quantum Design) has to be used, giving a remarkable higher contribution to the measured signal than the low-temperature glues. Finally, inhomogeneities along the sample axis are produced by the surrounding copper foil, as well as a platinum resistance heater and a thermocouple which are positioned next to the sample area. All this yields a considerable background signal. For a detailed determination of the background signal, reference measurements were performed with Pd samples of different weight and with different applied  $H$  (6 and 9 T). For the hard axis of  $\text{CeRu}_4\text{Sn}_6$  at a magnetic field of 9 T, the background signal reaches about 20 % of the sample signal.

### 3.3 Torque magnetometry

In addition to the above described magnetization measurements, torque magnetometry measurements of  $\text{CeRu}_4\text{Sn}_6$  were made with the torque magnetometer option in the PPMS. This measurement option was developed by Quantum Design in collaboration with the IBM Research Division, Zurich Research Laboratory and the Physik-Institut of the University of Zurich, Switzerland. The torque magnetometer measures the magnetization component perpendicular to the applied magnetic field (torque  $\vec{\tau} = V \vec{M}_V \times \mu_0 \vec{H}$ ). Therefore, this measurement technique is a useful tool to measure magnetic anisotropies in single crystals. Usually, this measurement device is used to measure magnetically ordered materials. However, within this study, the anisotropy of a paramagnetic material, namely  $\text{CeRu}_4\text{Sn}_6$ , was investigated. The aim of the measurements was to resolve the anisotropy with higher precision than possible with the above discussed magnetization measurements. Three differently oriented samples were measured.

Figure 3.3 displays schematic drawings of the used torque-lever chip and the chosen sample

geometry. The torque-lever chip is used in conjunction with the platform board assembly and the horizontal rotator option from Quantum Design. Samples should have a weight of less than 10 mg and should have a maximal contact area to the sample stage of 1.5 mm x 1.5 mm. The measured signal is limited to below  $5 \cdot 10^{-5}$  Nm. Larger torque may break the torque-lever chip. The torque is measured via two piezoresistor paths by a high-precision Wheatstone bridge arrangement. The right panel displays the schematic drawing for one of the samples (only the crystallographic directions change for the other two samples). All three samples were polished almost cylindrically to avoid geometrical shape impact to the measured signal. A parasitic contribution is generated if a non rotation symmetric sample is rotating in the applied  $H$ . Unfortunately, one side of the cylindrical shaped sample had to be flattened, because the mounting of the sample and the thermal coupling required this procedure. The cylindrically shaped samples had a diameter and a length of about 1 mm and were glued with super glue (Loctite gel and liquid) to the sample stage. The recommended fixing procedure with Apiezon N did not work for the samples used here.

The calibration of the torque-lever chip was made by the standard calibration routine. At first, the system cools down and the temperature dependence of the resistance and the imbalance of the Wheatstone bridge is measured accurately. These results are used to determine the corrections due to the thermal stress and magnetoresistance effects caused by the wires in the horizontal rotator and the PPMS probe. At lowest temperature, a magnetic field of 9 T is applied and the system begins to warm up. During the warm up, an electrical current of  $\pm 1.96$  mA is applied through the calibration coil (situated on the torque-lever sample stage) at several temperatures leading to a magnetization of about  $\pm 7.5 \cdot 10^{-10}$  Am<sup>2</sup>. The chip is positioned perpendicular to the field direction and produces a torque of about  $\pm 7 \cdot 10^{-6}$  Nm. By relating the change in the resistance ratio to the known torque value, a calibration table is calculated which correlates a resistance ratio to the torque, named torque coefficient. At the end, the system calculates the best fit to the torque coefficient values to obtain a relation over the entire temperature range. Due to inconsistencies between torque magnetometry and direct magnetization measurements, the calibration process was repeated after the measurements on CeRu<sub>4</sub>Sn<sub>6</sub> and no deviation was detected. Also the comparison to other calibration tables leads to no abnormal behaviour of the used torque-lever chip. Therefore, torque measurements on a single crystal with a defined anisotropy are planned to clarify the inconsistencies between torque magnetometry and direct magnetization measurements.

Each sample was measured at several temperatures between 3 and 325 K. The anisotropy between the in-plane directions [100] and [110] was measured with an applied  $H$  of 9 T as the measured signal was small. The signals achieved from these measurements were nevertheless well below the maximum allowed signal strength. By contrast, for the torque measurements between the in-plane directions ([100] and [110]) and the [001] direction the signal was large and the applied  $H$  had to be reduced from 9 T. At each temperature and field, the sample was rotated by 367.5° and then turned back to the starting position. Both directions were measured with a step size of 7.5°. Additionally, the zero field signal was determined at each temperature.



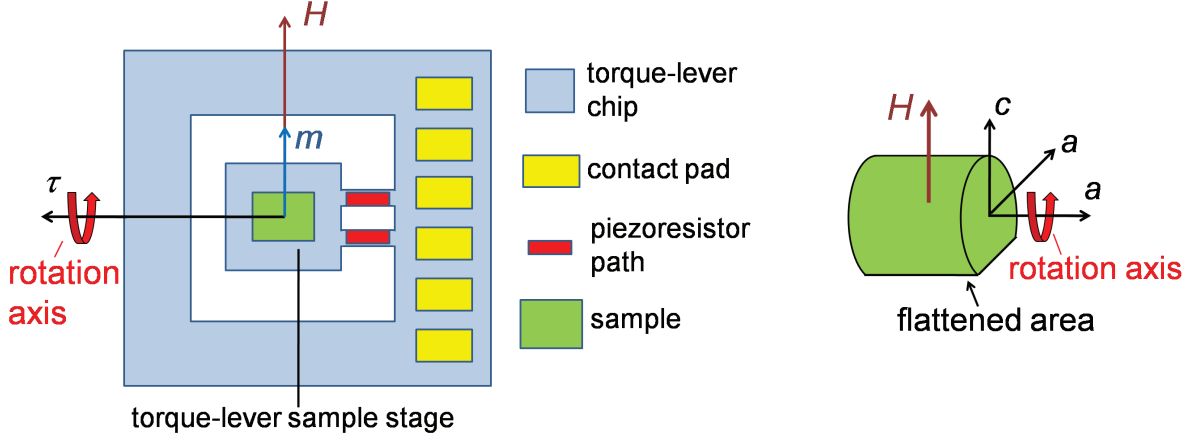


Figure 3.3: The left panel shows a schematic drawing of the torque-lever chip (Quantum Design) used in conjunction with the horizontal rotator option of the PPMS (Quantum Design). The direction of the measured torque  $\tau$  and exemplary directions of the magnetization  $m$  and the applied magnetic field  $H$  are included. The chip is rotated with respect to the rotation axis (along  $\tau$ ) in a constant applied  $H$ . The right panel shows a schematic drawing of a used  $\text{CeRu}_4\text{Sn}_6$  sample geometry for torque magnetometry measurements. The crystallographic directions vary for each sample. The shown directions display the conditions for torque measurements between the  $a$  and  $c$  direction. The sample is fixed with the flattened area (bottom) to the torque-lever sample stage.

The gravitational contribution determined by these zero-field measurements was subtracted from the measured data. In addition, the empty torque-lever chip was measured with an applied  $H$  of 9 T. The background signal derived from these measurements was necessary for the data analysis of the small signal measured between the in-plane directions.

### 3.4 Thermopower

Thermopower measurements along the three main directions ( $[100]$ ,  $[001]$  and  $[110]$ ) were made in collaboration with M. Ikeda (IFP, TU Vienna), using a homemade device set-up by E. Bauer (IFP, TU Vienna). We employed the toggled heating technique [81]. Figure 3.4 shows a schematic drawing of the set-up. If a temperature gradient  $\Delta T_1$  was applied by heating one side with the resistance strain gauge, a thermovoltage  $U_{Co, sample}^1$  was measured within the electrical circuit constantan (Co) wire -  $\text{CeRu}_4\text{Sn}_6$  - Co wire by

$$U_{Co, sample}^1 = (S_{Co} - S_{sample}) \Delta T_1 + U_{Co, add} \quad . \quad (3.1)$$

This equation includes both the thermopower of constantan ( $S_{Co}$ ) and of the measured sample ( $S_{sample}$ ), and a spurious voltage term  $U_{Co, add}$ . These spurious voltages are due to thermocouple-

wire inhomogeneities, non-thermal ideality of the cold end unit and electrical offsets of the voltmeter. The thermovoltage within the gold/iron (AuFe0.07%, called AuFe hereafter) wire - CeRu<sub>4</sub>Sn<sub>6</sub> - AuFe wire circuit  $U_{AuFe, sample}^1$  was measured in the same way. Next, the other side of the sample was heated and the thermovoltages  $U_{Co, sample}^2$ ,

$$U_{Co, sample}^2 = (S_{Co} - S_{sample})(-\Delta T_2) + U_{Co, add} \quad , \quad (3.2)$$

and  $U_{AuFe, sample}^2$  were measured. The spurious voltages were eliminated by subtracting the thermovoltages  $U^1$  and  $U^2$  (Eqn. 3.1 and Eqn. 3.2), which yields

$$U_{Co} = U_{Co, sample}^1 - U_{Co, sample}^2 = (S_{Co} - S_{sample})(\Delta T_1 + \Delta T_2) \quad (3.3)$$

and

$$U_{AuFe} = U_{AuFe, sample}^1 - U_{AuFe, sample}^2 = (S_{AuFe} - S_{sample})(\Delta T_1 + \Delta T_2) \quad . \quad (3.4)$$

Finally,  $S_{sample}$  was calculated by combining Eqn. 3.3 and Eqn. 3.4 to

$$S_{sample} = S_{Co} - \frac{U_{Co}(S_{Co} - S_{AuFe})}{U_{Co} - U_{AuFe}} \quad . \quad (3.5)$$

The temperature of the sample was determined with Ge- and Pt-sensors mounted in a drill hole in the heat sink.  $S_{Co}$  and  $S_{AuFe}$  were calculated from calibration tables for  $S$  of the Co and AuFe wires, respectively.  $U$  was measured with a nanovoltmeter (Keithley Instruments, Inc.).

At each temperature, a voltmeter was connected successively to both electrical circuits by a multiplexer (Burster Präzisionsmesstechnik GmbH & Co KG) (Fig. 3.4). The samples were glued with GE varnish 7031 (Cryophysics GmbH) to resistance strain gauges which were mounted on the heat sink. The Co wires were spot welded to the AuFe wires at their tops and subsequently contacted electrically and thermally with conductive silver paint to the sample surface. The opposite tops of the Co and AuFe wires were soldered to copper wires. To avoid spurious voltages due to temperature differences between the contacts, they were thermally coupled (electrically isolated) with a heat sink at room temperature.

Here, CeRu<sub>4</sub>Sn<sub>6</sub> samples were measured from 5 to 300 K along the [100], [001] and [110] direction. The samples were separated from batch G2 with a typical sample geometry of approximately 4.0 mm x 1.5 mm x 0.5 mm.

## 3.5 Optical spectroscopy

As part of this thesis high-quality CeRu<sub>4</sub>Sn<sub>6</sub> single crystals were synthesized for optical spectroscopy measurements along the [100] and [001] direction. The measurements required samples

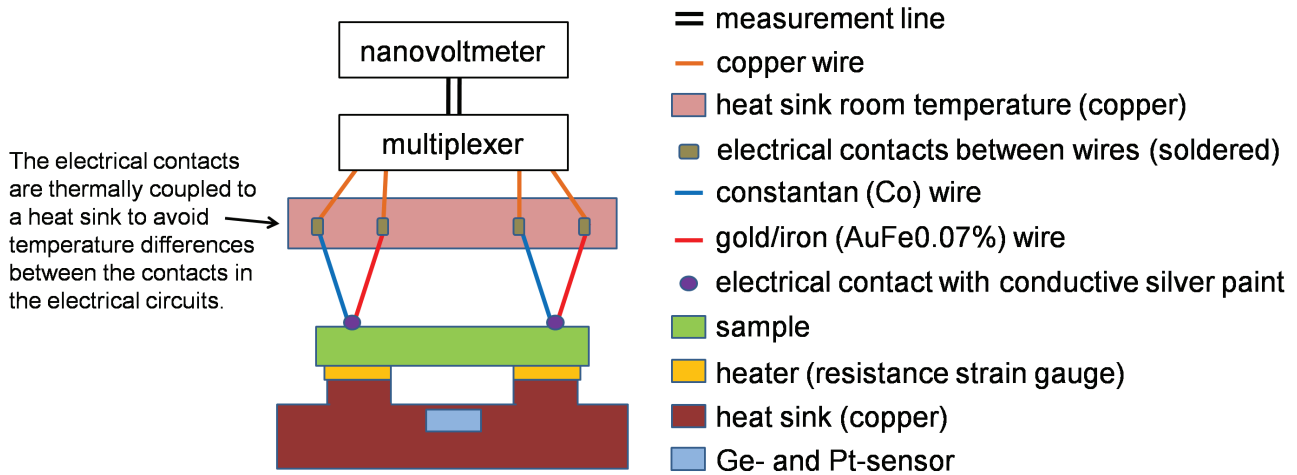


Figure 3.4: Schematic drawing of the thermopower measurement set-up.

with smooth oriented surfaces and the maximum possible diameter. Thus, two disc-like samples were cut from batch G3 after orienting it with a Laue diffractometer and magnetization measurements. The separated discs had a plane elliptical surface with a minor and major axis of about 4 mm and 6 mm, respectively. The oriented surfaces included the main directions [100] and [001], which were marked with a small oriented lateral polished surface. Exemplary, one disc is shown in Fig. 3.5.

The measurements were done by V. Guritanu, J. Sichelschmidt (both at Max Planck Institute for Chemical Physics of Solids, Dresden, energy range: 5 meV - 30 eV), T. Weig and M. Scheffler (both at 1. Physikalisches Institut, Universität Stuttgart, energy range: 0.5 - 5 meV). Near-normal incidence reflectivity spectra were measured between 6 and 200 K with different spectrometers in an energy range from 0.5 meV to 30 eV. Linearly polarized light was used with the electric field parallel to the [100] direction and parallel to [001] axis. The results were published recently [16].

### 3.6 X-ray absorption spectroscopy (XAS) measurements

Frequently, a combination of inelastic neutron scattering and magnetic susceptibility measurements is used to determine the crystalline electric field (CEF) level scheme of a  $4f$  state. For the former, large samples are needed. The latter can be complicated by interaction effects. In this case one can resort to XAS measurements, which are a powerful tool to determine the ground state of the CEF-split  $4f$  wave function ( $\text{CePd}_2\text{Si}_2$  [82],  $\text{CePt}_3\text{Si}$  [83]). As part of this thesis, several high-quality  $\text{CeRu}_4\text{Sn}_6$  single crystals with almost cubic shape (length of about 1 mm) and two parallel surfaces that include both the [100] and the [001] direction were prepared for XAS. Small imperfections and different prepared surfaces of the separated pieces were useful

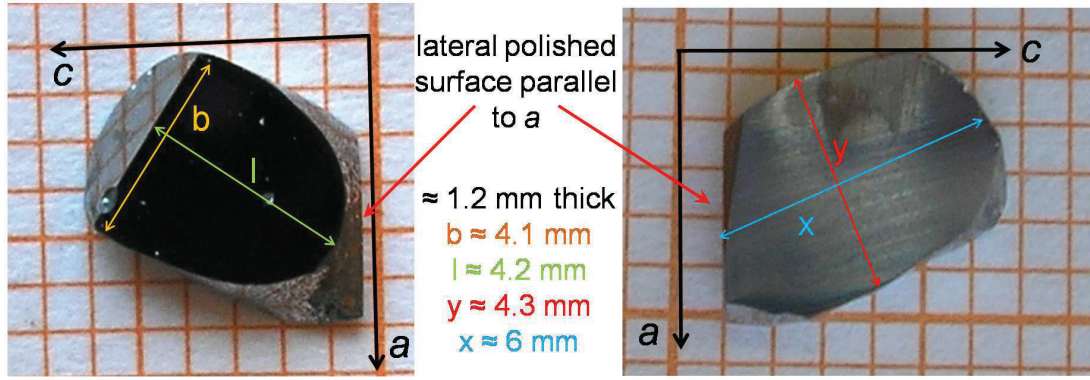


Figure 3.5: Photographs of both sides of one separated  $\text{CeRu}_4\text{Sn}_6$  disc (batch G3). This sample was used for optical spectroscopy measurements by V. Guritanu and J. Sichelschmidt (Max Planck Institute for Chemical Physics of Solids, Dresden).

marks for the indication of the orientations. Figure 3.6 shows the documentation for one such sample prepared for XAS measurements.

The XAS measurements were performed by F. Strigari in the group of A. Severing (2. Physikalisches Institut at the Universität zu Köln) at the National Synchrotron Radiation Research Center (NSRRC, Dragon beamline BL08A) in Taiwan. Within these measurements, the core-hole excitations of the  $3d$  electrons into the  $4f$  states are investigated (Fig. 3.7). The measured spectra show two dominant absorption energy ranges, which are 895 - 905 meV for the  $M_4$  and 877 - 887 meV for the  $M_5$  excitation. The ground state doublet of the CEF split  $4f$  wave function is measured by the polarization dependent absorption intensities for the X-rays (Sect. 6.6). Therefore, the X-rays were polarized with the electrical field parallel and perpendicular to  $[001]$  axis. Due to the thermal population of the first excited CEF-split doublet, the temperature  $T$  should be much lower than the energy of the first CEF excitation ( $k_B T \ll \Delta E_{\text{CEF}1}$ ).

In addition to the  $M_4$  and  $M_5$  excitations, the  $L_3$  excitations were investigated with XAS measurements in the partial fluorescence yield (PFY) mode (Sect. 6.6).

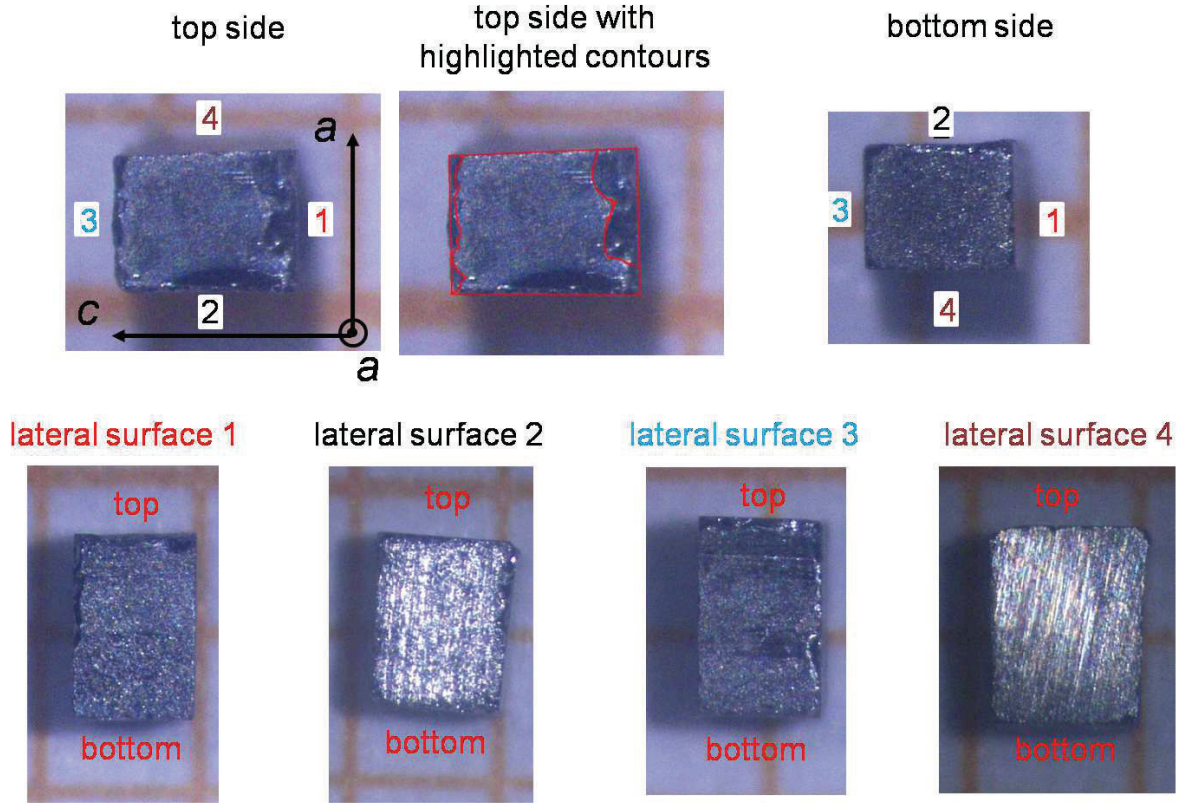


Figure 3.6: Documentation of a separated  $\text{CeRu}_4\text{Sn}_6$  single crystal for XAS measurements. Small imperfections and differently prepared surfaces were useful marks of the almost cubic oriented samples.

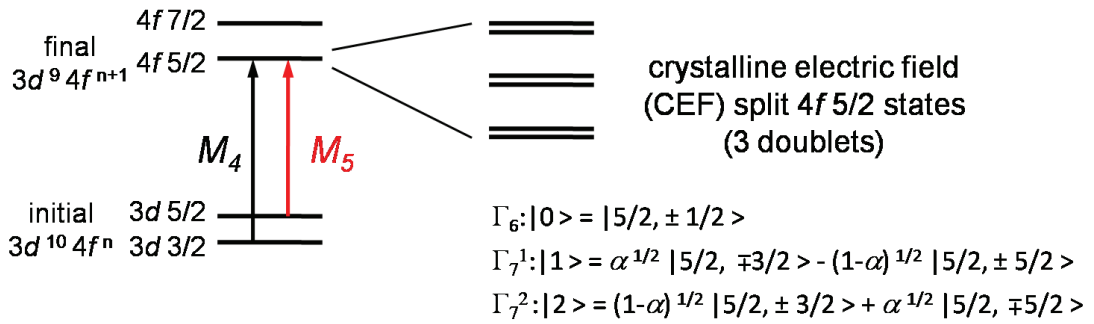


Figure 3.7: The left panel shows the electron energy levels relevant for the XAS measurements, including the core-hole excitations  $M_4$  and  $M_5$ . In the right panel, the CEF-split energy levels of the  $4f\ 5/2$  states are shown and their eigenstates (three doublets) with the respective site symmetry are listed.



# Chapter 4

## Crystallography and single crystal growth

### 4.1 Crystal structure

As already mentioned in the introduction,  $\text{CeRu}_4\text{Sn}_6$  crystallizes in a body-centered tetragonal structure of space group  $\text{I}\bar{4}2\text{m}$ , with the lattice constants  $a = 6.8810 \text{ \AA}$  and  $c = 9.7520 \text{ \AA}$  (Fig. 4.1) [40, 84]. Each Ce atom is surrounded by a polyhedron of 4 Ru and 12 Sn atoms (Fig. 4.2) with the point symmetry  $\text{D}_{2d}$  (= Schoenflies notation (S-notation) for  $\bar{4}2\text{m}$  in Hermann-Mauguin notation (HM-notation)). The point group  $\text{D}_{2d}$  is not abelian and exhibits the subgroups  $\text{C}_s$ ,  $\text{C}_2$ ,  $\text{D}_2$ ,  $\text{C}_{2v}$  and  $\text{S}_4$  ( $\text{C}_n = n$ -fold rotation axis,  $\text{D}_n = n$ -fold rotation axis plus  $n$  twofold axes perpendicular to that axis and  $\text{S}_{2n} = 2n$ -fold rotation-reflection axis). Exemplary symmetry operations are the rotation by  $90^\circ$  along the  $[001]$  direction followed by mirroring with respect to the  $(001)$  plane (S-notation  $\text{S}_4$ , HM-notation  $\bar{4}$ ), the rotation along the  $[100]$  direction by  $180^\circ$  (S-notation  $\text{C}_2$ , HM-notation 2) and the mirroring with respect to the  $(110)$  plane (HM-notation  $\text{m}$ ). Within the polyhedron, the nearest neighbours of Ce are the 4 Ru atoms at a distance of  $3.2964 \text{ \AA}$ . The distances from Ce to the Sn atoms are  $3.3634$ ,  $3.4405$  and  $3.7102 \text{ \AA}$ . The atomic coordinates are listed in Tab. 4.1 [40].

As a result of the peculiar relation between the lattice constants  $a$  and  $c$ ,  $\sqrt{2} \cdot a \approx c$ ,  $\text{CeRu}_4\text{Sn}_6$  can also be represented by a quasi-cubic unit cell, with a deviation of about  $0.2\%$  from a

Table 4.1: Atomic coordinates of  $\text{CeRu}_4\text{Sn}_6$  in the tetragonal unit cell [40].

element	site	Wyckoff position	atomic coordinates		
			$[100]$	$[010]$	$[001]$
Ce	Ce	$2a$	0.0000	0.0000	0.0000
Ru	Ru	$8i$	0.8294	0.8294	0.4211
Sn	Sn1	$8i$	0.8213	0.8213	0.7048
Sn	Sn2	$4c$	0.0000	0.5000	0.0000
$a = 6.8810 \text{ \AA}$ , $c = 9.7520 \text{ \AA}$					



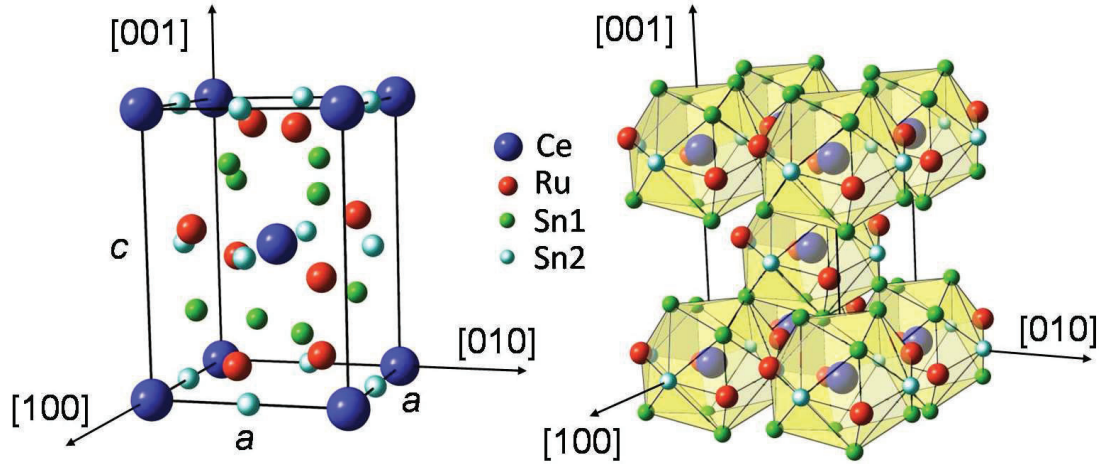


Figure 4.1: A unit cell of  $\text{CeRu}_4\text{Sn}_6$  is schematically shown in the left panel [40,84,85]. The right panel shows a polyhedral representation of the crystal structure. The polyhedral cages are formed by 4 Ru and 12 Sn atoms (coordination number 16).

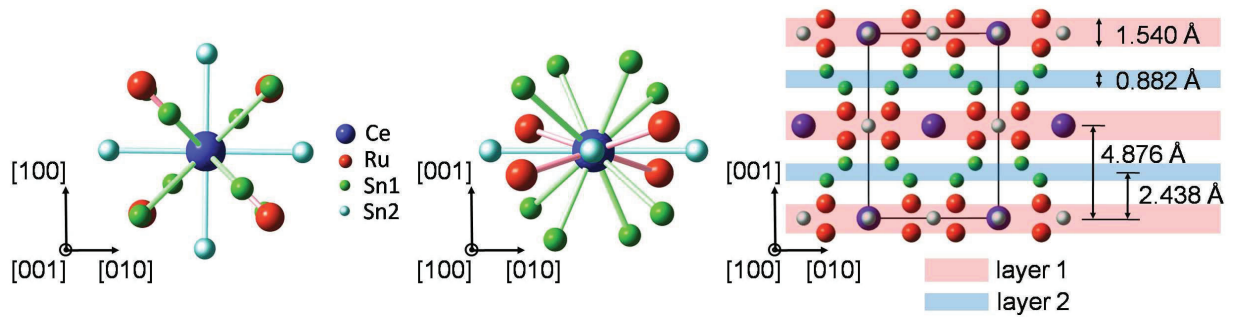


Figure 4.2: A Ce atom (blue), with the cage atoms (Ru (red), Sn1 (green) and Sn2 (cyan)) surrounding it, is presented in the left and middle panel. In the left (middle) panel the view along the  $[001]$  ( $[100]$ ) direction is shown. The point symmetry of the Ce site is  $D_{2d}$ .  $\text{CeRu}_4\text{Sn}_6$  exhibits two different Sn sites (Sn1 and Sn2). The 4 Sn2 atoms are situated in the basal (001) plane and the 8 Sn1 atoms are located slightly (by  $1.999 \text{ \AA}$ ) below and above the basal plane. In the right panel the layered structure for  $\text{CeRu}_4\text{Sn}_6$  is shown (unit cell marked with black line) [40,84,85].



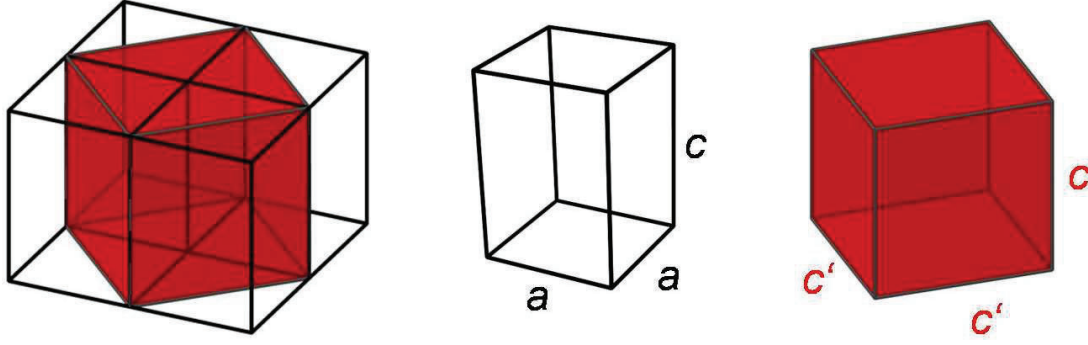


Figure 4.3: The tetragonal crystal structure of  $\text{CeRu}_4\text{Sn}_6$  can be approximated with a quasi-cubic cell, with a deviation to a cubic structure of about 0.2%. The left panel shows both types of unit cell, the middle panel shows the tetragonal unit cell, and the right panel shows the quasi-cubic unit cell. The diagonal direction in the basal (001) plane is named  $c'$ .

cubic structure (where  $\sqrt{2} \cdot a = c$ ). Both unit cells are shown in Fig. 4.3. The diagonal of the tetragonal basal plane will be denoted by  $c'$  throughout this thesis.

### Can 1- or 2-dimensional features be discerned in the crystal structure?

Measurements on  $\text{CeRu}_4\text{Sn}_6$  single crystals reveal that the physical properties are similar for the directions [100] and [110] lying within the basal plane, but distinctly different along the [001] direction perpendicular to it. This raises a question whether 1- or 2-dimensional structures can be discerned in the crystal structure of  $\text{CeRu}_4\text{Sn}_6$ .

Within the basal (001) plane, Ce ( $2a$  position) and Sn2 atoms ( $4c$  position) are situated at the (0,0,0) and (0,1/2,0) positions (and their crystallographic equivalents), respectively (Fig. 4.1, 4.2 and 4.4). The rest of the Ce-surrounding cage atoms (Ru and Sn1 at the  $8i$  position) are placed in the (110) plane (Fig. 4.2). Their distances to the (001) plane are 0.707 Å (1.999 and 2.879 Å) for the Ru atoms (Sn2 atoms). Hence, a layered structure is formed along the [001] direction, with Ce-Ru-Sn1 layers (layer 1, width 1.540 Å, layer distance of  $c/2 = 4.876$  Å) and intermediate Sn2 layers (layer 2, width 0.882 Å, distance to Ce-Ru-Sn1 layers is  $c/4 = 2.438$  Å) (Fig. 4.2). The atomic structure of  $\text{CeRu}_4\text{Sn}_6$  is displayed in Fig. 4.4 for views along the directions [100] (left), [001] (middle) and [110] (right). The central unit cell is indicated with black lines.

Due to the indication of a layered structure in  $\text{CeRu}_4\text{Sn}_6$  (Fig. 4.2), the crystal structure was investigated within an electronic transport approach via localized electron shells around the respective atoms along the [100], [001] and [110] directions (Fig. 4.5- 4.9). This approach is compared to theoretical calculations by P. Wissgott [9] including anisotropic hybridization effects. The left panel of Fig. 4.4 shows a view along the [100] direction, which shows that the Ce (blue) and Sn2 (cyan) atoms along [100] are surrounded by alveolar positioned Ru

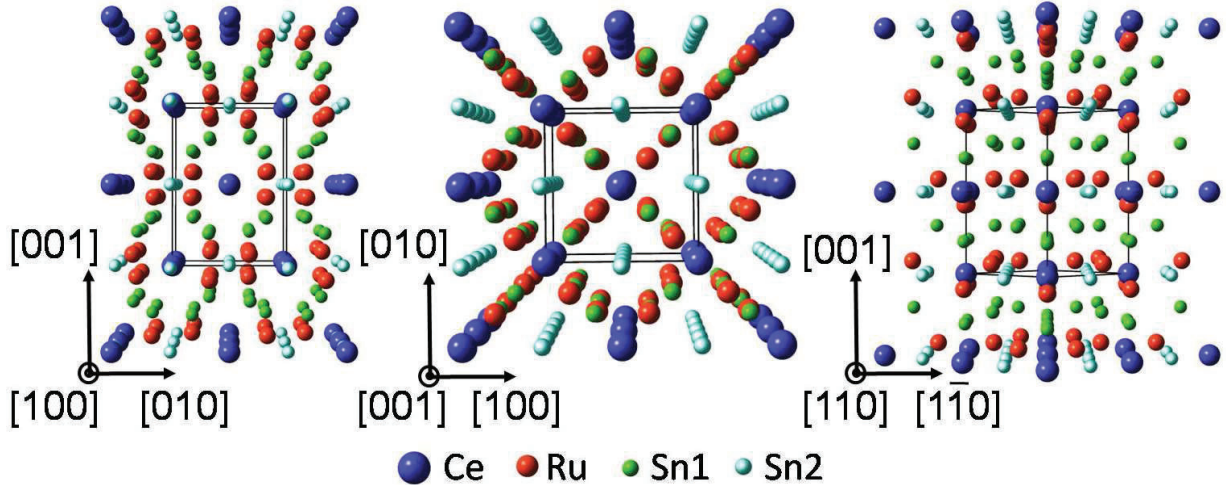


Figure 4.4: The crystal structure of  $\text{CeRu}_4\text{Sn}_6$  is displayed along the three investigated main directions  $[100]$  (left),  $[001]$  (middle) and  $[110]$  (right) [40, 85].

(red) and Sn1 (green) atoms. The direct and indirect (zigzag) atomic chains along  $[100]$  are displayed in a 1-dimensional presentation in Fig. 4.5. Additionally, the 3-dimensional properties of the Ce-containing atomic chains along  $[100]$  is presented in Fig. 4.6. These figures show the atomic configuration, the extensions in comparison to the direct  $[100]$  direction in % and the 3-dimensional properties (for Ce-containing chains) of the  $[100]$  chains. The chains are shown for a length of  $2a$  or  $a$ . One direct Ce-containing  $[100]$  chain ( $[100]_1$ ) exists with alternating Ce and Sn2 atoms (no extension). Interestingly, all other Ce-containing chains ( $[100]_2$ ,  $[100]_3$  and  $[100]_4$ ) lead to an extension of more than 36.5 %. Additionally, pure Sn chains ( $[100]_5$ ,  $[100]_7$  and  $[100]_8$ ) and Ru-Sn chains ( $[100]_6$ ,  $[100]_9$  and  $[100]_{10}$ ) are found along  $[100]$  in  $\text{CeRu}_4\text{Sn}_6$ .

Next, the  $[001]$  direction was investigated. A view along  $[001]$  on the crystal structure of  $\text{CeRu}_4\text{Sn}_6$  is shown in Fig. 4.4 (middle panel) and the atomic chains along  $[001]$  are displayed in Fig. 4.7 for a length of  $2c$  ( $c$ ). Here, the distance between the Ce atoms is  $c = 9.7520 \text{ \AA}$  for the pure Ce chain ( $[001]_1$ ). Due to the comparably large distance between the Ce atoms, non-Ce atoms are likely to have a strong influence on the electronic transport along  $[001]$ . The chain ( $[001]_2$ ) with the smallest atomic distances exhibits two non-Ce atoms between the Ce atoms (distance of the Ce atoms is  $c$ ). The  $[001]_2$  chain is realized via the displayed Ce-Ru-Sn1-Ce path (Fig. 4.7). In addition, a pure Sn2 ( $[001]_4$ ) and a Ru-Sn1 chain ( $[001]_3$ ) exist along  $[001]$ . Note that the lowest electrical resistivity was measured along this direction.

Finally, the atomic chains along  $[110]$  are shown in Fig. 4.8 (1-dimensional presentation) and Fig. 4.9 (3-dimensional illustration) for a length of  $2c'$ . A view along the  $[110]$  direction on the crystal structure of  $\text{CeRu}_4\text{Sn}_6$  is displayed in Fig. 4.4 (right panel). The pure Ce-chain ( $[110]_1$ ) exhibits a large direct distance ( $c' = 9.7310 \text{ \AA}$ ), similar to the  $[001]$  direction. Also here, the chain ( $[110]_4$ ) with the smallest atomic distances exhibits two non-Ce atoms (Ru) between the Ce atoms. Its length extension is only 1.9 % in comparison to the direct Ce-Ce distance. In

addition, Ce-Ru-Ce ( $[110]_3$ ) and Ce-Sn2-Sn2-Ce ( $[110]_2$ ) chains exist with a length extension of 6.8 and 20.7 %, respectively. Finally, pure Sn1 ( $[110]_5$  and  $[110]_6$ ), pure Sn2 ( $[110]_8$ ), Ru-Sn1 ( $[110]_7$ ) and Ru-Sn2 chains ( $[110]_9$ ) can be found.

The anisotropy of  $\text{CeRu}_4\text{Sn}_6$  between the (001) plane and the perpendicular [001] direction was suggested to result from an anisotropic hybridization strength along the different crystallographic directions, resulting in the formation of energy gaps at the Fermi energy only for directions with strong hybridization (Sect. 5) [5]. To further explore this conjecture, the chains derived above and the directional dependence of the chains that contain Ce atoms was investigated. Figure 4.10 shows the 4*f*-electron orbitals for the pure ( $J, m_j$ )-states (left top) and the Wannier orbitals for Ce-*f*-electron orbitals in  $\text{CeRu}_4\text{Sn}_6$ , which were calculated by P. Wissgott within his PhD thesis [9]. The Wannier orbitals include the information about the basic Bloch states derived by local density approximation (LDA) calculations and display a real space picture instead of the *k*-space picture of the electronic dispersion. The spreads of the Wannier orbitals of the ( $J=5/2, m_j=\pm 1/2$ )- and ( $J=5/2, m_j=\pm 3/2$ )-*f* states, which were found to be the states most probably occupied (Sect. 6.1.1), are both about  $1 \text{ \AA}^2$  [9]. For the ( $J=5/2, m_j=\pm 5/2$ )-*f* state, the spread is about  $1.8 \text{ \AA}^2$  [9]. The spread for the Ru-4*d* (Sn-5*p*) orbitals was calculated to be about  $2.3$ - $5.8 \text{ \AA}^2$  ( $5.9$ - $18.1 \text{ \AA}^2$ ). Note that the directional dependence of these orbitals is the essential feature for different hybridization strength along different directions. Within Wissgott's PhD thesis, the  $m_j=\pm 1/2$  state was found to be the most strongly hybridized one (Fig. 5.2, left panel): it hybridizes strongly with Ru-4*d* and Sn2-5*p* states (Fig. 5.2, right panel) [9].

Electronic and thermal transport measurements (Sects. 6.2 to 6.6) as well as theoretical calculations (Sect. 5) revealed a stronger hybridization within the (001) plane in comparison to the perpendicular [001] direction. As mentioned above, the theoretical calculations performed by Wissgott [9] indicate that the Ce-4*f* electrons hybridize most strongly with Ru-4*d* and Sn2-5*p* electrons (Fig. 5.2, right panel). Below, the atomic chains along the different crystallographic directions are compared in order to relate structural features to these results. Since the direct overlap of the Ce-derived orbitals along [001] and [110] is small (atomic distance  $> 9.7 \text{ \AA}$ ), these chains ( $[001]_1$  and  $[110]_1$ ) are not considered important for transport. For the (100)-plane directions [100] and [110], only Ce chains including Ru (red) and/or Sn2 (cyan) were found ( $[100]_1$  to  $[100]_3$  and  $[110]_2$  to  $[110]_4$ ), except for one chain ( $[100]_4$ ) that includes two neighbouring Sn1 atoms (green), with a length extension of more than 50 % (Figs. 4.5, 4.6 and 4.8). Neglecting this extended chain, perfect agreement with the theoretical result is found: All Ce-containing chains with short interatom distances in the (100) plane include Ru and/or Sn2 atoms. This can also be seen from the layered structure of this compound. By contrast, a Ce-Ru-Sn1-Ce chain ( $[001]_2$ ) with a small length extension of 8.3 % is only found along [001] (Fig. 4.7). Here, the distance between Ce and Ru is larger than for the [100] and [110] direction, namely  $4.429 \text{ \AA}$  instead of  $3.296 \text{ \AA}$ . The deviations of the Ru atoms from a straight chain are  $46.6^\circ$ ,  $13.5^\circ$  and  $22.0^\circ$  for the [100], [110] and [001] direction, respectively. A remarkable difference in accordance with the anisotropic behaviour can be found in the angle between the Ce-Ru bond and the (100)

plane. This angle is  $13.5^\circ$  ( $\theta = 76.5^\circ$ ) for the  $[100]$  and  $[110]$  direction, and  $68.0^\circ$  ( $\theta = 22.0^\circ$ ) for the  $[001]$  direction. Therefore, a different hybridization strength for the two Ce-Ru pairs is anticipated due to the  $\theta$ -dependence of the Wannier orbitals (Fig. 4.10). In conclusion, the lower hybridization strength between Ce and Ru for the  $[001]$  direction in comparison to the  $(001)$ -plane directions can be traced back to both a larger Ce-Ru-distance and a different angle  $\theta$  of the Ce-Ru bonds. The direct Ce-Sn2-Ce chain  $[100]_1$  with Sn2 in the  $(001)$  plane ( $\theta = 90^\circ$ ) suggests to be strongly hybridized, too. So, a stronger hybridization strength for large  $\theta$  next to the  $(001)$  plane is in agreement with these findings.

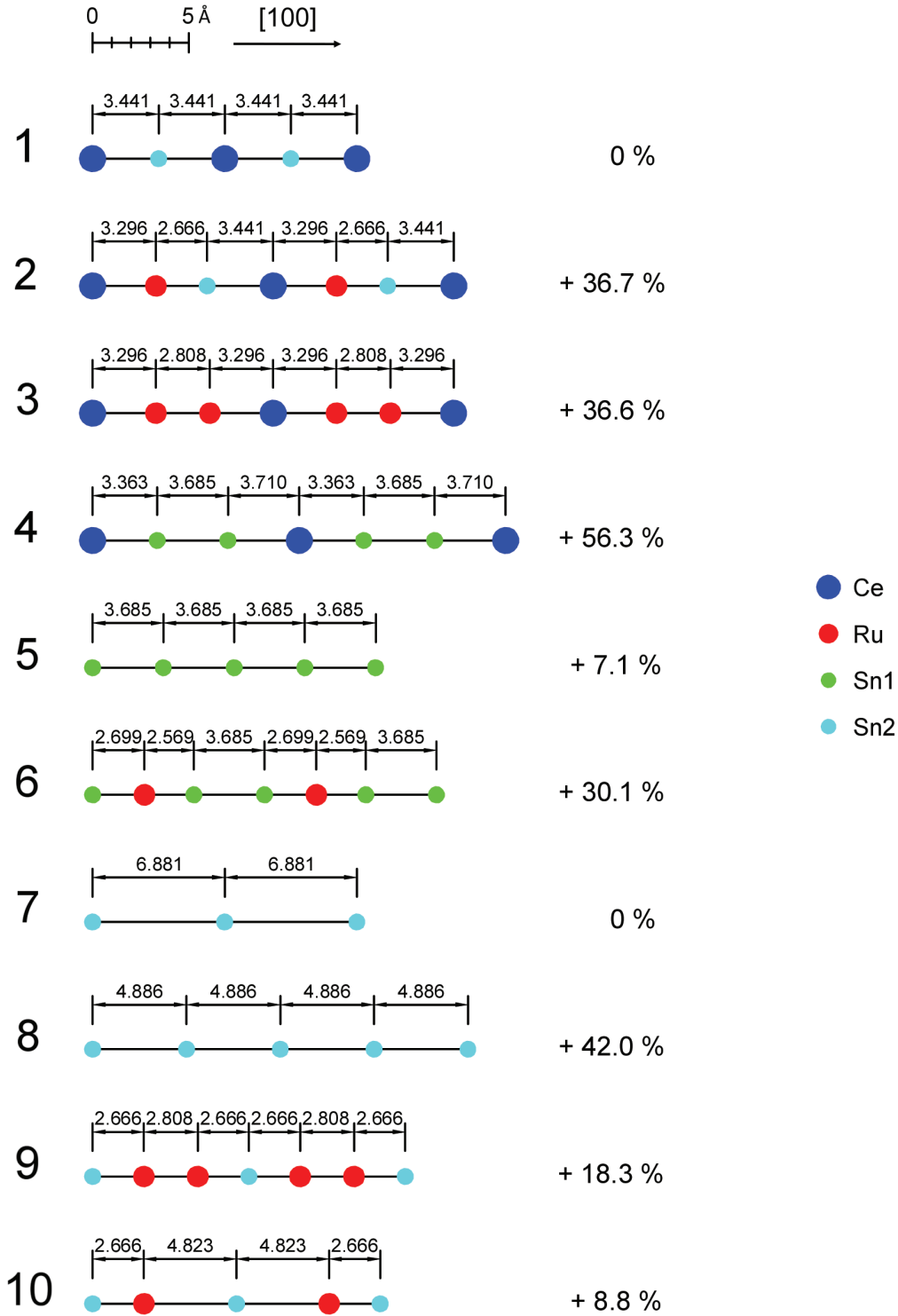


Figure 4.5: Direct and indirect (zigzag) atomic chains ( $[100]_i$ ,  $i = 1$  to 10) along [100] for CeRu<sub>4</sub>Sn<sub>6</sub>. All displayed chains span a distance of  $2a$  along [100]. Their extensions with respect to a straight chain with bond angles of  $180^\circ$  are specified in %. Different views on the Ce-containing chains are shown in Fig. 4.6 in a 3-dimensional representation.

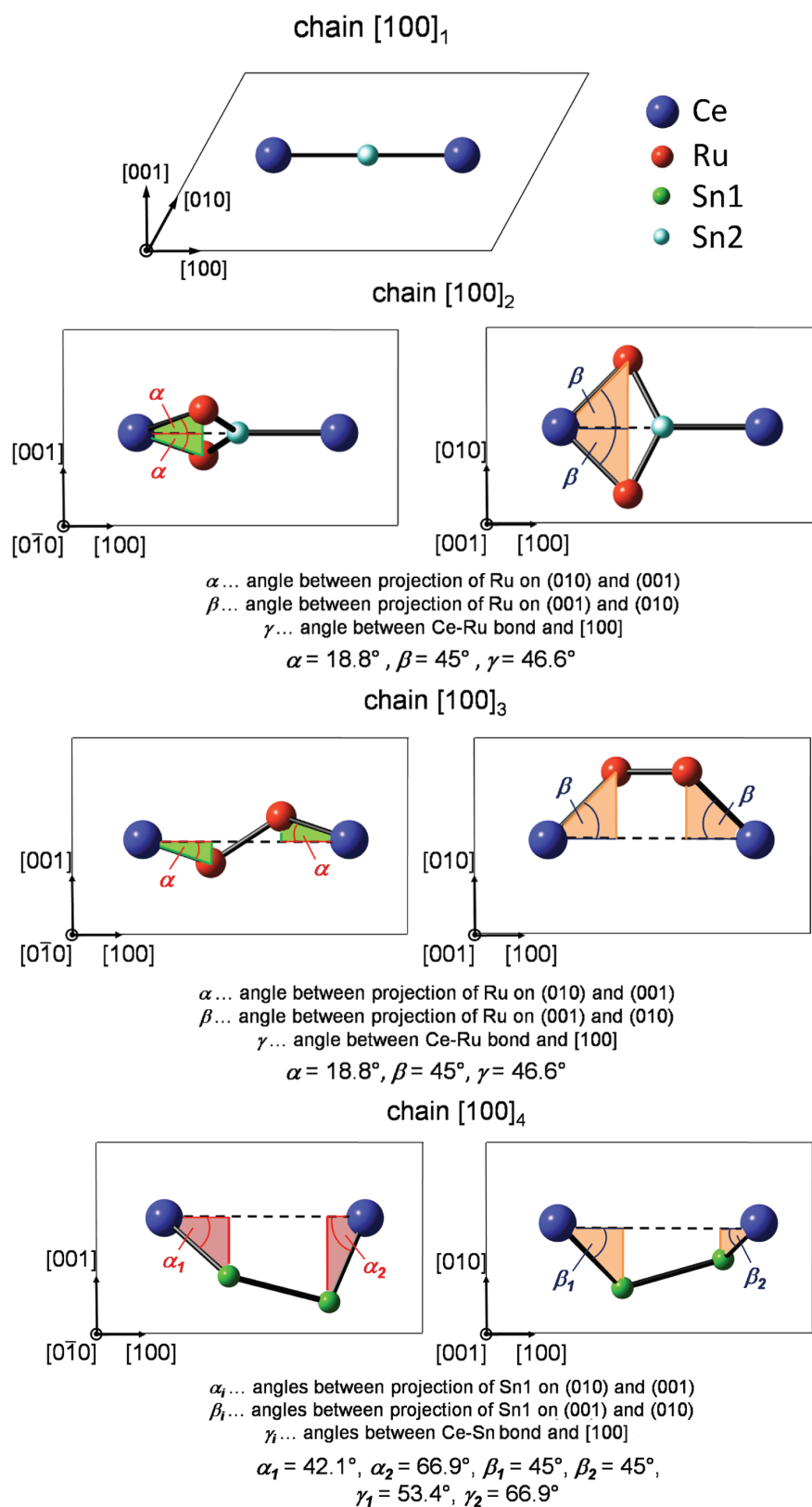


Figure 4.6: 3-dimensional representations of the direct and indirect Ce-containing atomic chains along  $[100]$ . The 1-dimensional representations are shown in Fig. 4.5.

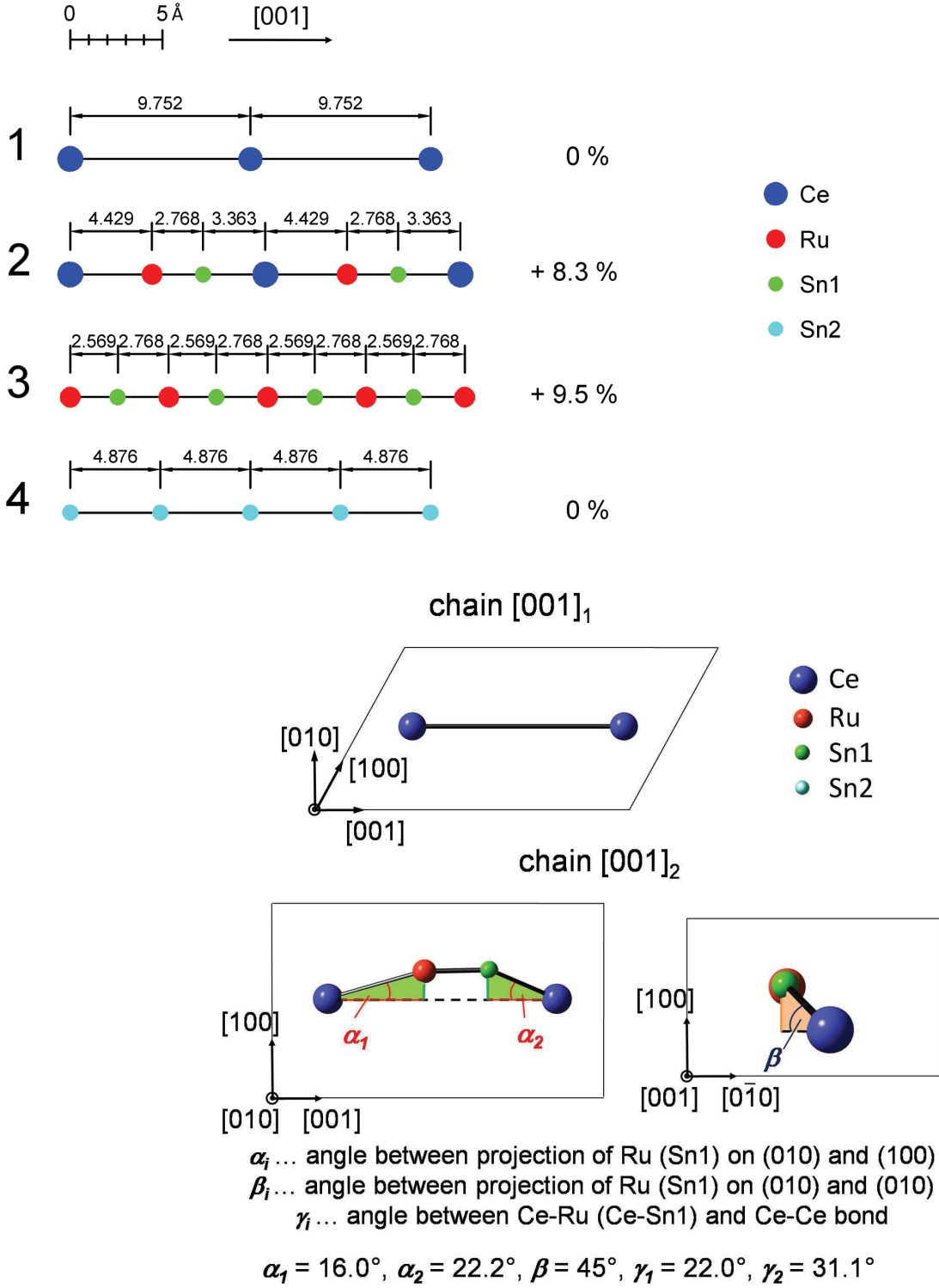


Figure 4.7: Direct and indirect (zigzag) atomic chains ( $[001]_i$ ,  $i=1$  to 4) along  $[001]$  for  $\text{CeRu}_4\text{Sn}_6$  (top). All 1-dimensional chains span a distance of  $2c$  along  $[001]$ . Their extensions with respect to a straight chain with bond angles of  $180^\circ$  are specified in %. At the bottom, the directional dependent presentations of the Ce-containing chains are displayed to show their 3-dimensional properties.



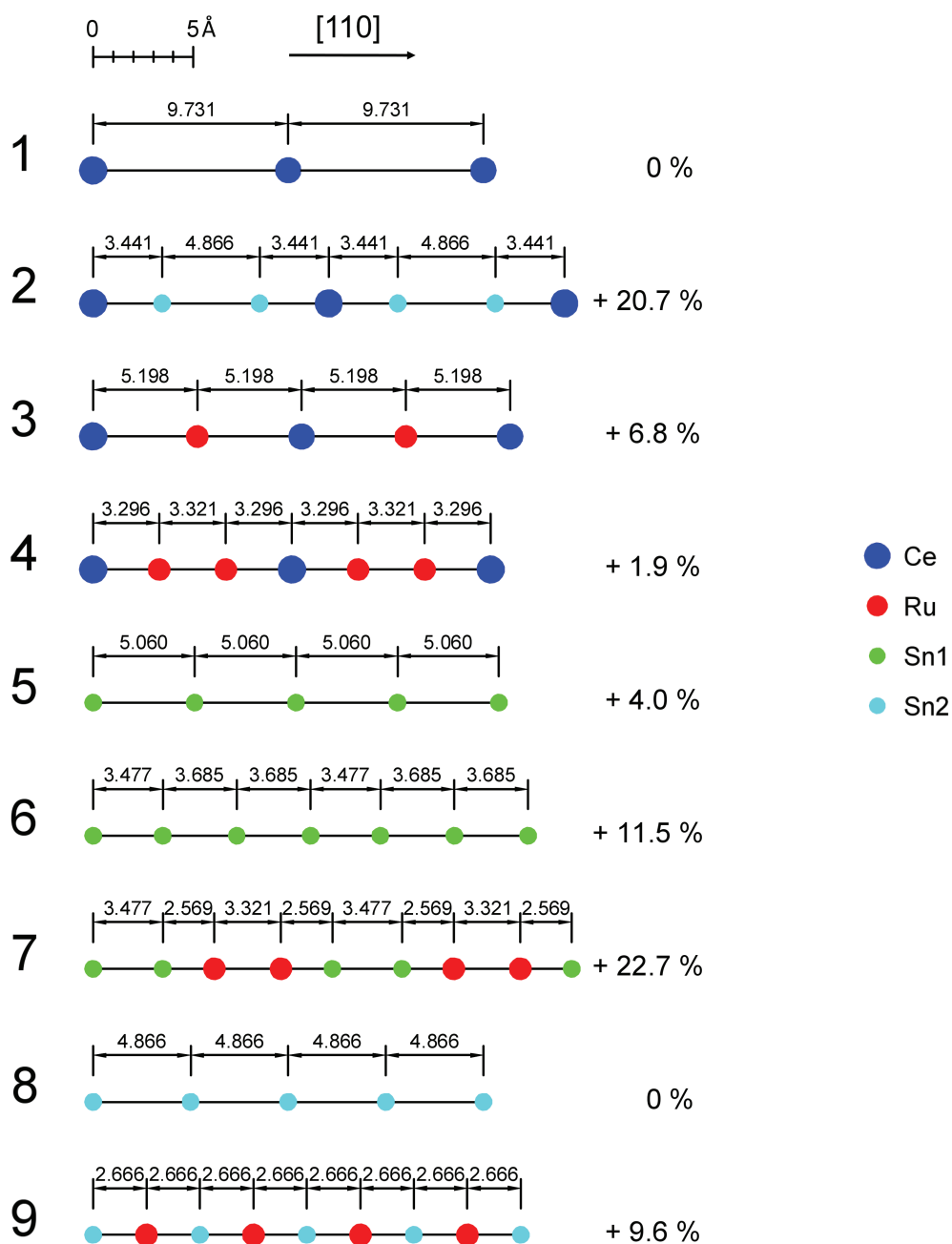


Figure 4.8: Direct and indirect (zigzag) atomic chains ( $[110]_i$ ,  $i=1$  to 9) along  $[110]$  for  $\text{CeRu}_4\text{Sn}_6$ . The displayed chains span a distance of  $2c'$  along  $[110]$ . Their extensions with respect to a straight chain with bond angles of  $180^\circ$  are specified in %. Different views on the Ce-containing chains are shown in Fig. 4.9 in a 3-dimensional representation.



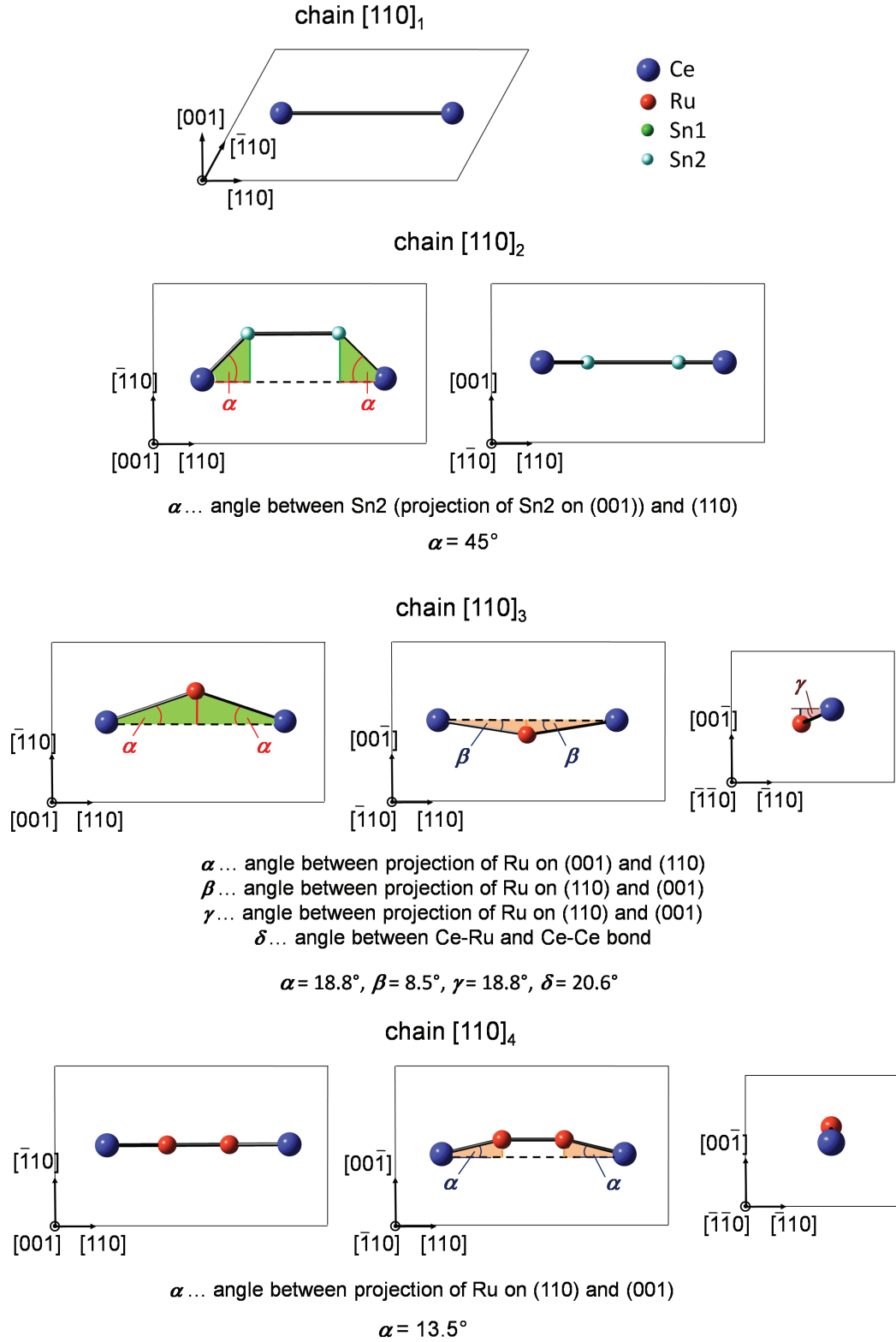


Figure 4.9: 3-dimensional representations of the direct and indirect Ce-containing atomic chains along  $[110]$ . The 1-dimensional representations are shown in Fig. 4.8.

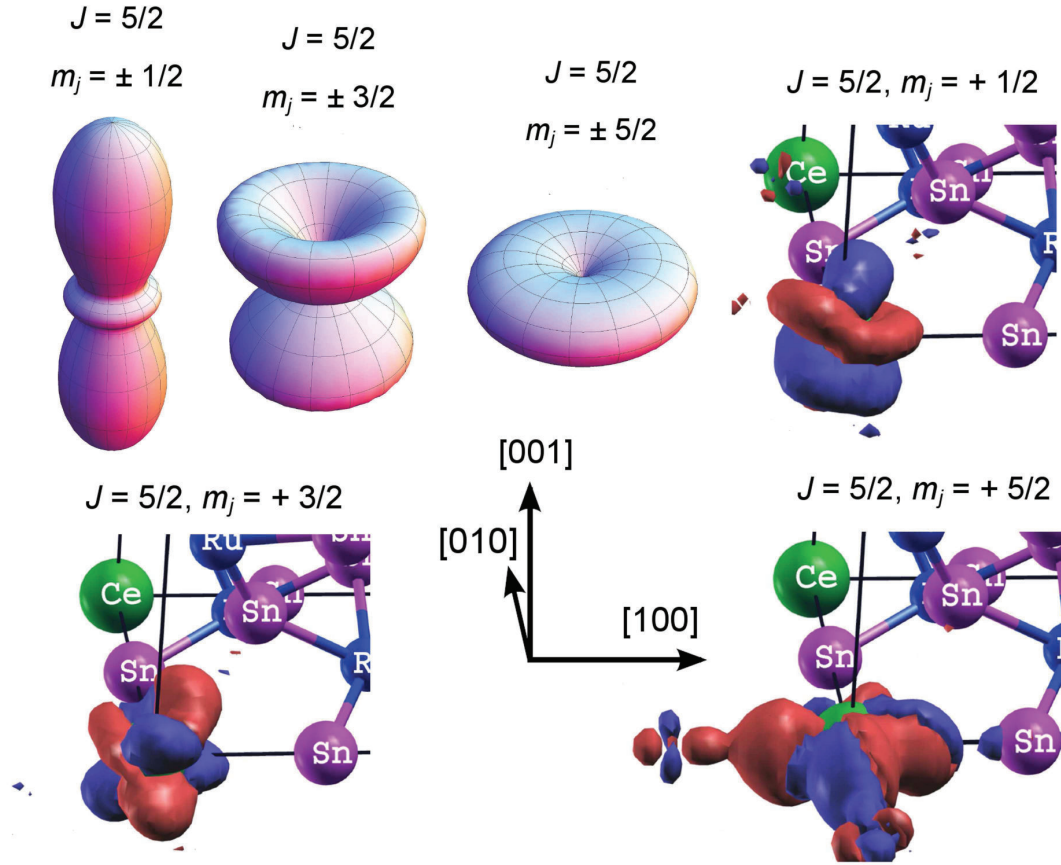


Figure 4.10: The Ce-4*f*-electron orbitals for  $J = 5/2$  in the  $(J, m_j)$ -base are displayed on the top left. In addition, the Wannier orbitals for  $J = 5/2$  ( $m_j = 1/2, 3/2$  and  $5/2$ ) are displayed, which were calculated by P. Wissgott [9]. The illustrations of the Wannier orbitals were extracted from P. Wissgott's PhD thesis [9]. While the Wannier orbital derived from  $(J = 5/2, m_j = 1/2)$  roughly keeps the unhybridized orbital shape along  $[001]$ , it gets strongly broadened within the  $(001)$  plane. The Wannier orbitals derived from  $(J = 5/2, m_j = 3/2)$  and  $(J = 5/2, m_j = 5/2)$  show a directional dependence perpendicular to  $[100]$  in contrast to the unhybridized orbitals. Especially the  $(J = 5/2, m_j = 5/2)$  Wannier orbital shows a strong directional dependence in the  $(001)$  plane. In addition, the  $(J = 5/2, m_j = 5/2)$  Wannier orbital is strongly broadened in the  $(001)$  plane.

## 4.2 Single crystal growth and orientation procedure

High quality single crystals are essential to study the material's intrinsic physical properties. This is particularly true for Kondo insulators. Due to their narrow energy gap, imperfections of the crystals may strongly alter the properties, especially at low temperatures. This has been shown for instance for CeNiSn [33,39]. Within this work, CeRu<sub>4</sub>Sn<sub>6</sub> single crystals were grown and investigated.

### 4.2.1 Single crystal growth

The single crystal growth was performed by the floating-solution-zone traveling heater method (THM) using optical heating in a four-mirror furnace (Crystal Corporation) with a growth rate of 0.3 - 0.5 mm/h. A schematic set-up is shown in the left panel of Fig. 4.12. The polycrystalline rods for the crystal growth were synthesized by melting together high purity Ce, Ru and Sn in a horizontal, water cooled copper boat using high-frequency heating. The melting procedure with the stoichiometric CeRu<sub>4</sub>Sn<sub>6</sub> rods was repeated several times to enhance the homogeneity of the resulting polycrystalline material. The purity of the starting materials was 99.99 % for Ce (Ames Lab) and Ru, and 99.9999 % for Sn. All synthesis steps were performed under protective Ar atmosphere after several purgings with Ar.

A self-flux technique was used since CeRu<sub>4</sub>Sn<sub>6</sub> melts incongruently. This was confirmed by A. Prokofiev and T. Nezu with differential thermal analysis (DTA) experiments which reveal multiple peaks on the heating and cooling curves (Fig. 4.11, left panel) [10]. They also reported that upon quenching the CeRu<sub>4</sub>Sn<sub>6</sub> melt predominantly the phases CeRuSn<sub>3</sub> and Ru<sub>4</sub>Sn<sub>7</sub> form. Hence, a flux technique for the single crystal growth of CeRu<sub>4</sub>Sn<sub>6</sub> was used. A. Prokofiev reported that a pure tin flux lead to the formation of undesired phases. Therefore, a suitable flux material was searched for in the ternary Ce-Ru-Sn composition to avoid foreign elements. Because a Ce-containing flux is expected to support the growth of the highly stable CeRuSn<sub>3</sub> phase, binary Ru-Sn self-fluxes were investigated. Finally, A. Prokofiev chose Ru<sub>2</sub>Sn<sub>3</sub> which has the same Ru:Sn ratio as CeRu<sub>4</sub>Sn<sub>6</sub>. In addition, Ru<sub>2</sub>Sn<sub>3</sub> is expected to suppress the formation of the Ce-rich phase CeRuSn<sub>3</sub>. The lowest melting composition in the Ru-Sn binary phase diagram is the eutectic at 1160 °C (42.5 at.% Ru and 57.5 at.% Sn). This composition is close to the Ru:Sn ratio of the chosen flux.

The composition dependence of the growth length of the single crystals was investigated in detail by T. Nezu and A. Prokofiev within T. Nezu's master thesis (Fig. 4.11, right panel) [10]. The measurements revealed a position-independent stoichiometry over the full growth length. Within this PhD thesis, a possible composition gradient along the growth direction was in addition studied by transverse magnetoresistivity measurements. For this analysis, three samples were separated from different positions of the longest single crystal grown within this work (batch G7). The measured samples were separated from the bottom (G7 BO1), the middle

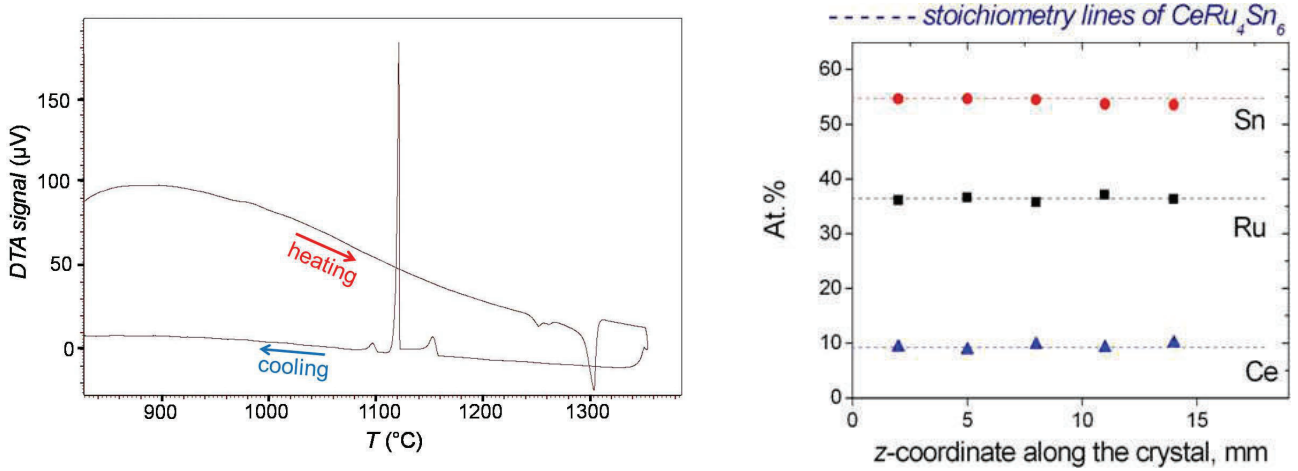


Figure 4.11: In the left panel a DTA analysis of  $\text{CeRu}_4\text{Sn}_6$  is shown (performed by T. Nezu [10]). The multiple peaked structure of the DTA signal confirms the incongruent melting of  $\text{CeRu}_4\text{Sn}_6$ . The right panel shows the element concentration in at.% with respect to the single crystal growth length  $z$  [10].

(G7 BO7) and the top (G7 TOP4) of this single crystal G7, corresponding to the beginning, the middle and the end of the single crystal growth, respectively. These measurements (Fig. 6.41) confirm that, within the accuracy of these measurements, no growth length dependence of the single crystal quality exists.

As an example, the right panel in Fig. 4.12 displays the rod resulting from the growth of batch G6, with the single crystal already being separated from the polycrystalline feed and seed rods.  $\text{CeRu}_4\text{Sn}_6$  is very brittle and therefore attention must be paid in handling the samples. Photographs of broken pieces of batch G6 reveal the characteristic shell-like fractured surfaces (Fig. 4.13). The sample broke when unmounting it from the mirror furnace.

As already mentioned, the first attempts to grow single crystalline  $\text{CeRu}_4\text{Sn}_6$  were made by T. Nezu and A. Prokofiev [10]. Two batches (B, G2) of their successful growth were used for measurements within this work. In addition, several tries growing new single crystals were initiated and the largest grown single crystal G7 is shown in Fig. 4.14. Table 4.2 shows all single crystals grown so far and the measurements performed on them.

## 4.2.2 Phase and domain purity analyses

After separating the central crystallized part from the polycrystalline rods, it was polished at the top and bottom of the grown zone. At first, polarized light was used to check the domain purity of the polished areas. Polarized light microscopy is a useful technique for the visualization of large scale domain misalignment and foreign phases on the specimen surface. If no sufficient domain purity was achieved, the respective surface was alternately polished and checked

Table 4.2: Grown and measured  $\text{CeRu}_4\text{Sn}_6$  single crystal samples within this work. Used abbreviations: R = resistivity, MR = magnetoresistivity, HE = Hall effect, M = magnetization, T = thermopower, TM = torque magnetometry, OS = optical spectroscopy, XAS = X-ray absorption spectroscopy, Prok = A. Prokofiev, Nezu = T. Nezu, Wink = H. Winkler.

batch name	grown by	result	date	exemplary measurements
B (G1)	Prok	success	10/2006	high field MR, R, MR
G2	Prok/Nezu	successful	02/2008	R, HE, MR, M, TM, T
G3	Prok/Wink	successful	11/2010	R, OS, M, TM, T, XAS
G4	Prok/Wink	fail	03/2011	-
G5	Prok/Wink	fail	05/2011	-
G6	Prok/Wink	successful	11/2011	HE, torque, TM
G7	Prok/Wink	successful	10/2012	MR, $\mu\text{SR}$ (planned)

again with polarized light, till a sufficiently large single domain was reached. Afterwards, the domain/phase purity and the correct stoichiometric composition were investigated with Laue and X-ray powder diffraction and with scanning electron microscopy (SEM) with energy dispersive X-ray spectroscopy (EDX) measurements. Exemplarily, photographs of the single crystal G6 and SEM images of samples separated from it are shown in Fig. 4.13. The SEM investigations reveal phase purity of all investigated samples of  $\text{CeRu}_4\text{Sn}_6$ .

The results of the powder diffraction analysis of small amounts of material from batches G3 and G7 are displayed in Fig. 4.15. Small amounts of foreign phases were detected on the free ingot surface in all growth runs. Hence, the surface layer was removed from all samples before the measurements. These foreign phases are visible for instance on batch G6 as a yellowish surface layer (Fig. 4.13, top). The bulk single crystalline material was, however, pure  $\text{CeRu}_4\text{Sn}_6$  with the exception of batch G7. In batch G7, a small amount ( $< 0.5\%$ ) of the foreign phase  $\text{Ru}_2\text{Sn}_3$  was detected by X-ray powder diffraction (Fig. 4.15). Interestingly, the formation of this phase was also reported for polycrystalline  $\text{CeRu}_4\text{Sn}_6$  by Strydom et al. [2].

Magnetoresistivity and electrical resistivity measurements revealed that samples separated from batch G2 show slightly differing behaviour in comparison to all others. Smaller deviations were also found for samples separated from the same batch and therefore differences without any batch dependence occurred, too. Hence, additional EDX measurements of the crystal compositions were performed for these differing samples. The EDX technique was chosen because it is nondestructive. These EDX investigations cannot identify a difference in stoichiometry or impurities within the measurement accuracy. In addition, the behaviour of the magnetoresistivity of samples separated from batch G7 (where a small amount of foreign phases was detected in the powder pattern) was investigated in detail and compared to results from phase pure batches (Fig. 6.41). This comparison revealed that no distinct effects of foreign phases on the properties

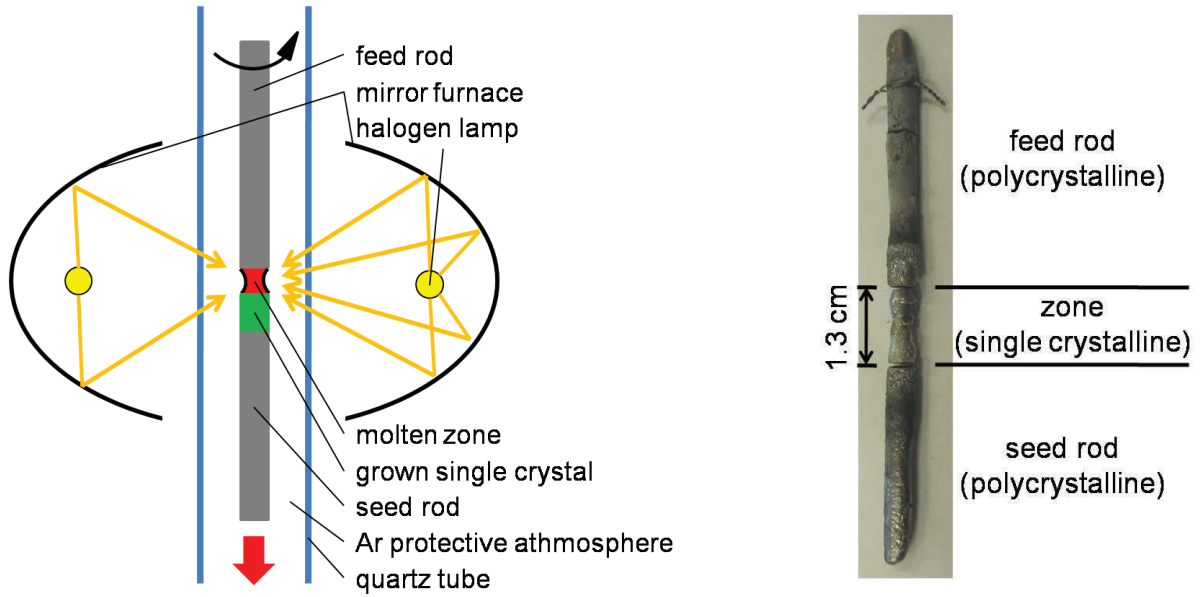


Figure 4.12: Schematic drawing of the floating zone technique (left). In addition, a resulting zone melted rod of CeRu<sub>4</sub>Sn<sub>6</sub> batch G6 is displayed in the right panel.

of G7 were detectable. Maybe non-detectable impurity concentrations yield noticeable changes in the density of states (DOS) and as a result, lead to diverging electronic transport properties. However, the origin of the discrepancies in the electrical transport measurements is not understood yet.

In conclusion, the phase purity analysis revealed the necessity to remove the surface layer of the grown single crystals and confirm the high quality of the single crystals in the bulk of all batches used within this thesis.

### 4.2.3 Orientation procedure

The special relation of the lattice parameters ( $c \approx \sqrt{2} \cdot a$ ) in CeRu<sub>4</sub>Sn<sub>6</sub> and the available Laue device (Kristalloflex 760, Siemens AG) lead to a complicated orientation process. As already mentioned in Sect. 4.1, the tetragonal unit cell of CeRu<sub>4</sub>Sn<sub>6</sub> can be approximated with a slightly distorted quasi-cubic cell (Fig. 4.3). As a result, the crystallographic directions  $c$  and  $c'$  of the quasi-cubic unit cell cannot be distinguished with the available Laue device. Thus, a specific procedure based on a sizable  $c$ - $c'$  anisotropy of the magnetization was used instead. At first, a small piece of the single crystalline material with three mutually orthogonal  $\langle 100 \rangle$  or  $\langle 110 \rangle$  directions (indistinguishable) was separated. Afterwards the  $\langle 001 \rangle$  and  $\langle 110 \rangle$  directions of this piece were determined with magnetization measurements. Magnetization measurements were chosen for orientation because they are comparably quick and do not require an involved sample preparation procedure. In addition, the magnetic anisotropy between the directions is



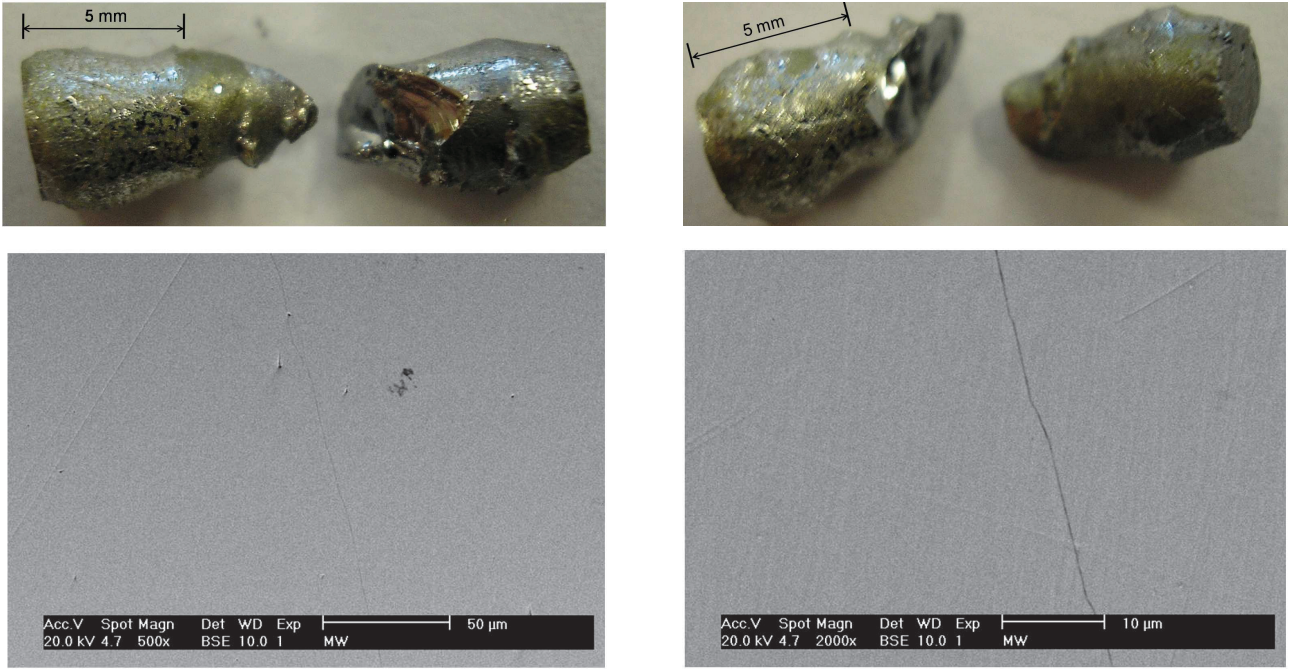


Figure 4.13: Photographs of the  $\text{CeRu}_4\text{Sn}_6$  single crystal G6 (top). The grown zone broke into two pieces. SEM images of a sample separated from batch G6 are shown on the bottom. They demonstrate the phase purity of this sample. The area displayed on the right is about 4 times smaller than the one on the left.

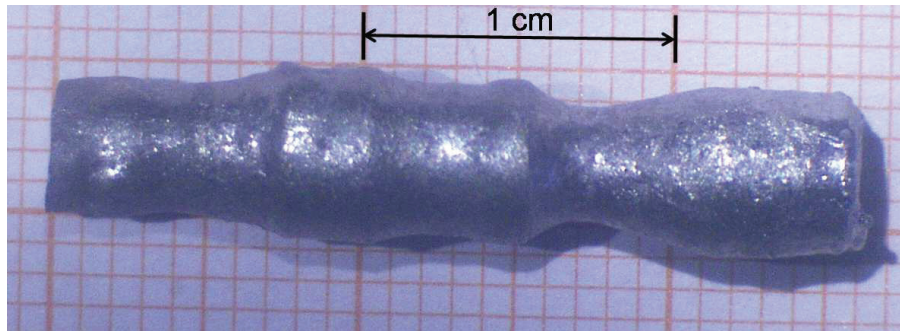


Figure 4.14: A photograph of the largest  $\text{CeRu}_4\text{Sn}_6$  single crystal (G7) grown in this thesis.

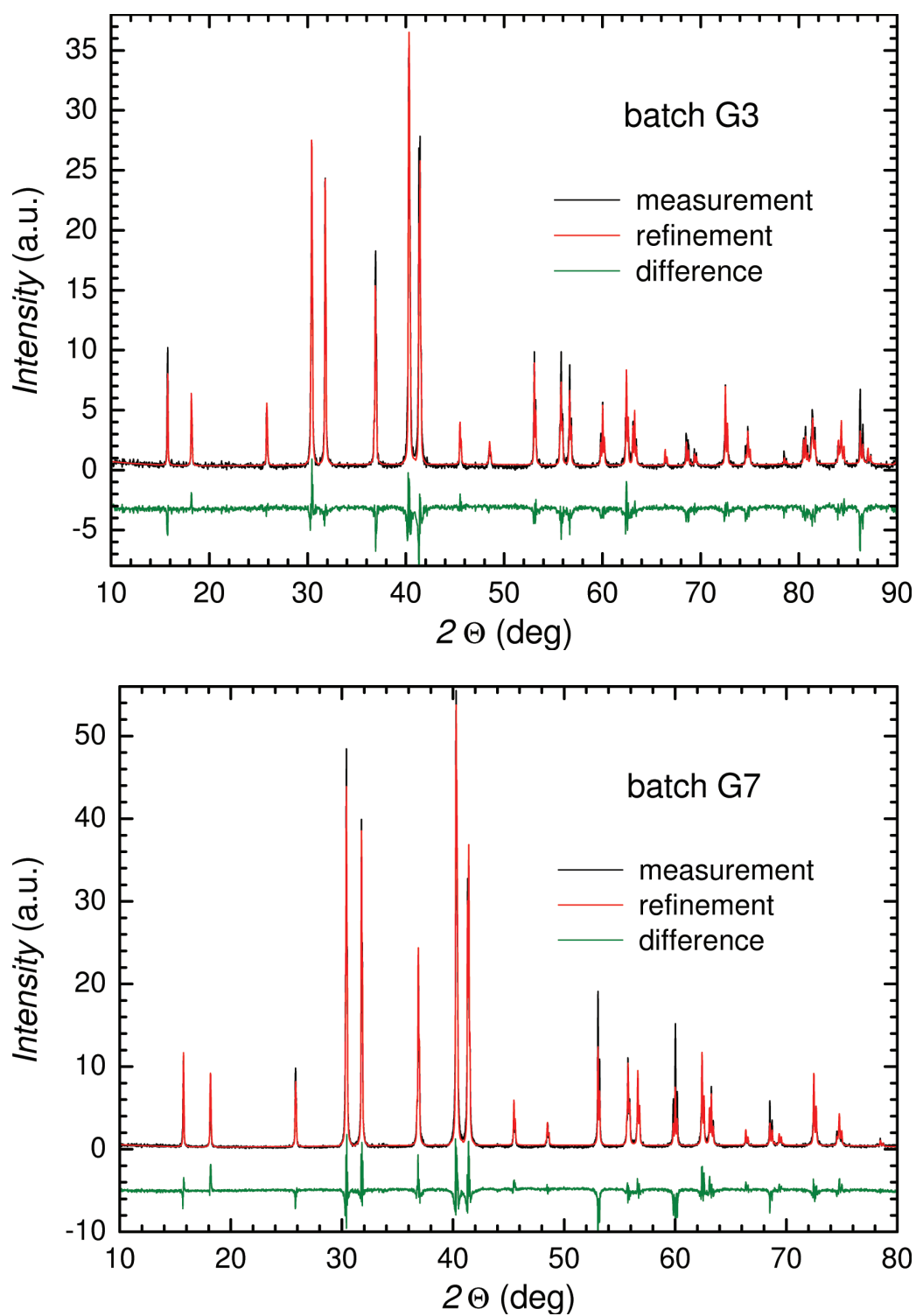


Figure 4.15: Powder diffraction patterns of  $\text{CeRu}_4\text{Sn}_6$  batch G3 (top) and G7 (bottom). The measured (black), refined (red) and difference (green, shifted downwards by a constant value) curves are displayed. The powder pattern of batch G7 exhibits a tiny amount of the foreign phase  $\text{Ru}_2\text{Sn}_3$  (less than 0.5 %), seen as small additional peaks around 34 and 44°. No additional peaks from other foreign phases are detected.



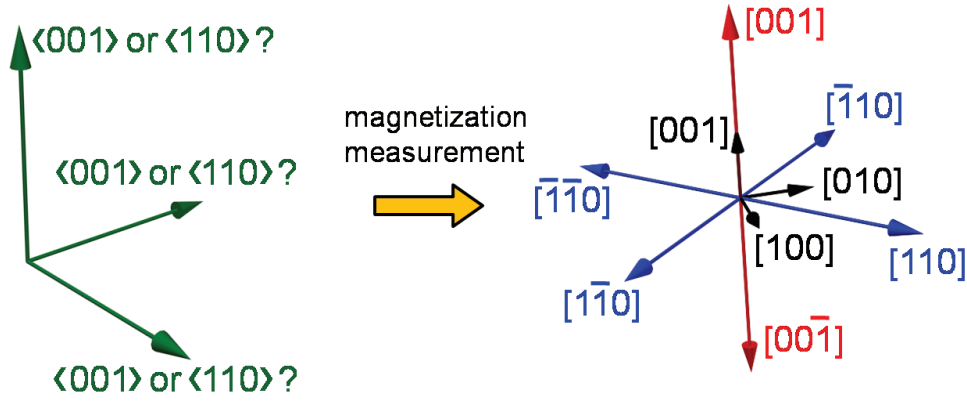


Figure 4.16: Schematic orientation process of  $\text{CeRu}_4\text{Sn}_6$  single crystals. Starting from three orthogonal  $\langle 001 \rangle$  or  $\langle 110 \rangle$  directions (left panel) to the resulting orientation (right panel) with magnetization measurements [49].

essentially sample and batch independent. The orientation derived for this single crystalline piece was then assigned to the entire single crystal. A schematic drawing is shown in Fig. 4.16. A detailed description of the orientation process and its difficulties can be found in the master thesis of the present author at the Vienna University of Technology [49].

#### 4.2.4 Finalizing sample preparation

At the end of the above described processes, the required samples were separated with a diamant saw (Well Diamantdrahtsägen GmbH) or an Accutom (Struers GmbH). Finally, the necessary geometry and surface properties of the cut pieces were achieved by polishing the separated material with silicon carbide and/or diamant abrasive paper.



# Chapter 5

## Theoretical calculations for $\text{CeRu}_4\text{Sn}_6$

In parallel to the experimental investigations on  $\text{CeRu}_4\text{Sn}_6$ , local density approximation plus dynamic mean-field theory (LDA+DMFT) calculations were performed within the PhD work of P. Wissgott in the group of K. Held at the Vienna University of Technology [9]. From the electronic band structure calculated in that work, optical conductivity, electrical resistivity and thermopower were derived and compared to experimental results of the present thesis. Since much reference will be made to these theoretical results, the key results are briefly discussed below. Note that the crystallographic directions are specified with  $a$  ( $\langle 100 \rangle$ ),  $c'$  ( $\langle 110 \rangle$ ) and  $c$  ( $\langle 001 \rangle$ ) within this chapter in accordance to the published data on  $\text{CeRu}_4\text{Sn}_6$ . So,  $a$ ,  $c'$  and  $c$  does not only nominate lattice constants, but also directions.

At first, the pure LDA electronic structure was investigated. It revealed a manifold of mixed Ce-4*f*, Ru-4*d* and Sn-5*p* bands around the Fermi level (Fig. 5.1). The Ce-4*f* bands are filled by 0.7 electrons and show a small hybridization tail below the Fermi energy  $E_F$  (0 eV) with mainly ( $J = 5/2$ ,  $m_j = \pm 1/2$ )-contribution (Fig. 5.1, right panel). The main manifold of the *f* states is situated above  $E_F$  (starting at about 0.1 eV above  $E_F$ ). This manifold is split by approximately 0.4 eV due to spin-orbit coupling into a separated  $J = 5/2$  and  $J = 7/2$  manifold. Because of the additional crystalline electric field (CEF) splitting of these manifolds, the  $J = 5/2$  states are split into  $m_j = \pm 5/2$  states at about 0.3 eV above  $E_F$  and  $m_j = \pm 3/2$  and  $m_j = \pm 1/2$  states centered both at roughly 0.2 eV above  $E_F$ . The latter ones are separated by approximately 0.05 eV, with the  $m_j = \pm 3/2$  state being lower in energy. In addition to the small contributions from the Ce-4*f* bands, the Ru-4*d* bands with small admixture of Sn-5*p* bands play the major role around the Fermi level. The partial density of states (DOS) of the Ru-4*d* bands with  $J = 5/2$  and  $J = 3/2$  revealed no  $J$ -dependent splitting. Furthermore, they are broadened by CEF effects within a range of almost 10 eV and exhibit a direct gap-like structure of about 0.1 eV at the Fermi level.

Subsequently, adequate Wannier orbitals of the localized 4*f* states were calculated which were used for the following LDA+DMFT calculation. Importantly, these LDA+DMFT calculations treated the Ce-4*f*  $J = 7/2$ , Ru-4*d* and Sn-5*p* states as background, whereas the Ce-4*f*  $J = 5/2$  states were handled on the full DMFT level. The DOS spectra revealed that the Ce-4*f*

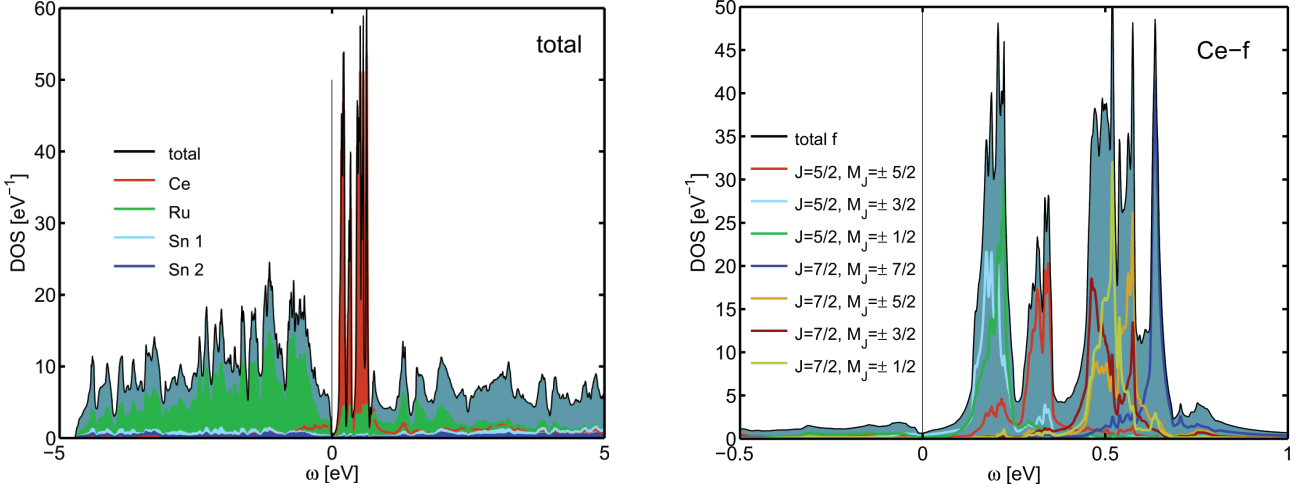


Figure 5.1: In the left panel the partial LDA DOS as a function of the energy  $\omega$  is shown for the most important atomic contributions, namely Ce-4*f*, Ru-4*d* and Sn-5*p*. The right panel displays the partial LDA DOS for the Ce-4*f* states in the  $(J, m_j \equiv M_j)$  base. Both plots were extracted from the PhD thesis of P. Wissgott [9].  $E_F$  is positioned at 0 eV.

$m_j = \pm 1/2$  states contribute most to the ground state (Fig. 5.2), which is in contrast to the LDA calculations which revealed mainly  $m_j = \pm 3/2$  as lower lying state. These differences probably occurred because the hybridization strength of the  $m_j = \pm 1/2$  states with the conduction electrons is enhanced within the LDA+DMFT calculations compared to the pure LDA treatment. The  $m_j = \pm 5/2$  state is the highest lying CEF doublet in both LDA and LDA+DMFT calculations.

The LDA+DMFT DOS spectra at 290 and 1160 K were derived by the maximum entropy method (Fig. 5.3). Within these investigations, the Kondo (or Abrikosov-Suhl) resonance evolves to lower temperatures, leading to a peak in the DOS slightly above the Fermi level. A detailed analysis at 290 K revealed that the Ce-4*f*  $m_j = \pm 1/2$  states hybridize strongly whereas the Ce-4*f*  $m_j = \pm 3/2$  states remain more localized. In comparison to the pure LDA calculations, the Sn-5*p* Wannier orbitals interact more strongly with the 4*f* states than the Ru-4*d* orbitals. Hence, a slightly larger *p* contribution to the Kondo effect is revealed.

Within the LDA+DMFT calculations, the lowest temperatures (below 290 K) were not accessible with the theoretical approach. Thus, the behaviour at lowest temperatures was mimicked by setting the imaginary part of the self energy to a constant value. This procedure revealed clearly anisotropic behaviour between the basal plane and the perpendicular *c* direction, which correctly describes the experimental trends. The origin of this anisotropic behaviour is best seen from the calculated *k*-dependent LDA+DMFT DOS, which is shown in Fig. 5.4. In the upper panel, which shows the DOS at 290 K, a broadening of the bands around  $E_F$  is seen. This implies a high scattering rate and is attributed to Kondo scattering. At lower temperatures,

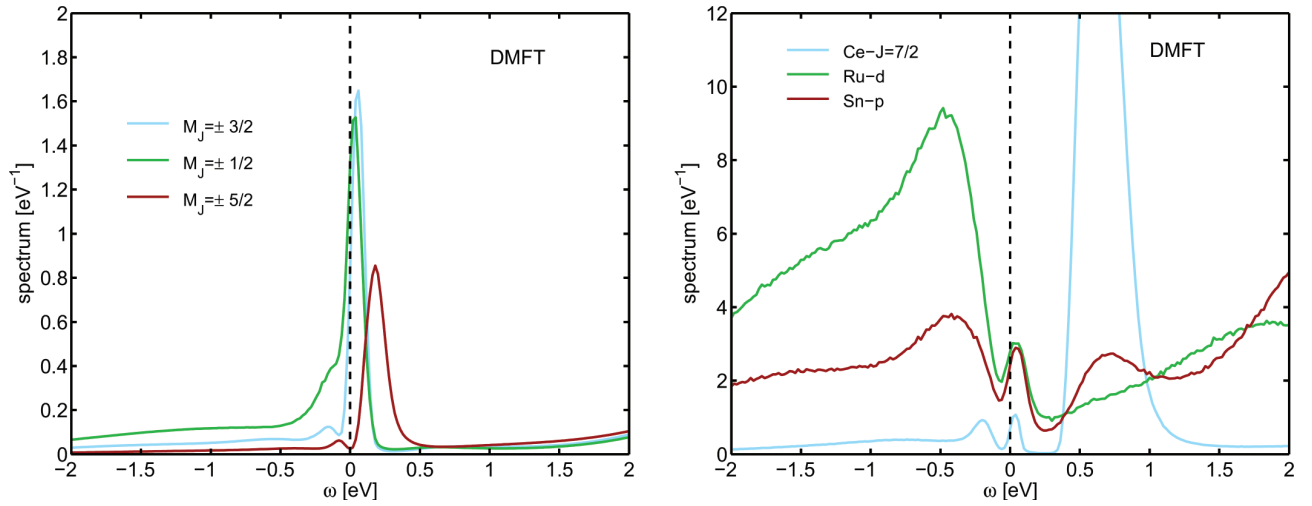


Figure 5.2: DOS spectra at 290 K for the Ce-4*f*  $J=5/2$  states (left) and the Ce-4*f*  $J=7/2$ , Ru-4*d* and Sn-5*p* states (right). The spectra were calculated by P. Wissgott [9] and the plots were extracted from his PhD thesis [9].

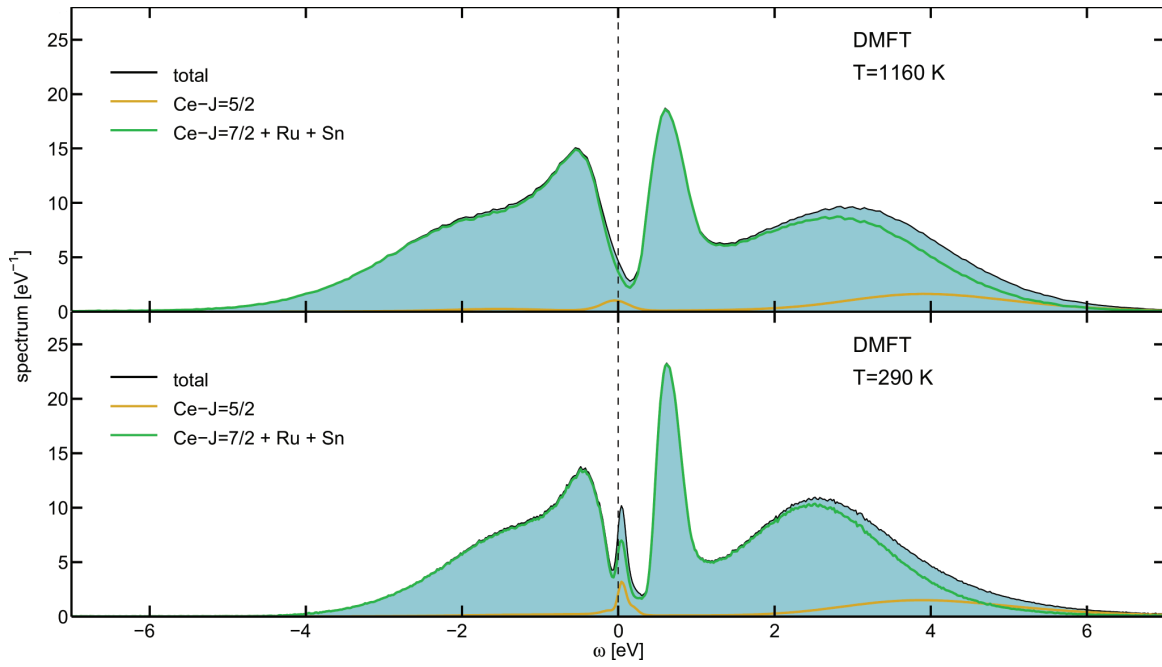


Figure 5.3: Overall DOS as a function of energy  $\omega$  for two different temperatures  $T$  (1160 K, top and 290 K, bottom) derived by LDA+DMFT calculations by P. Wissgott [9]. A Kondo resonance emerges at lower temperatures, leading to a peak in the DOS slightly above  $E_F$ . Both plots were extracted from the PhD thesis of P. Wissgott [9].

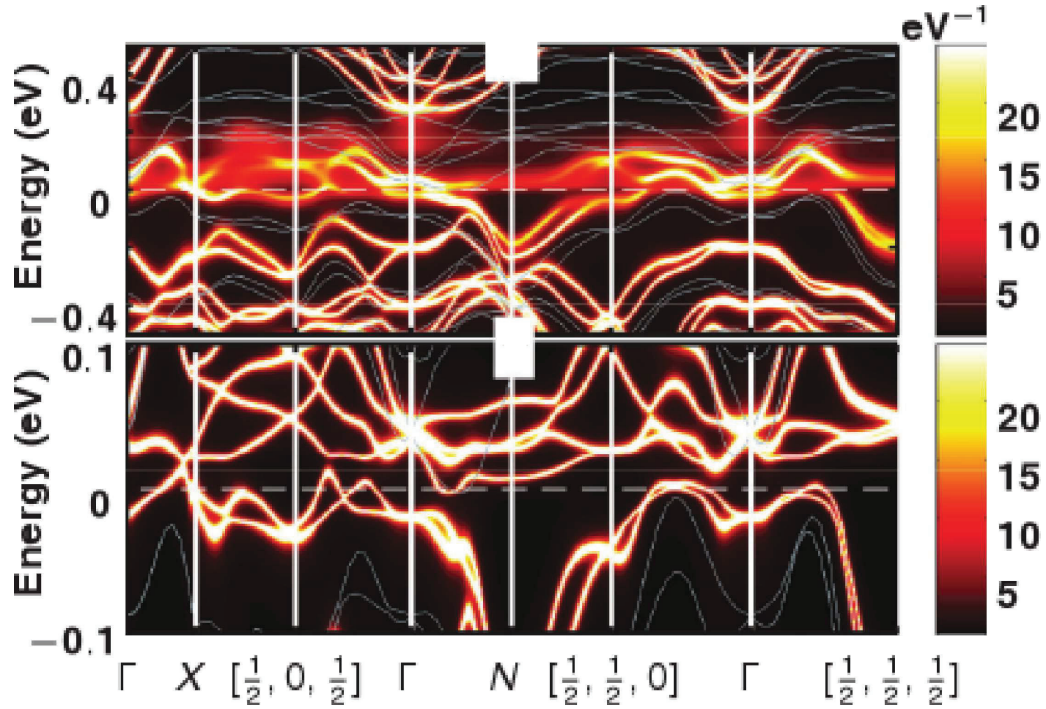


Figure 5.4: The upper panel shows the  $k$ -resolved LDA+DMFT band structure of  $\text{CeRu}_4\text{Sn}_6$  at 290 K. The lower panel mimics the situation at low temperatures and is obtained by setting the self energy  $\Sigma$  of the LDA+DMFT calculation for  $T = 290$  K to  $\Sigma = \Re(\Sigma) + 0.005i$  eV. The fixed imaginary part to a small value leads to a resolution of more features in the band structure. It reveals a gapped structure around  $E_F$  (0 eV) in a broad range of the Brillouin zone. A pronounced band crossing at  $E_F$  is only seen for the direction  $\Gamma$  to  $X$ , which corresponds to the  $c$  direction. Additionally, gray lines for the band structure derived via LDA calculations are included. These results were calculated within the PhD thesis of P. Wissgott [9] and the plots were extracted from [16].

the bands are narrower and a remarkable difference between the  $c$  and the in-plane directions becomes apparent (Fig. 5.4, bottom). In a broad range of the Brillouin zone, a direct gap is established around  $E_F$ . This is particular true for the basal (001) plane (Fig. 5.4 from  $\Gamma$  to  $[\frac{1}{2}, \frac{1}{2}, 0]$ ). On the other hand, no gap is found along the perpendicular  $c$  direction (Fig. 5.4 from  $\Gamma$  to  $X$ ).

The optical spectroscopy, electrical resistivity and thermopower calculated from this LDA+DMFT DOS [9] are discussed in the respective experimental subsections (Sect. 6.6, 6.2 and 6.5).

# Chapter 6

## Experimental investigations

This chapter presents the experimental results observed within this thesis. Magnetization, torque magnetometry, electrical resistivity, Hall effect, magnetoresistivity and thermopower measurements were performed and are discussed in Sects. 6.1 to 6.5. In addition, the results of the X-ray absorption spectroscopy, optical spectroscopy investigations and cleaving tests in combination with STM investigations performed by collaborators on  $\text{CeRu}_4\text{Sn}_6$  samples provided within this thesis are discussed (Sect. 6.6). Note that the crystallographic directions are specified with  $a$  ( $\langle 100 \rangle$ ),  $c'$  ( $\langle 110 \rangle$ ) and  $c$  ( $\langle 001 \rangle$ ) in accordance to the published data on  $\text{CeRu}_4\text{Sn}_6$ . So,  $a$ ,  $c'$  and  $c$  does not only denominate lattice constants, but also directions.

### 6.1 Magnetic properties

In this section the temperature dependent magnetic susceptibility, field dependent magnetization (Sect. 6.1.1), and torque magnetometry measurements (Sect. 6.1.2) on  $\text{CeRu}_4\text{Sn}_6$  single crystals synthesized within this thesis are presented, analyzed and discussed. Note that within this thesis the magnetic susceptibility  $\chi$  is given by

$$\chi = M/H \quad . \quad (6.1)$$

The magnetic susceptibility in the linear response regime  $\chi_{LR}$  is defined to

$$\chi_{LR} = \lim_{H \rightarrow 0} \frac{\partial M(H)}{\partial H} \quad . \quad (6.2)$$

Both equations include the magnetization  $M$  and the magnetic field  $H$ .

### 6.1.1 Direct magnetization measurements

The first magnetization measurements on single crystalline  $\text{CeRu}_4\text{Sn}_6$  were performed by Nezu [10] and afterwards by the present author [49] within their master theses. Due to slight inconsistencies (batch dependencies, background problems), additional magnetization measurements were performed on new  $\text{CeRu}_4\text{Sn}_6$  single crystals and the temperature range of these measurements was increased up to about 1000 K. The measurement techniques and devices (SQUID, VSM) were introduced in Sect. 3.2. As discussed in Sect. 4.2, each single crystalline grain had to be oriented by magnetization measurements. This is why many samples were measured.

Firstly, the high-temperature behaviour is presented and an analysis in terms of pure crystalline electric field (CEF) effect is discussed. Secondly, the low-temperature behaviour and a Pauli susceptibility description are discussed.

#### High-temperature magnetization and crystalline electric field approach

Figure 6.1 (Figure 6.2) shows the (inverse) magnetic susceptibility  $\chi$  ( $1/\chi$ ) (Eqn. 6.1) as a function of the temperature  $T$  along the three main directions  $a$ ,  $c$  and  $c'$ . In the entire temperature range, a pronounced anisotropy is seen between the out-of-plane direction  $c$  and the in-plane directions  $a$  and  $c'$ .  $\text{CeRu}_4\text{Sn}_6$  exhibits an easy basal plane (large  $\chi$ ) and a perpendicular hard  $c$  axis (Fig. 6.1). Some features are better seen in  $1/\chi(T)$  (Fig. 6.2).  $1/\chi_c(T)$  decreases at first almost linearly (Curie-Weiss behaviour) from 1000 K towards lower temperatures until a minimum is reached at  $T_{min,1/\chi} = 360$  K, followed by a non-linear increase, a maximum at  $T_{max,1/\chi} = 75$  K, and a pronounced decrease towards the lowest measured temperatures. By contrast, the in-plane directions  $a$  and  $c'$  show a steady decrease of  $1/\chi_a(T)$  and  $1/\chi_{c'}(T)$ , respectively. At about 50 K, a shoulder in  $1/\chi(T)$  along the in-plane directions occurs (Fig. 6.2). For both in-plane directions, no extended range of exactly linear temperature dependence is seen.

From these measurements a small difference between the two in-plane directions  $a$  and  $c'$  is seen, especially at high temperatures. To confirm this anisotropy, torque magnetometry measurements between 3 and 325 K were made (Sect. 6.1.2). By contrast to the magnetization measurements presented above, no in-plane anisotropy could be revealed by this technique between 40 and 325 K. We attribute the disagreement between these results to misalignment and sample geometry effects during the direct magnetization measurements. Therefore, between 40 and 325 K no intrinsic anisotropy can be discerned in the basal plane. Unfortunately, we do not have a torque magnetometry setup for measurements above 325 K. Nevertheless, we believe that also here differences in  $\chi_a$  and  $\chi_{c'}$  seen in the direct measurement are extrinsic and due to the above mentioned effects.

At highest temperatures, a Curie-Weiss (CW) law (Chap. 2) was fit to the  $\chi(T)$  data along the different crystallographic directions (Fig. 6.2). The fit parameters (paramagnetic Weiss



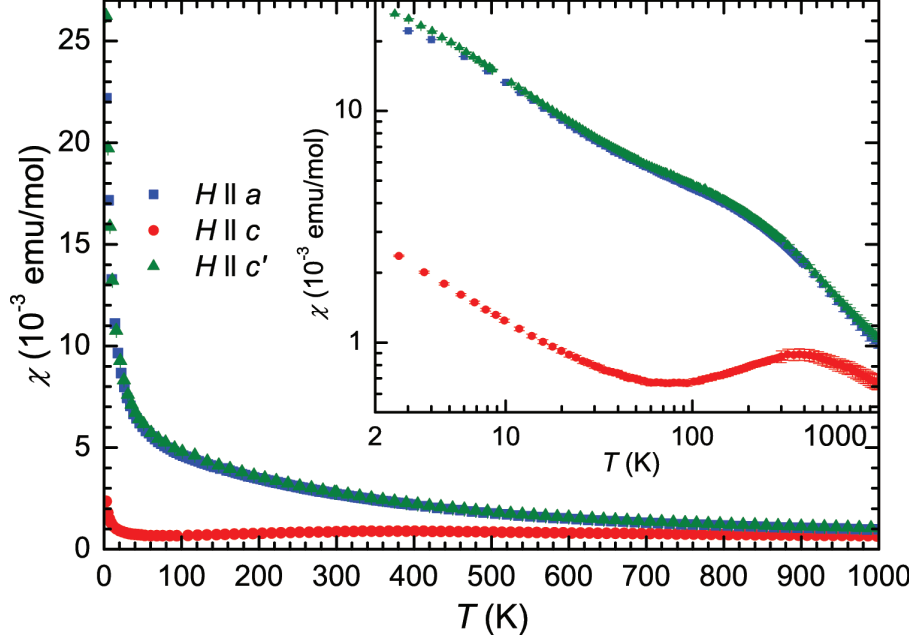


Figure 6.1: The susceptibility  $\chi$  as a function of temperature  $T$  (on a semilogarithmic scale) up to 1000 K along the three investigated main directions  $a$  (blue),  $c$  (red) and  $c'$  (green) is shown (in the inset) (sample G2\_B\_3). The error bars are plotted as lines. Pronounced anisotropy between the in-plane directions ( $a$ ,  $c'$ ) and the out-of-plane direction  $c$  is seen. The differences between the in-plane directions, measured with direct magnetization measurements, have been investigated with torque magnetometry between 3 and 300 K. These measurements revealed that anisotropy is measurable only below 25 K. Hence, we attribute the mismatch of the direct measurements to misalignment effects.

Table 6.1: Directional dependent Weiss temperatures  $\Theta$  and effective moments  $\mu_{eff}$  revealed by fitting the inverse susceptibility of  $\text{CeRu}_4\text{Sn}_6$  single crystals at  $T > 500$  K (Fig. 6.2).

crystallographic direction	$\Theta$ (K)	$\mu_{eff}$ ( $\mu_B/\text{Ce}$ )
$a$	$-143 \pm 50$	$3.05 \pm 0.1$
$c$	$-1780 \pm 1020$	$3.8 \pm 0.9$
$c'$	$-82.5 \pm 22.5$	$2.9 \pm 0.1$

temperature  $\Theta$ , effective moment  $\mu_{eff}$ ) are listed in Tab. 6.1. The differences between the two in-plane directions  $a$  and  $c'$  is within the error bars. The fits are included in Fig. 6.2 (lines).  $\mu_{eff}$  for a free  $\text{Ce}^{3+}$  ion is  $2.54 \mu_B$ . The corresponding slope is indicated as dashed blue line with an arbitrary  $\Theta$  (-120 K) in Fig. 6.2. The discrepancies of  $\mu_{eff}$  of the a free  $\text{Ce}^{3+}$  ion and measurements are preserved by including an additional Pauli susceptibility term estimated via Hall effect measurements at 300 K. This indicates that the Ce-4f  $J = 5/2$  multiplet is not fully thermally populated even at the highest temperatures measured. Therefore, the total CEF split energy of the  $J = 5/2$  multiplet is expected to be in the range of a few tens (hundreds) of meV (K) in agreement to the findings in other physical properties measurements listed a.  $\Theta$  for  $\text{CeRu}_4\text{Sn}_6$  assumes values comparable to other Kondo insulators: -1030 K for FeSi [86], -125 K for  $\text{Ce}_3\text{Bi}_4\text{Pt}_3$  [51], -100 K for  $\text{YbB}_{12}$  [87] and -75 K for UNiSn [88].

As a first approach, a simple crystalline electric field (CEF) model is used to analyse the magnetic anisotropy of  $\text{CeRu}_4\text{Sn}_6$ . All calculations were performed with the software package McPhase 4.8 [89]. A detailed theoretical description of CEF effects and the consequences for  $\text{CeRu}_4\text{Sn}_6$  is given in Sect. 2.8. The available information relevant for the CEF analysis is summarized as follows:

- Br uning et al. performed  $\chi$  measurements on polycrystalline  $\text{CeRu}_4\text{Sn}_6$  in 2010 [46]. They suggested no (marginal) CEF splitting in  $\text{CeRu}_4\text{Sn}_6$  (6-fold degenerate ground state) based on thermopower and  $\chi$  measurements above  $T = 30$  K up to 800 K.
- Inelastic neutron scattering (INS) measurements on polycrystalline  $\text{CeRu}_4\text{Sn}_6$  were performed by Strydom and Adroja [45]. They found a peak in the spectrum at about 30 meV ( $\approx 350$  K) which was attributed to a CEF excitation.
- Local density approximation and dynamic mean-field theory (LDA+DMFT) calculations by Wissgott revealed that the lowest lying Ce-4f  $J = 5/2$  states are  $m_j = \pm 1/2$  and  $m_j = \pm 3/2$  [9]. The  $m_j = \pm 5/2$  states are well separated (Chapt. 5, [9]).
- Resonant X-ray absorption spectroscopy (XAS) measurements by Strigari et al. [15] on single crystalline  $\text{CeRu}_4\text{Sn}_6$  revealed best agreement between measurement and simulation for an almost pure Ce-4f  $J = 5/2$   $m_j = \pm 3/2$  ground state (Sect. 6.6). However, surface and self-absorption effects might distort the signal and a Ce-4f  $J = 5/2$   $m_j = \pm 1/2$  ground

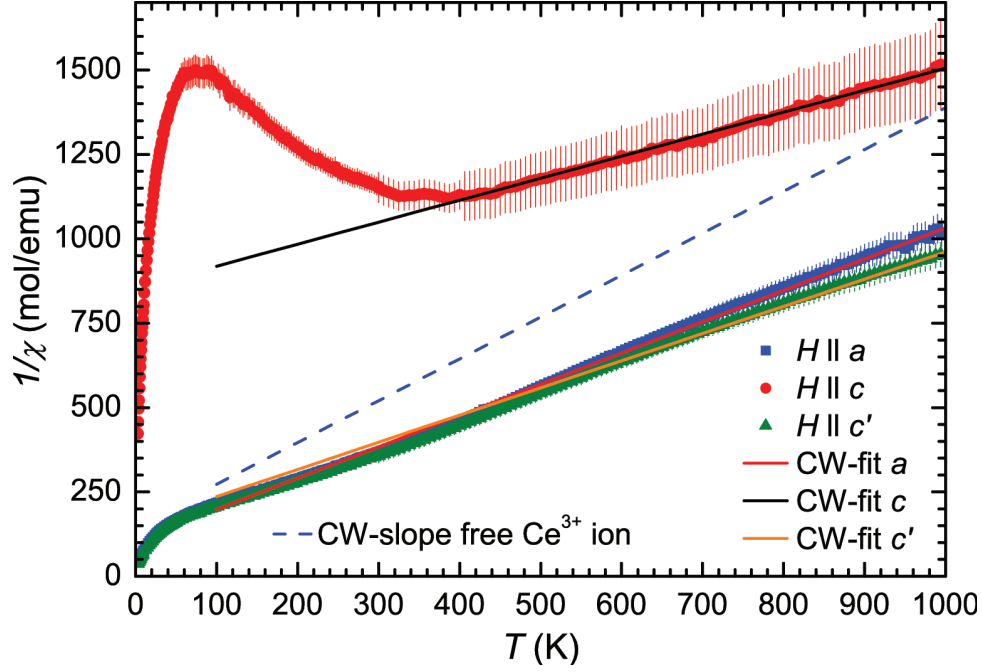


Figure 6.2: Inverse magnetic susceptibility  $1/\chi$  as a function of temperature  $T$  (sample G2\_B\_3). Additionally, the CW behaviour calculated for fully free  $\text{Ce}^{3+}$  ions (blue dashed line) and the CW fits (black, red and orange line) for the different directions are included.

state cannot be excluded. Therefore, non-resonant inelastic x-ray measurements (bulk sensitive) shall be performed shortly to confirm this result. A  $\text{Ce-}4f$   $J=5/2$   $m_j=\pm 5/2$  contribution to the ground state could already be excluded. The polarization dependence did not change up to about 200 K which suggests that the first excited CEF level lies at least 17 meV ( $\approx 200$  K) above the ground state doublet.

Next, the assumptions used within this CEF approach are listed:

- The point symmetry of the Ce atom is  $D_{2d}$  and no structural changes are assumed over the entire temperature range.
- An energy of about 30 meV is assumed between the ground state doublet and the first excited doublet with a sizable transition probability (result of INS measurements, indications for large first CEF splitting from XAS measurements).
- The CEF parameter  $B_2^0$  is positive because of the easy plane/hard axis character of  $\text{CeRu}_4\text{Sn}_6$ .
- Due to expected hybridization effects at low temperatures, the magnetic susceptibility is fit only in the high temperature range ( $T > 500\text{K}$ ).

- Finally, calculations for both an almost pure  $m_j = \pm 3/2$  ( $J = 5/2$ ) (predicted by XAS measurements (Sect. 6.6)) and for a pure  $m_j = \pm 1/2$  ( $J = 5/2$ ) (indicated by LDA+DMFT [9]) ground state doublet are performed.

The most important theoretical background used within this calculations is briefly discussed below (Sect. 2.8). Based on the Kramers theorem, the  $\text{Ce}^{3+}$  ion in  $\text{CeRu}_4\text{Sn}_6$  is a Kramers ion. Hence, together with the tetragonal point symmetry  $D_{2d}$  (Sect. 4.1), the spin-orbit split lower lying Ce-4f  $J = 5/2$  multiplet is split into three Kramer doublets. The states in the  $(J, m_j)$  basis are

$$\begin{aligned} |0\rangle &= |5/2, \pm 1/2\rangle \quad , \\ |1\rangle &= \alpha^{1/2} |5/2, \pm 3/2\rangle + (1 - \alpha)^{1/2} |5/2, \mp 5/2\rangle \quad \text{and} \\ |2\rangle &= (1 - \alpha)^{1/2} |5/2, \mp 3/2\rangle - \alpha^{1/2} |5/2, \pm 5/2\rangle \quad , \end{aligned} \quad (6.3)$$

where  $\alpha$  is the mixing coefficient ( $0 \leq \alpha \leq 1$ ). For a  $\text{Ce}^{3+}$  ion in a tetragonal point symmetry the CEF Hamilton operator  $H_{CEF}$  (Eqn. 6.4) has three CEF parameters:  $B_2^0$ ,  $B_4^0$ , and  $B_4^4$ . With the respective Stevens operators  $O_i^m$  [77] the CEF Hamilton reads

$$H_{CEF} = B_2^0 O_2^0 + B_4^0 O_4^0 + B_4^4 O_4^4 \quad . \quad (6.4)$$

In a first approach, a simple point-charge model (PCM) was used to calculate possible CEF parameters for a first excited CEF-split doublet at 30 meV and to determine the main contributions to the ground state doublet ( $m_j = 1/2, 3/2$  or  $5/2$ ). In general, an approach with (screened) point charges situated at the atomic positions is only valid for ionic compounds [90]. Due to the metallic behaviour of  $\text{CeRu}_4\text{Sn}_6$  in the range of interest for CEF calculations, the localized ions are screened by conduction electrons. In addition, a significant influence of the on-site valence electron structure (and its directional dependence) is discussed by Schmitt [90]. Nevertheless, the (screened) neighboring ions determine the basic point symmetry and therefore the splitting scheme. These findings were confirmed by Coehoorn [91] by electronic band structure calculations. By contrast, Duthie and Heine discovered that the magnitude of the CEF parameters is not changed by screening effects but a sign change can occur for several metallic compounds [92]. Hashimoto et al. showed that reliable results for the CEF parameters  $B_i^m$  of  $\text{RECu}_2$  compounds (RE = rare earth) can be derived if a screening factor is used [93]. As a result of these findings, the point charge  $q$  of the atoms surrounding Ce were changed within  $\pm 3e$  with a step size of 0.1 e. The cage surrounding Ce consists of 4 Ru atoms and 12 Sn atoms with two different Sn sites (Sn1 and Sn2, Fig. 4.2). At first, the different Sn sites were set to the same  $q$  for calculations. Charge neutrality via the Pauling scale of electronegativity is reached by  $q = -0.81e$  for Ru and  $0.04e$  for Sn in  $\text{CeRu}_4\text{Sn}_6$  with a  $\text{Ce}^{3+}$  configuration. Due to the results discussed above, charge neutrality is an unfeasible limitation in metal-like compounds and was therefore enforced.

Figure 6.3 displays the CEF parameters ( $B_2^0$ ,  $B_4^0$  and  $B_4^4$ ), the CEF splitting energy between the ground state and the first excited doublet ( $E_1 - E_0$ ) and  $m_j$  of the contribution with largest weight in the ground state doublet as a function of the Ru and Sn charges for the above described simple PCM calculation. With the assumptions listed above a broad band exists where the splitting energy is about 30 meV ( $\pm 5$  meV), as indicated by experiments, and  $B_2^0 > 0$ . This region is marked with a gridded yellow area in Fig. 6.3 (middle panel,  $E_1 - E_0$ ) or with two red lines at the borders of this energy range (remaining panels in Fig. 6.3). Within this region  $B_2^0$  varies between 6.6 and 3.9 meV at  $q_{Sn} = -3$  e ( $q_{Ru} = -1.52$  e) and 2.45 e ( $q_{Ru} = -0.1$  e), respectively. All configurations within this energy range include a pure  $m_j = \pm 1/2$  ground state doublet; no configuration with mainly  $m_j = \pm 3/2$  character was found. The area of charge neutrality in  $\text{CeRu}_4\text{Sn}_6$  ( $q_{Ru} = -6/4 q_{Sn} - 3/4 q_{Ce}$ ,  $q_{Ce} = 3$  e) is limited to  $q_{Sn} = 0 \pm 0.125$  e in the band discussed above. Due to the limited validity of an almost ionic picture for metal-like  $\text{CeRu}_4\text{Sn}_6$  and the importance of the valence electrons in the publications discussed above, this result yield no limitation for further analysis.

In the next PCM approach, the two different Sn sites were decoupled and different point charges were allowed for the two Sn sites. The charge ranges ( $\pm 3$  e) were the same as used before. Within these calculations, also satisfying combinations of point charges (CEF parameters) were found to obey the restrictions listed above. Several possibilities with a mainly  $m_j = \pm 5/2$  or pure  $m_j = \pm 1/2$  ground state doublet were found, with a first excited CEF doublet around 30 meV, as indicated by experiments. Unfortunately, the results cannot be displayed due to the need of a 4-dimensional representation. Interestingly, also within this approach, no ground state with mainly  $m_j = \pm 3/2$  contribution was revealed with the necessary energy splitting between the lowest lying doublets.

In conclusion, both PCM approaches revealed that no ground state with mainly  $m_j = \pm 3/2$  contribution was found with the restrictions listed above. The first PCM approach leads to a pure  $m_j = \pm 1/2$  ground state doublet, the second one yield additionally several possibilities with mainly  $m_j = \pm 5/2$  character. Another interesting result of both PCM model calculations are the values of the CEF parameters.  $B_2^0$  is of the order of a few meV,  $B_4^0$  was in the order of a few 1/100 meV and  $B_4^4$  is of the order of a few 1/10 meV.

In an alternative approach, the CEF parameters were varied themselves over specific ranges in the next step. Due to the manifold of possible combinations of CEF parameters satisfying the restrictions listed above, limitations on the CEF parameters based on experimental results were made. The first CEF parameter,  $B_2^0$ , is positive because, as already mentioned,  $\text{CeRu}_4\text{Sn}_6$  exhibit an easy basal plane/hard  $c$  axis behaviour. In addition, the absolute value of  $B_2^0$  can be determined from the anisotropy in the paramagnetic Weiss temperatures,  $\Theta_{a,c'} - \Theta_c$ , that can be determined by magnetic susceptibility measurements at temperatures well above the CEF splitting energies [94, 95].  $B_2^0$  is given by the Elliot formula [96]

$$B_2^0 = \frac{10}{3(2J-1)(2J+3)}(\Theta_{a,c'} - \Theta_c) \quad (6.5)$$

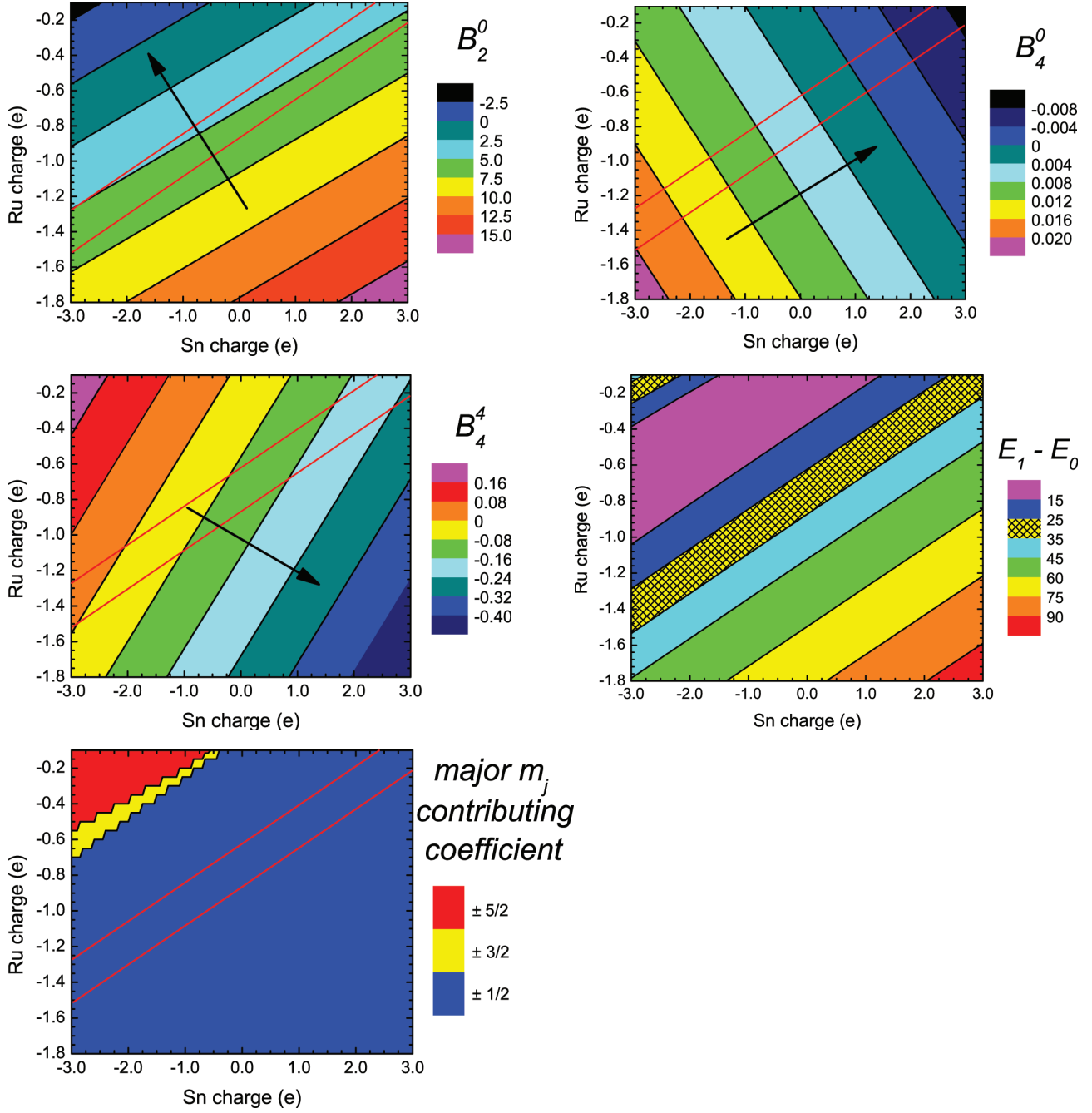


Figure 6.3: The CEF parameters  $B_2^0$  (top, left),  $B_4^0$  (top, right) and  $B_4^4$  (middle, left), the splitting energy between the lowest lying doublets  $E_1 - E_0$  (middle, right) and the quantum number  $m_j$  of the major contribution to the ground state doublet (bottom, left) as a function of the Ru and Sn charges are shown in contour plots. These values were calculated with a simple point-charge model applied for  $\text{Ce}^{3+}$  in  $\text{CeRu}_4\text{Sn}_6$ .

where  $J$  is the total angular momentum. Although the CW regime with the full  $\text{Ce}^{3+}$  moment was not reached up to the highest measured temperatures in  $\text{CeRu}_4\text{Sn}_6$  (Fig. 6.2), a rough estimation of  $B_2^0$  was made. Using the  $\Theta$  values obtained from the fits (Tab. 6.1),  $B_2^0$  is calculated with Eqn. 6.5 to about 8 meV. If the highest  $1/\chi$  values were extrapolated with the slope of the CW law for the full  $\text{Ce}^{3+}$  moment, the resulting  $\Delta\Theta$  would also result in  $B_2^0$  values in the range of a few meV. These values are in good agreement with the PCM calculations above which revealed the same order of magnitude for  $B_2^0$ . In comparison to other tetragonal Ce systems like  $\text{CeIrIn}_5$  ( $B_2^0 = -1.3$  meV, [97]),  $\text{CeRhIn}_5$  ( $B_2^0 = -1.3$  meV, [97]) and  $\text{CeCu}_{2.2}\text{Si}_2$  ( $B_2^0 = -0.8$  meV, [98]),  $B_2^0$  for  $\text{CeRu}_4\text{Sn}_6$  is enhanced and exhibit the opposite sign.

Exemplarily, calculations for  $B_2^0 = 6$  meV and varying  $B_4^0$  and  $B_4^4$  are displayed in Fig. 6.4. The values for  $B_4^0$  and  $B_4^4$  are changed within a ten times larger range than the values derived in the former PCM investigations. Figure 6.4 shows the energy difference between the ground state and the first excited doublet ( $E_1 - E_0$ ) (top panel, left side), the total angular momentum quantum number  $m_j$  of the major contribution to the ground state doublet (top panel, right side) and the coefficient  $\alpha^{1/2}$  or  $(1-\alpha)^{1/2}$  of the major contribution (Eqn. 6.3) in contour plots. An energy splitting  $E_1 - E_0$  of  $30 \pm 5$  meV, as indicated by experiments, is found in two small bands which are symmetric in  $B_4^4$  (gridded yellow area). The crossover from pure  $m_j = \pm 1/2$  to mainly  $m_j = \pm 3/2$  character of the ground state doublet is positioned exactly at the minimal calculated energy difference between the lowest lying doublets ( $E_1 - E_0$ ). Thus, one energy band is situated in the pure  $m_j = \pm 1/2$  ground state regime (left one) and the other one is situated in the  $m_j = \pm 3/2$  dominated regime of the ground state doublet (right). Note that the step-like structure is due to the chosen step size of the CEF parameters  $B_4^0$  and  $B_4^4$ .

XAS experiments revealed an almost pure  $m_j = \pm 3/2$  ground state doublet (coefficient almost 1, see results listed above). Therefore, the results for  $B_2^0 = 6$  meV with a  $m_j = \pm 3/2$  dominated ground state doublet (right energy band in Fig. 6.4) were further investigated. The restrictions by INS (energy splitting about 30 meV) and XAS (almost pure  $m_j = \pm 3/2$  with coefficient almost 1) measurements in combination with the  $B_2^0$  value of a few meV (here  $B_2^0 = 6$  meV used) derived by the PCM model and CW fits (Fig. 6.2) in combination with the Elliot formula (Eqn. 6.5) yield a small range of possible  $B_4^0$  and  $B_4^4$  parameters (Fig. 6.4).  $B_4^0$  and  $B_4^4$  are variable approximately in the range of (0.205 - 0.23) meV and ((-0.7) - (+0.7)) meV, respectively (indicated with dashed lines in Fig. 6.4).

The CEF scheme and the calculated (measured)  $1/\chi(T)$  are shown for  $B_2^0 = 6$  meV,  $B_4^0 = 0.218$  meV and  $B_4^4 = 0.3$  meV in Fig. 6.5. The energy splitting between the ground state doublet (almost pure  $m_j = \pm 3/2$ ) and the first (second) excited doublet is 29.9 meV (125.4 meV). At the lowest temperature,  $1/\chi(T)$  cannot be mimicked with this modification. In addition, the large increase of  $1/\chi_c(T)$  at low temperatures with the maximum at about 75 K and the minimum at 360 K cannot be reproduced by the fit either. Also the high-temperature  $1/\chi_c(T)$  exhibits remarkable differences between measurement and calculation. An additional Pauli



susceptibility contribution  $\chi_0$  yields only marginal improvement for  $1/\chi_c(T)$ , mainly at highest temperatures (Pauli susceptibility contribution estimated via Hall effect measurements at 300 K). By contrast,  $1/\chi_a(T)$  and  $1/\chi_c'(T)$  are mimicked appropriately for  $T > 200$  K. An additional  $\chi_0$  contribution leads to a small depletion of  $1/\chi_a(T)$  ( $1/\chi_c'(T)$ ).

Also other combinations of CEF parameters with an almost pure  $m_j = \pm 3/2$  ground state were investigated. The slope of  $1/\chi(T)$  changes, but the behaviour of  $1/\chi_c(T)$  cannot be mimicked properly. Hence, the conclusions for an almost pure  $m_j = \pm 3/2$  ground state doublet are the same as discussed above and shown in Fig. 6.5, namely that it does not represent the data well.

Therefore, alternatively to an almost pure  $m_j = \pm 3/2$  ground state doublet (Fig. 6.5), a pure  $m_j = \pm 1/2$  ground state doublet with the restrictions listed above was investigated (Fig. 6.6). As expected, the steep increase of  $1/\chi_c(T)$  with increasing  $T$  at lowest temperatures and the minimum in  $1/\chi_c(T)$  was mimicked best within this approach. Note that the steep increase of  $1/\chi_c(T)$  at lowest temperature is not fully understood yet and strong influences of the Kondo physics are suggested in this temperature range. The extrinsic or intrinsic nature of these features (steep increase and minimum in  $1/\chi_c(T)$ ) is still under discussion (Sect. 6.1.2). The minimum in  $1/\chi_c(T)$  at 360 K is suggested to be intrinsic which is indicated by torque magnetometry either. Additionally, the high-temperature behaviour of  $1/\chi(T)$  is described properly for all measured directions. The CEF parameters were determined to  $B_2^0 = 3.7$  meV,  $B_4^0 = -0.05$  meV and  $B_4^4 = 0.6$  meV, which leads to an energy splitting of 30.6 meV between the two lowest lying doublets (Fig. 6.6).

In conclusion, no adequate CEF model with an almost pure  $m_j = \pm 3/2$  ground state was found to describe the high-temperature magnetization of  $\text{CeRu}_4\text{Sn}_6$  within the approaches discussed above (Fig. 6.5). By contrast, the pure  $m_j = \pm 1/2$  ground state scheme revealed overall agreement with  $1/\chi$  measured at high temperatures (Fig. 6.6). Hence, these results indicate that the ground state doublet exhibits pure  $m_j = \pm 1/2$  states. As expected, the magnetic low-temperature behaviour cannot be described with a pure CEF model, confirming hybridization effects of the localized  $4f$  electrons with the itinerant electrons found in several investigations within this thesis. In comparison to the pure  $m_j = \pm 1/2$  ground state doublet calculation of  $1/\chi(T)$ , a higher  $1/\chi(T)$  value was measured indicating a loss of magnetization strength at temperatures below about 300 K (Fig. 6.6).

### Low-temperature magnetization and sample quality investigations

Figure 6.7 shows  $\chi(T)$  and  $1/\chi(T)$  below 350 K with additional points (orange squared dots) revealed by torque magnetometry measurements (see Sect. 6.1.2). As already discussed in the high-temperature subsection,  $1/\chi_c(T)$  reaches a minimum at about 360 K and a maximum at about 75 K. In general,  $\chi_c$  derived from torque magnetometry measurements (Sect. 6.1.2) is very small and changes the sign at about 175 K. By contrast,  $1/\chi_a(T)$  and  $1/\chi_c'(T)$  show a



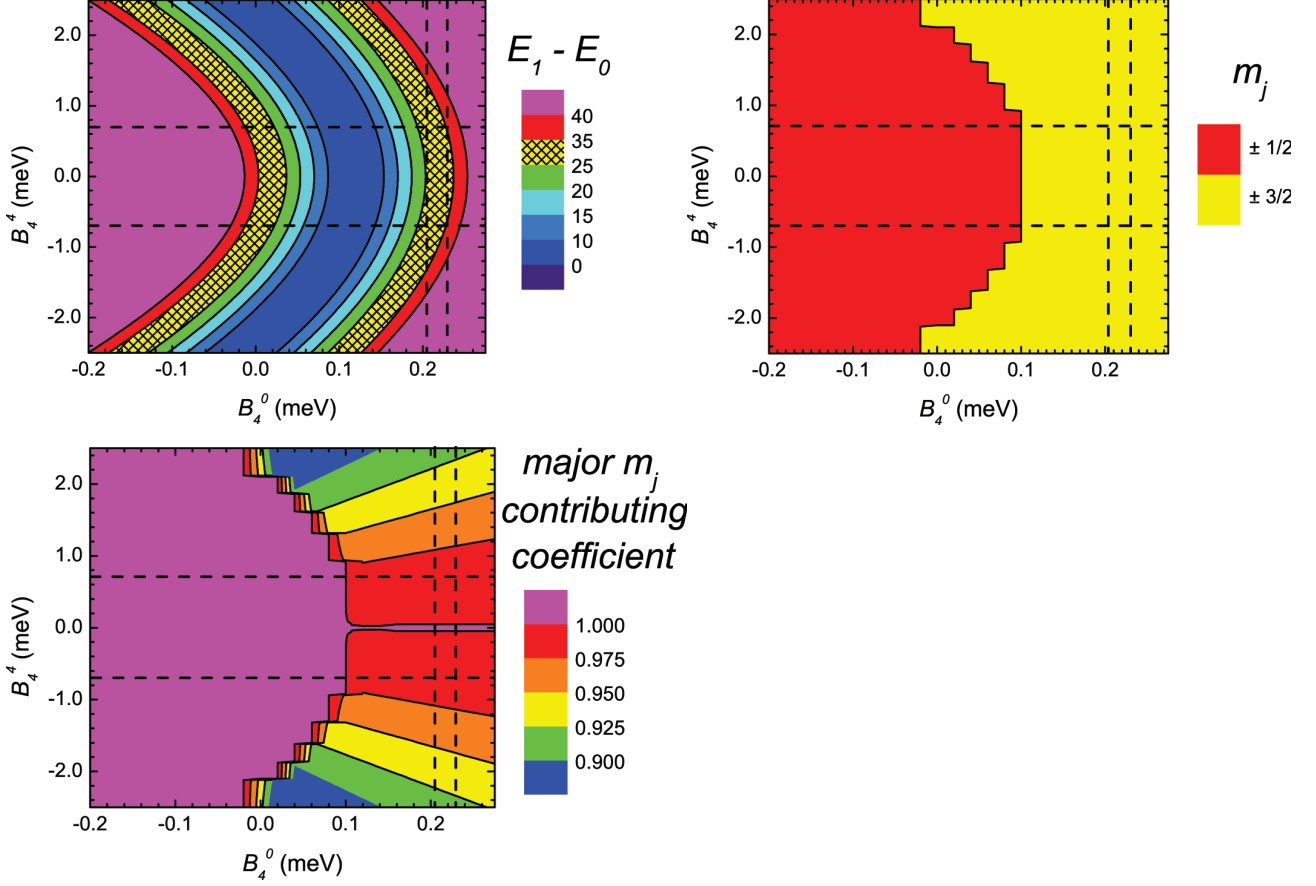


Figure 6.4: Contour plots of several calculated quantities plotted as a function of the CEF parameters  $B_4^0$  and  $B_4^4$  for a constant  $B_2^0 = 6$  meV. The splitting energy of the ground state and the first excited doublet (top panel, left), the major contribution to the ground state doublet ( $J, m_j$ ) (top panel, right) and the coefficient of the major contribution ( $\alpha^{1/2}$  or  $(1-\alpha)^{1/2}$ ) (Eqn. 6.3) of the ground state (lower panel, left) are shown. The energy bands within 25 to 35 meV are marked with a gridded yellow area which exhibit neither a pure  $m_j = \pm 1/2$  ground state doublet (left band) or a mainly  $m_j = \pm 3/2$  ground state doublet ( $B_4^0$  positive). The borders of the region of interest are indicated by black dashed lines.

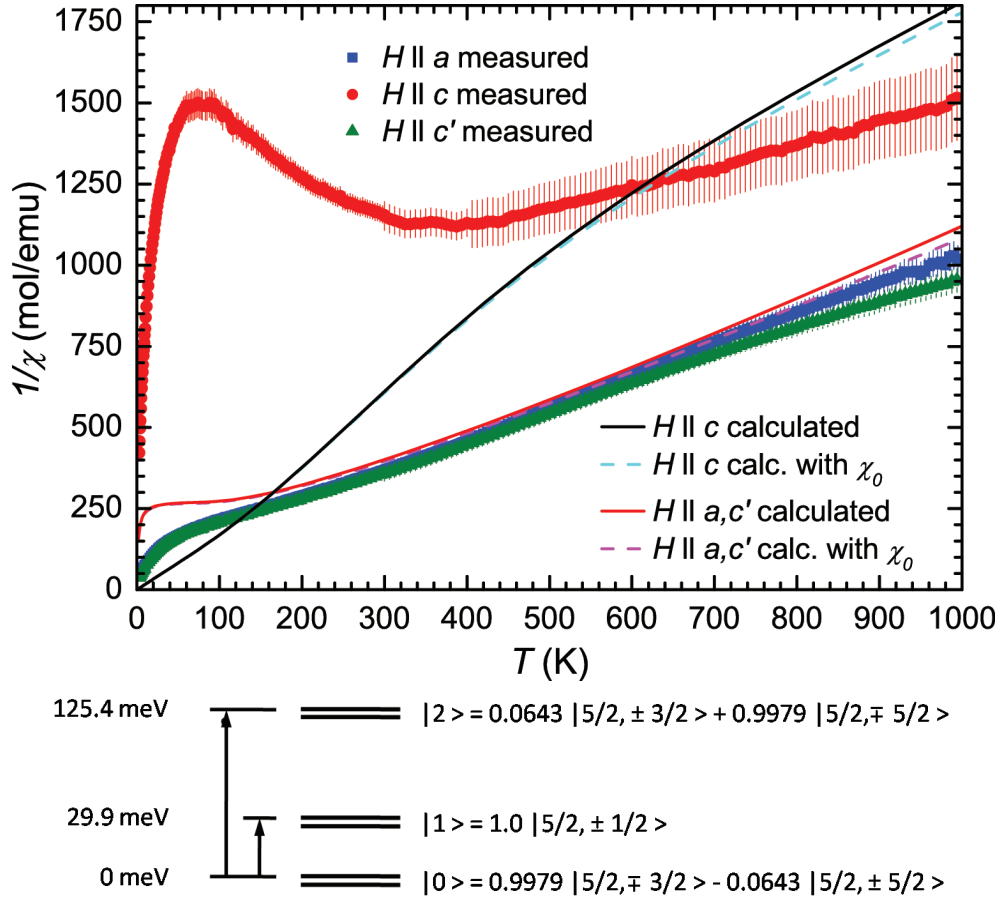


Figure 6.5: Calculated (McPhase 4.8 [89]) and measured inverse magnetic susceptibility  $1/\chi$  (sample G2\_B\_3) as a function of temperature  $T$  are shown on top. Nice agreement between measured and calculated curves at high temperatures within the in-plane directions was found, by contrast to  $1/\chi_c$ . An additional Pauli contribution  $\chi_0$  yields a small depletion of  $1/\chi$  (estimated via Hall effect measurements). Additionally, the respective CEF scheme is added (lower panel).

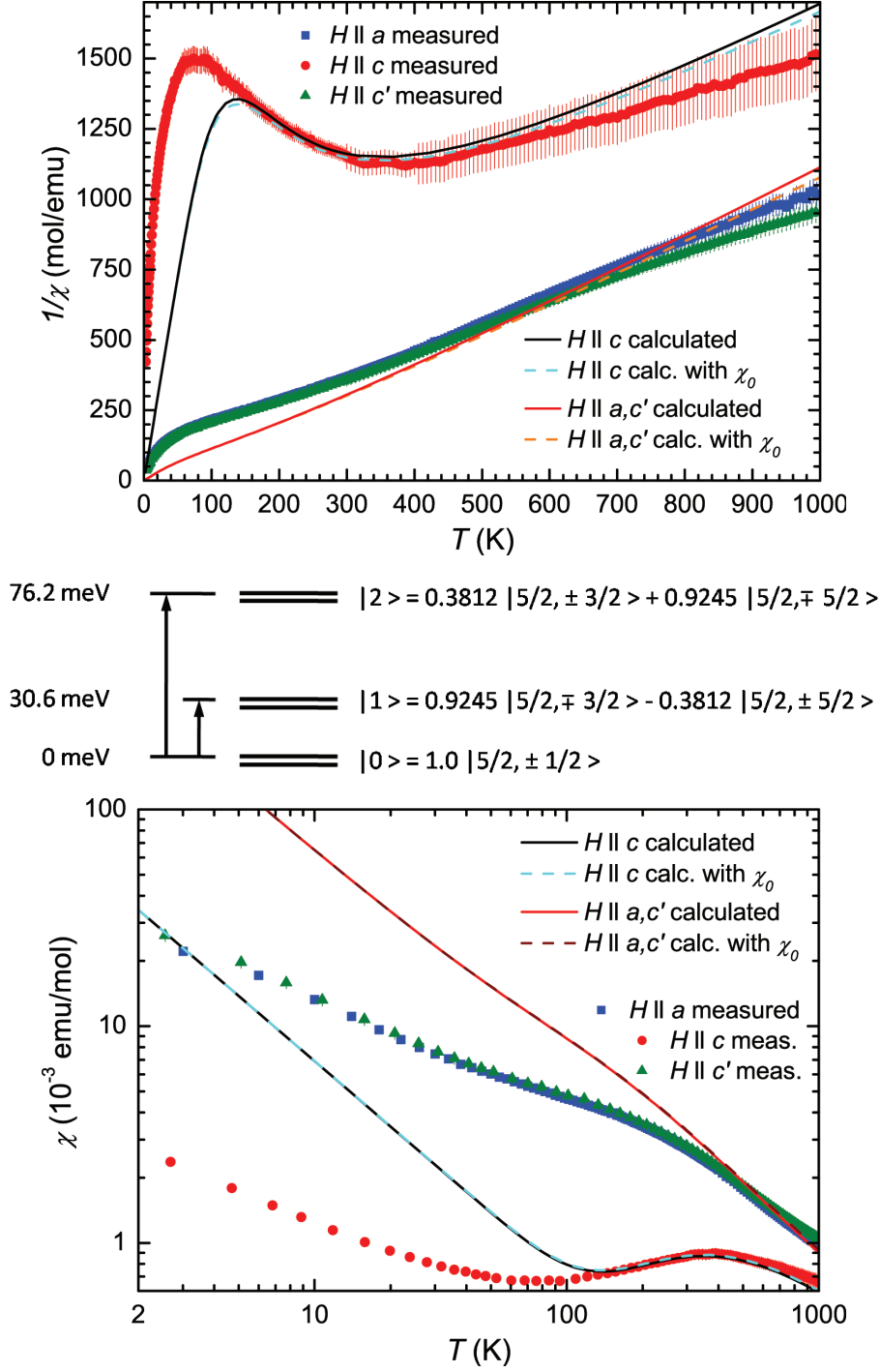


Figure 6.6: Measured and calculated (McPhase 4.8 [89]) (inverse) magnetic susceptibility  $\chi$  ( $1/\chi$ ) (sample G2\_B\_3) as a function of temperature  $T$  are shown (top and bottom panel). A CEF scheme with a pure  $m_j = \pm 1/2$  ground state doublet yields remarkable better agreement with the measured  $1/\chi$  than with a mainly  $\pm 3/2$  ground state doublet. Additionally, calculated  $1/\chi$  ( $\chi$ ) curves with an added Pauli-susceptibility term  $\chi_0$  (value estimated via Hall effect measurements at 300 K) are shown (dashed lines). The respective CEF scheme is shown in the middle panel.

steady almost linear decrease with decreasing temperature between 60 and 350 K. Below 60 K, a stronger reduction is seen for  $1/\chi_a(T)$  and  $1/\chi_c(T)$ . Interestingly, the decrease of  $\chi$  with decreasing  $T$ , characteristic of Kondo insulators, was not detected over the entire temperature range, except for  $\chi_c$ , where a maximum was detected at about 360 K (Fig. 6.1, inset). This maximum can also be attributed to CEF effects (Fig. 6.6). Additionally, the upturn of  $\chi_c$  at lowest temperatures contradicts to characteristic  $\chi$  of Kondo insulators found, e.g., in the fully gapped compound  $\text{Ce}_3\text{Bi}_4\text{Pt}_3$  at about 80 K [51] and in the nodal Kondo insulator  $\text{CeNiSn}$  at about 12 K [33]. So the origin of the maximum in  $\chi_c$  is not understood yet.

Additionally to the  $T$  sweeps at a constant magnetic field  $H$ ,  $H$  sweeps at low temperatures were performed (Fig. 6.8). Within these measurements, linear behaviour of the magnetization  $M_c(H)$  was found for  $T \geq 9$  K up to  $\mu_0 H = 7$  T (Fig. refCeRuSn:linearMHdeviation). Linear behaviour of  $M_a(H)$  and  $M_c'(H)$  was measured for  $T \geq 25$  K up to  $\mu_0 H = 7$  T (Fig. refCeRuSn:linearMHdeviation). These findings are in good agreement with the data on polycrystalline  $\text{CeRu}_4\text{Sn}_6$  of Brüning et al. [46]. In that work, a strong field dependence of  $\chi$  was detected for  $T < 20$  K. Also the absolute values of  $M(H)$  of our single crystals are in agreement with the polycrystal data of Bruening et al. [46]. In the lower panel of Fig. 6.8 (right) a comparison of  $M_a(H)$ ,  $M_c(H)$  and  $M_c'(H)$  of our single crystals at 3 K is shown. The difference of  $M(H)$  between the in-plane directions is attributed to misalignment effects because comparable marginal anisotropy was measured by torque magnetometry measurements ( $< 1.5\%$  at 9 T) (Sect. 6.1.2). At 3 K, the pronounced anisotropy of  $M(H)$  yields an  $\approx 10$  times higher signal at 7 T along the in-plane directions than along  $c$ . The absolute values of  $M(H)$  confirm that a pure CEF picture cannot describe the low  $M(H)$  values at lowest temperatures. In the following the absolute values of  $M(H)$  are discussed with different approaches.

At first, the contribution of impurities  $M_{imp}$  to  $M(H)$  is discussed. For this purpose, the sample quality of the  $\text{CeRu}_4\text{Sn}_6$  samples of different batches is compared by magnetization measurements (Fig. 6.9). The investigated samples are G2\_B\_3 (batch G2), G3\_B\_1 (batch G3) and MProbe (measured within the author's master thesis [49]). These measurements reveal discrepancies of  $\chi_c(T)$  below about 100 K. As already mentioned in Sect. 4.2, these differences cannot be attributed to measurable stoichiometric discrepancies.  $M(H)$  for G3\_B\_1 shows a higher value along both directions than G2\_B\_3 (Fig. 6.9, right panel), indicating a higher impurity concentration in G3\_B\_1. If  $\Delta M_c$  of G3\_B\_1 and G2\_B\_3 is fully ascribed to a directional independent impurity magnetization  $M_{imp}$ , a  $M_{imp}$  value of about  $0.01 \mu_B/\text{Ce}$  is reached at 3 K and 7 T. This  $M_{imp}$  value leads to an impurity concentration of about 0.03 atoms per formula unit (0.3 at.%) at 3 K and 7 T for impurities with spin  $s = 1/2$ . Therefore, the discrepancies of  $M_c'(H)$  of about  $0.05 \mu_B/\text{Ce}$  are unlikely due to impurities. Instead, the differences in  $M$  and  $\chi$  of different batches are attributed to misalignment effects: this can be seen by the difference of  $M_a(H)$  and  $M_c'(H)$  for sample G2\_B\_3 (Fig. 6.8, lower panel, right side) and sample MProbe (Fig. 6.9, right panel). Torque magnetometry measurements revealed a remarkably smaller difference between  $M_a(H)$  and  $M_c'(H)$  ( $< 1.5\%$  ( $0.004 \mu_B/\text{Ce}$ ) at 3 K and

9 T) (Sect. 6.1.2). The misalignment is discussed in detail in Sect. 6.1.2, suggesting a strong sensibility for measurements with  $H$  pointing along the hard  $c'$  axis.

Next, the absolute value of  $\chi$  was compared with a Pauli susceptibility contribution  $\chi_0$  within the Landau-Fermi liquid (LFL) theory. The charge carrier concentrations  $n$  of  $6.7 \cdot 10^{25}$  and  $5.0 \cdot 10^{25}$  charge carriers per  $\text{m}^3$  at 3 K for the  $c$  and in-plane directions, respectively, were obtained from Hall effect measurements (Sect. 6.3). With  $\chi_0 = 2N(E_F)\mu_B^2$  and a free electron gas approach,  $\chi_0$  was calculated at 3 K to  $2.5 \cdot 10^{-5}$  and to about  $2.3 \cdot 10^{-5}$  emu/mol for the  $c$  and in-plane directions, respectively. These values are two (four) orders of magnitude lower than the measured ones, but can be enhanced to appropriate values by an effective mass  $m^* \approx 1100 m_e$  ( $m^* = 88 m_e$ ) for the in-plane directions ( $c$  direction). In addition, the Sommerfeld-Wilson ratio ( $\gamma/\chi$ ,  $\gamma$  is the coefficient of the linear specific heat term) was analyzed, which is  $\approx 2-5$  for a wide range of heavy fermion materials. In  $\text{CeRu}_4\text{Sn}_6$ ,  $\gamma$  was determined to 40 mJ/mol K<sup>2</sup> by Pöttgen et al. [40] and to 80 mJ/mol K<sup>2</sup> by Brüning et al. [46]. A Sommerfeld-Wilson ratio of 2 is achieved with  $\gamma = (850 \pm 50)$  mJ/mol K<sup>2</sup>. Hence, the position of  $\text{CeRu}_4\text{Sn}_6$  in comparison to the Sommerfeld-Wilson ratio of HF compounds is shifted either to higher  $\gamma$  or to lower  $\chi$ .

Finally, the picture of localized Ce  $4f$  electrons in the CEF environment derived above is discussed for low temperature.  $1/\chi(T)$  was fitted linearly with  $1/\chi = T/C + \text{const}$  ( $\text{const}$  = constant parameter) at lowest temperatures describing, e.g.,  $1/\chi_{c'}(T)$  satisfyingly from lowest temperatures up to about 8 K (Fig. 6.9, left panel, inset). The slopes yield an effective moment  $\mu_{eff}$  of 1.2-1.4  $\mu_B/\text{Ce}$  along  $c'$ . In comparison, the CEF level scheme with the pure  $m_j = 1/2$  ground state doubled (dominating  $m_j = 3/2$  ground state doublet) configuration lead to  $\mu_{eff} = 0.742 \mu_B/\text{Ce}$  ( $\mu_{eff} = 1.660 \mu_B/\text{Ce}$ ) for the  $c'$  direction in the same temperature range.  $M$  shows pronounced anisotropy at lowest temperature (Fig. 6.9, right panel) with  $M_{a,c'} \approx 0.275 \mu_B/\text{Ce}$  and  $M_c \approx 0.03 \mu_B/\text{Ce}$  (approximately 1/10 of the in-plane value) at 3 K and 7 T. If the pure  $m_j = 1/2$  ground state doublet CEF level scheme is probed, only  $\approx 21\%$  of the full moment ( $M_{c,calc,1/2} = 1.28 \mu_B/\text{Ce}$ ) is reached at 7 T and 3 K. The dominating  $m_j = 3/2$  ground state doublet scheme fails in general to describe the measurements in this temperature range because the directional dependence of the calculated hard and easy axis is opposite to the measured dependence. As expected for strongly interacting  $4f$  electrons at low temperatures in  $\text{CeRu}_4\text{Sn}_6$ , a pure CEF description of the low temperature behaviour cannot describe the results properly.

## Summary and discussion

Direct magnetization measurements on  $\text{CeRu}_4\text{Sn}_6$  reveal pronounced magnetic anisotropy between the easy plane (basal plane, including  $a$  and  $c'$ ) and the hard  $c$  axis over the entire temperature range from 2 to 1000 K (Fig. 6.1).  $M_c$  is much smaller (about  $0.03 \mu_B/\text{Ce}$  at 3 K and 7 T) than  $M_a$  and  $M_{c'}$  (about  $0.275 \mu_B/\text{Ce}$  at 3 K and 7 T). Interestingly, no well-defined

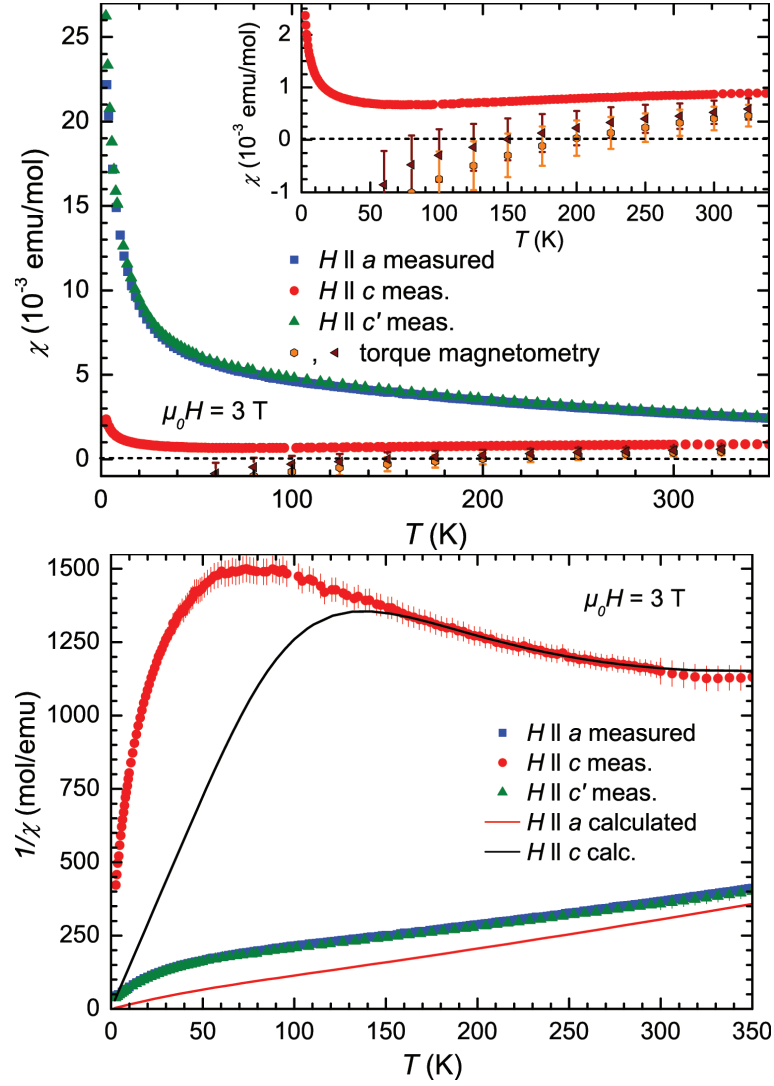


Figure 6.7: The upper (lower) panel shows the direct measured (inverse) magnetic susceptibility  $\chi$  ( $1/\chi$ ) as a function of temperature  $T$  with an applied magnetic field of 3 T (sample G2\_B\_3). Additionally,  $\chi_c$  revealed by torque magnetometry is displayed (orange and brown symbols). The inset in the upper plot shows  $\chi_c$  in detail.

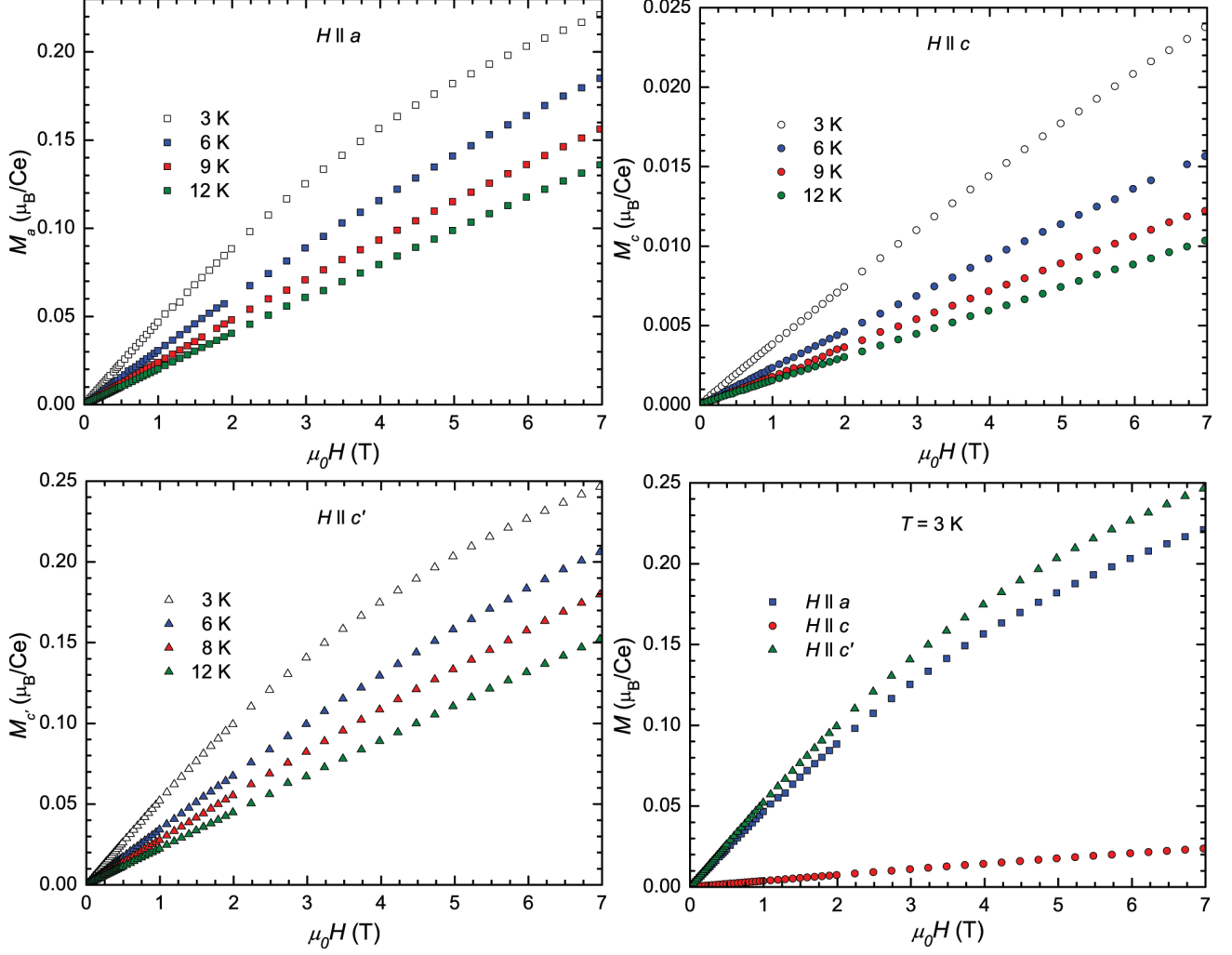


Figure 6.8: Magnetization  $M$  at constant temperatures  $T$  as a function of the magnetic field  $\mu_0 H$  along the  $a$  (top panel, left),  $c$  (top panel, right) and  $c'$  (lower panel, left) is shown (sample G2\_B\_3). A comparison at 3 K is shown in the lower panel on the right. A pronounced anisotropy between the in-plane and the out-of-plane direction was found. The discrepancy between the in-plane directions is suggested to small misalignment yielding to moderate deviations.

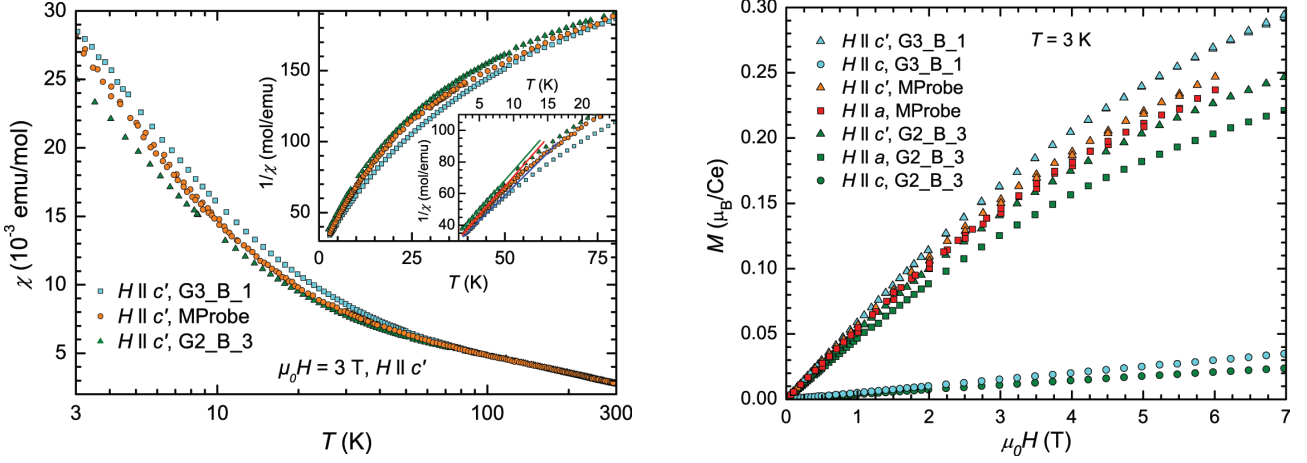


Figure 6.9: The left (right) panel shows the magnetic susceptibility  $\chi$  and inverse susceptibility  $1/\chi$  (magnetization  $M$ ) as a function of temperature  $T$  (the magnetic field  $H$  at 3 K) for different batches of  $\text{CeRu}_4\text{Sn}_6$  (G3\_B\_1, MProbe, G2\_B\_3). First deviations for  $\chi$  ( $1/\chi$ ) were found below about 100 K. The low temperature behaviour of  $1/\chi$  was fitted with a Curie Weiss law revealing that the increases at lowest temperatures are described by an effective moment  $\mu_{eff}$  of 1.2-1.4  $\mu_B/\text{Ce}$ . Due to the characteristics of the  $M$  discrepancies, we concluded that mainly misalignment effects cause the deviations between the different  $\text{CeRu}_4\text{Sn}_6$  samples (batches).

maximum in  $\chi(T)$  was found. Such a feature is usually considered as a hallmark of Kondo insulators and is for instance observed in  $\text{Ce}_3\text{Bi}_4\text{Pt}_3$  at about 80 K [51]. In  $\text{CeRu}_4\text{Sn}_6$ , a maximum is only seen in  $\chi_c$  at about 360 K. However, this maximum could alternatively be attributed to CEF effects (Fig. 6.6). Hence, its origin is still unclear.

An analysis of the magnetic susceptibility data above 300 K with a CEF model for localized Ce 4*f* electrons, that takes also INS and XAS results into account, yields a pure  $m_j = \pm 1/2$  ground state as best solution (Fig. 6.6). It is in particular the pronounced minimum in  $1/\chi_c(T)$  at 360 K which is not reproduced if the ground state is composed of  $m_j = \pm 3/2, \pm 5/2$  states. This simple CEF approach fails at low temperatures, indicating that here the localized Ce 4*f* moments strongly interact with the conduction electrons.

At the lowest accessed temperatures (3 K), the sample quality of different  $\text{CeRu}_4\text{Sn}_6$  batches was investigated and confirmed to be very high (Fig. 6.9). Another important result of this analysis was the demonstration that the magnetic response depends sensitively on small misalignment of the investigated crystal direction with respect to the magnetic field direction (Fig. 6.9).



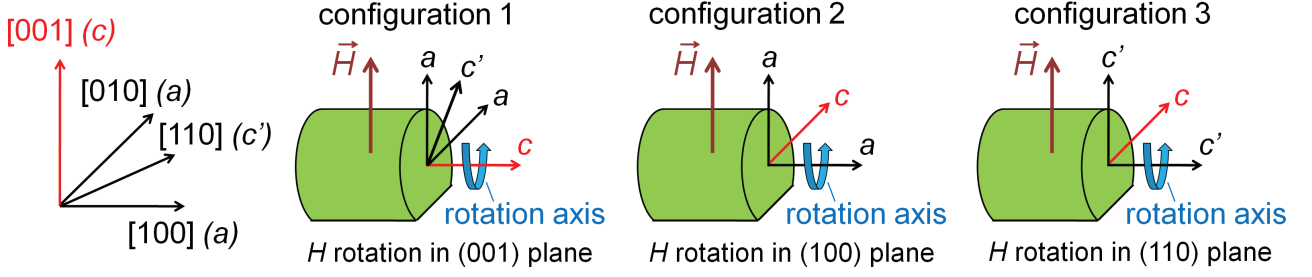


Figure 6.10: Schematic drawings of the  $\text{CeRu}_4\text{Sn}_6$  samples (green) used for torque magnetometry measurements. Three almost cylindrical  $\text{CeRu}_4\text{Sn}_6$  samples were prepared for measuring the magnetic torque within the basal plane ((001)-plane, left drawing), orthogonal to the basal plane including  $a$  ((100)-plane, middle drawing) and orthogonal to the basal plane including  $c'$  ((110)-plane, right drawing). The direction of the magnetic field  $\vec{H}$  and the crystallographic directions  $a$ ,  $c$  and  $c'$  are indicated (directions shown in detail in the left panel).

### 6.1.2 Torque magnetometry

Torque magnetometry is a useful tool to investigate anisotropic magnetic behaviour in single crystals. As discussed in Sect. 6.1.1, due to the strong magnetization anisotropy a perfect alignment of the  $\text{CeRu}_4\text{Sn}_6$  samples with respect to the magnetic field is essential. Hence, torque magnetometry measurements were performed because they eliminate misalignment problems in the direction of rotation. The device used and the sample geometry are discussed in detail in Chap. 3. Three almost cylindrical  $\text{CeRu}_4\text{Sn}_6$  samples were prepared and oriented with their cylindrical axis along the crystallographic  $a$ ,  $c$  and  $c'$  direction, respectively. Consequently, the magnetic anisotropy was measured within the basal plane ((001)-plane;  $a$  -  $c'$ ; batch G3; Fig. 6.10, left drawing), orthogonal to the basal plane including the  $a$  direction ((100)-plane;  $a$  -  $c$ ; batch G3; Fig. 6.10, middle drawing) and orthogonal to the plane including the diagonal of the basal plane  $c'$  ((110)-plane;  $c$  -  $c'$ ; batch G6; Fig. 6.10, right drawing). The detailed theoretical description of the used formalism and the physical background of magnetic anisotropy is discussed in Chap. 2. Note that within this thesis the magnetic susceptibility  $\chi$  is given by

$$\chi = M/H \quad . \quad (6.6)$$

The magnetic susceptibility in the linear response regime  $\chi_{LR}$  is defined to

$$\chi_{LR} = \lim_{H \rightarrow 0} \frac{\partial M(H)}{\partial H} \quad . \quad (6.7)$$

Both equations include the magnetization  $M$  and the magnetic field  $H$ .

The magnetic torque  $\vec{\tau}$  is defined by

$$\vec{\tau} = \mu_0 V \vec{M}_{vol} \times \vec{H} \quad , \quad (6.8)$$

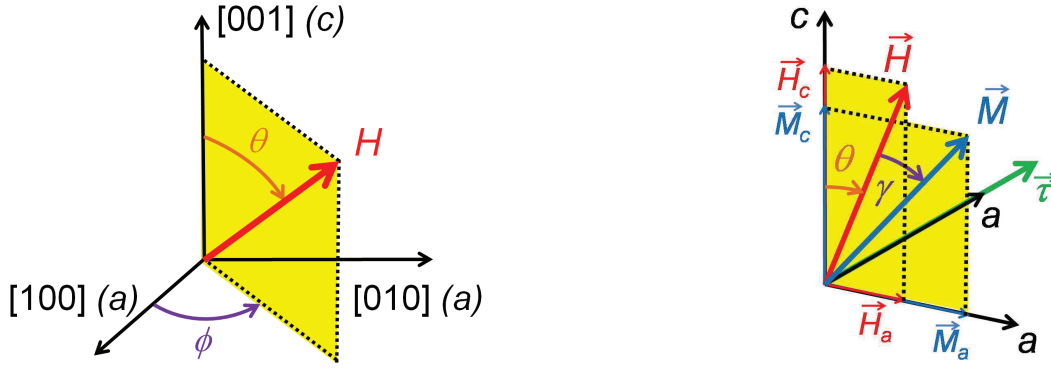


Figure 6.11: The left panel shows the nomination used for torque magnetometry investigations within this thesis. The right panel displays a schematic drawing of the directional dependences within a standard torque measurement for a tetragonal paramagnetic sample with an easy axis  $a$ . Here, the magnetic field  $\vec{H}$  is rotated within the (010) plane by the rotation angle  $\theta$  with respect to the  $c$  direction. In addition, the magnetization  $\vec{M}$ , the torque  $\vec{\tau}$ , the tetragonal main directions ( $a$ ,  $c$ ) and the angle  $\gamma$  between  $\vec{M}$  and  $\vec{H}$  are displayed. Geometrical dependences:  $\vec{H} = \vec{H}_c + \vec{H}_a = |\vec{H}| \cos(\theta) \hat{c} + |\vec{H}| \sin(\theta) \hat{a}$ ;  $\vec{M}_c = \chi_c \vec{H}_c$ ;  $\vec{M}_a = \chi_a \vec{H}_a$  [99, 100].

with the vacuum permeability  $\mu_0$ , the volume  $V$ , the volume magnetization  $\vec{M}_{vol}$  and the magnetic field  $\vec{H}$ . During the torque measurements, the direction of  $\vec{H}$  with respect to the crystal was rotated by the angle  $\theta$  or  $\phi$  within a plane that contains two main crystallographic directions (Fig 6.11, left panel). The direction of the magnetization  $\vec{M} = \vec{M}_{vol} V$  is situated between the direction of  $\vec{H}$  and the nearest easy axis within the rotation plane ( $a$  direction in Fig 6.11, right panel). The angle between  $\vec{M}$  and  $\vec{H}$  is named  $\gamma$ . If one assumes that the local minima/maxima in the anisotropy energy  $E_{aniso}$  are situated along the main directions ( $a$ ,  $c$  and/or  $c'$ ) and  $\vec{M}$  can be described by  $M_a$  and  $M_c$ , the direction of  $\vec{M}$  is determined by the different values of the magnetic susceptibility  $\chi$  along the main directions. This approach is described, e.g., by Aviani et al. [99] and Xiao et al. [100] and displayed schematically in Fig. 6.11 (right panel). Consequently,  $\Delta\chi$  was calculated for the out-of-plane rotations by

$$\tau = \frac{\Delta\chi_{mol}}{2} \mu_0 H^2 N_{mol} \sin(2\theta) \quad (6.9)$$

and for the in-plane rotation by

$$\tau = \frac{\Delta\chi_{mol}}{2} \mu_0 H^2 N_{mol} \sin(4\phi) \quad , \quad (6.10)$$

with the number of moles  $N_{mol}$ .

Equations 6.9 and 6.10 are confirmed by starting with the anisotropic energy density for tetragonal systems  $E_{aniso,tetr}$  (Eqn. 2.39, Sect. 2.9). The resulting directional dependent magnetic torque for rotation within the (001) plane (configuration 1 in Fig. 6.10,  $\theta = 90^\circ$  in Fig. 6.11),

$\tau_{a,c'} \equiv -\partial E_{aniso,tetr}/\partial\phi$ , is given by

$$\tau_{a,c'} = -K_3 ( -2 \cos(\phi) \sin(\phi)^3 + 2 \cos(\phi)^3 \sin(\phi) ) = -\frac{1}{2} K_3 \sin(4\phi) \quad . \quad (6.11)$$

The torque for rotation within the (100) plane (configuration 2 in Fig. 6.10,  $\phi = 90^\circ$  in Fig. 6.11),  $\tau_{a,c} \equiv -\partial E_{aniso,tetr}/\partial\theta$ , is given by

$$\tau_{a,c} = K_1 \sin(2\theta) + 4 K_2 \sin(\theta) \cos(\theta)^3 = (K_1 + K_2) \sin(2\theta) + \frac{1}{2} K_2 \sin(4\theta) \quad . \quad (6.12)$$

Finally, the magnetic torque  $\tau_{c,c'} \equiv -\partial E_{aniso,tetr}/\partial\theta$  for rotation within the (110) plane (configuration 3 in Fig. 6.10,  $\phi = 45^\circ$  in Fig. 6.11) is

$$\begin{aligned} \tau_{c,c'} &= K_1 \sin(2\theta) + 4 K_2 \sin(\theta) \cos(\theta)^3 - K_3 \sin(\theta)^3 \cos(\theta) \\ &= (K_1 + K_2 - \frac{1}{4} K_3) \sin(2\theta) + (\frac{1}{2} K_2 + \frac{1}{8} K_3) \sin(4\theta) \quad . \end{aligned} \quad (6.13)$$

The angular dependence for the different terms of all three equations (Eqns. 6.11-6.13) are shown in Fig 6.12 (left panel). Additionally, a calculated curve for  $\tau_{a,c}$  with  $K_1 = 1$  and  $K_2 = 1/4$  is compared to a pure sinusoidal curve in Fig. 6.12 (right panel). The  $K_2$ -including term leads to a distortion of the sinusoidal behaviour produced by the  $K_1$ -including first term. Note that all contributing terms to  $\tau_{dir}$  are sinusoidal with doubled or quadrupled frequency ( $2\theta$ ,  $4\theta$  or  $4\phi$ ).

With the above equations the anisotropy constants  $K_i$  can only be determined in the magnetically saturated regime. Since CeRu<sub>4</sub>Sn<sub>6</sub> is paramagnetic in the entire measurement ranges the  $K_i$  could not be determined. Instead, an analysis of the  $T$  dependence of  $K_i$  and the description of  $K_i$  by crystalline electric field (CEF) parameters in the paramagnetic state, proposed by Kuz'min [101], was performed. Here the anisotropy energy  $E_{aniso,tetr,Kuz}$  for a tetragonal crystal containing Ce atoms is written as [101]

$$E_{aniso,tetr,Kuz}(\theta, \phi) = K_{1,Kuz} \sin(\theta)^2 + K_{2,Kuz} \sin(\theta)^4 + K_{3,Kuz} \sin(\theta)^4 \cos(4\phi) \quad , \quad (6.14)$$

with the anisotropy constants  $K_{1,Kuz}$ ,  $K_{2,Kuz}$  and  $K_{3,Kuz}$ . In comparison to the definition of  $K_i$  by Nagata et al. (Eqn. 2.39),  $K_{i,Kuz}$  differ by sign and/or constant coefficients. However, the  $T$  dependence for  $K_i$  and the respective  $K_{i,Kuz}$  (for the same  $i$ ) is identical.  $K_i$  are given in the high-temperature expansion (HTE) for the single-ion anisotropy energy used within that approach ( $\mu_B H$  and  $B_l^m$  small in comparison to  $kT$ ) by

$$K_{1,Kuz} = -3 B_2^0 d_2 T^{-2} + O(T^{-3}) \quad , \quad (6.15)$$

$$K_{2,Kuz} = 35 B_4^0 d_4 T^{-4} + O(T^{-5}) \quad (6.16)$$

and

$$K_{3,Kuz} = B_4^4 d_4 T^{-4} + O(T^{-5}) \quad , \quad (6.17)$$

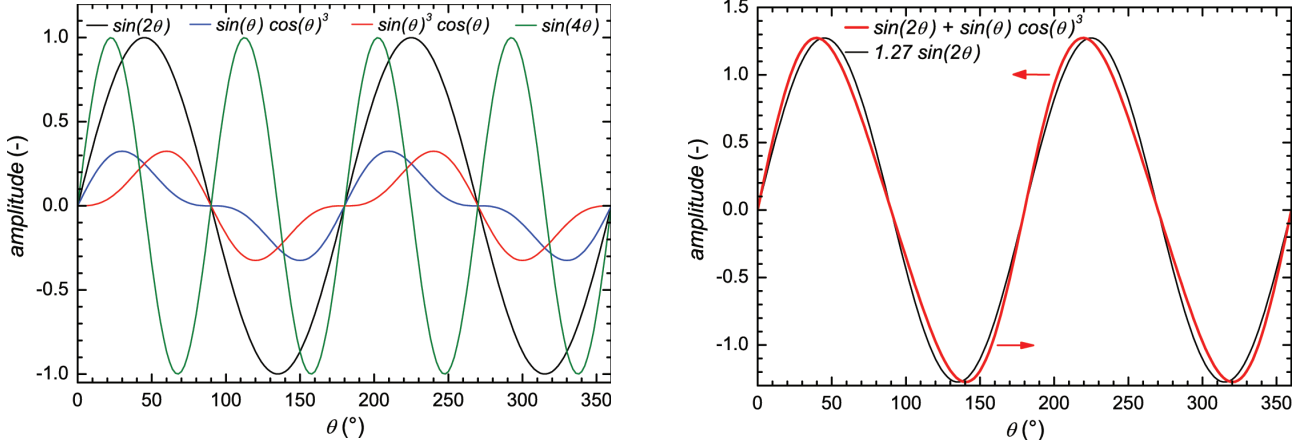


Figure 6.12: The left panel shows the angle dependence of the terms involved in the magnetic torque equations (Eqns. 6.11 - 6.13). In the right panel, a calculated curve for  $\tau_{a,c}$  with  $K_1 = 1$  and  $K_2 = 1/4$  (Eqn. 6.12, red line) is compared with a pure sinusoidal curve (black line). Consequently, a dominant  $K_1$  constant tends to a pure sinusoidal curve (black line) while a dominant  $K_2$  constant shows a distorted sinusoidal curve induced by the  $K_2$ -including term in Eqn. 6.12 with quadrupled frequency (red line).

with

$$d_n = N \left( \frac{g_j \mu_B H}{4 k_B} \right)^n \frac{(2J + n + 1)!}{(2n + 1)!!(2J + 1)(2J - n)!} \quad (6.18)$$

The equations above include the CEF parameters  $B_l^m$ , the temperature  $T$ , the number of Ce atoms  $N$ , the Landé factor  $g_j$ , the Bohr magneton  $\mu_B$ , the magnetic field  $H$ , the Boltzmann constant  $k_B$  and the total angular quantum number  $J$ . In analogy with  $\tau_{dir}$ , we again determine the torque by

$$\tau_{K_{uz}}(\theta) \equiv -\partial E_{aniso,tetr,K_{uz}}/\partial \theta = \sum_{n=2,4} \tau_n \sin(n\theta) \quad (6.19)$$

for the rotations of  $H$  in the (100) and (110) plane, with  $\tau_n$  given by

$$\tau_2 = -K_{1,K_{uz}} - (K_{2,K_{uz}} \pm K_{3,K_{uz}}) = 3 B_2^0 d_2 T^{-2} + O(T^{-3}) - (35 B_4^0 \pm B_4^4) d_4 T^{-4} + O(T^{-5}) \quad , \quad (6.20)$$

and

$$\tau_4 = \frac{1}{2}(K_{2,K_{uz}} \pm K_{3,K_{uz}}) = \frac{1}{2} (35 B_4^0 \pm B_4^4) d_4 T^{-4} + O(T^{-5}) \quad , \quad (6.21)$$

with the upper (plus) and lower (minus) sign for the rotation of  $H$  in the (100) and (110) plane, respectively.  $\tau$  for the rotation of  $H$  in the (001) plane is given by

$$\tau_{ac',K_{uz}}(\phi) \equiv -\partial E_{aniso,tetr,K_{uz}}/\partial \phi = -4K_{3,K_{uz}} \sin(4\phi) = -4 (B_4^4 d_4 T^{-4} + O(T^{-5})) \sin(4\phi) \quad . \quad (6.22)$$

The CEF parameters  $B_2^0$ ,  $B_4^0$  and  $B_4^4$  can be determined from terms of lowest power in  $1/T$  in Eqns. 6.19-6.22. For this purpose, torque measurements within the (100), (110) and (001) plane were performed as a function of temperature (3-325 K) within this thesis.  $K_{i,\text{Kuz}}$  (Eqns. 6.15-6.17) lead to  $\tau_n \propto T^{-n}$  and  $\tau_{ac',\text{Kuz}} \propto T^{-n}$  (Eqns. 6.19-6.22). As a result, the  $K_{1,\text{Kuz}}$ -including ( $B_2^0$ -including) term is the dominant contributing value to the torque at high temperatures. By contrast, the  $K_{2,\text{Kuz}}$ - and  $K_{3,\text{Kuz}}$ -including ( $B_4^0$ - and  $B_4^4$ -including) terms are detectable at lower temperatures with quadrupled frequency.

Both  $\text{CeRu}_4\text{Sn}_6$  samples which include the hard  $c$  axis in the plane of rotation ( $H$  rotates within (100) and (110) plane) display a pure sinusoidal  $\tau(\theta)$  with doubled frequency ( $2\theta$ ) over the entire temperature range (3 to 325 K). Exemplarily,  $\tau_{c,c'}$  (configuration 3 in Fig. 6.10, rotation within (110) plane) at 100 K with an applied field of 3.25 T is shown in Fig. 6.13, together with sketches of the measurement geometry. In addition,  $\tau_{a,c}$  (configuration 2 in Fig. 6.10, rotation within (100) plane) and  $\tau_{c,c'}$  (configuration 3 in Fig. 6.10, rotation within (110) plane) at different temperatures are shown between 15 and 300 K (Fig. 6.14) and between 3 and 10 K (Fig. 6.15), which display the pure doubled frequency ( $2\theta$ ) component to  $\tau(\theta)$  over the entire temperature range. Note that these measurements were made with different samples ( $\tau_{a,c}$  with sample G3\_A\_a\_II and  $\tau_{c,c'}$  with sample G6\_A\_1). Due to the different sample masses, the absolute values of  $\tau_{a,c}$  and  $\tau_{c,c'}$  cannot be compared within these figures (for a comparison of the different directions, see Figs. 6.17 and 6.18). Due to the highly pronounced easy plane character of  $\text{CeRu}_4\text{Sn}_6$ , a dominant  $K_1$  contribution to  $\tau(\theta)$  was expected from direct magnetization measurements. In addition, the  $T$ -dependence of the  $K_{i,\text{Kuz}}$  contributing terms and the CEF parameters determined in Sect. 6.1.1 imply a dominant  $\tau(\theta)$  contribution with doubled frequency ( $2\theta$ ). Due to the  $T$ -dependence of  $\tau_n$ , detailed investigations of  $\tau(\theta)$  at the lowest  $T$  were made, but no contributions with quadrupled frequency ( $4\phi$ ) could be resolved (Fig. 6.15).

Next, we describe the torque measurements for the rotation of the magnetic field within the (001) plane (configuration 1 in Fig. 6.10). Figure 6.16 shows  $\tau_{a,c'}(\phi)$  at several temperatures with  $\mu_0 H = 9$  T and schematic drawings of the sample geometry.  $\tau_{a,c'}(\phi)$  is theoretically described with the anisotropy constant  $K_3$  ( $K_{3,\text{Kuz}}$ ) and a sinusoidal curve with dependence of  $4\phi$  (Eqns. 6.11 and 6.22). Above 40 K, no sign of magnetic anisotropy (no angle dependent signal) was detected in  $\tau_{a,c'}(\phi)$ . The first sign of magnetic anisotropy is seen at 40 K (not shown). Clear evidence for anisotropy was found at 25 K. The anisotropy increased steadily to lower temperatures (Figs. 6.16 and 6.18).

Firstly, the experimental results were investigated with Eqns. 6.9 and 6.10 to determine  $\Delta\chi$  within the three rotation planes measured. A comparison between  $\Delta\chi$  derived via the torque magnetometry (TM) analysis including the hard  $c$  axis ( $\Delta\chi_{a,c}$  and  $\Delta\chi_{c,c'}$ ) and the results from direct magnetization (DM) measurements (sample G2\_B\_3) is shown in Fig. 6.17. In addition,  $\chi_{c,\text{calc},ac}(H)$  and  $\chi_{c,\text{calc},cc'}(H)$  are shown, which were calculated by

$$\chi_{c,\text{calc},ac}(H) = \chi_a^{DM}(H) - \Delta\chi_{a,c}^{TM}(H) \quad (6.23)$$

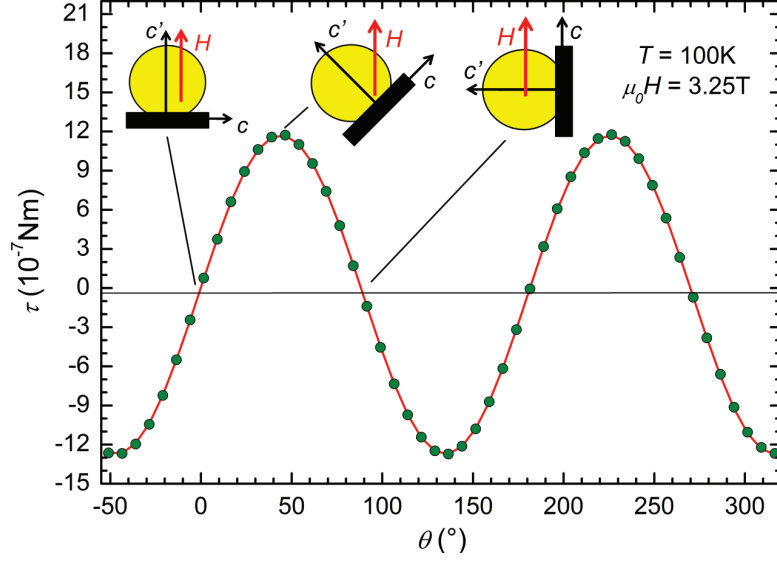


Figure 6.13: Torque  $\tau$  for a rotation within the (110) plane (configuration 3 in Fig. 6.10, sample batch G6) at 100 K with an applied magnetic field  $\mu_0 H = 3.25$  T as a function of the rotation angle  $\theta$ . The graph includes the torque  $\tau$  (green points) and a sinusoidal fit (red line) with doubled frequency ( $2\theta$ ) describing the data ideally. Additionally, schematic drawings of the measurement geometry for  $\theta = 0, 45$  and  $90^\circ$  are added. The CeRu<sub>4</sub>Sn<sub>6</sub> sample (yellow, almost cylindrical geometry) is mounted on the sample platform (black) which was rotated within the (110) plane in a constant  $H$  (constant direction and  $H$  value) during the measurement procedure.

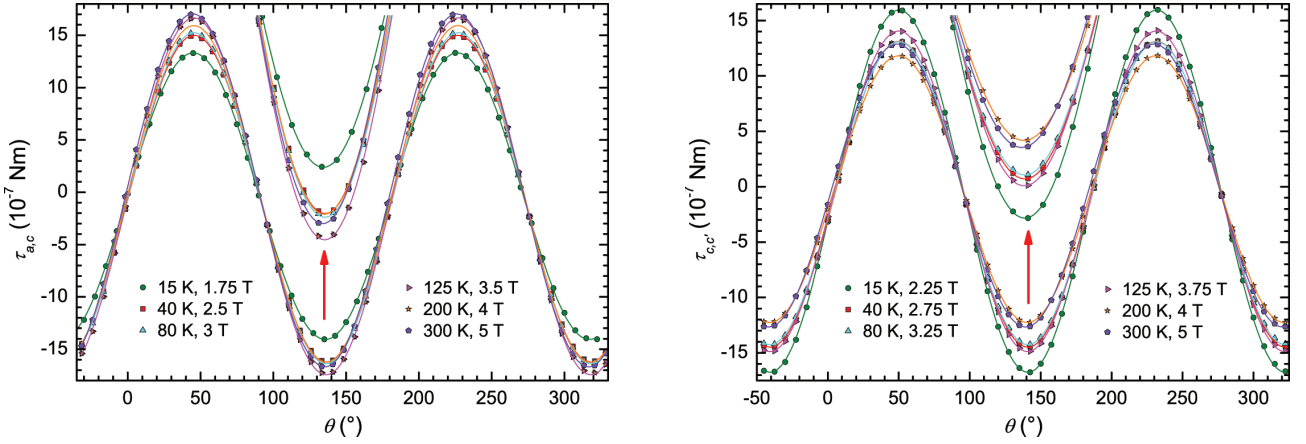


Figure 6.14: The left panel shows the torque  $\tau_{a,c}$  (configuration 2 in Fig. 6.10, sample batch G3) at different temperatures  $T$  and magnetic fields  $H$  as a function of the rotation angle  $\theta$ . The right panel displays  $\tau_{c,c'}$  (configuration 3 in Fig. 6.10, sample batch G6) at the same  $T$  as a function of  $\theta$ . A sinusoidal fit (indicated with lines) with doubled frequency ( $2\theta$ ) mimics  $\tau_{a,c}$  and  $\tau_{c,c'}$  over the entire temperature range ideally. The minima of  $\tau$  at about  $150^\circ$  are shown in detail (marked with a red arrow).



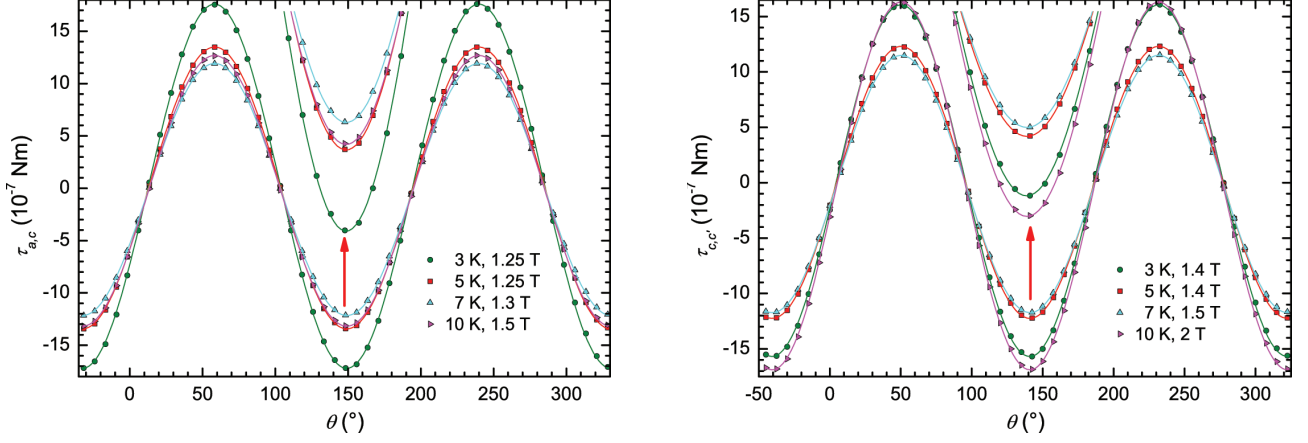


Figure 6.15: The left panel shows the torque  $\tau_{a,c}$  (configuration 2 in Fig. 6.10, sample batch G3) at different temperatures  $T$  and magnetic fields  $H$  as a function of the rotation angle  $\theta$ . The right panel displays  $\tau_{c,c'}$  (configuration 3 in Fig. 6.10, sample batch G6) at the same  $T$  as a function of  $\theta$ . A sinusoidal fit (indicated with lines) with doubled frequency ( $2\theta$ ) mimics  $\tau_{a,c}$  and  $\tau_{c,c'}$  over the entire temperature range ideally. The minima of  $\tau$  at about  $150^\circ$  are shown in detail (marked with a red arrow). Here, no admixture of a quadrupled contribution to  $\tau$  can be resolved.

and

$$\chi_{c,calc,cc'}(H) = \chi_{c'}^{DM}(H) - \Delta\chi_{c,c'}^{TM}(H) \quad , \quad (6.24)$$

respectively. TM measurements indicate a higher anisotropy between the easy plane and the hard  $c$  axis than determined via DM measurements, in particular at low temperatures (see  $\chi_{c,calc,ac}(H)$ ,  $\chi_{c,calc,cc'}(H)$  and  $\chi_c(H)$  in Fig. 6.17). Below about 175 K,  $\chi_{c,calc,ac}(H)$  and  $\chi_{c,calc,cc'}(H)$  changes sign and the discrepancy to the direct measured  $\chi_c(H)$  becomes very large. Therefore, a detailed discussion of possible error sources is given below:

- Magnetic impurities were discussed in detail in Sect. 6.1 concerning the sample/batch dependencies and their directional behaviour. With the assumption of isotropic magnetic impurities (distributed randomly in  $\text{CeRu}_4\text{Sn}_6$ ), an isotropic  $\chi$  enhancement would be expected. Thus, the susceptibility difference  $\Delta\chi$  measured by TM and DM measurements is expected to be largely unaffected by impurities.
- Next, background signals to  $\chi$  in the DM measurements caused by the glue used for fixing the sample on the sample holder were investigated.  $\chi_{glue} \approx 1.5 \cdot 10^{-5} \text{ emu/T}$  is almost temperature independent over the entire temperature range and was subtracted from the data. The absolute value of  $\chi_{back}$  was determined to a maximum of 3 % (11 %) of  $\chi_a$  and  $\chi_{c'}$  ( $\chi_c$ ) below 300 K (maximum value at 300 K along the in-plane directions and at 75 K along the  $c$  axis). At 3 K, the percentual contribution of  $\chi_{back}$  to  $\chi_a$  and  $\chi_{c'}$  ( $\chi_c$ ) is decreased to about 0.3 % (3 %). Unfortunately, the glue mass is only poorly

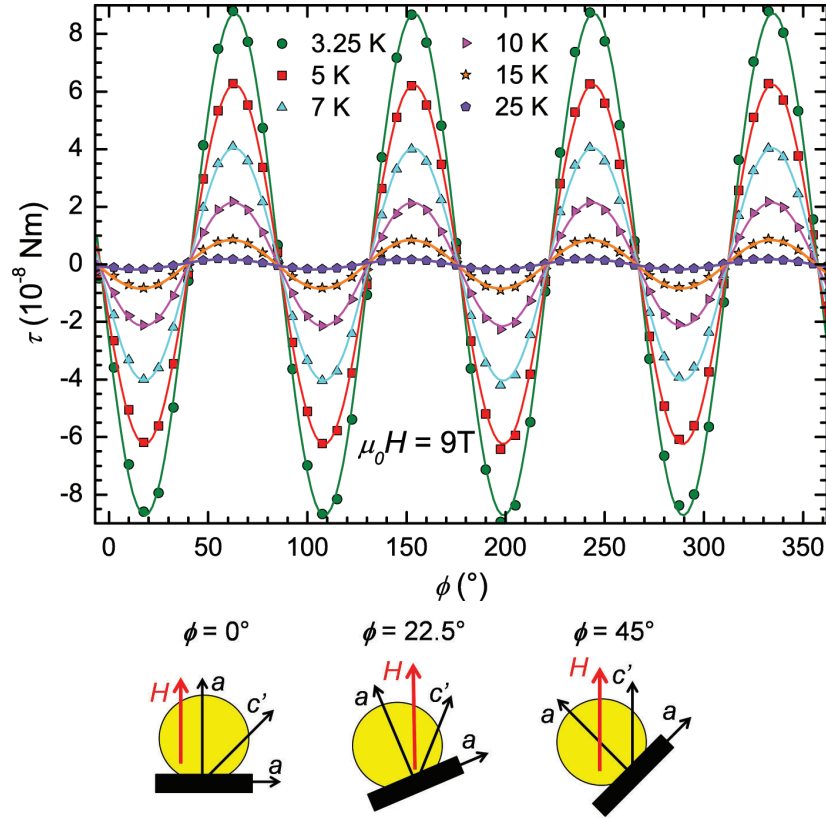


Figure 6.16: Torque  $\tau_{a,c'}$  (configuration 1 in Fig. 6.10, sample G3\_A\_a\_II) as a function of the angle  $\phi$  at different temperatures  $T$  below 25 K, with an applied magnetic field  $\mu_0 H = 9$  T. The graph includes the measured points (symbols) and the fits according to Eqn. 6.11 (lines). Schematic drawings for the  $\phi$ -dependent geometries are added on the bottom (sample (yellow), sample platform (black) and magnetic field  $H$  direction (red arrow)).



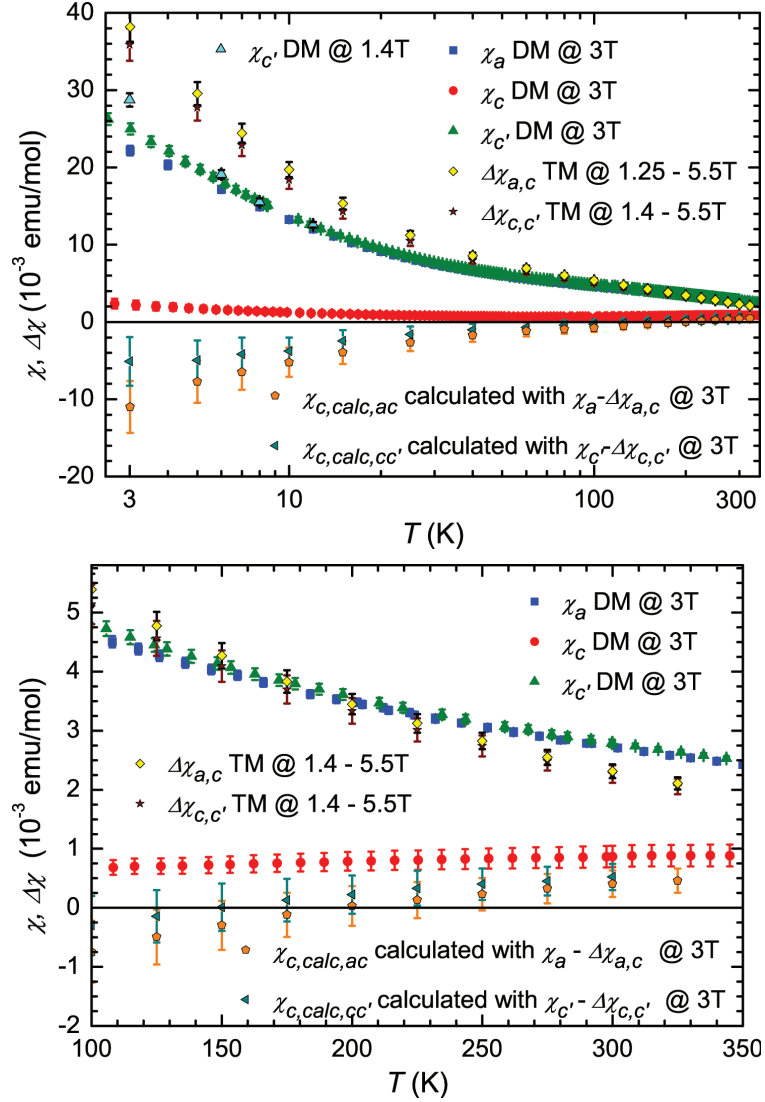


Figure 6.17: Magnetic susceptibility  $\chi$  (susceptibility anisotropy  $\Delta\chi$ ) of  $\text{CeRu}_4\text{Sn}_6$  determined by direct magnetization (DM) and torque magnetometry (TM) measurements as a function of temperature  $T$  (top: 3-350 K, semilogarithmic plot; bottom: 100-350 K). Here,  $\Delta\chi$  derived by TM measurements with rotations of the magnetic field  $H$  in the  $c$ -including planes ((100) and (110), configurations 2 and 3 in Fig. 6.10) are presented. The DM measurements were performed with sample G2\_B\_3 and the torque measurements with sample G3\_A\_a\_II (G6\_A\_1) for the rotation within the (100) plane ((110) plane).  $\chi_{c,calc,ca}$  and  $\chi_{c,calc,cc'}$  were determined via Eqns. 6.24 and 6.23 including the batch (Eqn. 6.30) and magnetic field (Eqns. 6.25 and 6.26) corrections discussed in the text.

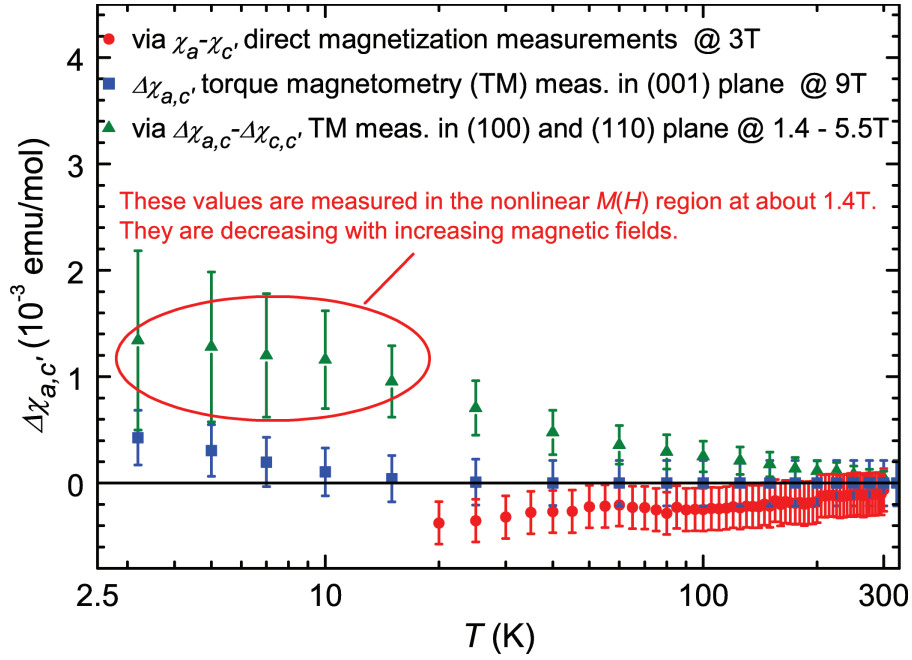


Figure 6.18: Comparison of the magnetic anisotropy in the (001) plane of  $\text{CeRu}_4\text{Sn}_6$  derived by torque and direct magnetization measurements. The difference of the magnetic susceptibility  $\Delta\chi_{a,c'}$  was derived by torque magnetometry (green and blue symbols) and by direct magnetization measurements (red symbols). The most significant direct measured torque magnetometry values (blue symbols, configuration 1 in Fig. 6.10, sample G3\_A\_a\_I) reveal that an anisotropy evolves below about 25 K, with an easier magnetization ability along the  $a$  ([100]) direction. Note that the absolute value is still under investigation.

determinable due to the small amount used. Therefore, the error is in the magnitude of  $\chi_{back}$  and reaches at maximum about 2 % (6 %) along the in-plane directions ( $c$  axis).

- The background signals in TM measurements were investigated, too. Firstly, the gravitational part was measured at each  $T$  (amplitude of about  $4 \cdot 10^{-8}$  Nm for the heaviest sample, yield at maximum 4 % of maximum in measurement signal) and was subtracted from the measured  $\tau$ . The gravitational signal has half or quarter the frequency ( $\theta$ ) of the sample signal ( $2\theta$ ,  $4\phi$ ) and is therefore well separable. Secondly, the sample holder itself (without sample and glue) was measured over the entire temperature with  $\mu_0 H = 0$  and 9 T. These measurements were required for the determination of the anisotropy within the (001) plane. At  $\mu_0 H = 9$  T, the sample holder contributes by a noisy signal with a band width of  $3 \cdot 10^{-9}$  Nm above 100 K. Below 100 K, a sinusoidal signal with a doubled frequency ( $2\theta$ ) and an amplitude of about  $3 \cdot 10^{-8}$  Nm was found. Note that this value is about 3 % of  $\tau$  for measurements including the hard  $c$  axis (measurements with  $H$  rotating in (100) or (110) planes). Due to the small absolute values at  $\mu_0 H = 9$  T and the fact that this contribution decreases with field strength, the background could not be determined in the  $H$  regions where TM measurements including the  $c$  axis were performed. Therefore, this contribution was not subtracted from the total  $\tau$  measured with  $H$  rotating in the (100) or (110) plane. This signal was subtracted only for  $\tau$  within the (001) plane, where all measurements were done at 9 T.
- Next, the  $M(H)$  dependencies (Figs. 6.8 and 6.19), which are non-linear below 9 K (20 K) for  $c$  (the (001) plane directions), are analyzed because  $\chi(T)$  in DM and  $\Delta\chi(T)$  in TM measurements were determined at different  $H$ . This is a problem because a determination of  $\chi_c$  by the combination of both data sets via Eqns. 6.23 and 6.24 should be done at the same field  $H$  if the  $M(H)$  curves are non-linear. Recall that the definition (Eqn. 6.6) we use here for  $\chi$  is  $\chi(H) = M(H)/H$  and not the linear-response definition (Eqn. 6.7)  $\chi_{LR} = \lim_{H \rightarrow 0} \frac{\partial M(H)}{\partial H}$ . To compensate for this effect, corrections were introduced

$$\chi_{c,calc,cc'}(H_1) = \chi_{c'}^{DM}(H_1) - \Delta\chi_{c,c'}^{TM}(H_2) \frac{\chi_{c'}^{DM}(H_1) - \chi_c^{DM}(H_1)}{\chi_{c'}^{DM}(H_2) - \chi_c^{DM}(H_2)} \quad (6.25)$$

and

$$\chi_{c,calc,ac}(H_1) = \chi_a^{DM}(H_1) - \Delta\chi_{a,c}^{TM}(H_2) \frac{\chi_a^{DM}(H_1) - \chi_c^{DM}(H_1)}{\chi_a^{DM}(H_2) - \chi_c^{DM}(H_2)} \quad (6.26)$$

The  $\chi^{DM}(H)$  values were taken from measured  $M(H)$  curves (Fig. 6.8) and are tabulated in Tabs. 6.2 and 6.3. Note that, e.g.,  $\chi(1.4 T) > \chi(3 T)$  in the non-linear  $M(H)$  range which is shown in Fig. 6.19, top panel) at 3 K. The  $\chi_{c,calc,ac}(T)$  and  $\chi_{c,calc,cc'}(T)$  in Fig. 6.17 contain this correction.

- The torque samples were prepared with almost cylindrical shape to avoid different demagnetization fields due to the sample shape with respect to the direction of  $H$  (Fig. 6.10). The  $\text{CeRu}_4\text{Sn}_6$  samples used for DM measurements were not spherical symmetric and

Table 6.2:  $M(H)$  data from Fig.6.8 that are relevant for the determination of  $\chi_{c,calc,ac}(T)$  (Eqn.6.26). MH refers to  $M(H)$  data from DM measurements on sample G2\_B\_3, TM indicates the conditions ( $T$  and  $H$ ) of TM measurements (top). The ratios of susceptibility differences at the field  $H_a$  and at 3 T are calculated for temperatures where  $M(H)$  data are available (bottom). Note that the sample dependence of the calculated ratios is negligible.

T (K)	available data	$H_a$ (T)	$\chi_a(H_a)$ (emu/mol)	$\chi_a(3T)$ (emu/mol)	$\chi_c(H_a)$ (emu/mol)	$\chi_c(3T)$ (emu/mol)
3	MH	1.25	0.02515	0.02345	0.00214	0.00206
3	TM	1.25	-	-	-	-
5	TM	1.25	-	-	-	-
6	MH	1.25	0.01712	0.01662	0.00131	0.00128
7	TM	1.3	-	-	-	-
9	MH	1.5	0.01339	0.01324	0.00101	0.00101
10	TM	1.5	-	-	-	-
12	MH	1.5	0.01136	0.01138	0.00086	0.00084
15	TM	1.75	-	-	-	-

T (K)	$H_a$ (T)	$\chi_a(H_a) - \chi_c(H_a)$ (emu/mol)	$\chi_a(3T) - \chi_c(3T)$ (emu/mol)	$\Delta\chi_{a,c}(H_a)/\Delta\chi_{a,c}(3T)$ (%)
3	1.25	0.02301	0.02139	7.6
6	1.25	0.01581	0.01533	3.1
9	1.5	0.01238	0.01222	1.2
12	1.5	0.01050	0.01054	-0.4

Table 6.3:  $M(H)$  data from Fig. 6.8 that are relevant for the determination of  $\chi_{c,calc,cc'}(T)$  (Eqn. 6.25). MH refers to  $M(H)$  data from DM measurements on sample G2\_B\_3, TM indicates the conditions ( $T$  and  $H$ ) of TM measurements (top). The ratios of susceptibility differences at the field  $H_{c'}$  and at 3 T are calculated for temperatures where  $M(H)$  data are available (bottom). Note that the sample dependence of the calculated ratios is negligible.

T (K)	available data	$H_{c'}$ (T)	$\chi_{c'}(H_{c'})$ (emu/mol)	$\chi_{c'}(3T)$ (emu/mol)	$\chi_c(H_{c'})$ (emu/mol)	$\chi_c(3T)$ (emu/mol)
3	MH	1.4	0.02874	0.02631	0.00212	0.00206
3	TM	1.4	-	-	-	-
5	TM	1.4	-	-	-	-
6	MH	1.4	0.01912	0.01861	0.00131	0.00128
7	TM	1.5	-	-	-	-
10	TM	2	-	-	-	-
12	MH	2	0.01258	0.01255	0.00085	0.0084
15	TM	2.25	-	-	-	-

T (K)	$H_{c'}$ (T)	$\chi_{c'}(H_{c'}) - \chi_c(H_{c'})$ (emu/mol)	$\chi_{c'}(3T) - \chi_c(3T)$ (emu/mol)	$\Delta\chi_{c,c'}(H_{c'})/\Delta\chi_{c,c'}(3T)$ (%)
3	1.4	0.02662	0.02425	9.8
6	1.4	0.01781	0.01732	2.8
12	2	0.01173	0.01171	1.8

therefore different demagnetization fields  $H_d = -NM$  ( $N$  = demagnetization factor) occurred for DM measurements along the different crystallographic directions. The reduction of  $H$  is given by  $H_{sample} = H_{external} + H_d$ . For  $\text{CeRu}_4\text{Sn}_6$ , the maximal reduction for  $\mu_0 H = 1 \text{ T}$  can be calculated at highest  $M \approx 3 \text{ emu/cm}^3 = 3000 \text{ A/m}$  and with  $N = 1$  to about 0.4 %. Thus, demagnetization effects are negligible.

- Next, misalignment effects in the DM measurements are discussed. They are believed to be relevant (Sect. 6.1.1) because the anisotropy measured by TM for rotations within the (001) plane (configuration 1 in Fig. 6.10) is higher than the one obtained from DM measurements (Fig. 6.18). The assumptions for this investigation are identical to the formalism used for calculating  $\Delta\chi$  in the TM analysis (Eqns. 6.9 and 6.10), namely  $\vec{M} = \vec{M}_c + \vec{M}_a$ ,  $\vec{M}_c = \chi_c \vec{H}_c$  and  $\vec{M}_a = \chi_a \vec{H}_a$ . Due to the almost isotropic magnetic behaviour within the easy (001) plane in  $\text{CeRu}_4\text{Sn}_6$ , the discussion of misalignment can be reduced from 3 to 2 dimensions. As displayed in Fig. 6.20, top left panel, the magnetic anisotropy leads to an angle  $\gamma$  between  $\vec{M}$  and  $\vec{H}$ . The angle between  $\vec{M}$  and the easy  $a$  axis is named  $\delta$ . The magnetization measured within the experiments is  $\vec{M}_H$  and the angle of displacement is  $\theta$  ( $90^\circ - \theta$ ) along the [001] axis (in-plane directions). With

$$\tan(\delta) = \frac{|\vec{M}_c|}{|\vec{M}_a|} = \frac{|\chi_c|}{|\chi_a|} \quad (6.27)$$

and

$$\gamma = 90 - \theta - \delta \quad , \quad (6.28)$$

the absolute value of the magnetization along the  $\vec{H}$  direction  $|\vec{M}_H|$  is given by

$$|\vec{M}_H| \equiv M_H = |\vec{M}| \cos(\gamma) = |\vec{M}| \cos(90 - \theta - \arctan(\frac{|\vec{M}_c|}{|\vec{M}_a|})) \quad . \quad (6.29)$$

The ratio of the reduced to the full magnetization along the main directions  $M_H/M_{H\parallel c}$  ( $M_H/M_{H\parallel a}$ ) as a function of the angle of misalignment  $\theta$  ( $90^\circ - \theta$ ) is shown in Fig. 6.20, bottom (top right) panel. The direction of  $M_H$  ( $\delta$ , Eqn. 6.27) is determined by the ratio  $|\chi_c|/|\chi_a| \propto \chi_a/\chi_c$ . So, the calculations were performed with  $\chi_a/\chi_c = 10$  (5) observed at about 3 K (175 K) in  $\text{CeRu}_4\text{Sn}_6$ . Due to the indications of higher anisotropy derived by TM, higher ratios were investigated, too. A sharp percentage increase of  $M$  is derived along the hard  $c$  axis (Fig. 6.20, bottom panel, inset). Thus, a correct alignment for DM measurements of  $\chi_c$  is crucial. Note that the high percentage along  $c$  is related to the a small signal. For the TM measurements performed within this thesis and DM measurements along the in-plane directions  $a$  and  $c'$ , this approach yields small contributions due to misalignment effects. For  $\chi_a/\chi_c = 10$  and a misalignment of  $10^\circ$ , the errors are: DM  $\Delta\chi_a \approx \Delta\chi_{c'} = -2.7\%$ , DM  $\chi_c = 9.0\%$  and TM with  $H$  rotating in (100) or (110) about  $-3.4\%$ . In conclusion, misalignment effects cannot be responsible for the discrepancies

Table 6.4: Enhancement of the magnetic susceptibility along the  $c'$  direction  $\chi_{c'}^*$  (Eqn. 6.30) in comparison to the measured value on sample G2\_B\_3  $\chi_{c'}(\text{G2\_B\_3})$  due to batch discrepancies. These values were used to calculate  $\chi_{c,calc,cc'}$  (Eqn. 6.24) shown in Fig. 6.17.

T (K)	3	5	7	10	15	25	40	60	80
$\chi_{c'}^* / \chi_{c'}(\text{G2\_B\_3})$	1.089	1.085	1.081	1.078	1.065	1.049	1.042	1.027	1.012

measured using this approach. Nevertheless, misalignment effects are suggested to cause remarkable discrepancies based on DM measurement results.

- Finally, we investigated errors caused by measuring  $\chi$  and  $\Delta\chi$  on different batches. For TM measurements, samples separated from batch G3 ( $\Delta\chi_{a,c'}$  and  $\Delta\chi_{a,c}$ ) and G6 ( $\Delta\chi_{c,c'}$ ) were investigated. Detailed DM measurements along all three directions ( $a$ ,  $c$  and  $c'$ ) were performed on sample G2\_B\_3 (batch G2). The low-temperature discrepancies between all samples measured along the  $c'$  axis within this thesis are shown in Fig. 6.9. These measurements indicate a higher  $\chi_{c'}$  in CeRu<sub>4</sub>Sn<sub>6</sub> below about 85 K than measured in sample G2\_B\_3. At 3 K,  $\chi_{c'}$  of sample G2\_B\_3 is about 15 % lower than measured on G3\_B\_1. Note that no dataset was measured along the  $a$  or  $c$  direction. Therefore, no  $\chi_{c,calc}$  (Eqns. 6.23 and 6.24) can be calculated using samples separated of the same batch. So  $\chi_{c'}^*$  was calculated by

$$\chi_{c'}^* = \frac{\chi_{c'}(\text{G2\_B\_3}) + \chi_{c'}(\text{G3\_B\_1}) + \chi_{c'}(\text{MProbe})}{3} \quad (6.30)$$

and used for calculating  $\chi_{c,calc,cc'}$  (Eqn. 6.24). In a first approach, the same corrections were made to calculate  $\chi_{c,calc,ac}$ . So, the corrections due to different sample batches are included in Fig. 6.17. The ratios of  $\chi_{c'}^*$  to  $\chi_{c'}(\text{G2\_B\_3})$  at several temperatures are listed in Tab. 6.4.

In conclusion, none of the above discussed error sources can account for the large negative  $\chi_{c,calc,ac}$  and  $\chi_{c,calc,cc'}$  values (Eqns. 6.24 and 6.23, Fig. 6.17).  $\chi_{c,calc}(T)$  turns negative below about 175 K leading to  $\chi_{c,calc} \approx (-0.005) - (-0.011)$  emu/mol at 3 K (Fig. 6.17). This value is about three orders of magnitude higher than typical diamagnetic susceptibilities of single elements like Bi, C (graphite, diamond) or Pb. Apparently, there is another not yet identified error source. We hope that future experiments with samples with known anisotropy will clarify the situation.

In addition to the detailed discussion within the out-of-plane planes, the anisotropy in the (001) plane was probed (configuration 1 in Fig. 6.10, sample G3\_A\_a\_II, Figs. 6.16 and 6.18), too. Figure 6.18 shows  $\Delta\chi_{a,c'}$  derived directly by TM measurements (blue symbols), indirectly by TM measurements with  $\Delta\chi_{a,c'} = \Delta\chi_{a,c} - \Delta\chi_{c,c'}$  (green symbols) and by DM measurements with

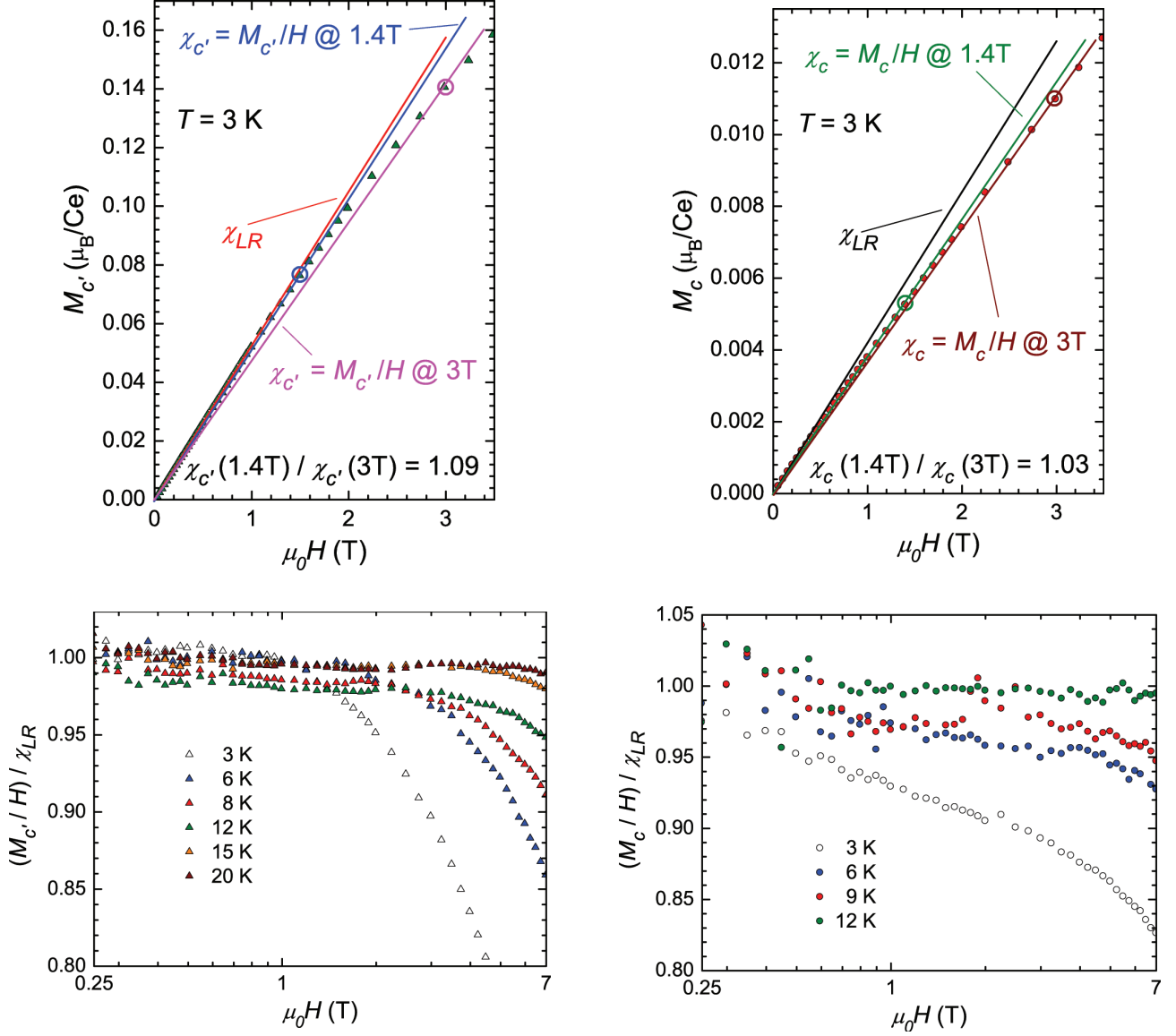


Figure 6.19:  $M(H)$  illustrating the field dependence of the magnetic susceptibility  $\chi = M/H$  in  $\text{CeRu}_4\text{Sn}_6$  at 3 K along the  $c'$  (left, top) and  $c$  (right, top) axis.  $\chi$  is compared at 1.4 and 3 T, which are the magnetic fields used for the comparison of TM (1.4 T) and DM (3 T) measurements (Fig. 6.17). The magnetic susceptibility in the linear response,  $\chi_{LR} = \lim_{H \rightarrow 0} \partial M(H) / \partial H$ , is also included.  $(M/H) / \chi_{LR}$  is plotted as a function of  $\mu_0 H$  at several temperatures in semilogarithmic plots for the  $c'$  axis (bottom, left) and for the  $c$  axis (bottom, right).



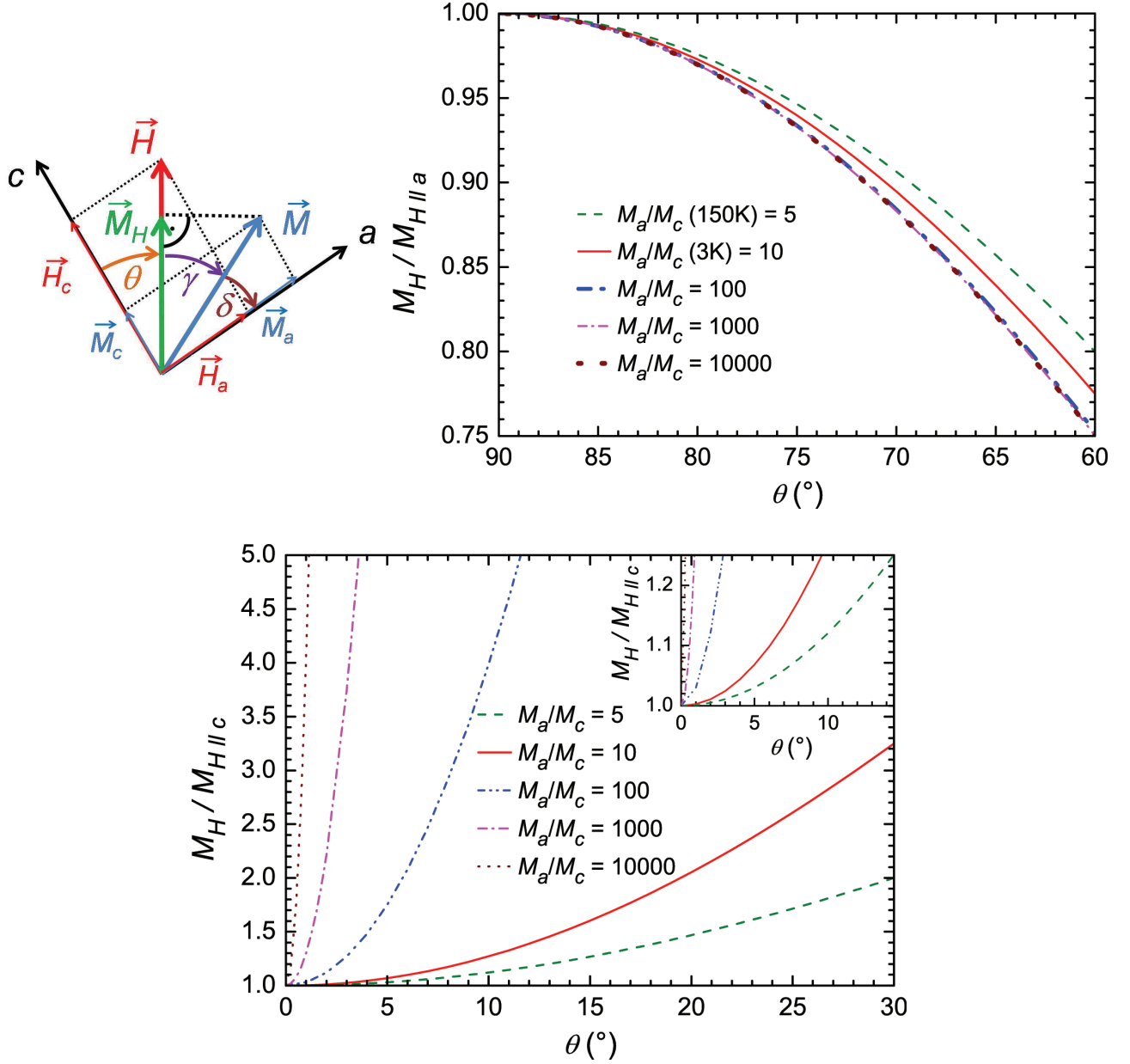


Figure 6.20: Investigation to calculate the angle dependence of misalignment in direct magnetization measurements on  $\text{CeRu}_4\text{Sn}_6$ . The left panel (top) defines the rotations. The magnetization  $M_H$  measured in the experiment is aligned along the field direction and the misalignment of the crystal axis  $c$  ( $a$ ) with respect to this field is defined by  $\theta$  ( $90^\circ - \theta$ ).  $M_H / M_{H||a}$  ( $M_H / M_{H||c}$ ) is shown as a function of the misalignment angle  $90^\circ - \theta$  ( $\theta$ ) in the top right panel (bottom panel). For these calculations, Eqn. 6.29 and  $\chi_a/\chi_c = 10$  (5) observed in the direct magnetization measurements at about 3 K (175 K) in  $\text{CeRu}_4\text{Sn}_6$  were used. Due to the indications of a higher anisotropy measured by torque magnetometry, higher ratios are investigated, too.

$\Delta\chi_{a,c'} = \chi_a - \chi_{c'}$  (red symbols). TM measurements revealed an easier magnetization along the  $a$  ([100]) than along the  $c'$  ([110]) axis. DM measurements in the linear  $M(H)$  range ( $> 20$  K) are included and are, within the error bar, consistent with an isotropic (001) plane above 20 K. At lower temperature,  $M(H)$  is non-linear and no accurate determination is possible with the available data. In contrast to the rotations including the out-of-plane direction  $c$ , the absolute value of  $\Delta\chi$  appears to be reliable. However, this result is still questionable because of the discrepancies found by calculating  $\chi_{c,calc,cc'}$  discussed above. Nevertheless, a small anisotropy is suggested to develop in the (001) plane below 25 K by the most significant TM measurements in the (001) plane (blue symbols) and an easier magnetization along the  $a$  than along the  $c'$  axis is found in this temperature range.

Next, the TM measurements were used to determine CEF parameters following the work by Kuz'min [101]. It was shown that the torque of anisotropic paramagnetic single crystals with  $4f$ -shell electrons contains important information about the CEF environment. High-temperature expansions of the angle dependence of  $\tau_{dir}$  allow for a unique determination of the CEF parameters (Eqns. 6.14-6.21). Note that this approach is valid in a non-interacting  $4f$ -electron regime, which is certainly not the case in CeRu<sub>4</sub>Sn<sub>6</sub> at low temperatures. Nevertheless, this approach was tested and revealed interesting results. Due to the temperature dependencies  $K_i \propto T^{-i}$  and the determined  $B_l^m$  relation ( $B_2^0/B_4^0 \approx 30-70$ ) for CeRu<sub>4</sub>Sn<sub>6</sub> from DM measurements (Sect. 6.1.1), a signature of the  $K_2$  contribution (quadrupled frequency ( $4\theta$ )) on the dominating  $K_1$  contribution (doubled frequency ( $2\theta$ )) is predicted to be unresolvable over the entire temperature range for the TM investigations. These predictions are in good agreement with the behaviour measured for  $\tau_{a,c}$  and  $\tau_{c',c}$  (configurations 2 and 3 in Fig. 6.10) over the entire temperature range (Figs. 6.14 and 6.15). Hence,  $B_2^0 \geq B_4^0$  revealed in Sect. 6.1.1 is confirmed. Additionally,  $B_2^0$  is calculated with Eqn. 6.20 to about 4.2 meV using the TM values between 250 and 325 K (275 and 325 K) with rotating  $H$  in the (100) and the (110) plane (Fig. 6.21). The TM values in this temperature range are likely in the non-interacting  $4f$ -electron regime where the model of Kuz'min should apply (Fig. 6.21).  $B_2^0$  is in good agreement with  $B_2^0$  determined with DM measurements (Sect. 6.1.1). This result indicates that the approach of independent localized  $4f$ -electrons works well above 275 K. At lower temperatures, the behaviour of  $\tau_n$  and  $\tau_{ac',Kuz}(\phi)$  cannot be mimicked properly with Eqns. 6.20-6.22 indicating the evolving hybridization between the localized Ce- $4f$  electrons with the itinerant  $d$ - and  $p$ -type electrons.

## Summary and discussion

Torque magnetometry measurements confirmed the pronounced anisotropy measured by direct magnetization measurements between the easy plane and the hard  $c$  axis. In fact, TM shows even more pronounced anisotropy, leading to a vanishing of  $\chi_c$  at about 175 K and to an unphysical high negative value of  $\chi_c \approx -1 \cdot 10^{-2}$  emu/mol at 3 K. The origin of the latter is not yet understood and further measurements are needed to clarify the situation.

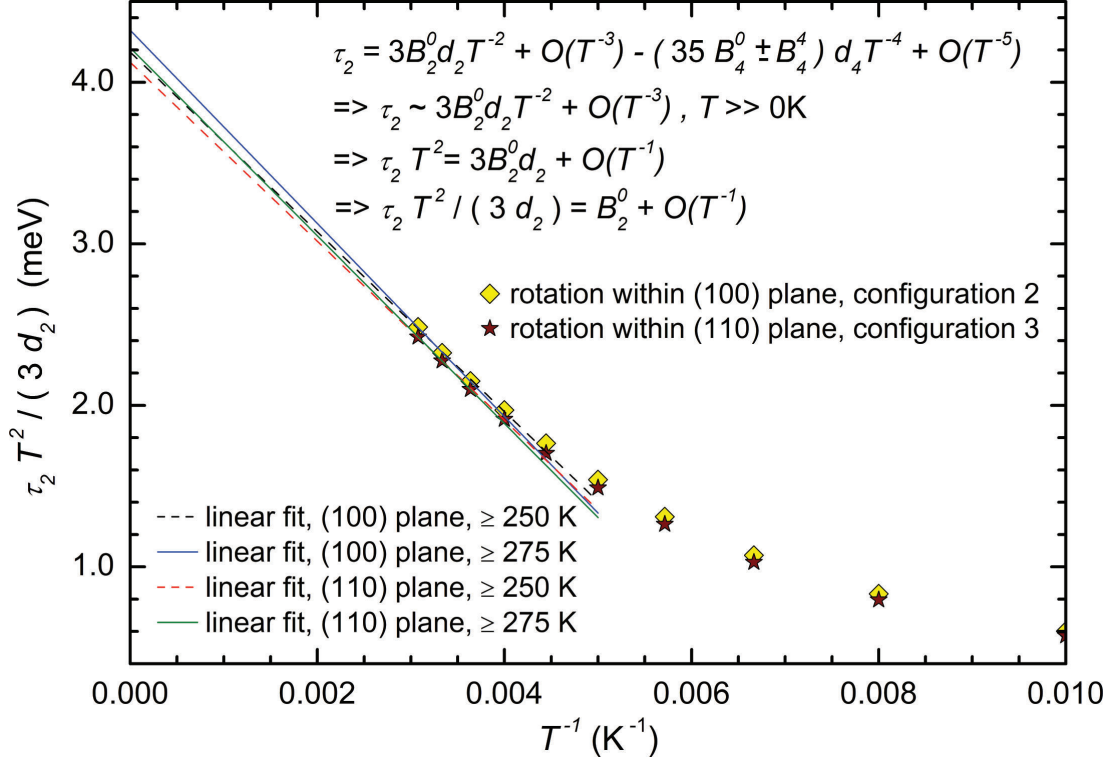


Figure 6.21: Determination of the crystalline electric field parameter  $B_2^0$  with TM measurements within the (100) (yellow symbols) and (110) plane (brown symbols) (configurations 2 and 3 in Fig. 6.10). The equation used includes the torque  $\tau$ , the temperature  $T$ , the function  $d_2$  (Eqn. 6.18) and  $B_2^0$ . Both fits lead to  $B_2^0 \approx 4.2$  meV. This value is in good agreement with  $B_2^0$  determined by direct magnetization measurements.

TM measurements at 9 T in the (001) plane revealed an increasing anisotropy with decreasing temperatures below 25 K (Fig. 6.18). In this temperature range, the  $a$  axis is easier magnetizable than the  $c'$  axis. Above 25 K, no anisotropy was detected.

Finally, TM measurements were used to determine CEF parameters, following an approach by Kuz'min [101].  $B_2^0$  was determined to about 4.2 meV (Fig. 6.21), which is in good agreement with the value derived by direct magnetization measurements (Sect. 6.1.1).

Table 6.5: Table of CeRu<sub>4</sub>Sn<sub>6</sub> single crystals used for electrical resistance, magnetoresistance and Hall effect measurements. Used abbreviations: R = resistivity, MR = magneto resistivity, HE = Hall effect, PPMS = physical property measurement system, DF = dilution fridge, HT = homemade high temperature set-up (E. Bauer).

sample name	measurements	geometrical infos	measurement device/info
B.2	high magnetic field MR	$j \parallel c$	PPMS, Rossendorf
B.3.1	R, MR, high magnetic field MR	$j \parallel a, j \parallel c'$	PPMS, Rossendorf
B.3.3	R, MR	$j \parallel c'$	PPMS, DF
G2_A_1	R, HE, MR	$j \parallel c$	DF, PPMS, HT
G2_A_2_1	R, HE, MR	$j \parallel c$	DF, PPMS
G2_B_2	R, HE, MR	$j \parallel a$	DF
G2_B_2 $\parallel a$	R, HE, MR	$j \parallel a$	PPMS, DF
G2_B_2 $\parallel c'$	R, HE, MR	$j \parallel c'$	PPMS, HT, DF
G3_A_A_c	R	$j \parallel a$	PPMS, HT
G6_A_2 $\parallel a$	R, HE, MR	$j \parallel a$	PPMS
G6_A_2 $\parallel c'$	R, HE, MR	$j \parallel c'$	PPMS
G7_BO1	R, MR	$j \parallel a$	PPMS
G7_BO7	R, MR	$j \parallel a$	PPMS
G7_TOP4	R, MR	$j \parallel a$	PPMS

## 6.2 Electrical resistivity

Electrical resistivity measurements were performed on several CeRu<sub>4</sub>Sn<sub>6</sub> single crystals from different batches in the temperature range from about 50 mK up to about 620 K with three different devices (Tab. 6.5). A detailed description of the used devices and procedures is given in Chap. 3. Within these measurements, slightly different behaviour was found for different CeRu<sub>4</sub>Sn<sub>6</sub> single crystals. Hence, a comparison between different CeRu<sub>4</sub>Sn<sub>6</sub> single crystals is added at the end of this section.

Figure 6.22 shows the electrical resistivity  $\rho(T)$  and its relative value  $\bar{\rho}(T)$  along the three different investigated directions  $a$  ( $\rho_a(T)$ , red),  $c$  ( $\rho_c(T)$ , blue) and  $c'$  ( $\rho_{c'}(T)$ , green) in a semilogarithmic plot. The samples of these measurements were separated from batch G2. Starting from high temperatures (about 620 K),  $\rho(T)$  decreases with decreasing temperature until a minimum at  $T_{min1} = 400$  K (355 K) along the in-plane directions ( $c$  direction) occurs. After this minimum, each curve shows a remarkable increase of  $\rho(T)$  with further decreasing temperature ending in a maximum at  $T_{max} = 11$  K (9.5 K) for  $\rho_a(T)$  and  $\rho_{c'}(T)$  ( $\rho_c(T)$ ). With further decreasing temperature,  $\rho(T)$  decreases slightly until another increase sets in, forming a minimum at  $T_{min2} = 2.5$  K (1.9 K) for  $\rho_a(T)$  and  $\rho_{c'}(T)$  ( $\rho_c(T)$ ).  $\rho_c(T)$  shows additionally a small hump at  $T_{hump} = 150$  K. Parts of the following investigations and of the discussion have already been published [102].

Table 6.6: Minima and maxima of electrical resistivity measurements for CeRu<sub>4</sub>Sn<sub>6</sub> single crystals separated from batch G2 (Fig. 6.22).

crystallographic direction	$T_{min1}$ (K)	$\rho_{min1}$ ( $\mu\Omega\text{cm}$ )	$T_{max}$ (K)	$\rho_{max}$ ( $\mu\Omega\text{cm}$ )	$T_{min2}$ (K)	$\rho_{min2}$ ( $\mu\Omega\text{cm}$ )
$a$	400	537.2	11	1607.0	2.5	1556.2
$c$	355	416.1	9.5	778.0	1.9	741.0
$c'$	400	583.1	11	1689.0	2.5	1643.9

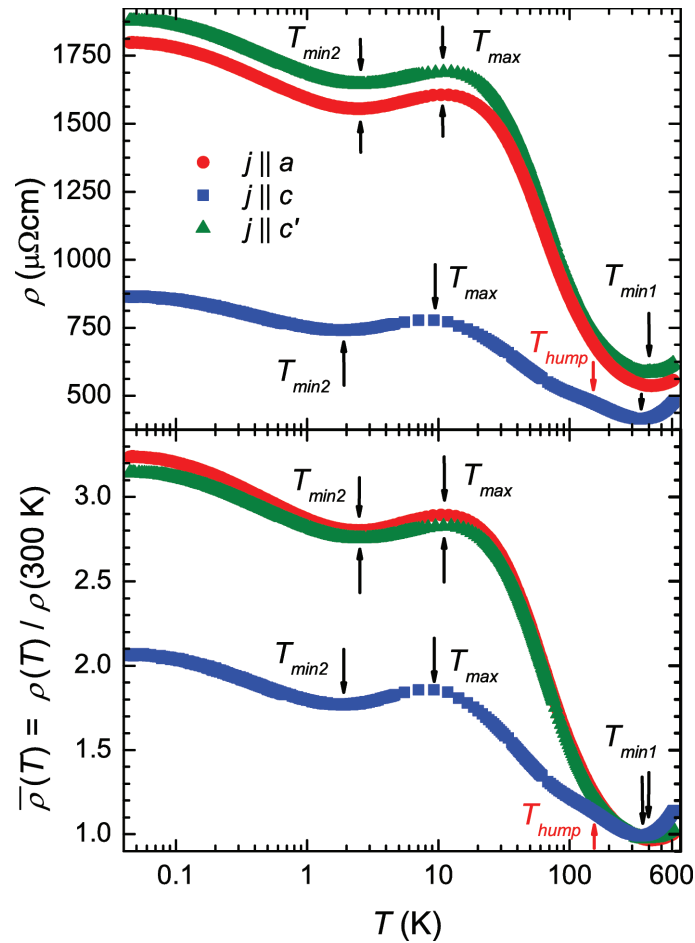


Figure 6.22: Electrical resistivity  $\rho$  measured on samples separated from batch G2 (G2\_B\_2 samples along in-plane axes, G2\_A\_1 along  $c$  direction) as a function of temperature  $T$  along the three investigated directions in a semilogarithmic plot (top). Pronounced anisotropy is found over the entire temperature range between the in-plane directions ( $a$ ,  $c'$ ) and the perpendicular  $c$  direction. The in-plane directions show similar behaviour, which is nicely seen in the relative resistivity plot  $\rho(T)/\rho_{300K}$  (bottom).

Two alternative approaches were made to explain the behaviour of  $\rho(T)$ . They are discussed in the following. At first, a two-gap structure in the electronic density of states (DOS), which is frequently found in simple semiconductors, was assumed. In this picture, the intermediate temperature behaviour is explained with an intrinsic gap, which was fitted with

$$\rho = \rho_1 e^{(\Delta/2k_B T)} \quad (6.31)$$

where  $\rho_1$  is a constant,  $\Delta$  is the energy gap and  $k_B$  is the Boltzmann constant. Within this picture, the second upturn at low temperatures is caused by a smaller extrinsic gap due to impurity states situated within the intrinsic gap. Since  $\rho(T)$  between  $T_{min1}$  and  $T_{max}$  cannot be described by Eqn. 6.31 over a wide temperature range, the data were fitted in two fitting intervals (12 K and 32 K), shifted with a step size of 2 K through the data (Fig. 6.23). Although reasonable values for the energy gap  $\Delta$  are obtained, no extended temperature range with a constant  $\Delta$  was found for any sample except for  $\rho_c(T)$  of sample G2\_A\_1; this measurement revealed a roughly constant energy gap of about 31 K in the temperature range between 60 and 100 K. Interestingly, an energy gap of about 30 K has also been found from electrical resistivity [1], thermopower [42] and  $^{119}\text{Sn}$  NMR investigations [43] on polycrystalline  $\text{CeRu}_4\text{Sn}_6$  samples. For the low-temperature increase below  $T_{min2}$  the procedure results in  $\Delta$  values that are 0.08-0.09 K. This appears unphysical and the results are therefore not shown. Thus, the model of a semiconducting material with a two-gap structure in the DOS is not convincing. In our publication [102] another illustration of these facts was used. There, two temperature ranges were fitted with Equ. 6.31 and displayed in plots. Naturally, the conclusion is the same.

The alternative second approach to explain the  $\rho(T)$  curves is based on the interpretation of  $\text{CeRu}_4\text{Sn}_6$  as Kondo insulator, which is also indicated by other physical properties, for instance by the optical conductivity [16]. In Kondo insulators, a hybridization gap is expected to develop below a characteristic temperature. Unfortunately, no quantitative predictions for the electrical resistivity have been made. The anisotropic hybridization in  $\text{CeRu}_4\text{Sn}_6$  leads to additional uncertainties. However, models for Kondo metals can be of some use. An important contribution to the temperature dependence of the resistivity comes from Kondo scattering which, in the incoherent scattering regime, leads to the well-known  $-\ln T$  result of single impurity models (Chap. 2) [17]. In the Kondo insulator  $\text{Ce}_3\text{Bi}_4\text{Pt}_3$ , for instance, this  $-\ln T$  behaviour is found for the electrical resistivity at high temperatures (vicinity of room temperature) [103]. In addition, the crystalline electric field split level scheme of the localized  $f$  electrons plays an important role, an effect that has been incorporated in the Coqblin-Schrieffer (CS) model (Chap. 2) [7, 59]. Although this is a single impurity model, it can qualitatively explain the electrical resistivity behaviour of Kondo lattice systems such as  $\text{CeAl}_3$  or  $\text{CeAl}_2$ . For a constant DOS, the CS model predicts different regions of  $-\ln T$  behaviour if the CEF split multiplets of the magnetic impurity are energetically well enough separated [55].

First, the phonon contribution to the electrical resistivity  $\rho_{ph}(T)$  has to be subtracted; it was approximated by  $\rho_{La}(T)$  of the non- $f$  reference compound  $\text{LaRu}_4\text{Sn}_6$  [41] with  $\rho_{ph}(T) = \rho_{La}(T) - \rho_{La,0}$  ( $\rho_{La,0}$  is the residual resistivity of  $\text{LaRu}_4\text{Sn}_6$ ). We restrict our analysis to temperatures



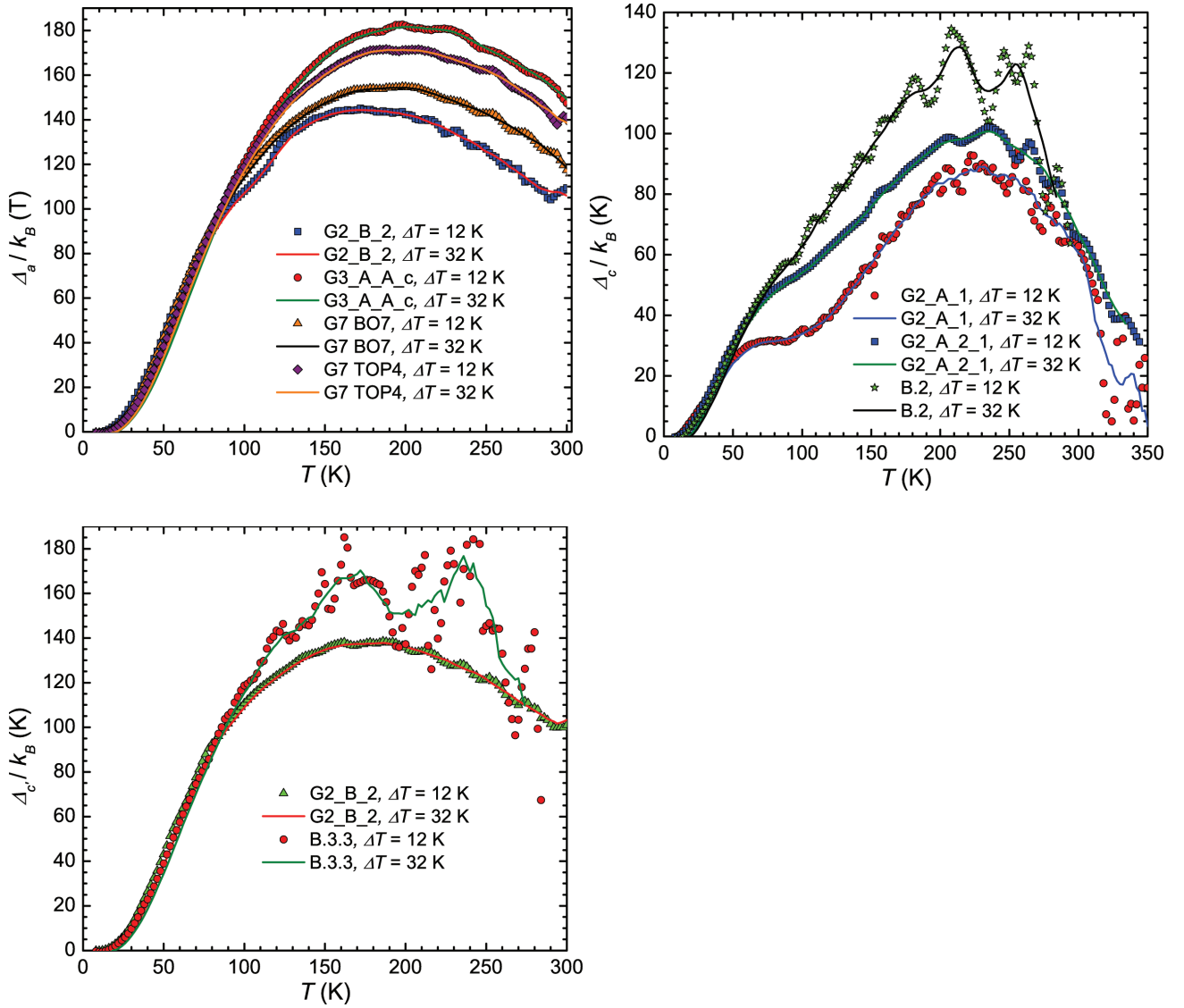


Figure 6.23: Energy gaps  $\Delta/k_B$  fitted with Eqn. 6.31 as function of temperature  $T$  along the  $a$ ,  $c$  and  $c'$  direction of several  $\text{CeRu}_4\text{Sn}_6$  samples. The fits were performed between 15 and 350 K. Two fitting intervals of 12 K and 32 K were chosen and their results are shown as dots and lines, respectively. The oscillations of some fits are caused by the interpolation process of  $\rho(T)$ . No simple semiconducting behaviour (with a constant gap value) can be found over a wide temperature range.

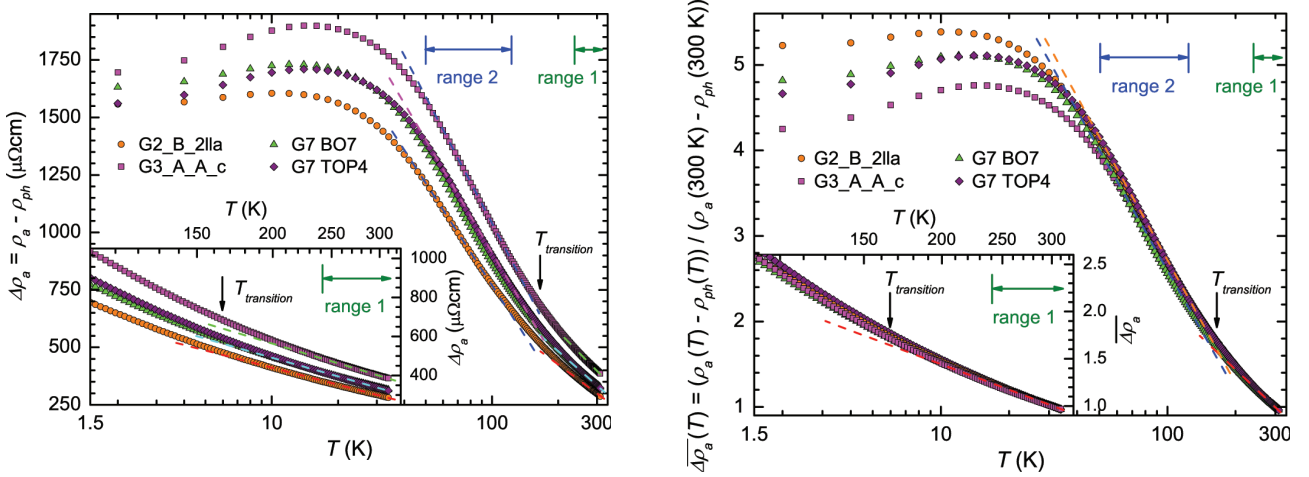


Figure 6.24: Electrical resistivity  $\Delta\rho_a$  and its relative  $\overline{\Delta\rho_a}(T)$  along the  $a$  direction of several samples as function of temperature  $T$  in a semilogarithmic plot.  $\rho_{ph}$  was derived from  $\text{LaRu}_4\text{Sn}_6$  [41]. The insets show the high-temperature behaviour. The linear slopes in range 1 and range 2 are indicated with dashed lines ( $-\ln T$  law) and the transition between these two ranges is indicated with  $T_{\text{transition}} = 165$  K.

below 310 K because of the available  $\rho_{La}(T)$  data.  $\Delta\rho(T) = \rho(T) - \rho_{ph}(T)$  and  $\overline{\Delta\rho}(T) = (\rho(T) - \rho_{ph}(T)) / (\rho(300 \text{ K}) - \rho_{ph}(300 \text{ K}))$  of several samples for the  $a$ ,  $c$  and  $c'$  direction are shown in Figs. 6.24 and 6.25 in semilogarithmic plots. Not shown here is that the upturn of  $\rho(T)$  below  $T_{\text{min}2}$  can be approximated in a narrow temperature range by a  $-\ln T$  law [102].

$\rho_a(T)$  measurements were performed with four samples with a well-defined rectangular cross section. Therefore, the absolute values of  $\rho_a(T)$  could be determined with good accuracy and are shown in Fig. 6.24, left panel. For  $\rho_c(T)$  and  $\rho_{c'}(T)$  measurements, only one sample per direction (batch G2) was measured with a well-defined cross section. Hence, the absolute resistance  $R$  of the samples with poorly-defined geometry has to be transferred to a specific resistivity  $\rho$  to compare the magnetic contribution  $\overline{\Delta\rho}(T)$  to  $\rho(T)$  (Fig. 6.25). This was made for each direction separately by  $\rho(T) = R(T) (\rho_{\text{ref}}(300 \text{ K}) / R(300 \text{ K}))$  with  $\rho_{\text{ref}}(300 \text{ K})$  of the geometrically well-defined G2 samples. Note that the influence of the residual resistivity  $\rho_0$  is neglected within this thesis. A determination of  $\rho_0$  at the lowest accessed temperatures is not meaningful because of the semiconducting nature of  $\rho(T)$ . This may result in errors in the rescaling process to determine  $\overline{\Delta\rho}(T)$  of the samples with poorly-defined form factor. Therefore, the  $R(T)$  curves of all samples were investigated to ensure that the characteristics in  $\overline{\Delta\rho}(T)$  are robust and not resulting from the scaling process. These investigations revealed that the scaling process does not change the characteristics. Therefore, the quantity ( $R(T)$ ,  $\rho(T)$ ,  $\Delta\rho(T)$  or  $\overline{\Delta\rho}(T)$ ) used for presentation is unimportant for the discussion below.

For each investigated direction and for almost all samples two temperature ranges (range 1 and range 2 in Figs. 6.24 and 6.25) were identified where  $\overline{\Delta\rho}(T) \propto -\ln T$  is observed. Fits in

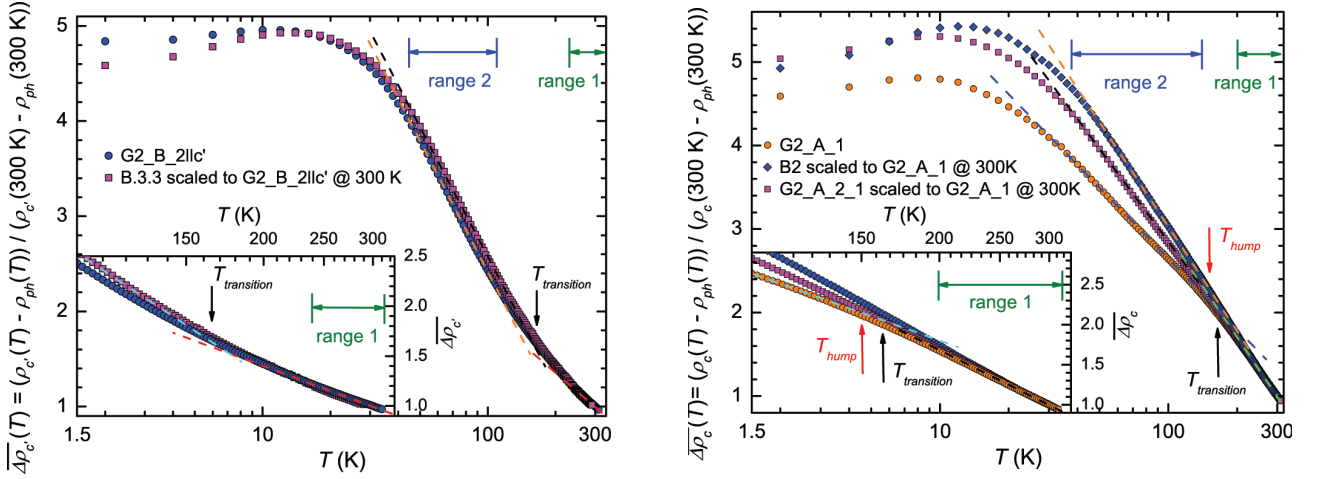


Figure 6.25: The relative electrical resistivity along the  $c$  axis  $\overline{\Delta\rho_c}(T)$  and along the  $c'$  axis  $\overline{\Delta\rho_{c'}}(T)$  as function of the temperature  $T$  are shown in semilogarithmic plots in the left and in the right panel, respectively.  $\rho_{ph}$  was derived from  $\text{LaRu}_4\text{Sn}_6$  [41]. The insets show the high-temperature behaviour. The linear slopes in range 1 and range 2 are indicated with dashed lines ( $-\ln T$  law) and the crossover between these two ranges is indicated with  $T_{\text{transition}} = 165$  K. The values of some samples were scaled to the  $\rho(300\text{ K})$  values of others (with better defined form factors) with the same orientation to subtract the phononic contribution. In the  $\overline{\Delta\rho_c}(T)$  plot, the position of the hump seen in  $\rho_c(T)$  is marked with  $T_{\text{hump}}$ .

these ranges are shown by dashed lines in Figs. 6.24 and 6.25. To compare the intermediate temperature range (between range 1 and 2) for different directions the transition temperature  $T_{transition} = 165$  K is introduced.  $T_{transition}$  is situated almost perfectly between the corners of range 1 and 2 for all directions and different samples.

Along the in-plane directions, the (negative) slope of the fit in range 2 is larger than in range 1. Along  $c$ , two of three samples showed clearly two temperature ranges with different slopes of  $-\ln T$  behaviour (G2\_A\_1 and G2\_A\_2\_1) (Fig. 6.25, right panel). In the third sample (B2), the different slope of the  $-\ln T$  law in range 1 and 2 is not as pronounced as in the other two samples. Unlike for the in-plane directions, the (negative) slope of the fit of  $\overline{\Delta\rho_c}(T)$  is smaller in range 2 than in range 1. The differences of  $\overline{\Delta\rho}(T)$  between different samples are attributed to extrinsic effects (in-gap states of impurities) and are discussed in the following subsection.

Some hints to understand the behaviour of  $\overline{\Delta\rho}(T)$  come from the Coqblin-Schrieffer (CS) model (Chap. 2) [7, 59]. Although this is a single impurity model, successful explanations of the electrical resistivity behaviour of Kondo lattice systems such as  $\text{CeAl}_3$  or  $\text{CeAl}_2$  were found. The CS model predicts that, for a constant DOS, the prefactor of the  $-\ln T$  term decreases with the thermal depopulation of the CEF levels (Eqn. 2.18, Chap. 2). The decrease of the  $-\ln T$  term with the thermal depopulation of the CEF levels was detected for  $\overline{\Delta\rho_c}(T)$ . Inelastic neutron scattering (INS) measurements [45] and X-ray absorption spectroscopy (Sect. 6.6) yield a CEF splitting between the lowest lying doublets of about 30 meV. Hence, the  $-\ln T$  behaviour in range 2 and 1 for  $\overline{\Delta\rho_c}(T)$  might be attributed to the Kondo scattering on the two lowest lying CEF doublets and on the ground state doublet, respectively. By contrast,  $\overline{\Delta\rho_a}(T)$  and  $\overline{\Delta\rho_{c'}}(T)$  cannot be described within this model because an increase of the slope is measured at lower temperatures. Another effect should not be ignored for this analysis. Optical conductivity measurements revealed that the DOS changes remarkably with decreasing temperature, leading to a metal-like DOS along  $c$  but to a gapped DOS within the (001) plane, containing  $a$  and  $c'$  [9, 16] (Chapt. 5 and Sect. 6.6). Therefore, the discrepancies for  $\overline{\Delta\rho_a}(T)$  and  $\overline{\Delta\rho_{c'}}(T)$  might be due to the strong temperature dependence of the DOS within the (001) plane. An indication for changes in the DOS is also found from Hall effect measurements: a change of the sign of the Hall coefficient  $R_H(T)$  was detected at 185 K for the in-plane directions  $a$  and  $c'$ . A smaller DOS yield a smaller contribution to  $\rho_{mag}$  (smaller increase to lower temperatures) and a shift of the maximum of the Kondo scattering contribution to lower temperatures (Eqn. 2.18 and Fig. 2.5, right panel; Chap. 2). The measurements show the opposite, namely a higher increase of the slope and a higher  $T_{max}$  along the in-plane directions than along the  $c$  axis (Figs. 6.24 and 6.25). Therefore, a higher DOS along the in-plane directions than along the  $c$  axis is suggested by the CS model. These findings are in contradiction to the other physical properties measurements, which reveal a higher DOS along the non-gapped  $c$  axis. Therefore, a pure CS model may be invalid to describe the behaviour found in  $\text{CeRu}_4\text{Sn}_6$ .

Table 6.7: Table of maxima and characteristic temperatures in  $\rho(T)$  measured for several  $\text{CeRu}_4\text{Sn}_6$  samples along different crystallographic directions.

$\rho_a(T)$		$\rho_c(T)$		$\rho_{c'}(T)$	
sample name	$T_{max}(\rho_a)$ (K)	sample name	$T_{max}(\rho_c)$ (K)	sample name	$T_{max}(\rho_{c'})$ (K)
G2_B_2  a	11.0	G2_A_1	9.5	G2_B_2  c'	11.0
G3_A_A_c	14.0	G2_A_2_1	10.0	B.3.3	12.0
G7_BO7	12.0	B.2	12.0		
G7_TOP4	14.0				
$T_{transition} = 165$ K (sample and directional independent)					
$T_{hump} = 150$ K, only seen in $\rho_c(T)$ of sample G2_A_1					

### Comparison of the electrical resistivity for different $\text{CeRu}_4\text{Sn}_6$ samples

Similar to the direct magnetization measurements (Sect. 6.1), slight differences in  $\rho(T)$  were found for different samples. In spite of these differences, the overall behaviour was reproducible and robust. Within this thesis, different  $\text{CeRu}_4\text{Sn}_6$  batches were grown (Sect. 4.2) and the samples are named by the respective batch name. In general, the G2 samples showed a smaller  $\rho(T_{max}) - \rho(T_{min2})$  value along all investigated directions. Additionally,  $T_{max}$  of the G2 samples is a few Kelvin smaller than in samples of batches B, G3 and G7 (Figs. 6.24 and 6.25, Tab. 6.7). The discrepancies at the lowest temperatures were investigated by magnetoresistance measurements and are discussed in detail in Sect. 6.4 .

$\overline{\Delta\rho_c}(T)$  ( $15 \text{ K} < T < 160 \text{ K}$ ) showed significant spread of different samples investigated while very robust behaviour was found for the in-plane directions (Figs. 6.24 and 6.25). Since also sample B.2 displays a slightly lower slope in range 2 than in range 1 in  $\overline{\Delta\rho_c}(T)$ , the smaller slope in range 2 appears to be intrinsic. Contributions from  $\overline{\Delta\rho}(T)$  along the in-plane directions yield an enhancement of the slope in range 2. Therefore, the discrepancies of the slopes in range 2 in  $\overline{\Delta\rho_c}(T)$  for different samples are attributed to misalignment effects.

The discrepancies in  $\overline{\Delta\rho}(T)$  seen at the lowest temperatures for different samples and directions might be due to a high sensitivity of  $\rho(T)$  on impurities, which leads to changes in the DOS in the vicinity of the Fermi level (see effects of impurities in  $\text{CeNiSn}$  [33, 39]). A detailed comparison of the magnetoresistance for different samples at low temperatures is found in Sect. 6.4. The significantly higher  $\Delta\rho_a(T)$  of sample G3\_A\_A\_c (Fig. 6.24, left panel) is not yet understood.

Magnetoresistance measurements revealed remarkable differences between  $\text{CeRu}_4\text{Sn}_6$  single crystals separated from batch G2 and B. Therefore,  $\rho_{c'}(T)$  was measured with sample B.3.3 and G2\_B\_2||c' between 0.05 and 300 K (Fig. 6.26). Above 10 K, only small discrepancies for the two samples were measured (more pronounced maximum in sample B.3.3) in  $\overline{\rho_{c'}}(T)$ . At lower

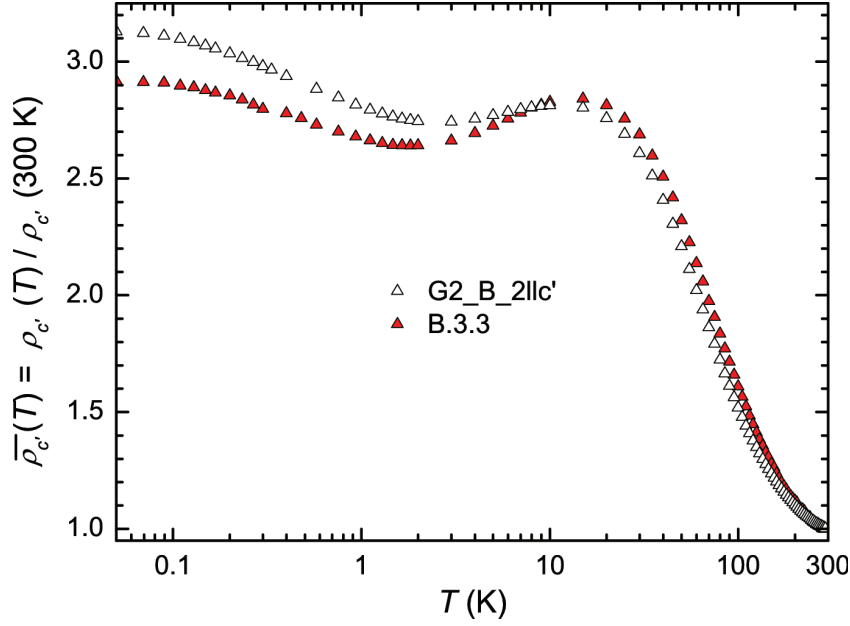


Figure 6.26: Relative electrical resistivity  $\overline{\rho}_c(T)$  as a function of temperature  $T$  along the  $c'$  direction for two different samples, namely G2\_B\_2|| $c'$  (white) and B.3.3 (red).

temperatures, a remarkable splitting of the curves is seen revealing a higher depletion at lowest temperatures for sample B.3.3 compared to G2\_B\_2|| $c'$ . Nevertheless, the characteristics (minimum around 2 K, maximum around 12 K) are the same. Magnetoresistance measurements revealed that these discrepancies cannot be reduced by applying magnetic fields.

## Summary

As expected,  $\rho(T)$  of  $\text{CeRu}_4\text{Sn}_6$  displays anisotropy between the in-plane ( $a$  and  $c'$ ) and perpendicular  $c$  direction(s) over the entire temperature range (Fig. 6.22). No indication of a reliable simple semiconductor-like behaviour of  $\rho(T)$  was found. By contrast, the CS model is at least partially in good agreement with the measurements at high temperatures (above 15 K) [7,59].

All  $\rho(T)$  measurements (sample and direction independent) revealed that two temperature ranges (range 1 and 2) with  $-\ln T$  behaviour exist above 15 K (Figs. 6.24 and 6.25). The center of the intermediate temperature range,  $T_{\text{transition}} = 165$  K, is almost directional independent. The relation of the slopes in the  $-\ln T$  ranges for  $\rho_c(T)$  are in agreement with the predictions of the CS model. Thus, the temperature dependence in these ranges may be attributed to Kondo scattering on the two lowest lying CEF doublets (splitting energy of about 30 meV [45]) and on the ground state doublet.

By contrast,  $\rho_a(T)$  and  $\rho_{c'}(T)$  do not follow the simple CS model. The gap formation along these directions (suggested by optical conductivity measurements and theoretical calculations [9,16], Chap. 5 and Sect. 6.6) leads to a pronounced reduction of the DOS with decreasing temperature.

A simple CS model predicts that the DOS is higher along the in-plane directions than along the  $c$  axis in  $\text{CeRu}_4\text{Sn}_6$ . Although the CS model fails, a change in the DOS cannot be excluded. The application of a CS model on  $\text{CeRu}_4\text{Sn}_6$  may not be appropriate. An additional indication for a changing DOS is found in Hall effect measurement because a sign change of the Hall coefficient is found at about 185 K for the  $a$  and  $c'$  direction with  $H \parallel c$  (Sect. 6.3).

The low-temperature  $\rho(T)$  is qualitatively understood as follows: The maximum at  $T_{max}$  indicates a transition from incoherent to coherent Kondo scattering. Unlike in heavy fermion metals the decrease in  $\rho(T)$  with decreasing  $T$  does not hold down to the lowest temperatures, but instead stops at  $T_{min2}$  below which  $\rho(T)$  reincreases. Presumably, the reduction of the density of states with decreasing  $T$  overrules the increase in scattering time in this temperature range.

The comparison of different batches revealed that small differences occur in  $\rho(T)$  for different samples but robust directional dependent characteristics are determined. Therefore, the sample quality is high enough to reveal intrinsic effects.

LDA+DMFT calculations for  $\text{CeRu}_4\text{Sn}_6$  were performed by P. Wissgott within his PhD thesis [9]. The resulting  $\rho(T)$  curves are shown in Fig. 6.27. At 290 K, the values were calculated with the computed LDA+DMFT self energy. At lower temperatures, the imaginary part of the computed LDA+DMFT self energy was set to 0.005 eV. These  $\rho(T)$  curves are less anisotropic than the measured data but nevertheless reproduce the key features. Note that the fine structure of the electronic band structure and the exact position of the chemical potential have a large influence on the behaviour of  $\rho(T)$ . Thus, the differences between theory and experiment are ascribed to features in the DOS which were not reproduced in the theoretical band structure.



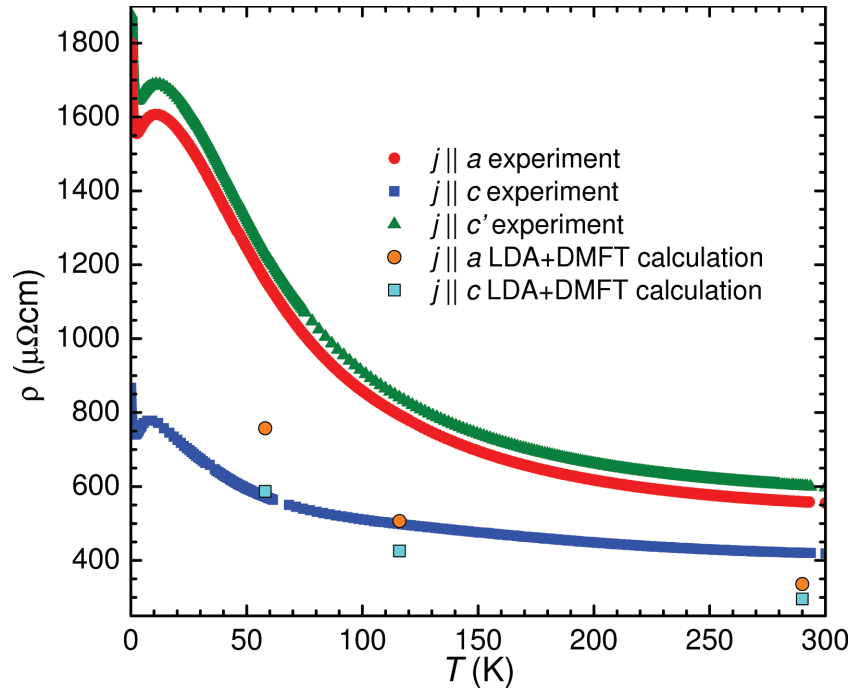


Figure 6.27: Theoretical and experimental electrical resistivity  $\rho$  as a function of temperature  $T$  along the main directions (batch G2). The theoretical values were calculated using LDA+DMFT by P. Wissgott [9].

### 6.3 Hall effect measurements

Hall effect measurements were performed on  $\text{CeRu}_4\text{Sn}_6$  samples separated from batch G2 and G6. The standard 6-point technique and devices used for the measurements are discussed in detail in Chap. 3. Throughout this section we adopt the following notations. Electrical current was applied along the three directions [100] ( $a$  axis), [110] ( $c'$  axis) and [001] ( $c$  axis). The corresponding Hall coefficients are denoted by  $R_{H,a}$ ,  $R_{H,c'}$  and  $R_{H,c}$ . The magnetic field direction is added in parenthesis as  $(H \parallel c)$ . For instance,  $R_{H,a}(H \parallel a)$  would be a Hall coefficient measurement with current along the  $a$  axis and with magnetic field along the perpendicular  $a$  axis.  $R_{H,a}(H \parallel c)$ ,  $R_{H,c}(H \parallel c')$  and  $R_{H,c'}(H \parallel c)$  measurements were performed with samples separated from batch G2.  $R_{H,a}(H \parallel a)$  and  $R_{H,c'}(H \parallel c')$  were measured on samples separated from batch G6.  $R_H(T)$  was determined by isothermal Hall resistivity ( $\rho_{Hall}$ ) measurements from the initial slope for non-linear  $\rho_{Hall}(H)$  curves for  $T \leq 10$  K (Eqn. 2.29, Fig. 6.30). At higher temperatures,  $\rho_{Hall}(T)$  was measured at 9 T and  $R_H$  was calculated by  $R_H = \rho_{Hall}(9\text{T}) / (\mu_0 H)$ . As for all other physical properties measured within this PhD thesis, anisotropy between the in-plane  $R_H$  ( $R_{H,a}$  and  $R_{H,c'}$ ) and  $R_{H,c}$  was observed.

Figure 6.28 shows a semilogarithmic plot of  $R_H(T)$  measured within this work. In Fig. 6.29 the high-temperature part is shown on linear scales. Figure 6.30 shows isothermal  $\rho_{Hall}(H)$  curves.  $R_{H,c}(T)(H \parallel c')$ ,  $R_{H,a}(T)(H \parallel a)$  and  $R_{H,c'}(T)(H \parallel c')$  remain positive over the entire temperature range. By contrast, a sign change from positive at lower to negative values at higher temperature was revealed at about 180 K for  $R_{H,a}(T)(H \parallel c)$  and  $R_{H,c'}(T)(H \parallel c)$  (Fig. 6.29). Interestingly, the sign change of  $R_H(T)$  is in the vicinity of the temperature range where the crossover between two  $-\ln T$  regimes (different slopes) occurs in the electrical resistivity (Sect. 6.2,  $T_{transition} = 165$  K). These features suggest a multiband structure and a change of the kind of majority carriers (hole type at low and electron type at high temperatures).

While the anisotropy of  $R_H(T)$  is small at high and at low temperatures, it is more pronounced at intermediate temperatures where a hump-like structure is seen at about 10 K (Fig. 6.28). Since the position of the hump correlates with the temperature of the maximum in  $\rho(T)$ , this structure might be due to the anomalous Hall effect (AHE) (Chap. 2).

In order to test this hypothesis the data were analyzed by plotting (Fig. 6.28, inset)

$$\Delta R_{H,a} = R_{H,a}(H \parallel c) - R_{H,a}(H \parallel a) = \gamma_{1,ac} \rho_{mag,a}(T) \chi_c(T) - \gamma_{1,aa} \rho_{mag,a}(T) \chi_a(T) \quad (6.32)$$

and

$$\Delta R_{H,c'} = R_{H,c'}(H \parallel c) - R_{H,c'}(H \parallel c') = \gamma_{1,c'c} \rho_{mag,c'}(T) \chi_c(T) - \gamma_{1,c'c'} \rho_{mag,c'}(T) \chi_{c'}'(T) \quad (6.33)$$

Since  $\chi_c \neq \chi_{a(c')}$ , a difference in the anomalous Hall effect is expected from Eqn. 2.32. Indeed, this difference resembles  $R_H^A(T)$  in heavy-fermion compounds (Fig. 2.8). The maxima in  $\Delta R_H(T)$ ,  $\rho_a(T)$ ,  $\rho_c(T)$  and  $\rho_{c'}(T)$  are listed in Tab. 6.8.  $T_{max}(\Delta R_H)$  are slightly shifted to lower

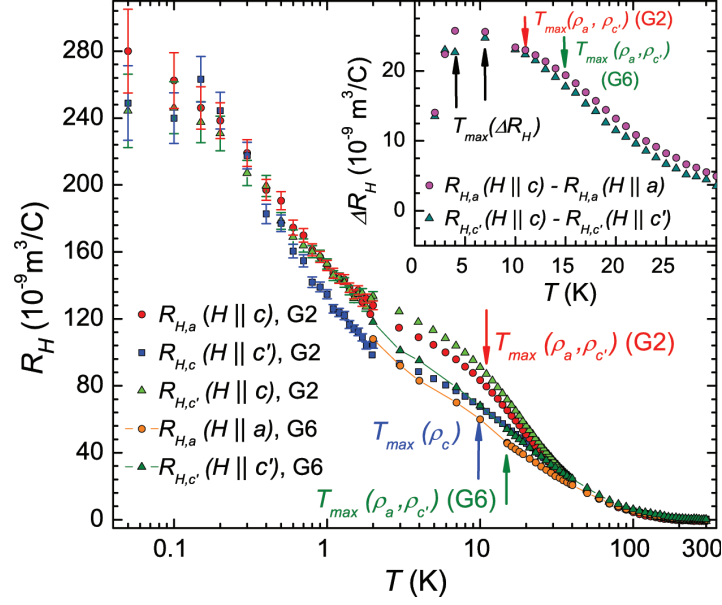


Figure 6.28: Hall coefficient  $R_H$  with current along the  $a$ ,  $c$  and  $c'$  directions and with different applied magnetic field  $\mu_0 H$  directions as a function of temperature  $T$  in a semi-logarithmic plot. These measurements were performed on  $\text{CeRu}_4\text{Sn}_6$  samples separated from batch G2 and G6. The positions of the maxima measured in the electrical resistivities  $\rho_a$ ,  $\rho_c$  and  $\rho_{c'}$  (Sect. 6.2) are indicated by  $T_{max}$ . The inset shows the difference  $\Delta R_{H,a}$  and  $\Delta R_{H,c'}$  for different directions of  $H$ , calculated from Eqs. 6.32 and 6.33.

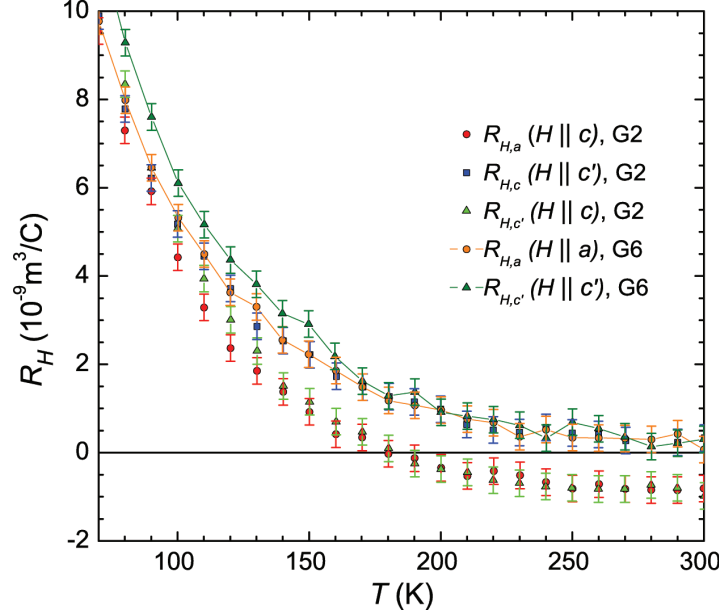


Figure 6.29: Hall coefficient  $R_H$  with current along the  $a$ ,  $c$  and  $c'$  directions and with different applied magnetic field  $\mu_0 H$  directions as a function of temperature  $T$ . These measurements were performed on  $\text{CeRu}_4\text{Sn}_6$  samples separated from batch G2 and G6. The plot shows the change of sign for  $R_{H,a}(H||c)$  and  $R_{H,c'}(H||c)$  at about 180 K.

Table 6.8: Temperature of the maxima  $T_{max}$  measured on  $\text{CeRu}_4\text{Sn}_6$  single crystals for the electrical resistivity  $\rho$  and for the difference of Hall coefficients  $\Delta R_H$ . The batches of the single crystals are added in parenthesis.

	$\rho_c(\text{G2})$	$\rho_a(\text{G2})$	$\rho_a(\text{G6})$	$\rho_{c'}(\text{G2})$	$\rho_{c'}(\text{G6})$	$\Delta R_{H,a}$	$\Delta R_{H,c'}$
$T_{max}$ (K)	9.5	11	15	11	15	4	7

temperatures in comparison to  $T_{max}(\rho_a)$  and  $T_{max}(\rho_{c'})$  (Tab. 6.8 and Fig. 6.28, inset). Due to the calculation of  $\Delta R_H(T)$  (Eqns. 6.32 and 6.33) with different samples, the shift of  $T_{max}(\Delta R_H)$  to lower temperatures (compared to  $T_{max}(\rho)$ ) is partially induced by the higher  $T_{max}(\rho)$  for G6 samples in comparison to G2 samples (Tab. 6.8).

Next, the absolute values for  $R_H^A(T)$  are discussed.  $\rho_{mag}(T)$  and  $\chi(T)$  were determined by electrical resistivity (Sect. 6.2) and magnetization measurements (Sect. 6.1.1), respectively. Therefore, the only unknown in Eqn. 2.32 is the coefficient  $\gamma_1$  describing the scattering of itinerant on localized electrons (Chapt. 2). Table 6.9 lists the  $\rho_{mag}(T) \cdot \chi(T)$  values (relations) at 10 K. These relations change by less than 5 % in the temperature range discussed below. Therefore, their temperature dependence can be neglected.

For an isotropic  $\gamma_1$  coefficient, the hump in  $R_H(T)$  due to the AHE should be strongly enhanced for  $R_{H,a}(T)(H||a)$  (orange symbols connected with lines in Fig. 6.28) and  $R_{H,c'}(T)(H||c')$  (dark

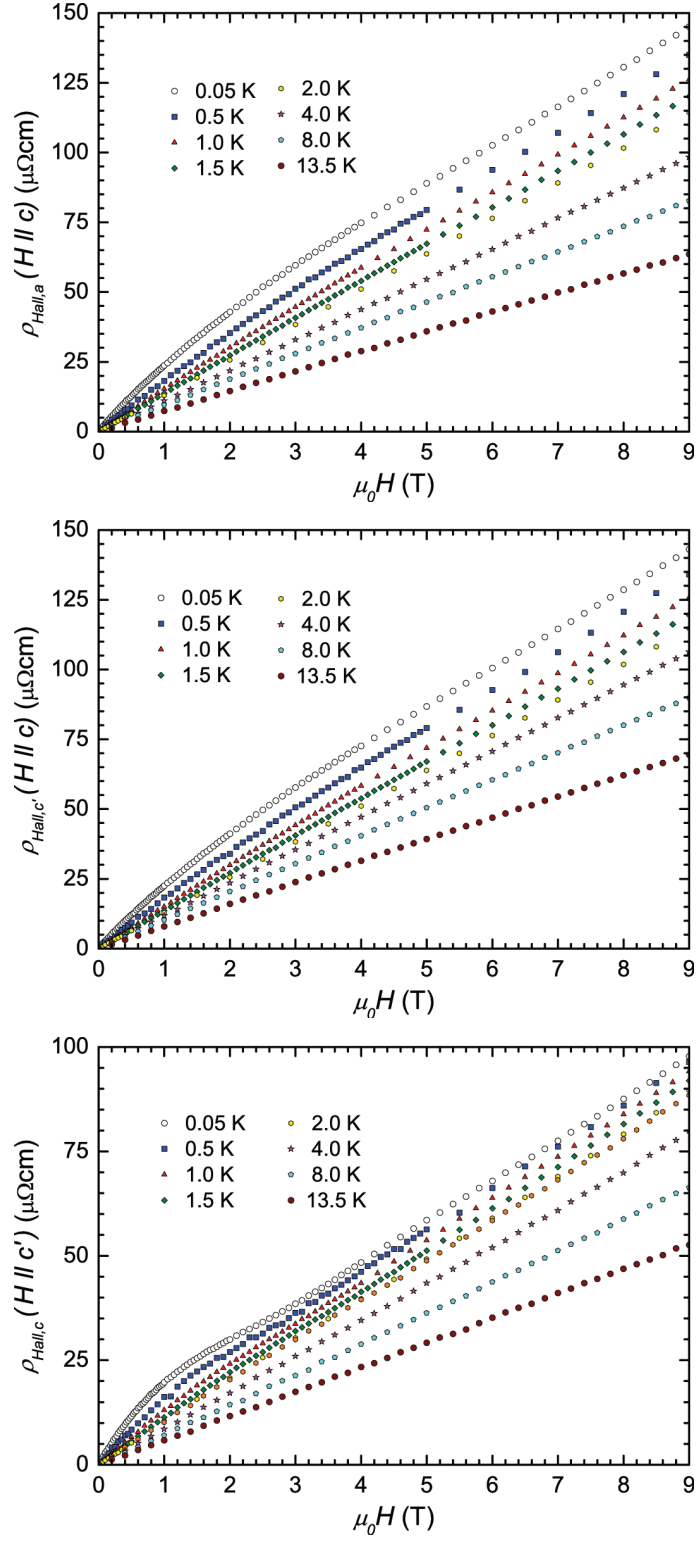


Figure 6.30: Hall resistivity  $\rho_{Hall}$  for current along the  $a$  (top),  $c'$  (middle) and  $c$  (bottom) axis as a function of magnetic field  $\mu_0 H$ , measured at different temperatures. For  $T \leq 10$  K,  $R_H$  was determined by the initial slope of these isotherms.

Table 6.9: Relations between different  $\rho_{mag}(T) \cdot \chi(T)$  values used for analysis of the anomalous Hall effect in  $\text{CeRu}_4\text{Sn}_6$ . The values are calculated as (column value) / (row value) at 10 K. The temperature dependence of these values is negligible.

	$\rho_{mag,a} \cdot \chi_a$	$\rho_{mag,c} \cdot \chi_c$	$\rho_{mag,c'} \cdot \chi_{c'}$	$\rho_{mag,a} \cdot \chi_c$	$\rho_{mag,c'} \cdot \chi_c$
$\rho_{mag,a} \cdot \chi_a$	1	1/23.8	1.1	1/10.5	1/10.1
$\rho_{mag,c} \cdot \chi_c$		1	26.1	2.2	2.4
$\rho_{mag,c'} \cdot \chi_{c'}$			1	1/11.6	1/11.0
$\rho_{mag,a} \cdot \chi_c$				1	1.1
$\rho_{mag,c'} \cdot \chi_c$					1

green symbols connected with lines in Fig. 6.28) in comparison to the other combinations of  $H$  and  $R_H(T)$  directions. This enhancement is seen best in the second row of Tab. 6.9 including the relations with respect to  $\rho_{mag,c} \cdot \chi_c$ . By contrast to these values, the measurements revealed that a sizable higher contribution of  $R_H^A(T)$  to  $R_H(T)$  was measured for all  $R_H(T)$  with  $H \parallel c$  (Fig. 6.28). Therefore, we suggest a higher  $\gamma_1$  coefficient for  $R_H^A(T)$  with  $H \parallel c$ . If a relation between  $\gamma_1(H \parallel c)$  and  $\gamma_1(H \parallel a(c'))$  of about 25 is used, good agreement for all  $R_H^A(T)$  contributions is found. Note that  $\gamma_1$  depends on the phase shifts linked to the possible scattering channels [74]. Thus, our results point to different scattering channels for  $H \parallel c$  and  $H \parallel a(c')$ .

The charge carrier concentration  $n$  (Equ. 2.30) and the Hall mobility  $\mu_H = R_H / \rho$  within a single-band model approach are shown in Fig. 6.31.  $n$  reaches a minimal value of about 0.0055 charge carriers per formula unit for all directions at the lowest temperatures. Pronounced anisotropy is seen for the Hall mobility. If a parabolic dispersion relation with a spherical symmetric Fermi surface is assumed, the effective mass  $m^*$  can be calculated with  $n = 0.0055$  carriers/f.u. and  $\gamma = 0.08$  J/mol K<sup>2</sup> [46] ( $\gamma = 0.04$  J/mol K<sup>2</sup> [40]) to  $m^* = 124 m_e$  ( $m^* = 62 m_e$ ) ( $m_e$  = electron mass).

Figure 6.32 shows  $R_H(T)$  and  $\mu_H(T)$  of the orthorhombic Kondo insulators (semiconductors)  $\text{CeNiSn}$  and  $\text{CeRhSb}$  [11]. The low-temperature behaviour of  $R_H(T)$  and  $\mu_H(T)$  shows similar characteristics as found for  $\text{CeRu}_4\text{Sn}_6$  (Figs. 6.28 and 6.31).  $R_H(T)$  and  $\mu_H(T)$  exhibit a logarithmic increase to lower temperatures for a single-band model approach. The charge carrier concentration at 0.5 K was calculated to 0.0012 and 0.0016 carriers/f.u. for  $\text{CeNiSn}$  and  $\text{CeRhSb}$ , respectively [11]. The increase of  $R_H(T)$  at lowest temperatures is due to the increase of  $\mu_H(T)$  to lower temperatures and not due to the change of the charge carriers within this model.

$\text{CeNiSn}$  was suggested to exhibit an anisotropic hybridization gap in the electronic DOS [5], as is also discussed for  $\text{CeRu}_4\text{Sn}_6$ . In Fig. 6.32,  $|R_H(T)|$  of  $\text{CeNiSn}$  is shown along the nodal (gapless)  $a$  direction [11] (the equivalent direction in  $\text{CeRu}_4\text{Sn}_6$  is the  $c$  direction). The increase of  $\mu_H$  implies an increase of  $\tau/m^*$  where  $\tau$  is the scattering time of the quasiparticles and  $m^*$  their effective mass. Ikeda and Miyake [5] attributed the increase of  $\mu_H$  to a larger  $\tau$  in the

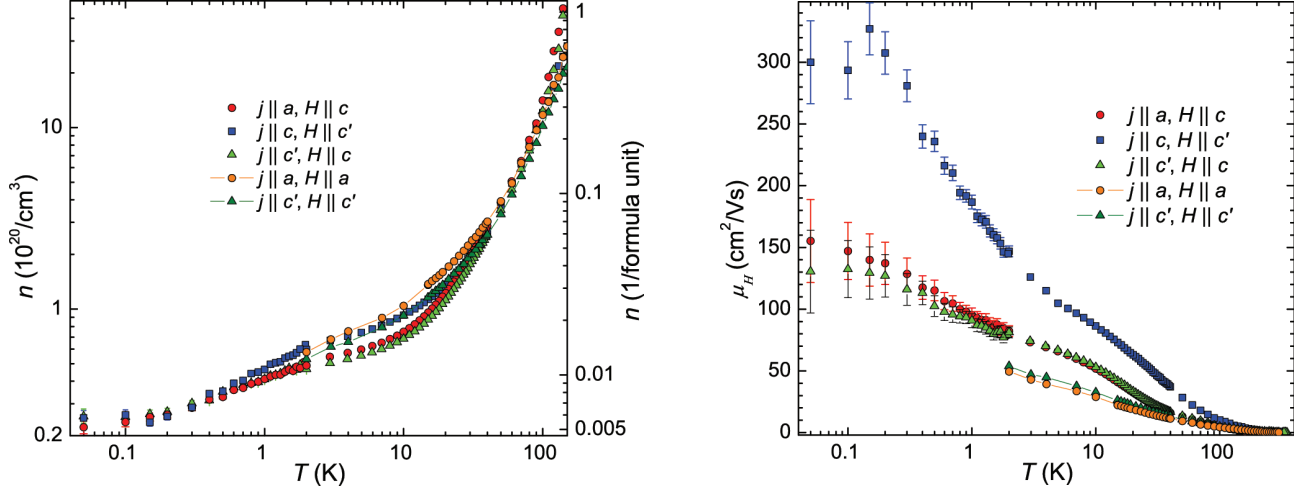


Figure 6.31: In the left panel the charge carrier concentration  $n$  is shown as a function of temperature  $T$  for different units of  $n$ . The right panel shows the Hall mobility  $\mu_H$  as a function of  $T$ .

pseudogapped state than in the normal Fermi-liquid state because of scattering restrictions in the  $k$ -space due to the narrow gapless region along the  $a$  axis. The higher logarithmic increase to lower temperatures in  $\mu_{H,c}(T)$  than  $\mu_{H,a}(T)$  ( $\mu_{H,c'}(T)$ ) might be explained by an equivalent argument (higher  $\tau$ ) or by a lower  $m^*$  along the gapless  $c$  axis of  $\text{CeRu}_4\text{Sn}_6$  (Fig. 6.31).

## Summary

Hall effect measurements revealed several anisotropic features between the in-plane directions and the  $c$  axis. The observed sign change of  $R_{H,a}$  and  $R_{H,c'}$  with  $(H||c)$  at about 180 K might be connected with the crossover between different  $-\ln T$  regimes in the electrical resistivity. The anisotropic hump-like structure at about 10 K is attributed to an anomalous Hall effect contribution. At the lowest temperatures  $R_H(T)$  is almost isotropic and reaches  $260 \cdot 10^{-9} \text{ m}^3/\text{C}$  at 50 mK for all directions, which corresponds to a single-band charge carrier concentration of only 0.0055 charge carriers per formula unit. Interestingly, this single-band model revealed an anisotropy of the Hall mobility which was compared to the results of the anisotropic Kondo insulator  $\text{CeNiSn}$  [5]. This comparison revealed similar low-temperature behaviour for  $R_H(T)$  and  $\mu_H(T)$  in  $\text{CeRu}_4\text{Sn}_6$  and  $\text{CeNiSn}$  (logarithmic increase of  $\mu_H$  with decreasing temperatures). An electronic DOS with an anisotropic hybridization in  $\text{CeRu}_4\text{Sn}_6$  might be supported by  $R_H(T)$  and  $\mu_H(T)$  within this analysis.

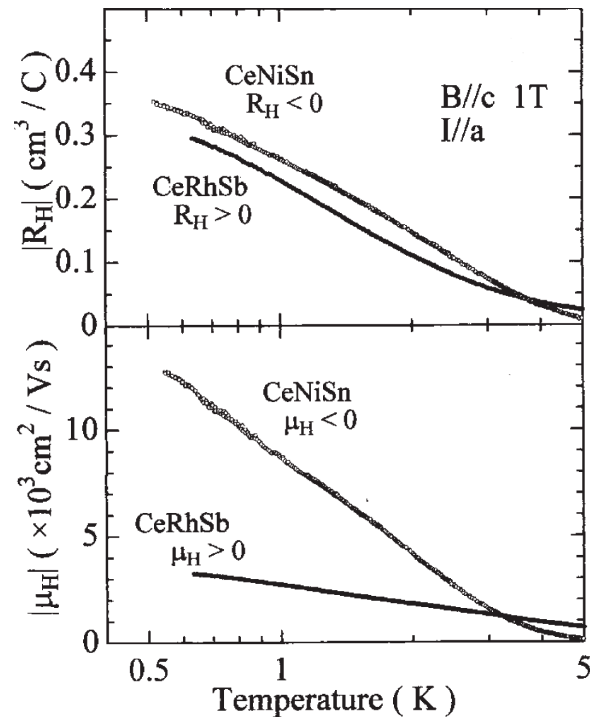


Figure 6.32: Hall coefficient  $R_H$  and Hall mobility  $\mu_H$  as a function of temperature  $T$  of the Kondo insulators (semiconductors) CeNiSn and CeRhSb in a semilogarithmic plot. This plot was extracted from [11].



## 6.4 Magnetoresistance

Magnetoresistance measurements are much employed for investigating Kondo insulators. In  $\text{SmB}_6$ , for instance, the closing of the gap in high magnetic field was investigated by magnetoresistance measurements (Fig. 6.54) [104, 105]. In  $\text{CeNiSn}$ , strong directional dependences of the magnetoresistance were observed which allow to extract information about the underlying anisotropic Fermi surface [12]. Within this thesis, both transverse and longitudinal magnetoresistance measurements were performed on  $\text{CeRu}_4\text{Sn}_6$  samples along the three investigated main directions. Additionally, high-field measurements were carried out in Rossendorf/Dresden by J. Larrea and F. Weickert on samples prepared within this PhD thesis. As already mentioned in Sect. 6.2, slight sample dependencies were found for different batches. These differences are most pronounced in the magnetoresistance. The overall behaviour, however, is the same for all batches. A detailed description about the used devices and measurement techniques is presented in Chap. 3. The following section presents the measurements along the three directions  $a$ ,  $c$  and  $c'$  as function of the field direction. In the next section, the batch dependent behaviour is discussed. Finally, field-dependent magnetoresistance isotherms are discussed. Throughout this chapter we adopt the following notations:

- Current direction: Electrical current was applied along the three directions [100] ( $a$  axis), [110] ( $c'$  axis) and [001] ( $c$  axis). The corresponding magnetoresistance  $\rho_B$  is denoted by  $\rho_{B,a}$ ,  $\rho_{B,c'}$  and  $\rho_{B,c}$ .
- Magnetic field direction: Spherical polar coordinates are used to define the direction of the magnetic field with respect to the crystal axes for the magnetoresistance with rotating magnetic field (Fig. 6.33). For instance,  $\rho_{B,c}(\phi = 0^\circ, \theta = 0-90^\circ)$  would be an electrical resistivity measurement along the  $c$  axis with magnetic field rotating from the  $c$  to the  $a$  axis. The longitudinal magnetoresistance is denoted by  $\rho_{B, \text{long}}$  and the respective direction, e.g. for the longitudinal magnetoresistance along the  $a$  axis by  $\rho_{B, \text{long}, a}$ . The transverse magnetoresistance is denoted by  $\rho_{B, \text{trans}}$  and the field direction is added in parenthesis. Thus, a transverse magnetoresistance measurement with an electrical current along the  $a$  axis and with a perpendicular magnetic field along  $c$  is referred to as  $\rho_{B, \text{trans}, a}(H \parallel c)$ .

### Investigations to determine the differences between longitudinal and transverse magnetoresistivity

Longitudinal and transverse  $\rho_B$  measurements may help to discriminate between contributions based on changes of the electronic bandstructure (Fermi surface) and contributions due to the magnetic deflection of charge carriers. Additionally, the angular dependence of  $\rho_B$  was investigated to determine the sensitivity of  $\rho_B$  to misalignment of the magnetic field. The samples used for these investigations were separated from batch G2 and exhibit a minimum in

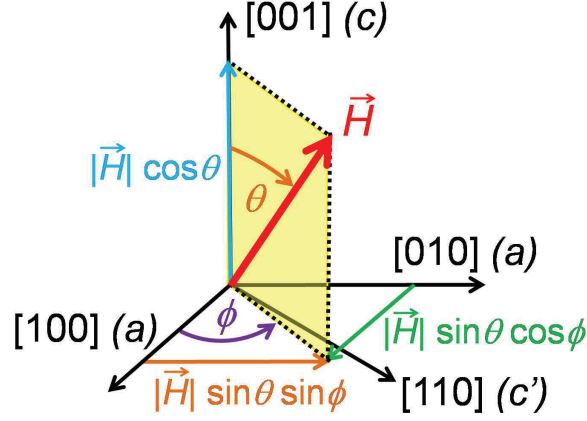


Figure 6.33: Schematic drawing of the notations (spherical polar coordinates) used for magnetoresistance measurements with rotating magnetic field  $H$ .

$\rho_{B,long,a}$ ,  $\rho_{B,trans,a}(H\|a)$ ,  $\rho_{B,long,c'}$ ,  $\rho_{B,trans,c'}(H\|c')$  and  $\rho_{B,long,c}$  above 2 K (Figs. 6.34, 6.40, 6.44 and 6.46). By contrast, no minimum above 2 K is detected for  $\rho_{B,trans,a}(H\|c)$ ,  $\rho_{B,trans,c'}(H\|c)$  and  $\rho_{B,trans,c}(H\|c')$  (Figs. 6.34, 6.44 and 6.46).

Firstly,  $\rho_{B,c}$  measurements were performed with rotating  $H$  within two different planes ((001) and (110)).  $\rho_{B,trans,c}(\phi=0-45^\circ, \theta=90^\circ)$  with  $\mu_0 H = 9$  T at several temperatures was investigated. The ratio  $\rho_{B,trans,c}(\phi, \theta=90^\circ) / \rho_{B,trans,c}(H\|a)$  is displayed in Fig. 6.35. Starting from  $\phi=0^\circ$  ( $H\|a$ ), a small decrease to  $\phi=45^\circ$  ( $H\|c'$ ) was measured. This small difference of  $\leq 0.5\%$  implies almost isotropic behaviour (a spurious Hall voltage would yield a deviation of  $\leq \pm 0.2\%$ ).

An empirical fit function

$$\rho_{B,c}(\beta) = \rho_{rel0} + P_1 \cos(m\beta)^\alpha + P_2 \sin(m\beta)^\alpha \quad (6.34)$$

was used to describe the data ( $\beta = \theta$  or  $\phi$ ). Equation 6.34 contains the rotation angle  $\beta$ , the multiplicity  $m$ , the exponent  $\alpha$  and the fit parameters  $\rho_{rel0}$ ,  $P_1$  and  $P_2$ . Equation 6.34 describes properly both  $\rho_{B,c}(\beta)$  measurements performed within this thesis (Figs. 6.35 and 6.36). Note that  $\rho_{B,c}(H)$  of the investigated curves show a small (no) minimum above 2 K (Fig. 6.34). Equation 6.34 contains three terms. The first term ( $\rho_{rel0}$ ) is an angle-independent constant term. The second (contains  $P_1$ ) and third term (contains  $P_2$ ) describe the contributions to  $\rho_{B,c}(H)$  for  $H$  pointing along a main direction ( $a$ ,  $c$  or  $c'$ ). The angle-dependent depletion of this contributions is described with a sinusoidal angle dependence (frequency  $m$ ) to the power of  $\alpha$ .

The fit parameters for  $\rho_{B,trans,c}(\phi)$  (Eqn. 6.34) are listed in Fig. 6.35 in the right panel.  $P_1$  and  $P_2$  decrease with increasing temperature. Also their difference decreases indicating the disappearance of the small anisotropy with increasing temperature. The small anisotropy, the higher  $\rho_{B,trans,c}(H\|a)$  compared to  $\rho_{B,trans,c}(H\|c')$  and the lowering of the anisotropy to

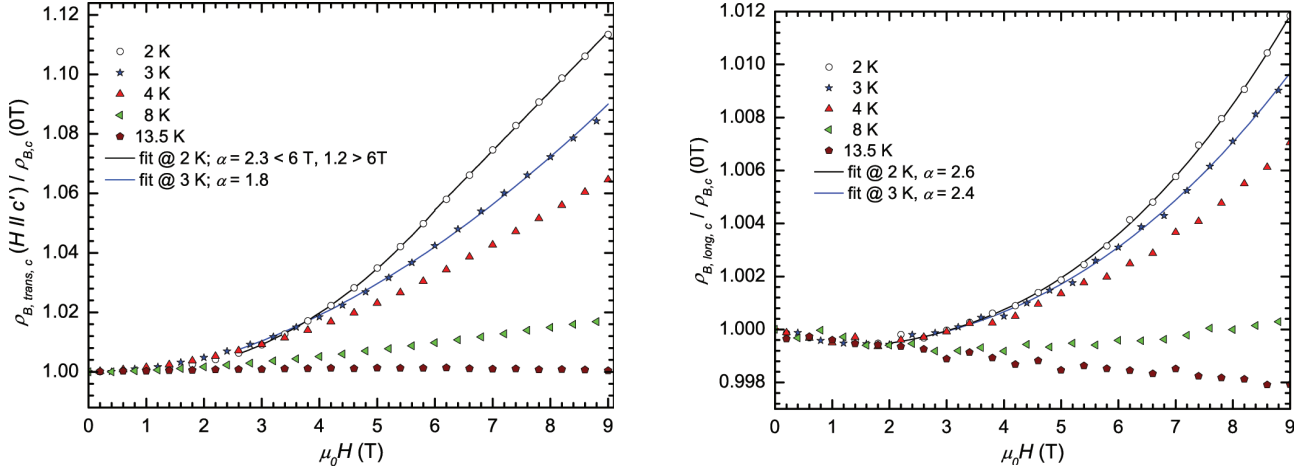


Figure 6.34: Relative transverse  $\rho_{B,trans,c}(H \parallel c') / \rho_{B,c}(0T)$  (left) and longitudinal  $\rho_{B,long,c} / \rho_{B,c}(0T)$  magnetoresistance (right) as a function of the magnetic field  $\mu_0 H$  at different temperatures. The exponential dependence of these curves ( $H^\alpha$ ) was fitted at the lowest temperatures (lines).

higher temperatures indicate an easier magnetization ability along the  $a$  axis in comparison to  $c'$  at lowest temperatures if the anisotropy is attributed to magnetization effects. These findings are in agreement with the results of torque magnetometry measurements (Fig. 6.18). The multiplicity  $m=2$  for  $\rho_{B,trans,c}(\phi)$  and the quadratic dependence of the sinusoidal terms for both  $\rho_{B,c}$  measurements (Figs. 6.35 and 6.36) cannot be ascribed to geometrical effects and to the field dependence along the main directions (see non-quadratic exponential behaviour in Fig. 6.34). However, appropriate results are found with the empirical Eqn. 6.34.

$\rho_{B,c}(\phi = 45^\circ, \theta = 0 - 90^\circ)$  measurements were performed at 2 and 3 K with magnetic fields of 3, 5, 7 and 9 T. The ratios  $\rho_{B,c}(\phi = 45^\circ, \theta) / \rho_{B,c}(0T)$  are shown in Fig. 6.36.  $\rho_{B,c}(\phi = 45^\circ, \theta)$  increases with increasing  $H$  and shows minima (maxima) for  $\theta = 0^\circ$  ( $\theta = 90^\circ$ ). The minima for  $\theta = 0^\circ$  are caused either by the longitudinal geometry (no transverse deflection) or by the dependence on the direction of  $H$  (scattering rate, density of states (DOS) around the Fermi level). Ongoing investigations indicate that the  $H$  direction is most important and the transverse or longitudinal application of  $H$  is of minor importance (Figs. 6.37, 6.44, 6.46, 6.49 and 6.50).  $\rho_{B,c}(\phi = 45^\circ, \theta) / \rho_{B,c}(0T)$  was fitted with Eqn. 6.34. The fits are included as dotted lines in Fig. 6.36 and their parameters are listed on the right. The ratio between the parameters  $P_1$  ( $H \parallel c$ ) and  $P_2$  ( $H \parallel c'$ ) varies between 1:5 and 1:8. Small misalignment of  $H$  with respect to the main directions ( $c$  and  $c'$ ) lead to only slight deviations. Therefore, a misalignment of  $H$  cannot cause the pronounced differences observed for  $\rho_{B,c}(H)$  above 2 K measured with different samples.

The following measurements within this subsection were performed with  $j$  along the in-plane directions  $a$  or  $c'$ . In Fig. 6.37  $\rho_{B,c'}(\phi = 45^\circ, \theta = 0 - 90^\circ) / \rho_{B,c'}(0T)$  at different temperatures and with different applied magnetic fields is presented. Note that  $\rho_{B,long,c'}$  of the samples investigated show a pronounced minimum already at temperatures above 2 K (Figs. 6.40, 6.44

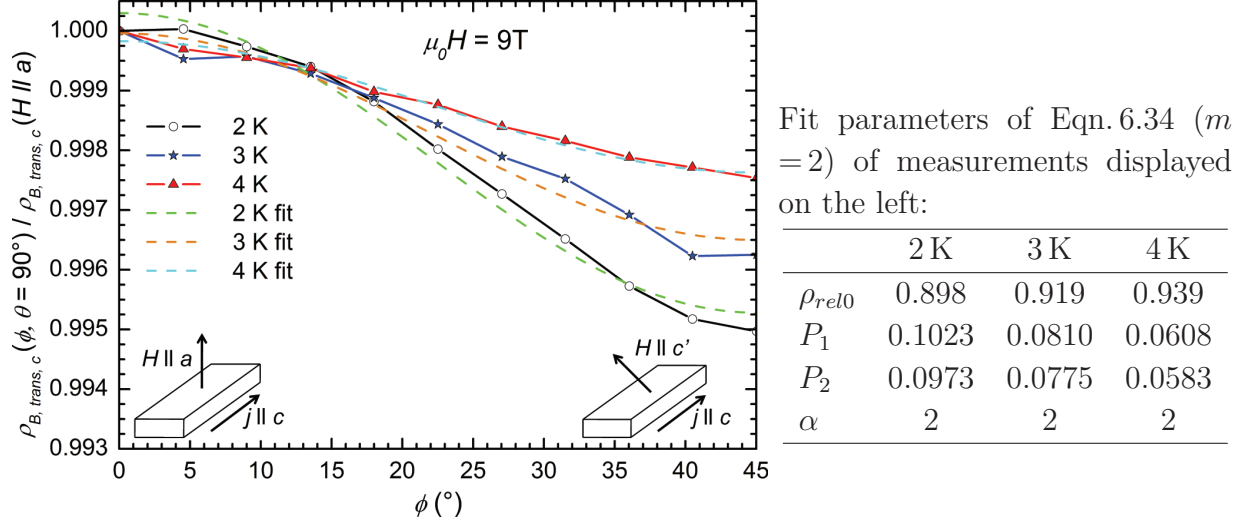
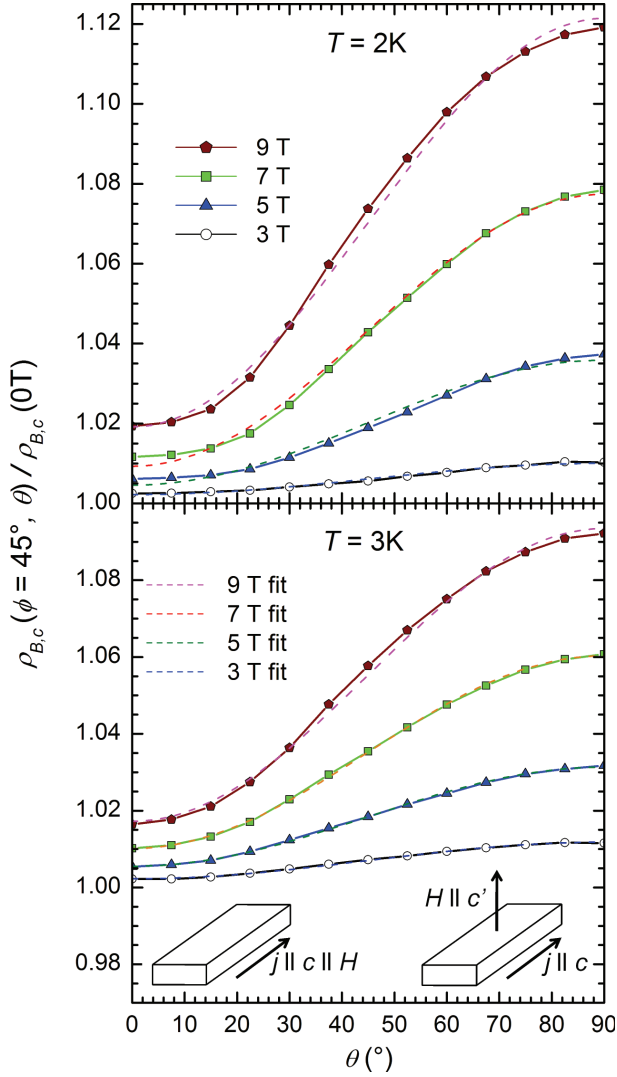


Figure 6.35: Ratios  $\rho_{B,trans,c}(\phi, \theta = 90^\circ) / \rho_{B,trans,c}(H \parallel a)$  (line + symbols) with an applied magnetic field  $\mu_0 H = 9$  T are shown in the left panel as a function of the rotation angle  $\phi$  at different temperatures. The fits (dashed lines) were calculated with Eqn. 6.34. Schematic drawings of the measurement geometry at  $\phi = 0$  and  $45^\circ$  are included as insets. The respective fit parameters  $\rho_{rel0}$ ,  $P_1$ ,  $P_2$  and  $\alpha$  are listed in the table on the right.

and 6.46). Therefore, the behaviour is expected to be more complicated in comparison to  $\rho_{B,c}$ . For  $\theta = 0^\circ$ , an increasing  $\rho_{B,trans,c'}(H \parallel c)$  with increasing  $H$  was detected between 2 and 8 K, leading to a maximal increase of about 1% at 9 T. For  $\theta = 90^\circ$ , a minimum of  $\rho_{B,long,c'}$  was measured between 4.2-6 T below 8 K (Fig. 6.44, 6.46 and 6.48). Due to the minimum shifting to lower temperatures,  $\rho_{B,c'}(\phi = 45^\circ, \theta) / \rho_{B,c'}(0T)$  shows a stronger depletion with lowering temperature. At 2 K,  $\rho_{B,c'}(\phi = 45^\circ, \theta) / \rho_{B,c'}(0T)$  is already negative for  $\theta \geq 8^\circ$ . Therefore, small misalignments of  $H$  with respect to the  $c$  direction would yield remarkable differences for  $\rho_{B,trans,c'}(H \parallel c)$ . Due to the evolving minimum in  $\rho_{B,long,c'}$  (Fig. 6.44), a simple approximation in the intermediate angle range with Eqn. 6.34 is not feasible. However, footprints of quadratic sinusoidal contributions at  $\theta = 0$  and  $90^\circ$  (estimated in Eqn. 6.34) can be clearly seen below 4 K (especially at 9 T).

As already mentioned in the introduction of this subsection, the transverse deflection contribution to  $\rho_B$  is of great interest. Therefore,  $\rho_{B,c'}(\phi = 45 - 135^\circ, \theta = 90^\circ)$  measurements were performed. Since  $H$  was rotated from  $\phi = 45 - 135^\circ$  ( $\theta = 90^\circ$ ) and  $j$  was applied along  $c'$  ( $\phi = 45$ ) the difference between these angles  $\Delta\phi$  was used for the discussion of these measurements. The results are shown in Fig. 6.38. The difference between  $\rho_{B,long,c'}(\Delta\phi = 0^\circ)$  and  $\rho_{B,trans,c'}(H \parallel c')(\Delta\phi = 90^\circ)$  reaches at maximum 2% (possible Hall contributions  $\leq \pm 0.2\%$ ). These findings imply that the direction of  $H$  is most important for the behaviour of  $\rho_{B,c'}$ . Furthermore, these results suggested that  $\rho_B$  is affected by changes of the DOS at the Fermi energy that depend on the magnetic field strength and its direction. The transverse deflection contributions are



Fit parameters of Eqn. 6.34 ( $m = 1$ ) of measurements displayed on the left at 2 K:

	3 T	5 T	7 T	9 T
$\rho_{rel0}$	1	1	1	1
$P_1$	0.00220	0.00457	0.00929	0.01915
$P_2$	0.01004	0.03584	0.07740	0.12141
$\alpha$	2	2	2	2

Fit parameters of Eqn. 6.34 ( $m = 1$ ) of measurements displayed on the left at 3 K:

	3 T	5 T	7 T	9 T
$\rho_{rel0}$	1	1	1	1
$P_1$	0.00226	0.00553	0.01015	0.01722
$P_2$	0.01179	0.03133	0.06032	0.09345
$\alpha$	2	2	2	2

Figure 6.36: The left panel shows the relative magnetoresistance  $\rho_{B,c}(\phi = 45^\circ, \theta) / \rho_{B,c}(0T)$  (line + symbols) with differing applied magnetic fields  $\mu_0 H$  as a function of the rotation angle  $\theta$  at 2 K (top) and 3 K (bottom). Fits according to Eqn. 6.34 are included as dashed lines. Schematic drawings of the measurement geometry at  $\theta = 0$  and  $90^\circ$  are shown as insets.  $H$  is rotated from the longitudinal orientation (along  $c$ ) to the perpendicular orientation (along the  $c'$ ). The fit parameters  $\rho_{rel0}$ ,  $P_1$ ,  $P_2$  and  $\alpha$  are listed in tables on the right.

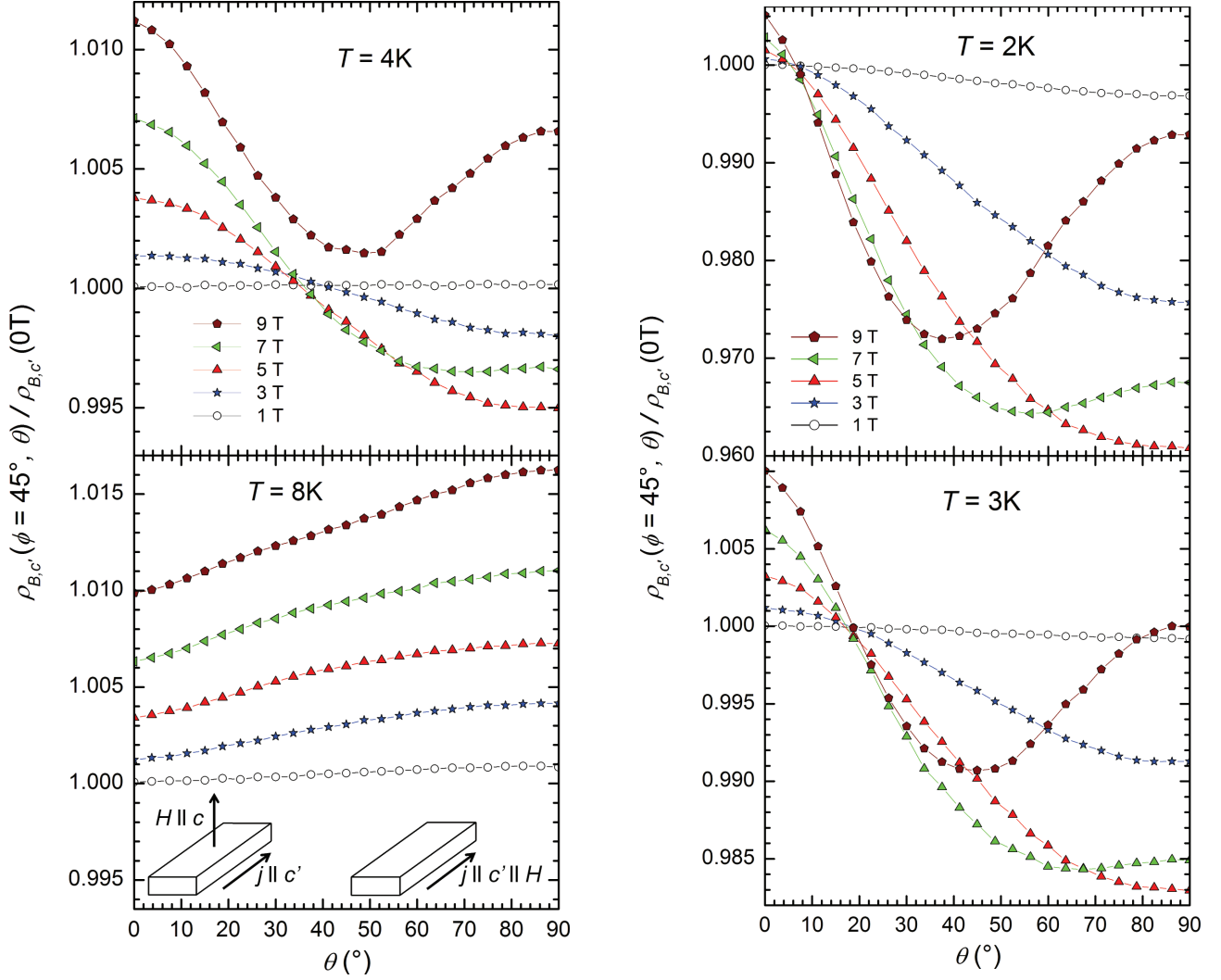


Figure 6.37: The left panel shows the relative magnetoresistance  $\rho_{B,c'}(\phi = 45^\circ, \theta) / \rho_{B,c'}(0T)$  for different applied magnetic fields  $\mu_0 H$  as a function of the rotation angle  $\theta$  at 4 K (top) and 8 K (bottom). Schematic drawings of the measurement geometry at  $\theta = 0$  and  $90^\circ$  are shown as insets. The right panel shows  $\rho_{B,c'}(\phi = 45^\circ, \theta) / \rho_{B,c'}(0T)$  at 2 (top) and 3 K (bottom).

negligible. Another indication of transverse deflection being negligible is found in  $\rho_{B,c'}(\phi = 45-135^\circ, \theta = 90^\circ)$  at 2 K with  $\mu_0 H = 9$  T. Its relative value is described by Eqn. 6.34 with the fit parameters  $\rho_{rel0} = 0.87$ ,  $P_1 = P_2 = 0.12341$  and  $\alpha = 1.82$  (Fig. 6.38, right panel, top, dashed line).

Finally, Fig. 6.39 shows  $\rho_{B,a}(\phi = 0^\circ, \theta = 0-90^\circ) / \rho_{B,a}(0T)$ . As expected, similar behaviour as determined for  $\rho_{B,c'}(\phi = 0^\circ, \theta = 0-90^\circ) / \rho_{B,c'}(0T)$  was found (Fig. 6.37). Due to the noticeable influences of extrinsic effects on the evolution of the minimum in  $\rho_{B,long,a}$  (Fig. 6.41), a reliable discussion of the slight differences between  $\rho_{B,a}(\phi = 0^\circ, \theta)$  and  $\rho_{B,c'}(\phi = 0^\circ, \theta)$  cannot be made. Nevertheless, the same conclusions as for  $\rho_{B,c'}(\phi = 0^\circ, \theta = 0-90^\circ) / \rho_{B,c'}(0T)$  can be made, namely detectable footprints of quadratic sinusoidal contributions at  $\theta = 0$  and  $90^\circ$  (especially at  $\theta = 90^\circ$  and  $\mu_0 H \geq 7$  T) and an additional directional dependent negative contribution.

In conclusion,  $\rho_B$  measurements with rotating magnetic field show similar behaviour for  $\rho_{B,a}$  and  $\rho_{B,c'}$  but very different behaviour for  $\rho_{B,c}$ .  $\rho_{B,c}$  can be described with an empirical equation (Eqn. 6.34). The increase of  $\rho_{B,c}(H)$  with increasing  $H$  is enhanced for  $H \parallel c'$  compared to  $H \parallel c$  (Fig. 6.36).  $\rho_{B,trans,c}$  is almost independent of the direction of  $H$  (Fig. 6.35). At the lowest temperatures,  $\rho_{B,long,a}(H)$ ,  $\rho_{B,trans,a}(H)(H \parallel a)$ ,  $\rho_{B,long,c'}(H)$  and  $\rho_{B,trans,c'}(H)(H \parallel c')$  exhibit a minimum (Figs. 6.37 and 6.39). The most surprising finding within these investigations is the similar behaviour of  $\rho_{B,long,c'}$  and  $\rho_{B,trans,c'}(H \parallel c')$  (Fig. 6.38). This result suggests a negligible deflection contribution to  $\rho_{B,c'}(\phi)$  and a dominant contribution of the  $H$ -direction dependent variation of the charge carrier concentration ( $H$ -direction dependent change of the DOS at the Fermi energy).



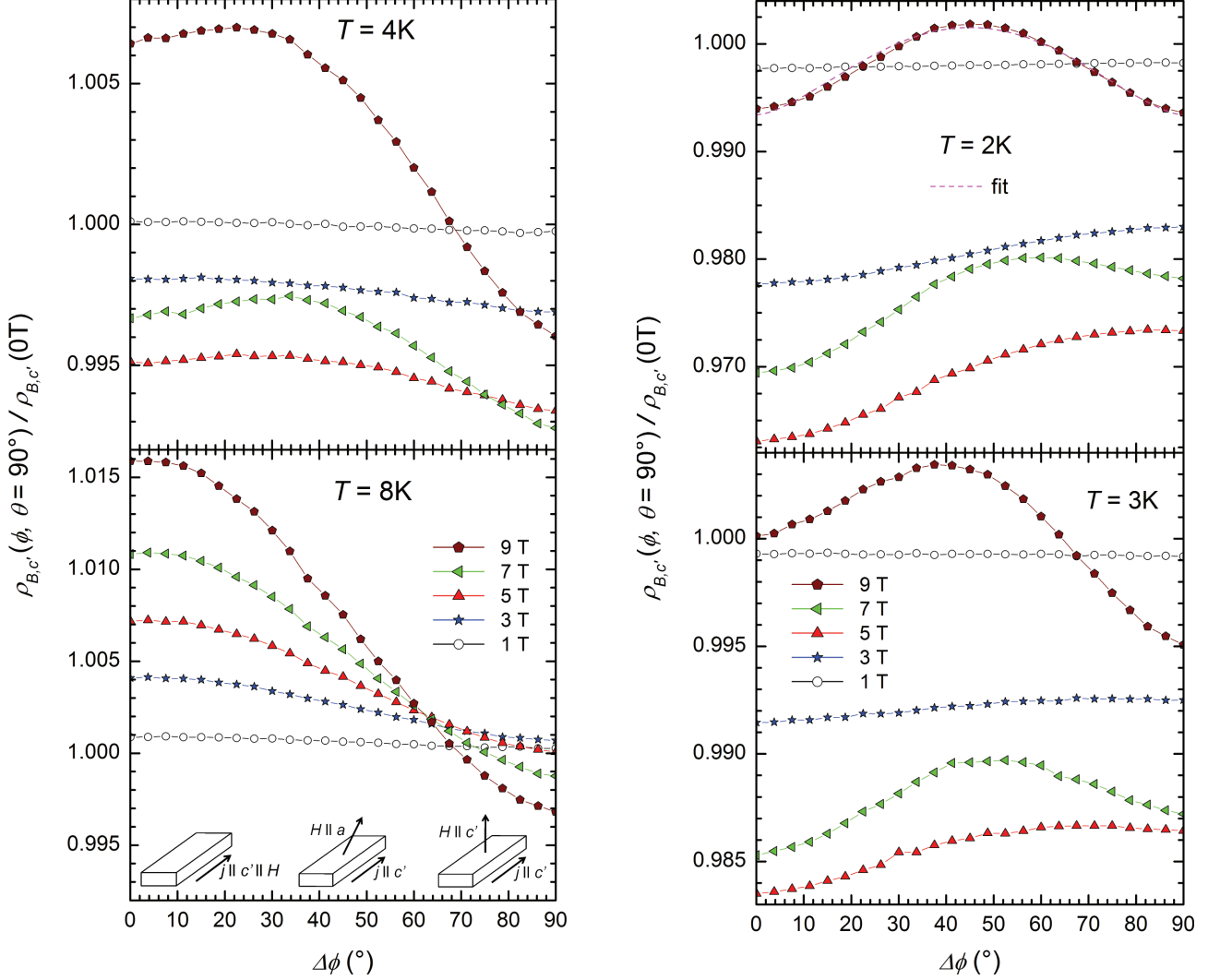


Figure 6.38: Relative magnetoresistance  $\rho_{B,c'}(\phi, \theta = 90^\circ) / \rho_{B,c'}(\mu_0 H = 0 \text{ T})$  for different applied magnetic fields  $\mu_0 H$  as a function of the rotation angle  $\Delta\phi$  at 2, 3, 4 and 8 K.  $\Delta\phi$  is the angle between the electrical current  $j$  and the  $H$  direction. Schematic drawings of the measurement geometry at  $\Delta\phi = 0, 45$  and  $90^\circ$  are shown as insets. Additionally, a fit according to Eqn. 6.34 with  $\rho_{rel0} = 0.87$ ,  $P_1 = P_2 = 0.12341$  and  $\alpha = 1.82$  at 2 K and 9 T is included as dashed magenta line.



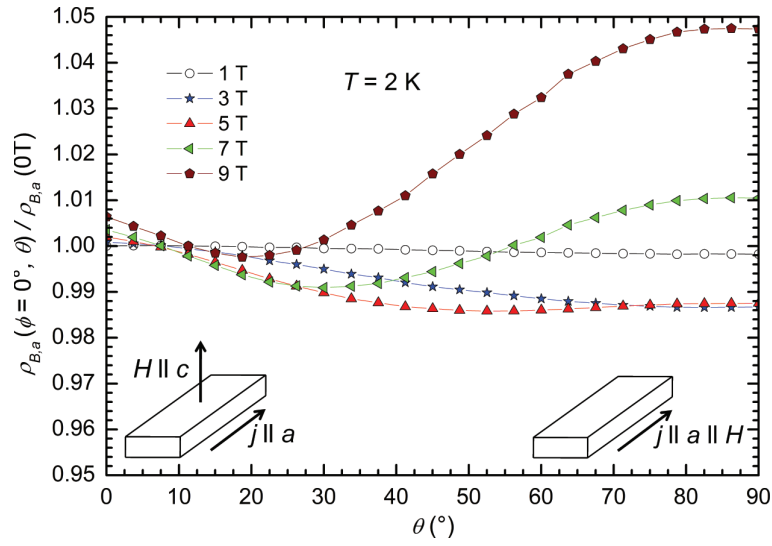


Figure 6.39: Relative magnetoresistance  $\rho_{B,a}(\phi = 0^\circ, \theta) / \rho_{B,a}(0T)$  for different applied magnetic fields  $\mu_0 H$  as a function of the rotation angle  $\theta$  at 2 K. Schematic drawings of the measurement geometry at  $\theta = 0$  and  $90^\circ$  are shown as insets. As expected, similar behaviour as measured for  $\rho_{B,c'}(\phi = 0^\circ, \theta)$  was found (Fig. 6.37).

**Comparison of magnetoresistance measurements for CeRu<sub>4</sub>Sn<sub>6</sub> samples separated from different batches**

Magnetoresistance measurements were performed with CeRu<sub>4</sub>Sn<sub>6</sub> samples separated from the batches B, G2, G3 and G7. Sample dependent differences in physical properties were most pronounced in  $\rho_B(H)$  measurements. In this subsection, these discrepancies are discussed with  $\rho_{B,long,c'}(H)$  measurements at first. Afterwards,  $\rho_{B,trans,a}(H)(H||a)$  measurements are presented for several CeRu<sub>4</sub>Sn<sub>6</sub> samples.

The discrepancies of  $\rho(T)$  for CeRu<sub>4</sub>Sn<sub>6</sub> samples from batch G2 and B are discussed in Sect. 6.2 and are shown in Fig. 6.26.  $\rho_{B,long,c'}(H)$  of the samples B.3.3, B.3.1 (measured by F. Weickert and J. Larrea in high magnetic fields) and G2\_B\_2||c' are displayed in Fig. 6.40.  $\rho_{B,long,c'}(H)$  for G2\_B\_2||c' (Fig. 6.40, top) exhibits a minimum below 4 K. This minimum gets more pronounced with decreasing temperature. At  $H \geq 9$  T and  $T \leq 1.5$  K the increase of  $\rho_{B,long,c'}(H)$  becomes linear. The absolute values are slightly shifted for different temperatures in the linear range. By contrast, the CeRu<sub>4</sub>Sn<sub>6</sub> samples separated from batch B exhibit the first footprints of a minimum at about 2 K. At 0.1 K, a remarkable minimum in  $\rho_{B,long,c'}(H)$  exists in accordance to the G2 sample. Another similarity to the G2 sample is the almost linear increase at higher  $H$  (above 9 T) and the almost perfect overlap of these linear ranges at the lowest temperatures (for B samples below 2.4 K). The slope of this linear increase is sizable larger ( $\approx 2$  times) for samples separated from batch B than for sample of batch G2.

Nevertheless, a general sample/batch-independent behaviour for  $\rho_{B,long,c'}(H)$  was found. Starting at  $\mu_0 H = 0$ , a minimum in  $\rho_{B,long,c'}(H)$  evolves at low temperatures (below 2-4 K) around 3-6 T followed by an almost linear  $H$ -dependent but  $T$ -independent increase above about 9 T and below about 2 K (below 1.5 K for G2 sample, below 2.4 K for B samples).

Further investigations were performed by measuring  $\rho_{B,trans,a}(H)(H||a)$ . Figure 6.41 shows this quantity for CeRu<sub>4</sub>Sn<sub>6</sub> samples separated from the batches B, G2, G3 and G7 at 2 K as a function of  $H$  (left panel) and of  $H^2$  (right panel).  $\rho_{B,trans,a}(H)(H||a)$  at 2 K exhibits a clear minimum at about 4 T for G2\_B\_2||a. Only  $\rho_{B,trans,a}(H)(H||a)$  for G7 BO7 shows a footprint of a minimum too. The other CeRu<sub>4</sub>Sn<sub>6</sub> samples show a comparable behaviour over the entire  $H$  range, with an almost quadratic increase above 4 T (Fig. 6.41, right panel, indicated with lines). This quadratic increase of  $\rho_{B,trans,a}(H)(H||a)$  at higher  $H$  was found also in G2\_B\_2||a and G7 BO7. The G7 samples were separated from different positions of the single crystal G7, with G7 BO1 at the beginning, G7 BO7 in the middle and G7 TOP4 at the end of the grown crystal (equivalent positions to the growth procedure). Interestingly, the G7 sample separated from the intermediate position (G7 BO7) does not show intermediate behaviour. Therefore, we suggest that tiny extrinsic effects lead to sizable differences in the minimum in  $\rho_{B,trans,a}(H)(H||a)$ . No indication of stoichiometry variation of the single crystals along the growth direction could be detected (Sect. 4.2).

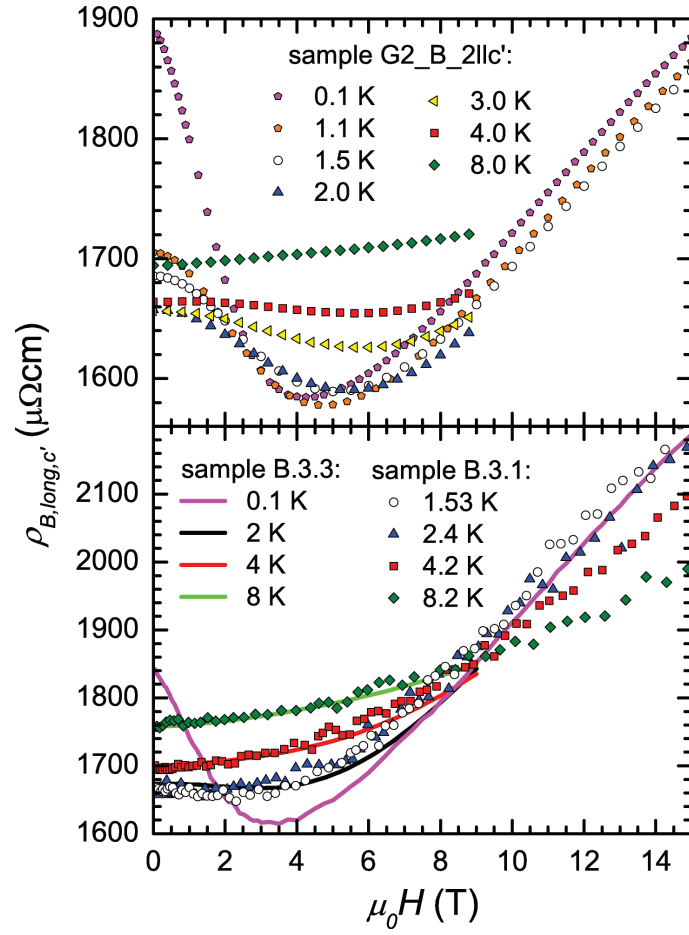


Figure 6.40: Comparison of the longitudinal magnetoresistance along the  $c'$  direction  $\rho_{B, \text{long}, c'}$  as a function of the applied magnetic field  $\mu_0 H$  at different temperatures  $T$  for samples separated from batch G2 (G2\_B\_2|| $c'$ , top) and B (B.3.3, B.3.1, bottom).

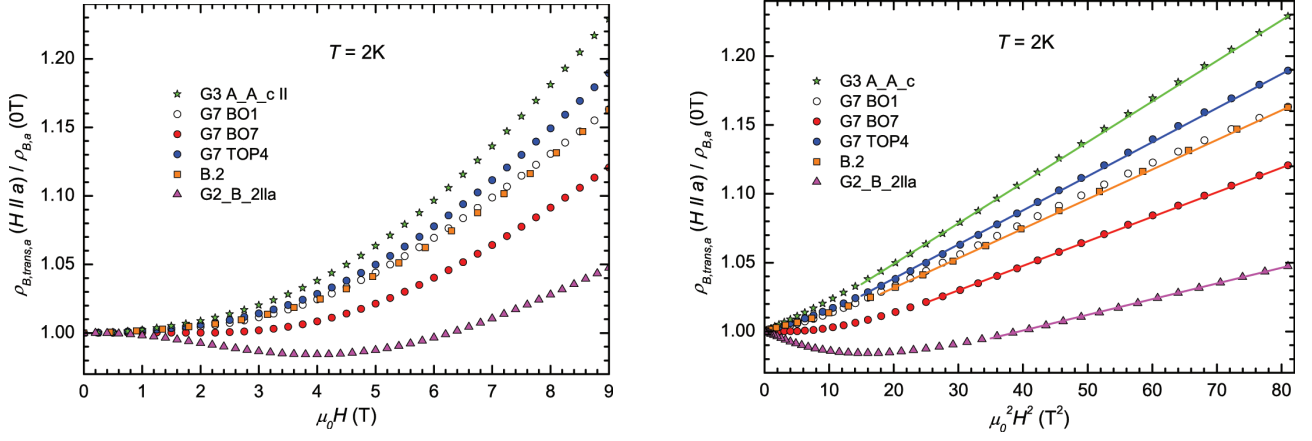


Figure 6.41: Relative transverse magnetoresistance along the  $a$  axis  $\rho_{B,trans,a}(H||a)/\rho_{B,a}(0T)$  for several  $\text{CeRu}_4\text{Sn}_6$  single crystals separated from different batches at 2 K, as function of the applied magnetic field  $\mu_0 H$  (left) and as function of  $(\mu_0 H)^2$  (right). The quadratic behaviour of  $\rho_{B,trans,a}(H||a)/\rho_{B,a}(0T)$  at high fields is indicated by linear fits.

In conclusion, for the same configuration, similar overall behaviour of  $\rho_B(H)$  was measured for all investigated samples, indicating that the behaviour is dominated by intrinsic materials properties. A noticeable discrepancy is the evolution of the minimum in  $\rho_{B,long,c'}(H)$  (Fig. 6.40) and  $\rho_{B,trans,a}(H)(H||a)$  (Fig. 6.41) at higher temperatures for  $\text{CeRu}_4\text{Sn}_6$  samples separated from batch G2 compared to the other single crystals. The comparison between  $\rho_{c'}(T)$  of samples separated from the batches G2 and B at  $\mu_0 H = 0$  T revealed that the G2 sample has a larger  $\rho_{c'}(T)$  value than the B sample at the lowest temperatures (Fig. 6.26). Together with the  $\rho_a(H)$  investigations above, this indicates a partial suppression of the higher  $\rho(T)$  value of G2 samples by the applied  $H$ . Note that the discrepancy cannot be totally suppressed within the entire measurement range for  $H||c'$  (different slopes of samples from the batches G2 and B, Fig. 6.40). Theoretical results of P. Wissgott (Chap. 5) [9] together with experimental results of optical conductivity measurements (Sect. 6.6) [16] point to the development of a hybridization gap in the (001) plane but not perpendicular to it. In Kondo insulators, small amounts of defects are known to influence low-temperature properties appreciably [33, 39]. So the discrepancies found in  $\rho_{B,trans,a}(H)(H||a)$  and  $\rho_{B,long,c'}(H)$  measurements are presumably due to small sample dependent extrinsic effects, which influence the DOS at the Fermi level most noticeably along the low DOS directions  $a$  and  $c'$ .

### Longitudinal magnetoresistance

Longitudinal magnetoresistance  $\rho_{B,long}$  measurements were performed with  $\text{CeRu}_4\text{Sn}_6$  samples separated from two different batches (B and G2). Samples separated from batch B were used for  $\rho_{B,long}$  measurements in high magnetic fields in Rossendorf/Dresden by J. Larrea and F.

Weickert. Additionally,  $\rho_{B,long}$  of another sample separated from batch B (B.3.3) and samples separated from batch G2 were measured at lower fields in the PPMS by the author and in the dilution fridge in collaboration with K.-A. Lorenzer. The discrepancies between the batches were discussed in the subsection above.

Figure 6.42 displays the ratio  $\rho_{B,long}(H)/\rho_B(0T)$  (top) and the derivative  $\partial\rho_{B,long}(H)/\partial H$  (bottom) of the high-field measurements along the  $a$  (left) and  $c'$  (right) direction. Similar behaviour is observed for both directions. At 1.5 K, a very shallow minimum is observed at  $H_{hf,min,long,a} = 1.7$  T and  $H_{hf,min,long,c'} = 2.3$  T (Fig. 6.42, Tab. 6.10), followed by a strong resistivity increase towards higher  $H$ . These increases end at a maximum in  $\rho_{B,long,c'}(H)$  and  $\rho_{B,long,a}(H)$  at  $H_{hf,max,long,c'} = 25.4$  T and  $H_{hf,max,long,a} = 20.0$  T.  $H_{hf,max,long,c'}$  for  $T \leq 4.2$  K and  $H_{hf,max,long,a}$  increase only slightly with increasing temperature (Tab. 6.10, Fig. 6.42). The resistivity decreases steadily with further increasing  $H$  above these maxima. In general,  $\rho_{B,long,c'}(H)$  shows a stronger field response at all temperatures than  $\rho_{B,long,a}(H)$ .

$\rho_{B,long,c}(H)$  shows distinctly different behaviour than  $\rho_{B,long}(H)$  along the in-plane directions (Fig. 6.43). Here, neither minima nor maxima are found up to 55 T. The zero of the derivative  $\partial\rho_{B,long,c}(H)/\partial H$  tentatively indicates a maximum  $H_{hf,max,long,c} \approx 57$  T (60 T) at  $T = 1.68$  K (3.32 K), that appears to increase with increasing temperature.

Detailed low-temperature investigations of  $\rho_{B,long}(H)$  were carried out with the PPMS device (dilution refrigerator set-up) for CeRu<sub>4</sub>Sn<sub>6</sub> samples separated from batch G2 in the  $H$  range from 0 to 9 T (15 T) (Figs. 6.44 and 6.45). Unfortunately, samples separated from batch G2 show a higher  $\rho(T)$  value at the lowest temperatures and a minimum in  $\rho_B(H)$  at the highest temperatures in comparison to all other samples. Therefore, the decrease in  $\rho_B(H)$  (batch G2) at the lowest magnetic field is probably partially produced by extrinsic effects. Note that this minimum exists also in CeRu<sub>4</sub>Sn<sub>6</sub> samples separated from batch B indicating that the minimum in  $\rho_B(H)$  at the lowest temperatures is an intrinsic effect. Figure 6.44 (Fig. 6.45) shows  $\rho_{B,long}(H)$  (the derivatives  $\partial\rho_{B,long}(H)/\partial H$ ) for the directions  $a$ ,  $c$  and  $c'$ . As expected, anisotropic behaviour of  $\rho_{B,long}(H)$  between the in-plane directions ( $a$  and  $c'$ ) and the perpendicular  $c$  axis is revealed.

The longitudinal resistivities all exhibit a minimum at lowest temperatures (Fig. 6.48). Interestingly, the positions of the minima  $H_{min,long,a}(T)$  and  $H_{min,long,c'}(T)$  are almost temperature independent below 0.5 K, which is seen as temperature-independent zero crossing in the respective  $\partial\rho_{B,long}(H)/\partial H$  (Fig. 6.45). These minima are pinned to  $H_{min,long,a,(T \leq 0.5 \text{ K})} \approx 4.1$  T and  $H_{min,long,c',(T \leq 0.5 \text{ K})} \approx 4.2$  T (Fig. 6.48).

The slopes of  $\rho_{B,long,a}(H)$  ( $\rho_{B,long,c'}(H)$ ) are identical at  $\mu_0 H \geq 3.5$  T and  $T \leq 0.5$  K (only shifted to higher absolute values with increasing  $T$ ) (Fig. 6.45). This is also found for  $\rho_{B,long,c}(H)$  at  $\mu_0 H \geq 9.5$  T and at  $T \leq 2$  K (no measurements performed with  $\mu_0 H \geq 9$  T above 2 K) (Fig. 6.45, bottom). The difference of the  $\rho_{B,long}(H)$  values is less than 2 % in this  $T$  and  $H$  ranges.

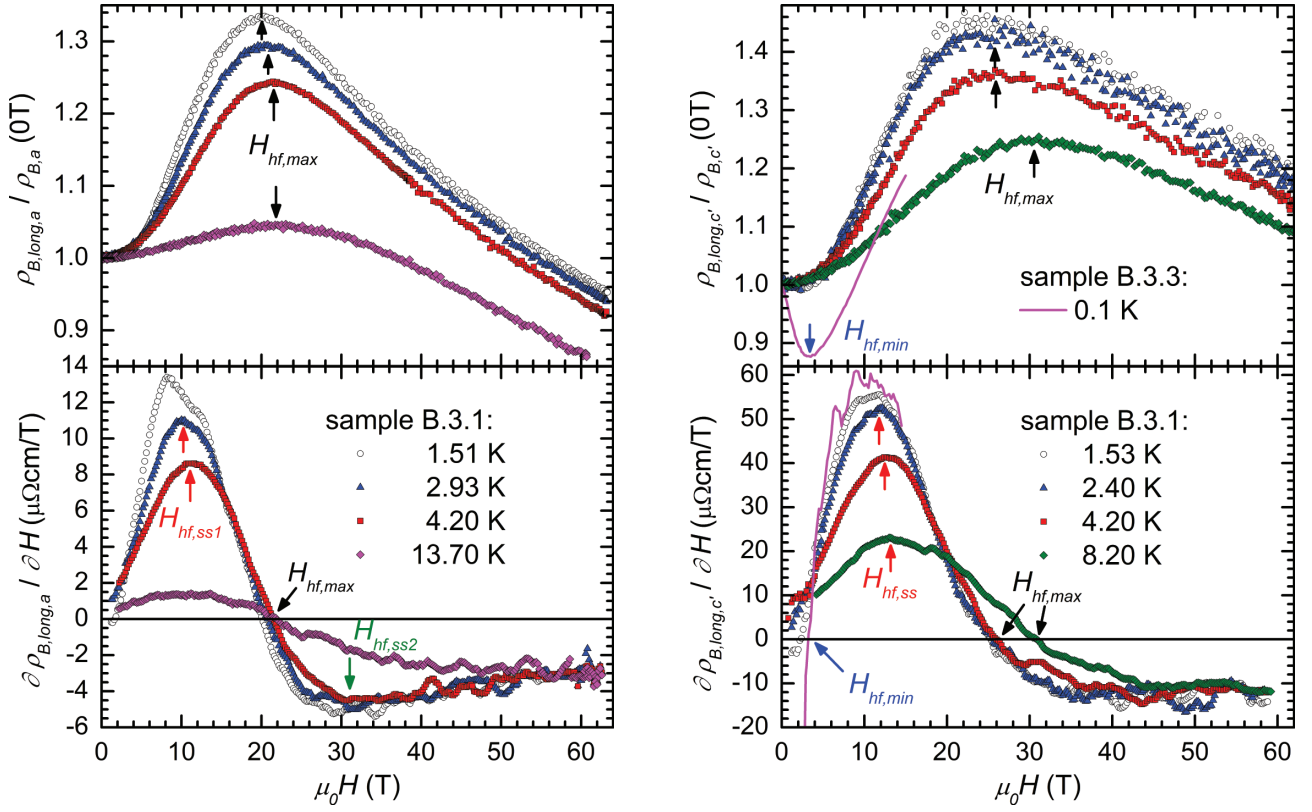


Figure 6.42: The left (right) panel displays the relative longitudinal magnetoresistance along the  $a$  direction  $\rho_{B, \text{long}, a} / \rho_{B, a}(0\text{T})$  ( $c'$  direction  $\rho_{B, \text{long}, c'} / \rho_{B, c'}(0\text{T})$ ) on top and the respective derivative  $\partial \rho_{B, \text{long}, a} / \partial H$  ( $\partial \rho_{B, \text{long}, c'} / \partial H$ ) at the bottom as a function of the applied magnetic field  $\mu_0 H$ . These measurements were performed by J. Larrea and F. Weickert with samples (batch B) prepared within this work. Similar behaviour along both directions was achieved. A stronger magnetic field response was seen in  $\rho_{B, \text{long}, c'}(H)$  compared to  $\rho_{B, \text{long}, a}(H)$ . The extrema are indicated with arrows and listed in Tab. 6.10.

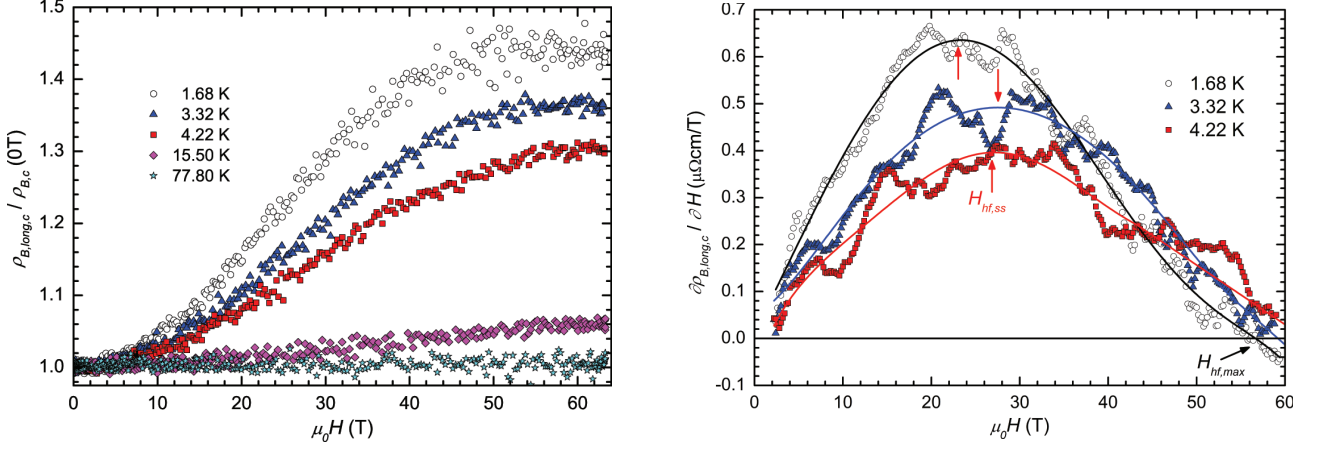


Figure 6.43: The left (right) panel displays the relative (derivative of the) longitudinal magnetoresistance along the  $c$  direction  $\rho_{B,long,c}/\rho_{B,c}(0T)$  ( $\partial\rho_{B,long,c}/\partial H$ ) as a function of the applied magnetic field  $\mu_0 H$ . These measurements were performed by J. Larrea and F. Weickert with  $\text{CeRu}_4\text{Sn}_6$  samples (batch B) prepared within this thesis. The extrema are indicated with arrows and listed in Tab. 6.10.

Table 6.10: Extrema of  $\rho_{B,long}(H)$  measurements in high magnetic fields at different temperatures in Rossendorf/Dresden. These measurements were performed by J. Larrea and F. Weickert with  $\text{CeRu}_4\text{Sn}_6$  samples (batch B) prepared within this thesis.  $\rho_{B,long,c'}(H)$  at 0.1 K was measured by the author in collaboration with K.-A. Lorenzer. Used abbreviations:  $H_{hf,max}$  = maximum in  $\rho_{B,long}(H)$ ,  $H_{hf,min}$  = minimum in  $\rho_{B,long}(H)$ ,  $H_{hf,ss}$  ( $H_{hf,ss1}$ ) = steepest positive slope in  $\rho_{B,long}(H)$ ,  $H_{hf,ss2}$  = steepest negative slope in  $\rho_{B,long}(H)$ .

extrema	$\rho_{B, long, a}(H)$				
	1.51 K	2.93 K	4.20 K	13.7 K	
$H_{hf, min}$ (T)	1.7	-	-	-	
$H_{hf, max}$ (T)	20.0	20.8	21.5	22.0	
$H_{hf, ss1}$ (T)	10	10.4	11	-	
$H_{hf, ss2}$ (T)	31.0	31.5	32.0	-	
	$\rho_{B, long, c'}(H)$				
	0.1 K	1.53 K	2.40 K	4.20 K	8.20 K
$H_{hf, min}$ (T)	3.0	2.3	-	-	-
$H_{hf, max}$ (T)	-	25.4	25.5	25.7	30.9
$H_{hf, ss}$ (T)	10.5	11.5	12.0	12.5	13.0
	$\rho_{B, long, c}(H)$				
	1.68 K	3.32 K	4.22 K		
$H_{hf, max}$ (T)	57	60	-		
$H_{hf, ss}$ (T)	23.2	27.5	27.2		



$\rho_{B,long,a}(H)$  and  $\rho_{B,long,c'}(H)$  show similar characteristics with increasing  $H$  till the respective  $H_{min,long}$  are reached (Fig. 6.44). At higher  $H$ , different characteristics are observable.  $\rho_{B,long,c'}(H)$  shows an almost linear behaviour with a very shallow decrease of the slope starting at the inflection point  $H_{ss,long,c'} = 11$  T. In  $\rho_{B,long,a}(H)$ , a reliable reduction of the increasing slope can be observed (starting at  $H_{ss,long,a} = 8.5$  T). In addition,  $\rho_{B,long,a}(H)$  measurements indicate a maximum in  $\rho_{B,long,a}(H)$  slightly above the achievable maximum field strength (15 T) within these measurements (Fig. 6.45). These findings are in accordance to the high field measurements, which revealed a higher lying maximum in  $\rho_{B,long,c'}(H)$  than in  $\rho_{B,long,a}(H)$  (Fig. 6.42).

### Transverse magnetoresistance

Additionally to  $\rho_{B,long}(H)$  investigations,  $\rho_{B,trans}(H)$  measurements were performed with the same CeRu<sub>4</sub>Sn<sub>6</sub> samples. An additional contribution to  $\rho_B(H)$  may differ between the longitudinal and the transverse geometry: The deflection of charge carriers due to the transverse geometry yields an additional contribution to  $\rho_B(H)$  due to the Lorentz force. Note that the difference between the longitudinal and transverse geometry above 2 K was investigated before (Fig. 6.38). Surprisingly, these investigations revealed that the difference between the longitudinal and transverse geometry above 2 K was negligible for  $\rho_{B,c'}(H)$ .

$\rho_{B,trans,a}(H||c)$  (top),  $\rho_{B,trans,c'}(H||c')$  (middle) and  $\rho_{B,trans,c}(H||c)$  (bottom) are shown in Fig. 6.46. Their derivatives are shown in the same order in Fig. 6.47. As expected,  $\rho_{B,trans,a}(H||c)$  and  $\rho_{B,trans,c'}(H||c)$  behave similarly, but distinctly different from  $\rho_{B,trans,c}(H||c')$ .

At lowest temperatures ( $T \leq 1.5$  K), minima evolve in  $\rho_{B,trans}$  (Fig. 6.48). An almost quadratic increase in  $\rho_{B,trans,a}(H||c)$  and  $\rho_{B,trans,c'}(H||c)$  was found for  $\mu_0 H \geq 11$  T and  $T \leq 2$  K. This quadratic increase is clearly seen in the linear increase of  $\partial\rho_{B,trans}/\partial H$  for  $\rho_{B,trans}$  along the  $a$  and  $c'$  axis (Fig. 6.47). The absolute decreases of  $\rho_{B,trans,a}(H||c)$  and  $\rho_{B,trans,c'}(H||c)$  are comparable. Also their minima are only slightly shifted (Fig. 6.48). Interestingly, the quadratic increase at  $H \geq 11$  T is comparable with the one found for  $\rho_{B,long,c}(H)$  (Fig. 6.50). This finding suggests a strong dependence of  $\rho_B(H)$  on the magnetic field direction and small dependences on the longitudinal or transverse orientation and on the electrical current direction. This  $H$ -dependence of  $\rho_B(H)$  is discussed in detail in the following subsection.

$\rho_{B,trans,c}(H||c')$  shows comparable behaviour to the one found for  $\rho_{B,long,a}$  and  $\rho_{B,long,c'}$  (Figs. 6.44 and 6.45, 6.46, 6.47, 6.49 and 6.50).  $\rho_{B,trans,c}(H||c')$  shows a decrease at lowest  $H$  and  $T$  ending in a minimum  $H_{min,trans,c}(H||c') \approx 2.8$  T at  $T \leq 0.5$  K. The following increase with increasing  $H$  is almost  $T$ -independent for  $H \geq 7$  T and  $T \leq 2$  K and ends in a maximum  $H_{min,trans,c}(H||c') \approx 14.5$  T. Also  $\rho_{B,trans,c}(H||c')$  measurements revealed that the direction of  $H$  determines dominantly the behaviour of  $\rho_B(H)$  in accordance with the findings above.



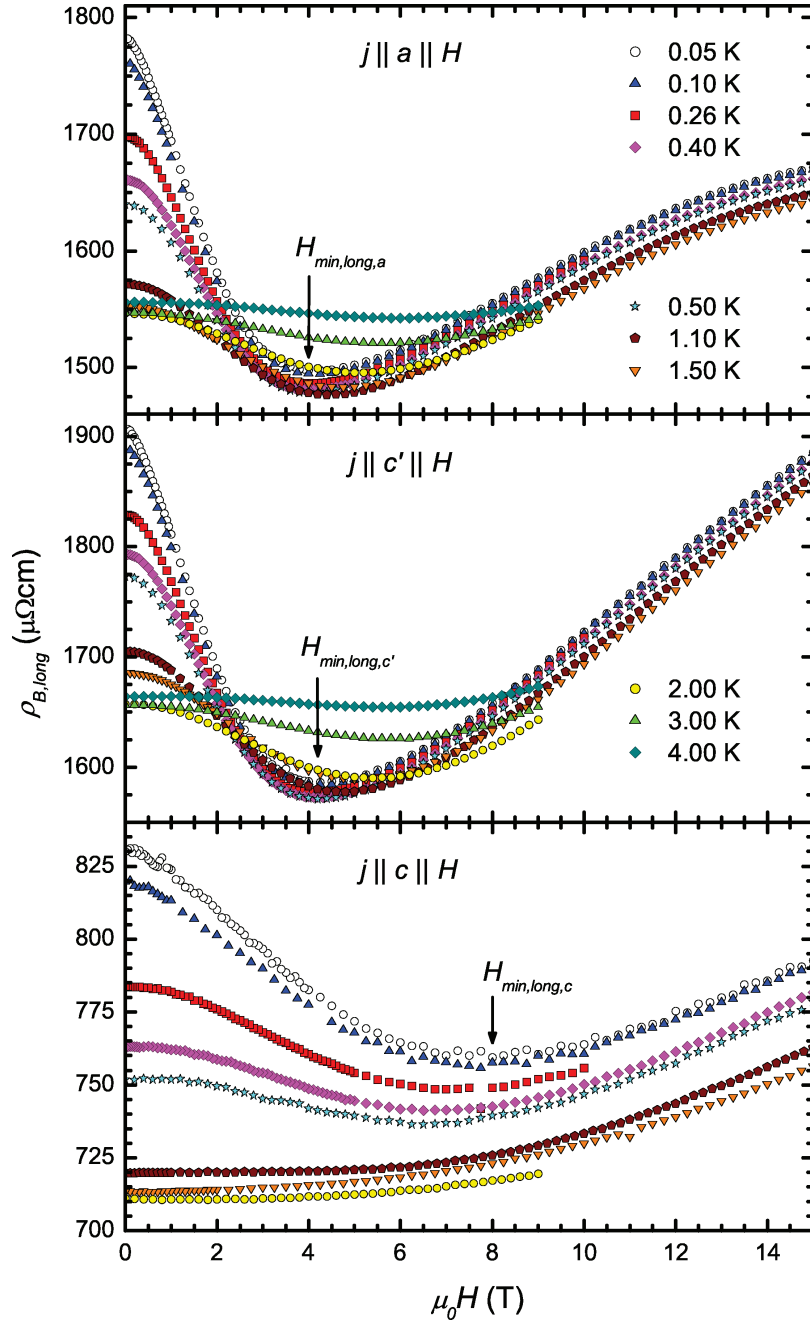


Figure 6.44: Longitudinal magnetoresistance  $\rho_{B,long}(H)$  along the three investigated main directions  $a$ ,  $c$  and  $c'$  as a function of the magnetic field  $\mu_0 H$  (samples batch G2). These measurements were performed in collaboration with K.-A. Lorenzer. The minima  $H_{min,long}$  in  $\rho_{B,long}(H)$  at the lowest temperatures are indicated with arrows.

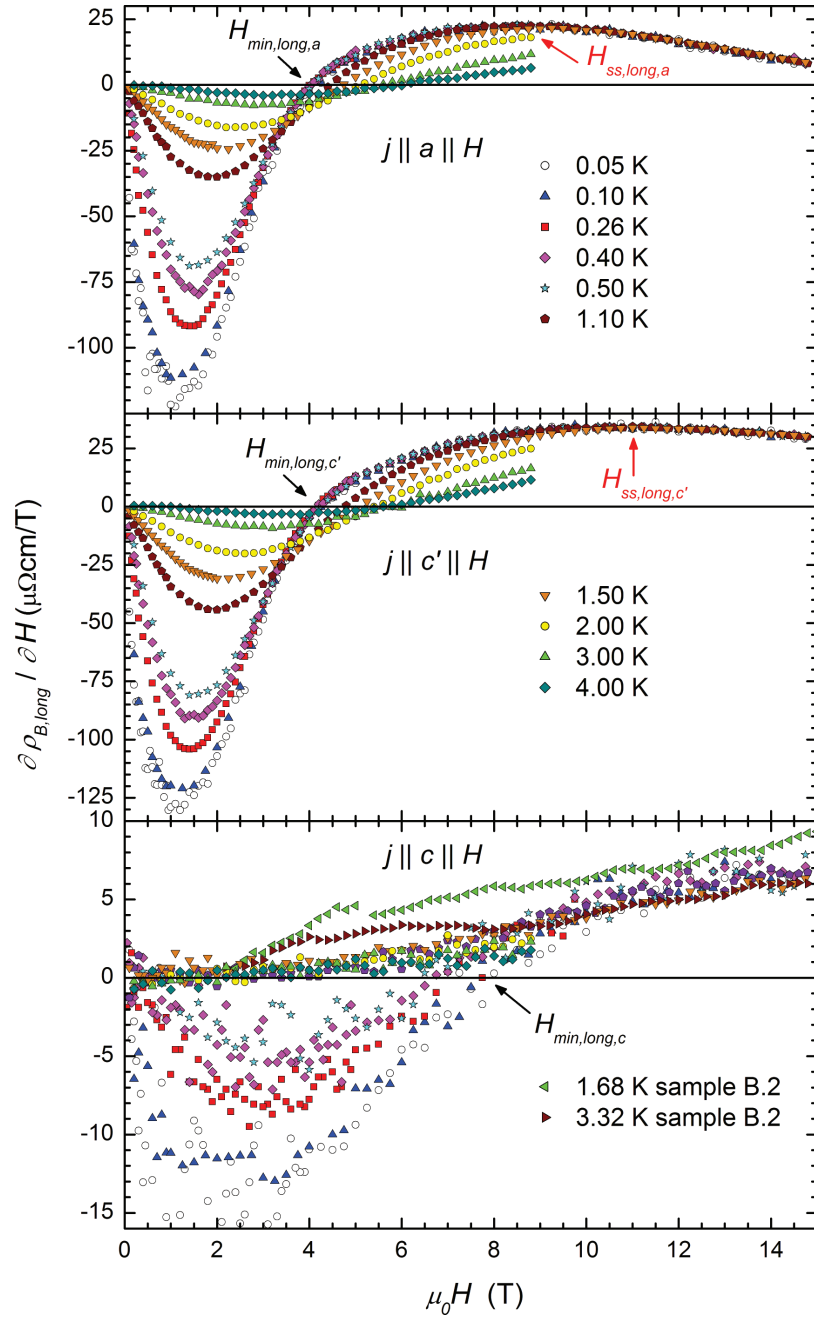


Figure 6.45: Derivative of the longitudinal magnetoresistance  $\partial \rho_{B,long}(H)/\partial H$  along the three investigated main directions  $a$ ,  $c$  and  $c'$  as a function of the magnetic field  $\mu_0 H$  (samples batch G2). These measurements were performed in collaboration with K.-A. Lorenzer. The extrema  $H_{min,long}$  and  $H_{ss,long}$  in  $\rho_{B,long}(H)$  are indicated with arrows.

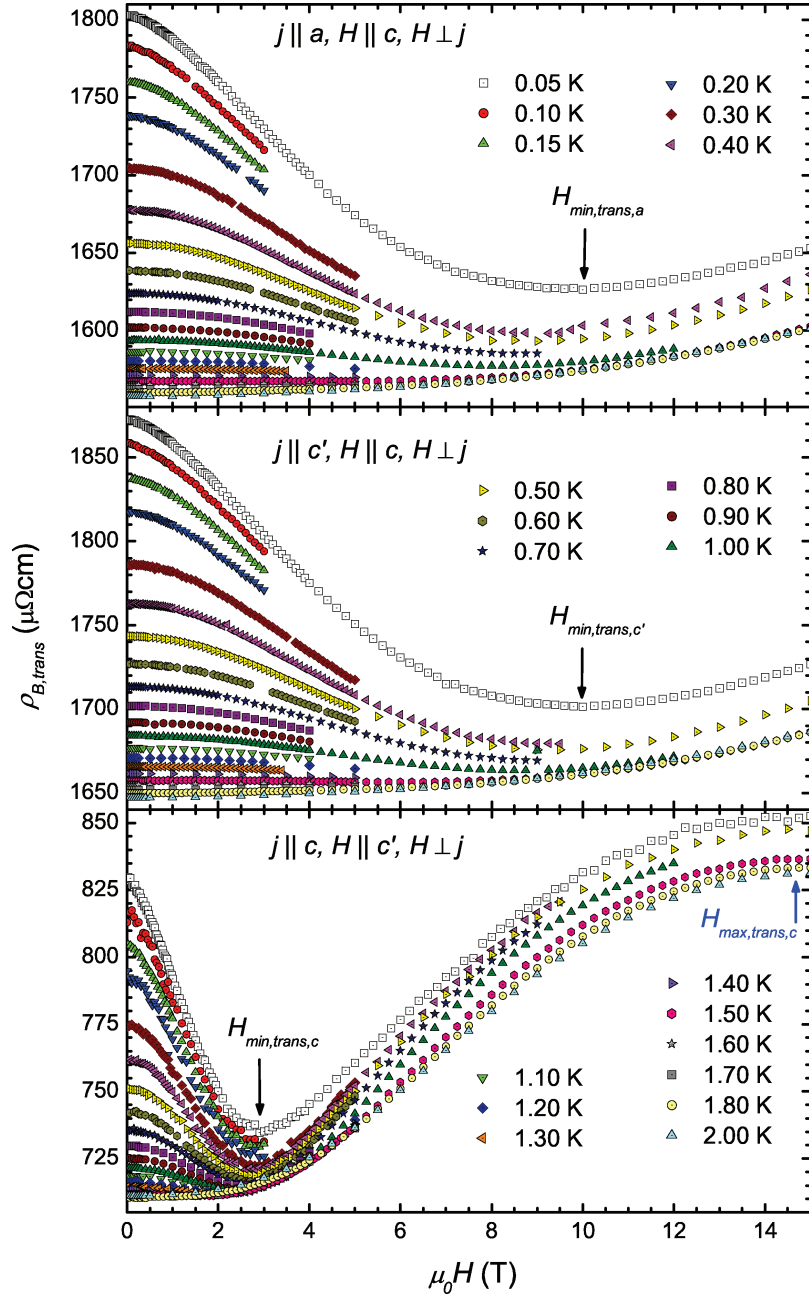


Figure 6.46: Transverse magnetoresistance  $\rho_{B,trans}$  along the three investigated main directions  $a$ ,  $c$  and  $c'$  as a function of the magnetic field  $H$  (samples batch G2). These measurements were performed in collaboration with K.-A. Lorenzer. The minima  $H_{min,trans}$  and maximum  $H_{max,trans,c}$  at the lowest temperatures are indicated with arrows.

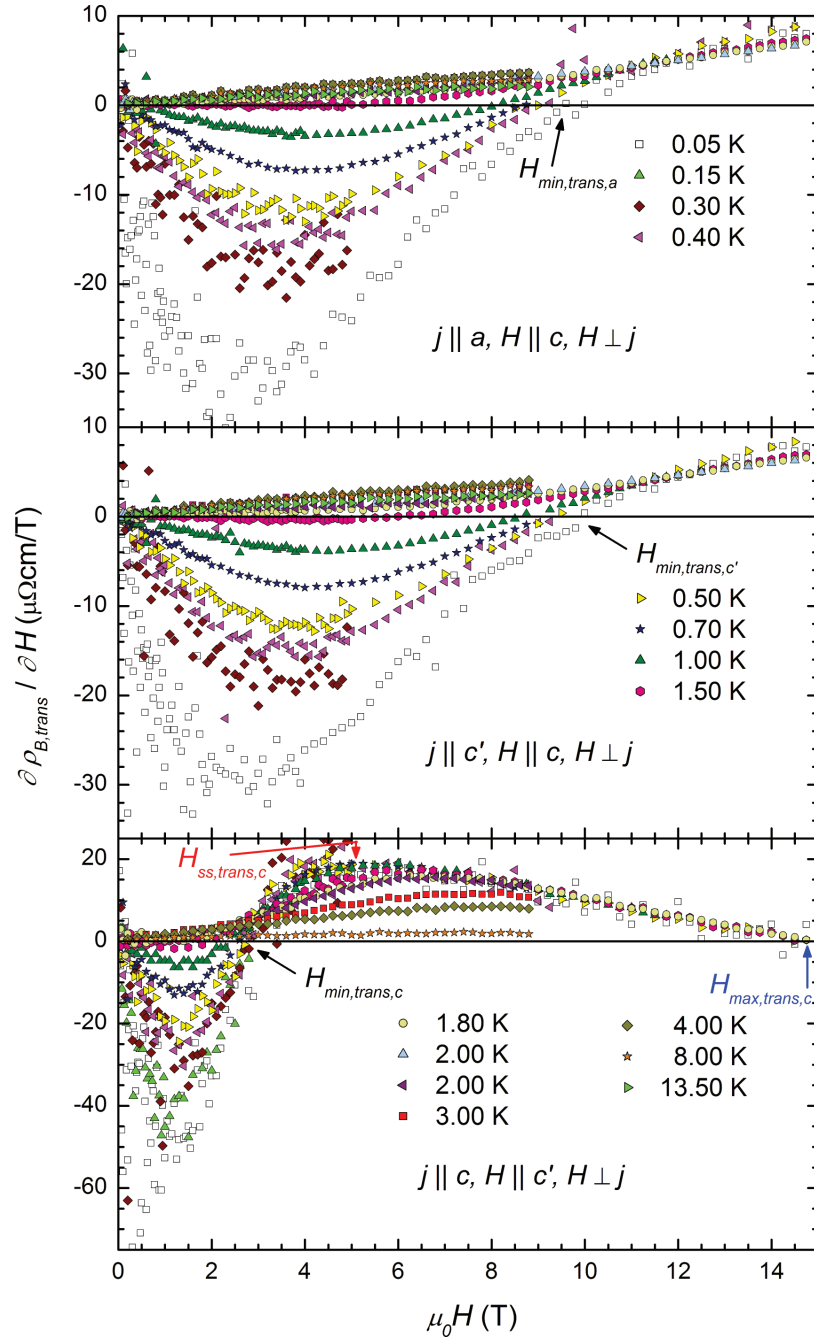


Figure 6.47: Derivative of the transverse magnetoresistance  $\partial \rho_{B,trans} / \partial H$  along the three investigated main directions  $a$ ,  $c$  and  $c'$  as a function of the magnetic field  $\mu_0 H$  (samples batch G2). These measurements were performed in collaboration with K.-A. Lorenzer. The extrema  $H_{min,trans}$ ,  $H_{ss,trans,c}$  and  $H_{max,trans,c}$  in  $\rho_{B,trans}(H)$  are indicated with arrows.

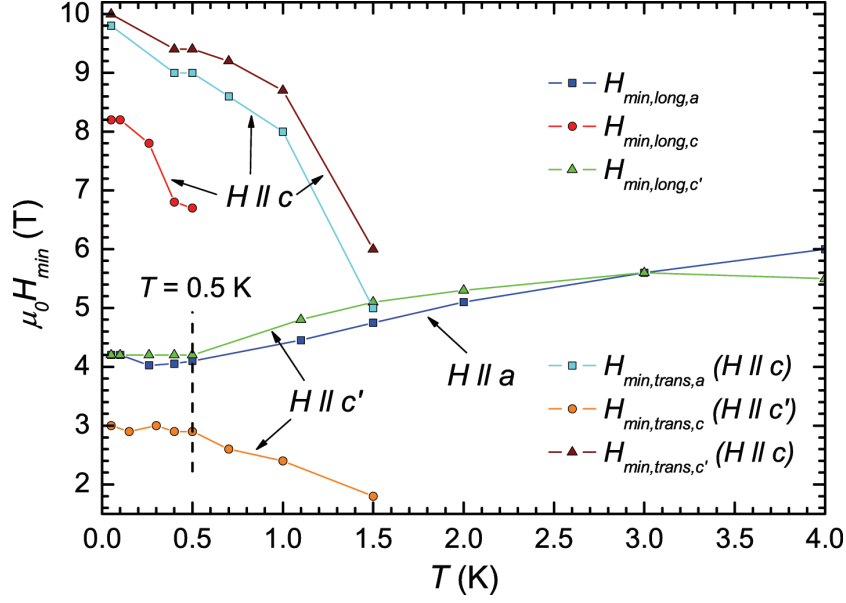


Figure 6.48: Minima in the magnetoresistance measurements (as a function of the magnetic field) (Figs. 6.44, 6.45, 6.46 and 6.47)  $H_{min}$  as a function of temperature  $T$ .

Interesting features of  $\rho_{B, long}(H)$  and  $\rho_{B, trans}(H)$  are found by plotting the magnetic fields of their minima as a function of temperature (Fig. 6.48):

- $H_{min, trans, a}(T)(H \parallel c)$  and  $H_{min, trans, c'}(T)(H \parallel c)$  (Fig. 6.48, cyan and brown data) show similar behaviour, namely a decrease with increasing temperature ending at 1.5 K. Also  $H_{min, long, a}(T)$  and  $H_{min, long, c'}(T)$  are similar over the entire temperature range (Fig. 6.48, green and blue data). In general,  $H_{min, a}(T)$  reaches slightly smaller absolute values than the  $H_{min, c'}(T)$  for both geometries in these curves.
- The characteristics of  $H_{min}(T)$  are mainly determined by the direction of  $H$  ( $H \parallel c$  or  $H \parallel a(c')$ ).
- For  $H_{min, c}(T)$ , a smaller absolute value and the disappearance of the minimum at lower temperatures is seen than for  $H_{min, a}(T)$  and  $H_{min, c'}(T)$  if the data with the same  $H$ -direction are compared.
- For  $T \leq 0.5$  K and  $H \parallel a$  or  $H \parallel c'$ ,  $H_{min}(T)$  reaches temperature-independent values ( $H_{min, long, a}(T) \approx H_{min, long, c'}(T) \approx 4.1$  T,  $H_{min, trans, c}(T)(H \parallel c') \approx 2.9$  T).

### Magnetic field direction dependence of the magnetoresistance

In the former subsections,  $\rho_B(H)$  curves with respect to their electrical current direction were shown and their  $T$ -dependence was discussed. Indications for a dominant  $H$ -direction depen-

dence of  $\rho_B(H)$  were found. Hence,  $\rho_B(H)$  is discussed with respect to the  $H$ -direction within this subsection (Figs. 6.49 and 6.50).

$\rho_B(H) - \rho_B(0\text{T})$  ( $H\parallel c$ ) and  $\partial\rho_B/\partial H$  ( $H\parallel c$ ) are shown in Figs. 6.49 and 6.50 (top). Similarities for the in-plane current directions  $a$  and  $c'$  are clearly revealed. By contrast, the initial decrease of  $\rho_{B,\text{long},c} - \rho_{B,c}(0\text{T})$  with increasing  $H$  is remarkably smaller at low  $H$  and at lowest  $T$ . Surprisingly, a current-direction independent increase of  $\rho_B(H\parallel c) - \rho_B(0\text{T})$  for  $H \geq 12\text{ T}$  and  $T \leq 2\text{ K}$  was measured. This is clearly seen in  $\partial\rho_B/\partial H$  ( $H\parallel c$ ), where the curves of the derivatives lie within a small band for  $H \geq 12\text{ T}$  (Fig. 6.50, top).

$\rho_B(H)$  measurements with  $H\parallel c'$  or  $H\parallel a$  are compared in Figs. 6.49 and 6.50 (bottom). The same characteristics in  $\rho_B(H)$  were found along all directions of  $j$ . Starting at  $\mu_0 H = 0\text{ T}$ ,  $\rho_B(H)$  decreases with increasing  $H$  reaching a minimum  $H_{\min}$  between 2 and 5 T at low temperatures (Fig. 6.48). The following increase of  $\rho_B(H)$  with increasing  $H$  yield a measurable inflection point  $H_{ss}$  (Fig. 6.50, bottom). A temperature-independent slope of  $\rho_B(H)$  was found for the lowest temperatures at magnetic fields higher than  $H_{\min}(H)$  along all directions. In general,  $\rho_B(H) - \rho_B(0\text{T})$  for  $H\parallel c'$  or  $H\parallel a$  shows a stronger depletion at  $H_{\min}(H)$  than for  $H\parallel c$ .  $H_{\min}(H)$  are shown in Fig. 6.48 and the inflection points  $H_{ss}(H)$  are at about 5, 10.5 and 12 T along the  $c$ ,  $a$  and  $c'$  direction (Tab. 6.10), respectively.  $H_{\max,\text{trans},c}(H)(H\parallel c')$  is measurable at about 14.5 T.  $\partial\rho_{B,\text{long},a}(H)/\partial H$  indicates a maximum in  $\rho_{B,\text{long},a}(H)$  around 18 T. A possible maximum in  $\rho_{B,\text{long},c'}(H)$  might exist at higher  $H$ .

## Magnetoresistance of other Kondo insulators

Within this subsection, magnetoresistance measurements of  $\text{CeRu}_4\text{Sn}_6$  are compared with the results of the Kondo insulators  $\text{CeNiSn}$  (orthorhombic, anisotropic gap opening) [12],  $\text{Ce}_3\text{Bi}_4\text{Pt}_3$  [14] and  $\text{SmB}_6$  [105], which was recently suggested to be a topological Kondo insulator [106].

$\rho_B(H)$  of  $\text{CeNiSn}$  shows remarkable dependencies on the direction of the magnetic field and electrical current direction at 0.45 K (Fig. 6.51). The increase of  $(\rho_B(H) - \rho_B(0\text{T}))/\rho_B(0\text{T})$  yield a value of 33 for  $j$  along the non-gapped axis  $a$  and  $H\parallel c$  at 15 T.  $\rho_{B,\text{long}}(H)$  along all axis change slightly around  $\rho_B(0\text{T})$ . Thus, in contrast to the case of  $\text{CeRu}_4\text{Sn}_6$ , the transverse vs. longitudinal application of  $H$  appears to be the dominating effect in  $\text{CeNiSn}$ . As discussed above, the influence of impurities are of great importance in Kondo insulators. Figure 6.52 shows the behaviour of different  $\text{CeNiSn}$  samples. Note that only sample #5 was purified using the solid state electrotransport (SSE) technique [13]. This technique is required to obtain high-quality single crystals of  $\text{CeNiSn}$ . The impurities in  $\text{CeNiSn}$  yield a strong enhancement of  $\rho(T)$  at the lowest temperatures [13]. This enhancement is reduced by applying a magnetic field (Fig. 6.52, c). As a result, the impurities mask, e.g., the maximum of  $\text{CeNiSn}$  at about 2 T with  $H\parallel a$  and  $j(I)\parallel c$  measured with the high-quality sample #5 (Fig. 6.52, b).

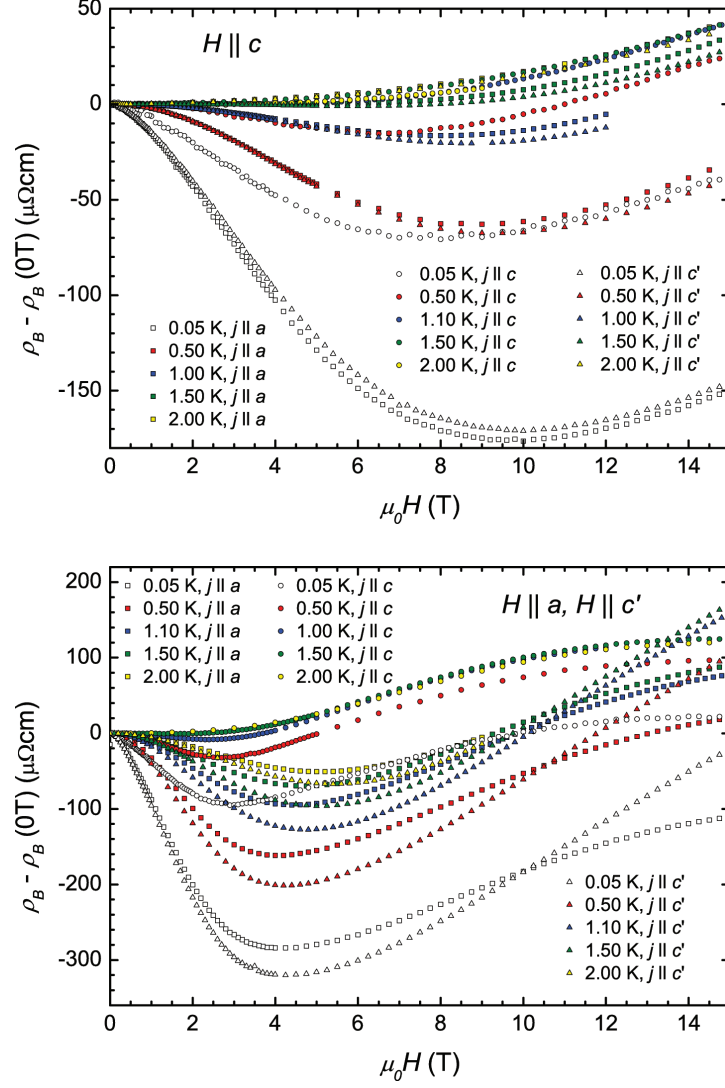


Figure 6.49: The upper (lower) panel shows the magnetoresistivity difference  $\rho_B - \rho_B(0T)$  with an applied magnetic field along the  $c$  direction (in-plane directions  $a$  and  $c'$ ) as a function the magnetic field  $\mu_0 H$  with the electrical current along the three investigated main directions  $a$ ,  $c$  and  $c'$ . These measurements were performed in collaboration with K.-A. Lorenzer.

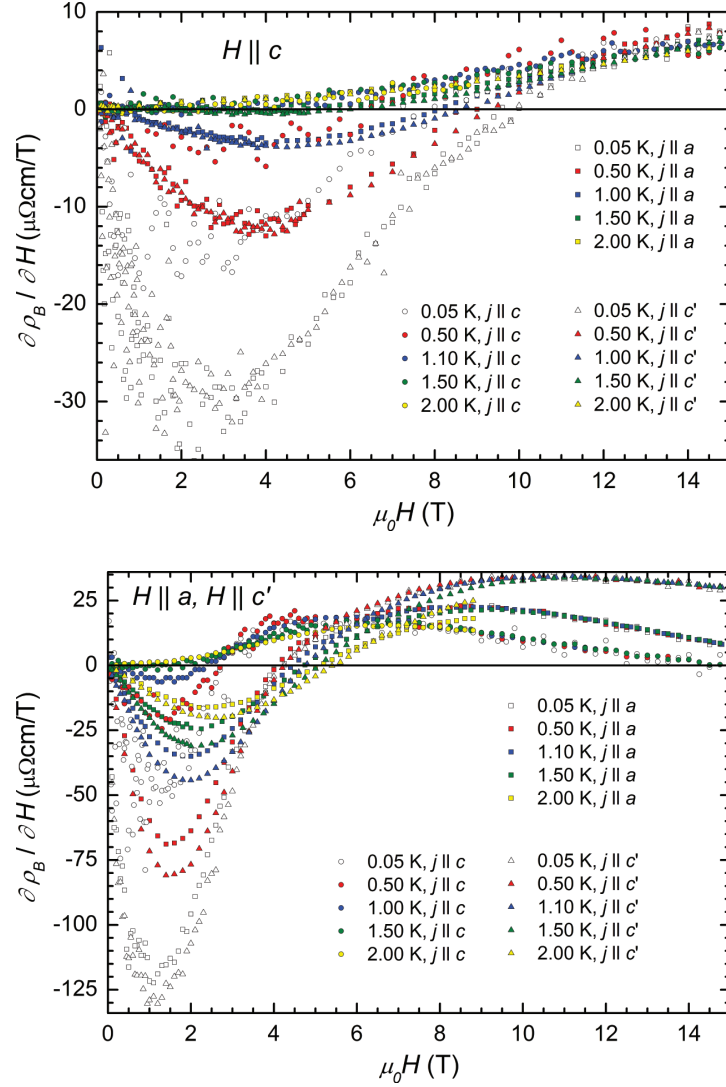


Figure 6.50: The upper (lower) panel shows the derivative of the magnetoresistivity  $\partial \rho_B(H)/\partial H$  with an applied magnetic field along the  $c$  direction (in-plane directions  $a$  and  $c'$ ) as a function the magnetic field  $\mu_0 H$  with the electrical current along the three investigated main directions  $a$ ,  $c$  and  $c'$ . These measurements were performed in collaboration with K.-A. Lorenzer.



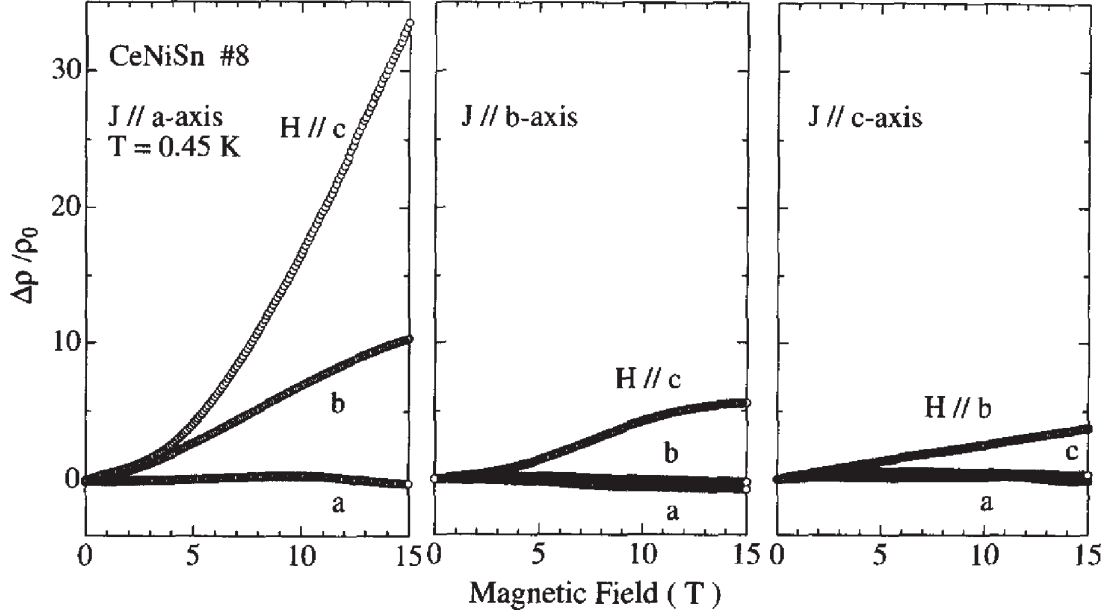


Figure 6.51: Magnetoresistance of CeNiSn [12]. The calculated energy gap by Ikeda and Miyake [5] does not open along the  $a$  axis.

$\text{Ce}_3\text{Bi}_4\text{Pt}_3$  shows a remarkable decrease of  $\rho_{B,\text{long}}(T)$  only below 20 K (Fig. 6.53). The authors report that the magnetic field dependence can be described with a simple model of a collapsing energy gap ( $\Delta \approx 37$  K) [14].

With the appearance of a minimum in  $\rho_B(H)$ ,  $\text{SmB}_6$  shows similar characteristics as found in  $\text{CeRu}_4\text{Sn}_6$ , but on absolutely different scales.  $\rho_B(H)/\rho_B(0\text{T})$  decreases to about 0.04 for  $\text{SmB}_6$  and at maximum to about 0.83 for  $\text{CeRu}_4\text{Sn}_6$  (Fig. 6.54). The minimum in  $\rho_B(H)$  was attributed to the closing of the energy gap [105].

## Summary and discussion

$\rho_B(\phi, \theta)$  measurements with rotating magnetic field were performed for several geometries. Within these investigations,  $\rho_{B,c}(\phi, \theta)$  was described reliably by an empirical function (Eqn. 6.34) (Figs. 6.35 and 6.36). Due to the temperature-dependent minimum in  $\rho_{B,\text{long},a}(H)$  and  $\rho_{B,\text{long},c'}(H)$  already above 2 K,  $\rho_{B,a}(\phi, \theta)$  and  $\rho_{B,c'}(\phi, \theta)$  cannot be described properly with Eqn. 6.34. An additional decrease of  $\rho_{B,a}(\phi, \theta)$  and  $\rho_{B,c'}(\phi, \theta)$  is observable with increasing  $\theta$  (Figs. 6.37 and 6.39). Surprisingly, similar behaviour (differences lower than 2 %) were found for  $\rho_{B,\text{long},c'}$  and  $\rho_{B,\text{trans},c'}(H \parallel c')$  (Fig. 6.38). Therefore, the charge carrier deflecting contribution in the transverse magnetoresistance appears to be negligible for  $\rho_B(H)$  of  $\text{CeRu}_4\text{Sn}_6$ .

Next, discrepancies in  $\rho_B(H)$  for different  $\text{CeRu}_4\text{Sn}_6$  single crystals were investigated; sample dependencies within this thesis are most pronounced in magnetoresistance measurements. The investigation revealed that the general characteristics (minimum in  $\rho_B(H)$  below 10 T at low

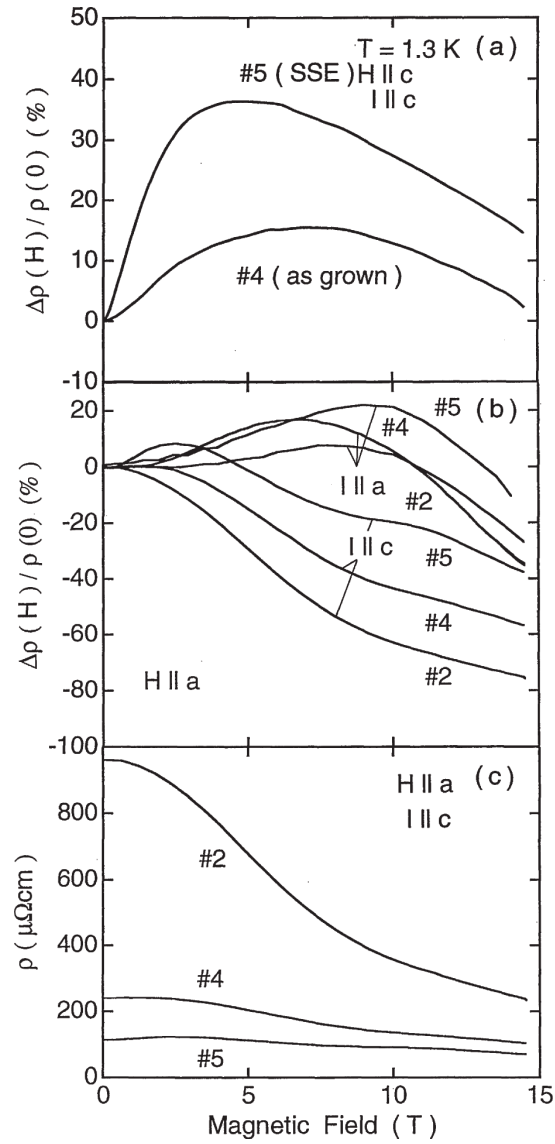
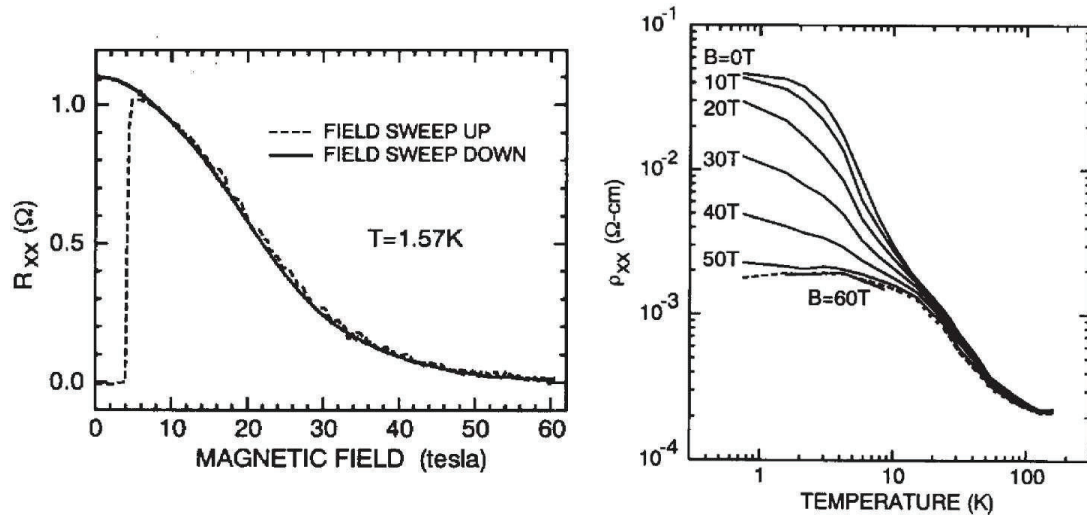
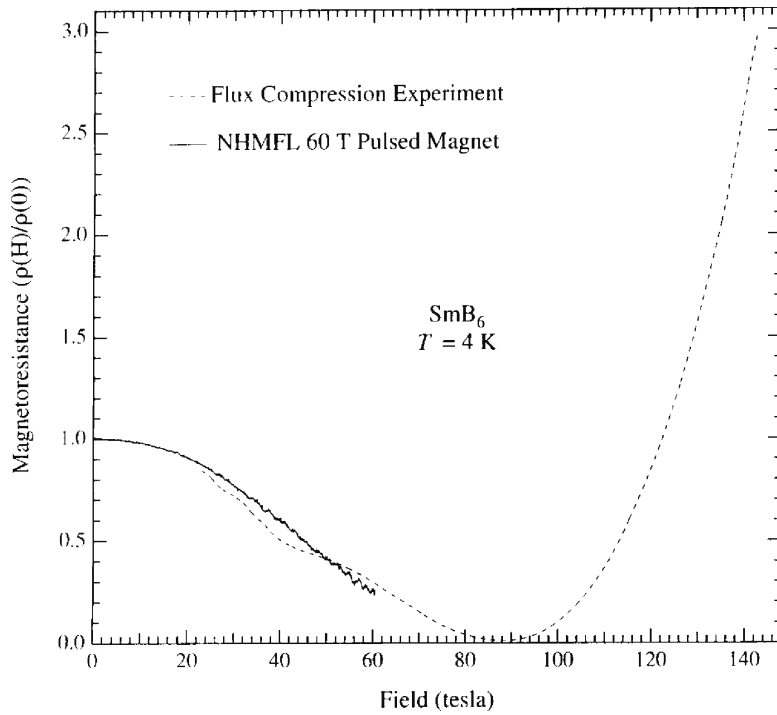


Figure 6.52: Magnetoresistance of different CeNiSn samples [13]. Only sample #5 was purified with the SSE technique.

Figure 6.53: Magnetoresistance of  $\text{Ce}_3\text{Bi}_4\text{Pt}_3$  [14].Figure 6.54: Magnetoresistance of  $\text{SmB}_6$  [105].

temperatures) are identical for all samples investigated. Slight differences were detected for the temperature evolution of these minima, their absolute values and the slopes of  $\rho_B(H)$  (Fig. 6.40 and 6.41). These differences are attributed to extrinsic effects which influence the low charge carrier DOS around the Fermi energy. In  $\text{CeRu}_4\text{Sn}_6$ , only marginal discrepancies were measured in comparison to other Kondo insulators like  $\text{CeNiSn}$  (Fig. 6.52) [13, 33, 39]. Due to comparably small discrepancies, the high quality of the  $\text{CeRu}_4\text{Sn}_6$  single crystals is confirmed by these results.

$\rho_{B,long}(H)$  measurements were performed by F. Weickert and J. Larrea at the High Field Laboratory at the Helmholtz-Zentrum Dresden-Rossendorf with  $\text{CeRu}_4\text{Sn}_6$  samples prepared within this thesis.  $\rho_{B,long,a}(H)$  and  $\rho_{B,long,c'}(H)$  exhibit a minimum  $H_{hf,min,long}$  at about 1.7 T and at about 2.3 T at  $T = 1.5$  K, respectively.  $H_{hf,max,long}$  is observed at about 20.5 T and about 25.5 T along the  $a$  and  $c'$  direction, respectively (Figs. 6.42 and 6.43). The extrema found within the high field measurements are listed in Tab. 6.10. Interestingly, identical slopes in both  $\rho_{B,long,a}(H)$  and  $\rho_{B,long,c'}(H)$  are found at  $\mu_0 H \geq 18$  T and  $T \leq 4.2$  K for each direction (see derivatives in Fig. 6.42). By contrast,  $\rho_{B,long,c}(H)$  shows only a maximum at  $\mu_0 H \approx 58$  T at the lowest temperatures and similar slopes at  $H \geq 35$  T and  $T \leq 4.2$  K (Fig. 6.43).

Finally,  $\rho_{B,long}(H)$  and  $\rho_{B,trans}(H)$  measurements were performed with the dilution refrigerator set-up in collaboration with K.-A. Lorenzer. These measurements revealed that the direction of  $H$  is most important for the behaviour of  $\rho_B(H)$ . This surprising feature is nicely seen in the temperature dependence of the minima  $H_{min}(T)$  in  $\rho_B(H)$  (Fig. 6.48) and in the magnetic field dependent representation of  $\rho_B(H)$  in Figs. 6.49 and 6.50. Hence, the direction of  $j$  and the relation between the direction of  $j$  and  $H$  play a minor role for  $\rho_B(H)$ .

If  $H$  is applied along  $c$ , similar slopes ( $j$  direction independent) were found for  $T \leq 2$  K and  $\mu_0 H \geq 10$  T (Figs. 6.49 and 6.50).  $\rho_B(H)(H \parallel a(c'))$  shows similar characteristics for all current directions; best seen in their derivatives  $\partial\rho_B(H)/\partial H$  (Fig. 6.50).  $\rho_B(H)(H \parallel a(c'))$  decreases with increasing  $H$ , reaching a minimum, followed by an increase of  $\rho_B(H)$ . The slope at  $H \geq H_{min}$  is temperature independent at lowest temperatures. An inflection point  $H_{ss}$  is observed below 15 T along all directions.  $\rho_{B,trans,c}(H)(H \parallel c')$  reaches a maximum at  $\mu_0 H = 14.5$  T. These features in  $\rho_B(H)$  are seen at the lowest magnetic fields in  $\rho_{B,c}(H)$ , followed by  $\rho_{B,a}(H)$  and finally in  $\rho_{B,c'}(H)$ .

If this order of directions ( $c$ ,  $a$  and  $c'$ ) is compared to the directional dependent hybridization strength along the different crystallographic axis, similarities with other physical properties can be found. The lowest hybridization strength would exist along  $c$ , which was determined by theoretical calculations by Wissgott (Sect. 5), optical spectroscopy measurements by Guritanu et al. (Sect. 6.6) [16] and indicated by several electrical transport measurements within this thesis. Comparing the in-plane directions  $a$  and  $c'$ , the hybridization strength is suggested to be higher along  $c'$  than along  $a$  by using the order discussed above. A higher hybridization strength along  $c'$  is slightly indicated by thermopower measurements, too (Sect. 6.5). Magnetoresistance

measurements indicates that the hybridization is remarkably less effected by a magnetic field along  $c$  than by a magnetic field along the in-plane directions.

Table 6.11: Minima and maxima of the thermopower  $S$  measured on  $\text{CeRu}_4\text{Sn}_6$  single crystals (Fig. 6.55).

crystallographic direction	$T_{\min 1}$ (K)	$S_{\min 1}$ ( $\mu\text{eV}$ )	$T_{\max}$ (K)	$S_{\max}$ ( $\mu\text{eV}$ )	$T_{\min 2} / T_{\min}$ (K)	$S_{\min 2} / S_{\min}$ ( $\mu\text{eV}$ )
$a$	270	59	121	69	15	-10.0
$c$	-	-	-	-	22	-28
$c'$	270	69	117	80	15	-9.4

## 6.5 Thermopower

$\text{CeRu}_4\text{Sn}_6$  exhibits interesting properties for thermoelectric and thermomagnetic refrigeration applications. The cage forming crystal structure and the classification as Kondo insulator are two promising characteristics which could reduce the thermal conductivity and lead to an enhanced thermopower  $S$ , respectively. Both these are key aspects for a high thermoelectric figure of merit. In addition, fundamental information about the electronic structure and the scattering processes along the investigated directions can be inferred from thermopower measurements.

Within this work, thermopower measurements were performed in collaboration with M. Ikeda (IFP, TU Vienna).  $\text{CeRu}_4\text{Sn}_6$  samples were separated by the present author from batch G2 along the crystallographic directions  $a$ ,  $c$  and  $c'$ .  $S(T)$  measurements were performed in a home-made device set-up by E. Bauer (IFP, TU Vienna). A detailed description of the measurement technique and the measurement procedure is given in Chap. 3. Figure 6.55 shows the results. As expected, a distinct anisotropy of  $S(T)$  between the out-of-plane direction  $c$  ( $S_c(T)$ ) and the in-plane directions ( $a$  ( $S_a(T)$ ),  $c'$  ( $S_{c'}(T)$ )) is observed. The overall temperature dependence of  $S_a(T)$  and  $S_{c'}(T)$  is very similar. Only above 50 K,  $S_{c'}(T)$  is slightly higher than  $S_a(T)$ . The minima and maxima in  $S(T)$  are listed in Tab. 6.11.

$S_a(T)$  and  $S_{c'}(T)$  decrease slightly upon decreasing  $T$  from 300 K, leading to a minimum of  $59 \mu\text{V/K}$  and  $69 \mu\text{V/K}$  at  $T_{\min 1}(S_a) = T_{\min 1}(S_{c'}) = 270 \text{ K}$ , respectively. With further decreasing  $T$ , a slight increase of  $S_a(T)$  ( $S_{c'}(T)$ ) is found, ending in a maximum of  $69 \mu\text{V/K}$  at  $T_{\max}(S_a) = 121 \text{ K}$  ( $80 \mu\text{V/K}$  at  $T_{\max}(S_{c'}) = 117 \text{ K}$ ). The following strong decrease of  $S_a(T)$  ( $S_{c'}(T)$ ) towards lower temperatures ends at a minimum of  $-10.0 \mu\text{V/K}$  ( $-9.4 \mu\text{V/K}$ ) at  $T_{\min 2}(S_a) = T_{\min 2}(S_{c'}) = 15 \text{ K}$ . The reincrease towards the lowest temperatures ends at a negative value of  $-2.5 \mu\text{V/K}$  and  $-1.3 \mu\text{V/K}$  at  $5.2 \text{ K}$  for  $S_a(T)$  and  $S_{c'}(T)$ , respectively.

$S_c(T)$  decreases with decreasing temperature between 300 and 22 K, with a noticeable change of the slope at about 80 K (Fig. 6.56, left panel). Here, no maximum is achieved over the entire temperature range. The minimum in  $S_c(T)$  of  $-28 \mu\text{V/K}$  is reached at  $T_{\min}(S_c) = 22 \text{ K}$ . It is about 3 times larger and shifted by 7 K compared to the minima measured along the in-plane directions. The following upturn towards lower temperatures ends at  $-8.8 \mu\text{V/K}$  at  $5.2 \text{ K}$ . Note

that the small kink at about 32 K for  $S_c(T)$  is attributed to measurement inaccuracies and is not considered as intrinsic.

In addition to the single crystal measurements, published data on polycrystals  $S_{poly}(T)$  [46] are included in Fig. 6.55. To compare  $S_{poly}(T)$  with the results of  $S(T)$  measured on single crystalline samples, the polycrystalline  $S(T)$  estimated from single crystal measurements was calculated by

$$S_{sc,poly}(T) = \frac{1}{3} (S_a(T) + S_c'(T) + S_c(T)) \quad (6.35)$$

and is also included in Fig. 6.55. Although the low temperature upturn of  $S_{poly}(T)$  cannot be accounted for by  $S_{sc,poly}(T)$  measurements, the temperatures of the minima ( $T_{min}$ ) are in good agreement ( $T_{min}(S_{sc,poly}) = 17.5$  K,  $T_{min}(S_{poly}) = 19.0$  K). At higher temperatures,  $S_{sc,poly}(T)$  yields higher values than  $S_{poly}(T)$ .

Similar characteristics of  $S(T)$  were found in many dilute Kondo systems, heavy fermion compounds and Kondo insulators [4, 8, 65, 67, 68, 70, 71]. These compounds exhibit two peaks in  $S(T)$  (maxima for Ce compounds) which were attributed to incoherent Kondo scattering on the full CEF-split multiplet and on the ground state, respectively (Chap. 2). Therefore, these peaks depend on the total CEF splitting energy  $\Delta_{CEF}$  and the Kondo temperature  $T_K$  leading to e.g. two clearly separated peaks (e.g. CeCu<sub>2</sub>Si<sub>2</sub> [67]) or two overlapping peaks (e.g. CeNiSn [4]) in  $S(T)$ . This dependence was investigated by substitution of Ce with La or by applying pressure for several compounds [67]. Exemplarily,  $S_b(T)$  of the anisotropic Kondo insulator CeNiSn exhibits two peaks (maxima at 20 and 100 K) which were attributed to the energy scales  $T_K$  and  $\Delta_{CEF}$  (Fig. 6.57). The upturn at lowest temperatures was attributed to the formation of an anisotropic energy gap at lowest temperatures [4]. A peaked structure of  $S(T)$  is also seen for the Kondo insulators (semiconductors) CeRhAs and CeRhSb [107].

In CeRu<sub>4</sub>Sn<sub>6</sub> (Fig. 6.55), a maximum at  $T_{max} = 120$  K ( $\equiv 10.4$  meV) is found in  $S_a(T)$  and  $S_c'(T)$ . Its origin cannot be assigned distinctively to  $\Delta_{CEF}$  or  $T_K$ . Using Eqn. 2.28, this leads to  $\Delta_{CEF} = (17 - 62)$  meV. This is in good agreement with the CEF-splitting scheme derived by direct magnetization measurements (Sect. 6.1.1, Fig. 6.6,  $\Delta_{CEF} = 76.2$  meV). Theoretical calculations by P. Wissgott [9] (Chap. 5) revealed that the Kondo temperature is in the vicinity of 290 K [16]. The upturn in  $S(T)$  at lowest temperatures is attributed to the anisotropic gap formation, in analogy to CeNiSn [4]. Note that the description of features in  $S(T)$  in a Kondo insulator with theoretical and experimental results of Kondo lattices or with theoretical results of single-impurity models are questionable. Interestingly, no maximum was observed in  $S_c(T)$  (Fig. 6.55).

The potential for thermoelectric application is determined by the thermoelectric figure of merit  $ZT$ . The thermal conductivity measurements for its calculation were performed by J. Hänel (IFP, TU Vienna) [108] and show, as expected, anisotropic behaviour between the in-plane directions and the perpendicular  $c$  direction. The maximal power factor  $PF = S^2\sigma$  ( $\sigma$  = electrical conductivity) is reached at the highest temperatures accessed with the  $S(T)$  measurements,

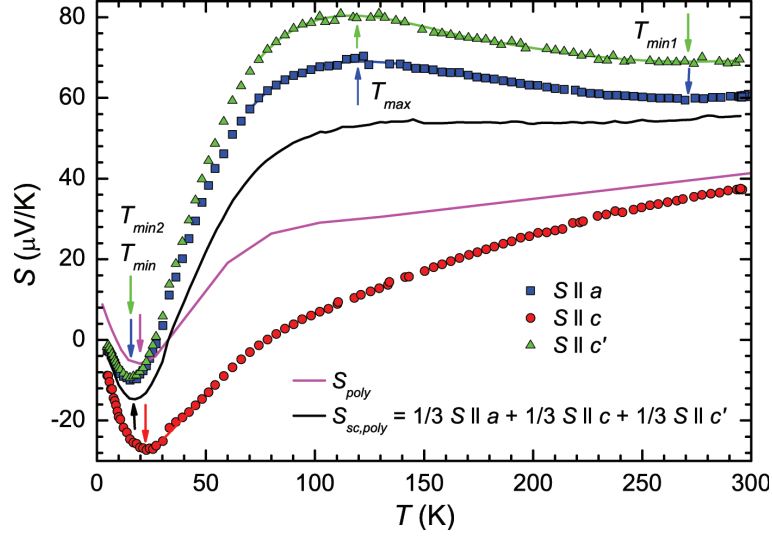


Figure 6.55: Thermopower  $S$  as a function of temperature  $T$  along the directions  $a$ ,  $c$  and  $c'$ . Additionally, literature data of polycrystalline  $\text{CeRu}_4\text{Sn}_6$ ,  $S_{poly}$  [46], and a theoretical polycrystalline  $S_{sc,poly}$ , calculated with the single crystal results (Eqn. 6.35) are shown. The maxima and minima in  $S(T)$  are indicated by arrows with the respective colors (Tab. 6.11).

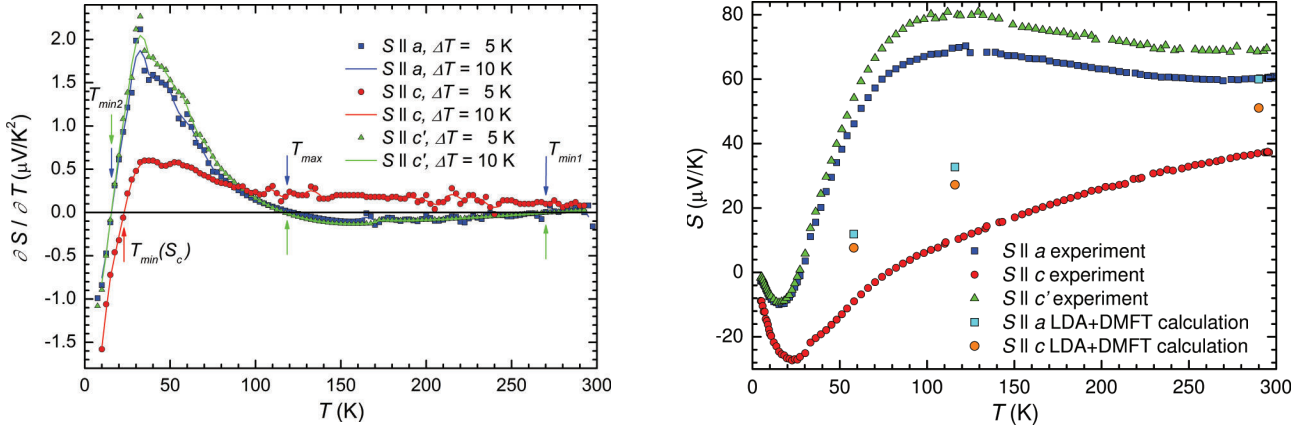


Figure 6.56: The left panel displays the temperature derivative of the thermopower  $\partial S(T)/\partial T$  as a function of temperature  $T$  with different fitting intervals  $\Delta T$  (5 and 10 K). The right panel shows a comparison between  $S$  measurements and LDA+DMFT calculations as a function of temperature  $T$ . The LDA+DMFT calculations were made by P. Wissgott [9].



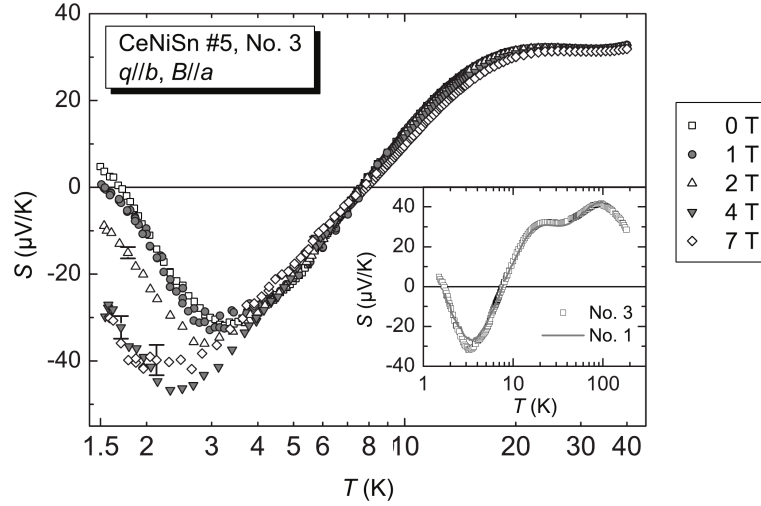


Figure 6.57: Thermopower  $S$  as a function of temperature  $T$  on a semilogarithmic plot. These measurements were performed by U. Köhler and the plot is extracted from her PhD thesis [4].

namely 295 K and 300 K for the  $c$  and  $a$  direction, respectively. At these temperatures, the values are  $ZT_c = 1.5 \cdot 10^{-2}$  and  $ZT_a = 1.7 \cdot 10^{-2}$ .

## Summary

Within this work, anisotropic behaviour of  $S(T)$  was measured between the in-plane directions ( $a$ ,  $c'$ ) and the perpendicular out-of-plane direction  $c$ . Comparable behaviour of  $S(T)$  was already found in dilute Kondo systems, heavy fermion compounds and Kondo insulators [4, 8, 65, 67, 68, 70, 71]. This behaviour is described properly with a single impurity Anderson model by Zlatić et al. [8]. The maxima in  $S_a(T)$  and  $S_{c'}(T)$  at 120 K can be attributed to be caused by incoherent Kondo scattering on the CEF-split multiplet and/or on the ground state (Chap. 2). A clear distinction as found in CeNiSn [4] is not feasible. However, if these maxima are attributed to the incoherent scattering on the CEF multiplet (calculated with Eqn. 2.28 to  $\Delta_{CEF} = (17-62)$  meV), similar total CEF splitting energies are found in comparison with CEF schemes revealed with direct magnetization measurements (Sect. 6.1.1, Fig. 6.6,  $\Delta_{CEF} = 76.2$  meV). Interestingly, no maximum was observed in  $S_c(T)$  (Fig. 6.55).

Finally,  $S(T)$  was compared to  $S_a(T)$  and  $S_{c'}(T)$  calculated with local density approximation + dynamic mean-field theory (LDA+DMFT) calculations by Wissgott [9] (Fig. 6.56, right panel). At 290 K, the values were calculated with the computed LDA+DMFT self energy. At lower temperatures, the imaginary part of the computed LDA+DMFT self energy was set to 0.005 eV. The calculated values are less anisotropic than the measured values and cannot mimic the peaked structure in  $S_a(T)$  and  $S_{c'}(T)$  at around 120 K. Note that the fine structure of the electronic bandstructure and the exact position of the chemical potential have a large influence

on the behaviour of  $S(T)$ . Thus, the differences are attributed to small features in the electronic band structure.

## 6.6 Measurements with grown/prepared $\text{CeRu}_4\text{Sn}_6$ single crystals by cooperating groups

As already mentioned in Chap. 3,  $\text{CeRu}_4\text{Sn}_6$  single crystals were grown and/or prepared for measurements performed by cooperating research groups (researchers).

At first, longitudinal magnetoresistance measurements at high magnetic fields were performed by J. Larrea and F. Weickert in Rossendorf/Dresden. These results were already shown and discussed in Sect. 6.4. Secondly, resonant X-ray absorption spectroscopy (XAS) and XAS partial fluorescence yield (PFY) mode measurements with several  $\text{CeRu}_4\text{Sn}_6$  samples separated from different batches were performed by F. Strigari in the group of A. Severing (2. Physikalisches Institut at the Universität zu Köln). Next, optical conductivity  $\sigma(\omega)$  measurements of single crystalline  $\text{CeRu}_4\text{Sn}_6$  samples (separated from batch G3) were performed by V. Guritanu, J. Sichelschmidt, T. Weig and M. Scheffler along the  $a$  and  $c$  direction. A summarizing article of  $\sigma(\omega)$ , LDA+DMFT calculations (Wissgott [9]) and electrical resistivity measurements was recently published [16]. Finally, first cleaving tests, scanning tunneling microscopy (STM) and preliminary scanning tunneling spectroscopy (STS) analysis were performed by S. Wirth (Max Planck Institute for Chemical Physics of Solids, Dresden).

### 6.6.1 X-ray absorption spectroscopy

Within this PhD thesis, an important task was the determination of the crystalline electric field (CEF) split level scheme of the Ce-4*f*  $J = 5/2$  multiplet in  $\text{CeRu}_4\text{Sn}_6$ . Firstly, an analysis of the CEF scheme was performed with magnetization measurements at high temperatures (Sect. 6.1.1) which revealed non-CW behaviour up to highest accessible temperatures (1000 K). Inelastic neutron scattering (INS) measurements on polycrystalline  $\text{CeRu}_4\text{Sn}_6$  indicated a CEF excitation of about 30 meV [45]. Combining both results, some evidence for a pure ( $J = 5/2$ ,  $m_j = \pm 1/2$ ) ground state doublet was found, but no final conclusion could be drawn. Hence additional investigations were performed with XAS measurements which were successfully achieved for other compounds, as, e.g.,  $\text{CePd}_2\text{Si}_2$  [82] and  $\text{CePt}_3\text{Si}$  [83].

The XAS experiments (and their analysis) were performed by F. Strigari in the group of A. Severing (2. Physikalisches Institut at the Universität zu Köln) at the National Synchrotron Radiation Research Center (NSRRC, Dragon beamline BL08A) in Taiwan [15]. The  $\text{CeRu}_4\text{Sn}_6$  samples studied here were grown and prepared within this thesis (Chapt. 3). A short description of this measurement technique is presented in Chapt. 3. Preliminary results were presented by F. Strigari at a poster session at the conference "Quantum Criticality & Novel Phases" in 2012 in Dresden.

Figure 6.58 displays the absorption intensities at 12 K (middle) and two simulations performed by F. Strigari with a dominating ( $J = 5/2$ ,  $m_j = \pm 1/2$ ) (top) and a dominating ( $J = 5/2$ ,  $m_j = \pm 3/2$ ) (bottom) ground state doublet [15]. The polarization dependence of the intensities measured implies that the dominating wave functions of the ground state doublet ( $J = 5/2$ ) are either  $m_j = \pm 1/2$  or  $m_j = \pm 3/2$ . Within that analysis, a ground state doublet with a dominating ( $J = 5/2$ ,  $m_j = \pm 5/2$ ) contribution was excluded. Interestingly, the most appropriate results were found with an additional small contribution ( $\leq 0.08$ ) of the higher lying spin-orbit split  $J = 7/2$  multiplet (same  $m_j$  as main contributing  $J = 5/2$  eigenstate). A comparison between simulation 1 ( $m_j = \pm 1/2$ ) and simulation 2 ( $m_j = \pm 3/2$ ) revealed that simulation 2 clearly lead to a better agreement with the measurements (Fig. 6.58). This finding is in contrast to the analysis of the direct magnetization measurements which suggested a pure ( $J = 5/2$ ,  $m_j = \pm 1/2$ ) ground state doublet (Sect. 6.1.1). Therefore, additional non-resonant inelastic X-ray scattering (NIXS) measurement are planned. NIXS measurements are bulk-sensitive and, therefore, will clarify whether the XAS spectra of Fig. 6.58 are modified by surface or self absorption effects.

In addition, the temperature dependence of the absorption intensities was investigated up to higher temperatures. Within these measurements, the polarization dependence remained constant up to 200 K implying that the first CEF-split energy level is positioned at least 17 meV above the ground state multiplet. This finding is consistent with the results of inelastic neutron scattering (INS) on polycrystalline  $\text{CeRu}_4\text{Sn}_6$  that associated a peak at about 30 meV with a CEF excitation [45]. Therefore, an energy splitting of 30 meV between the lowest lying doublets was assumed for the CEF investigations of direct magnetization measurements (Sect. 6.1.1).

Alternatively to the  $M_4$  and  $M_5$  excitations investigated here, investigations have been made on the  $L_3$  excitations. Therefore, XAS in the partial fluorescence yield (PFY) mode measurements were performed by F. Strigari in the group of A. Severing. The  $L_3$  excitations are used to investigate the Kondo scale by studying the temperature dependence of the small additional hump at 5740 eV in the spectra (Fig. 6.59) caused by the  $f^0$ -contribution (excitation in the  $4f^0$ -state). The fact that this hump is only very slightly reduced at 160 K suggests a Kondo temperature of at least this order of magnitude.

## 6.6.2 Optical reflectivity measurements

Optical reflectivity in the far-infrared and THz frequency range is a useful technique to investigate the low energy scales in strongly correlated electron systems. As such, it is commonly used to study Kondo semiconductors or insulators such as, e.g.,  $\text{YbB}_{12}$  [109]. Within this thesis, two  $\text{CeRu}_4\text{Sn}_6$  single crystals were separated from batch G3. Optical reflectivity measurements were performed by V. Guritanu in the group of J. Sichelschmidt at Max Planck Institute for Chemical Physics of Solids (Dresden) in the energy range of 5 meV - 30 eV (frequency range: 1.2 THz - 7.3 PHz) and by T. Weig and M. Scheffler at 1. Physikalisches Institut (Universität Stuttgart) in the energy range of 0.5 - 5 meV (frequency range: 0.12 - 1.2 THz). The electrical

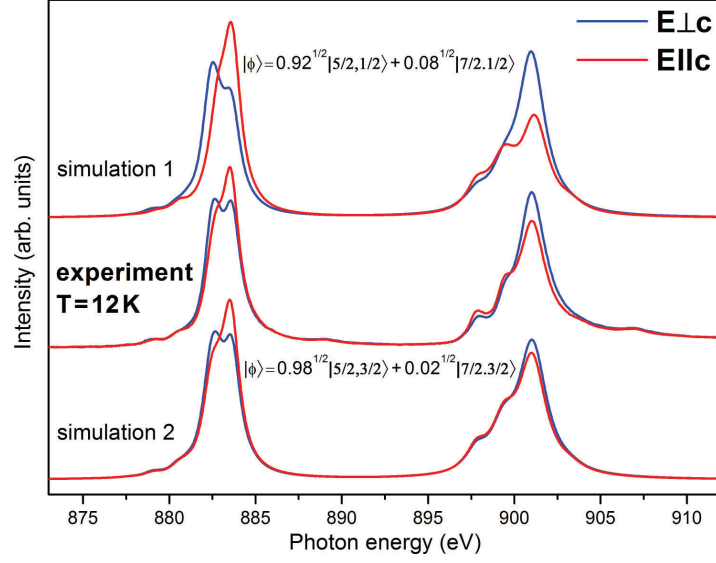


Figure 6.58: Polarization-dependent absorption intensities as a function of the photon energy derived by resonant X-ray absorption spectroscopy. The measurements (middle) and simulations (simulation 1 (top) and simulation 2 (bottom) with different wave functions  $|\phi\rangle$ ) were performed by F. Strigari [15] on  $\text{CeRu}_4\text{Sn}_6$  samples prepared within this thesis. The electrical field  $E$  of the polarized X-rays was oriented perpendicular (blue lines) and parallel (red lines) to the crystallographic  $c$  direction. Here, the results at 12 K are presented. This plot was presented on a poster by F. Strigari [15] at the conference "Quantum Criticality & Novel Phases" in Dresden in 2012 .

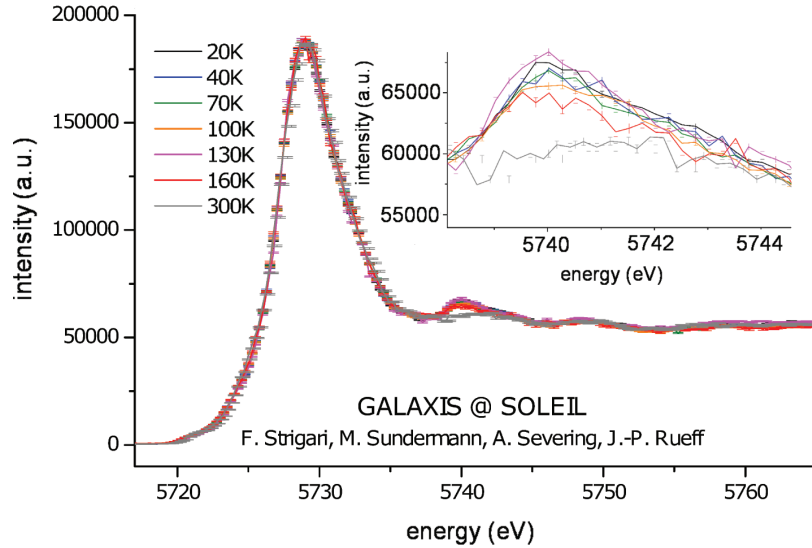


Figure 6.59: L-edge XAS-PFY measurements on  $\text{CeRu}_4\text{Sn}_6$  at several temperatures by F. Strigari in the group of A. Severing. The hump at 5740 eV (shown in detail in the inset) is used to investigate the Kondo temperature scale.

field component of the light was applied parallel to the  $a$  and  $c$  direction. Each group investigated only one sample, so different samples were measured in the different energy ranges. The measurement technique and the  $\text{CeRu}_4\text{Sn}_6$  single crystals used are discussed in Chap. 3.

The optical reflectivity spectra as a function of the energy (wave number),  $R(\omega)$ , are shown in the left panel of Fig. 6.60 [16]. These spectra were measured with the electrical field  $E$  parallel to the  $a$  (top) and  $c$  (bottom) direction at different temperatures between 6 and 300 K. In the intermediate frequency range,  $R(\omega)$  shows a larger decrease with decreasing temperature along the  $a$  (marked with an arrow in Fig. 6.60, left panel, top) than for the  $c$  direction [16]. These findings are consistent with electrical resistivity measurements (Sect. 6.2) which revealed a lower electrical conductivity along the  $a$  axis over the entire temperature range. The real part of the optical conductivity  $\sigma_1(\omega)$  was calculated from  $R(\omega)$  by V. Guritanu with a Kramers-Kronig fitting method [110]. Importantly,  $R(\omega)$  measured in the THz frequency range (dots in Fig. 6.60, left panel) is close to unity which yields a strong dependence of  $\sigma_1(\omega)$  on small variations of  $R(\omega)$ . Hence,  $\sigma_1(\omega)$  was calculated by a weighted average over finite frequency ranges in the THz frequency regime.  $\sigma_1(\omega)$  with  $E\parallel a$  ( $E\parallel c$ ) are shown in the right top (bottom) panel of Fig. 6.60 [16]. The values of the dc electrical conductivity are added as symbols at Energy = 0 meV in this plot.

$\sigma_1(\omega)$  shows pronounced anisotropic behaviour especially at lowest temperatures and frequencies. Metal-like behaviour is found for  $E\parallel c$  which is suggested by the Drude-like feature in  $\sigma_1(\omega)$  at lowest temperatures below about 25 meV. By contrast,  $\sigma_1(\omega)$  for  $E\parallel a$  is decreasing with decreasing energy at lowest temperatures, behaviour typical for semiconductors. However,  $\sigma_1(\omega \rightarrow 0)$  for  $E\parallel a$  remains finite at the lowest temperatures and frequencies accessed, which is in agreement with the finite dc electrical conductivity. This behaviour implies that the gap is not yet fully formed or that residual in-gap states are present within a gapped density of states along  $a$ .

In conclusion,  $\sigma_1(\omega)$  suggests metal-like behaviour along the  $c$  and semiconductor-like behaviour along the  $a$  direction. These results are consistent with a higher hybridization strength along the  $a$  direction suggested by other physical properties (thermopower (Sect. 6.5), electrical resistivity (Sect. 6.2) and magnetoresistance (Sect. 6.4)) measured within this work and by theoretical calculations by Wissgott [9] (Chap. 5).

In addition, the temperature dependence of the calculated integrated spectral weight  $N_{eff}$  was investigated by V. Guritanu (not shown) [16]. The lower  $N_{eff}$  along both directions at low temperatures and energies is attributed to the pseudogap formation as opposed to the existence of a simple uncorrelated bandgap because the low-temperature loss of  $N_{eff}$  persists up to at least 0.6 eV. Such behaviour of  $N_{eff}$  suggests strong correlations of the charge carriers in contrast to electronic band effects and was also observed in other Kondo insulator, e.g., FeSi [86]. Importantly, this characteristic is found, though more weakly, also for the  $c$  direction. Therefore, at least an onset of Kondo gap formation appears to occur also along the  $c$  direction,

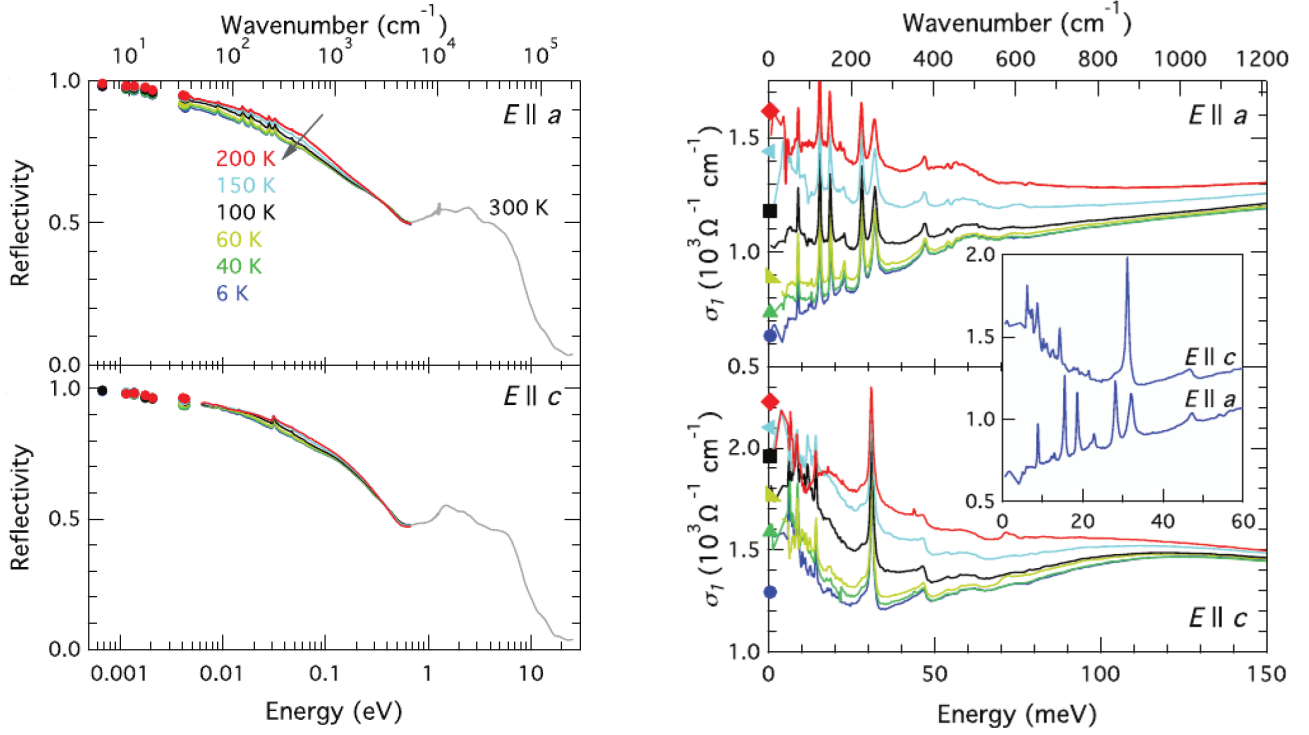


Figure 6.60: The optical reflectivity as a function of the energy (wavenumber) is shown in the left panel with the electrical field  $E$  of the incoming radiation along the two crystallographic directions  $a$  (top) and  $c$  (bottom) at different temperatures. The right panel presents the calculated optical conductivity  $\sigma_1(\omega)$  as a function of the energy (wavenumber) at low energies for different temperatures. The inset shows a comparison of  $\sigma_1(\omega)$  for the two different orientations of  $E$  at 6 K.  $\sigma_1(\omega)$  was calculated by V. Guritanu with a Kramers-Kronig fitting method [110]. These plots have recently been published in [16].

which is consistent with electrical resistivity and magnetoresistance measurements (Sects. 6.2 and 6.4), which show similar characteristics along all directions.

### 6.6.3 Cleaving tests, scanning tunneling microscopy and preliminary scanning tunneling spectroscopy analysis

In  $\text{CeRu}_4\text{Sn}_6$ , the most important question is the nature of the  $k$ -dependent electronic band structure at the Fermi energy at low temperatures. An excellent measurement technique to investigate this property is angle-resolved photoemission spectroscopy (ARPES). For ARPES measurements, a pristine flat surface of the sample is required. This is usually obtained by cleaving the samples in ultra-high vacuum (UHV), frequently at low temperatures. If the sample has a preferential plane of fraction, the sample breaks along this plane and the requirements



for measurements are fulfilled.

To test the possibility of ARPES measurements on  $\text{CeRu}_4\text{Sn}_6$ , cleaving tests were performed by S. Wirth at Max Planck Institute for Chemical Physics of Solids in Dresden in a low-temperature UHV scanning tunneling microscope (STM) such that the cleaved surface could be directly imaged in the STM after the cleaving process. First, cleaving tests were performed at 300 K. Their results and a photograph of the sample (batch G3, samples separated from piece G3\_B\_1\_bottom) after the cleaving process are shown in Fig. 6.61. These cleaving tests yield no preferential plane of fraction and a height difference in the line scan of about 1.7 nm (Fig. 6.61, bottom, right panel). Thus, the sample surface achieved by the cleaving process at 300 K is unusable for ARPES measurements.

In a second step, several samples (batch G3, samples separated from piece G3\_B\_1\_bottom) were cleaved at 20 K. Figure 6.62 shows images for a successful cleave. The roughness in the 60 nm x 60 nm area imaged in Fig. 6.62, top, is about a few hundreds pm (line scan in Fig. 6.62, bottom). In this area, no sizable terraces or atomically flat areas are detectable. Fourier transformations of several line scans were performed to see whether periodic structures can be resolved. This was not the case and the cleaved surface exhibits no ordered structure. Nevertheless, the surface is potentially usable for ARPES measurements. These are now planned to be performed in collaboration with S. Kimura at SPring-8 in Japan.

In addition to the cleaving tests, preliminary scanning tunneling spectroscopy (STS) measurements on  $\text{CeRu}_4\text{Sn}_6$  were performed by S. Wirth. Two spectra measured at 4.7 K are shown in Fig. 6.63. The red curve was measured with higher resolution than the black curve. These measurements revealed a low residual DOS at the Fermi energy, indicating a partially gapped DOS at the Fermi energy (pseudogap), in good agreement with the measurements performed within this thesis and by collaborators.



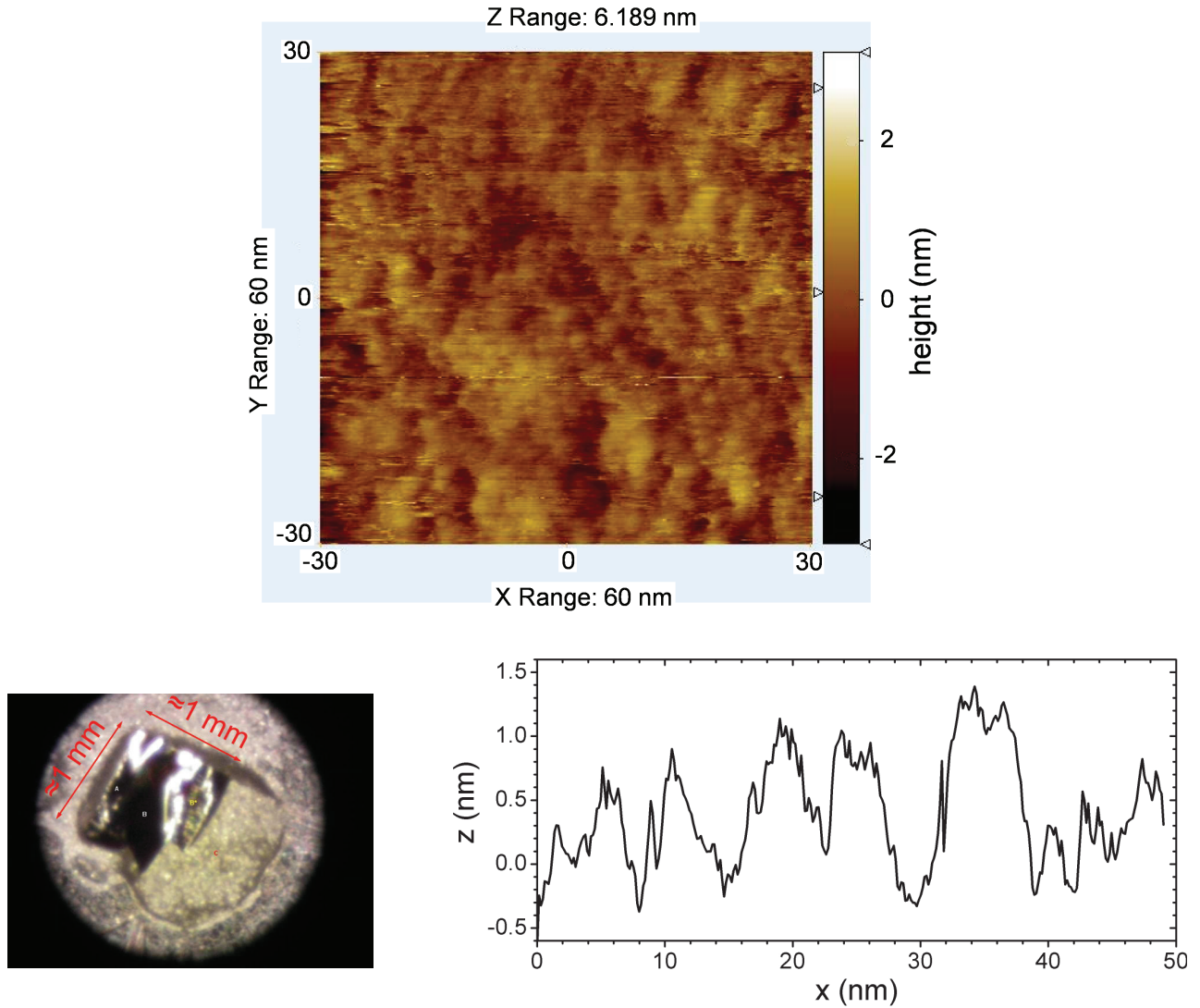


Figure 6.61: Results of the cleaving tests at 300 K on  $\text{CeRu}_4\text{Sn}_6$ . A STM image of a 60 nm x 60 nm surface of  $\text{CeRu}_4\text{Sn}_6$  (top), a photograph of the cleaved surface (bottom, left) and a line scan with a length of 50 nm (bottom, right) are presented. The in-situ cleaving process and the STM investigations were performed by S. Wirth (Max Planck Institute for Chemical Physics of Solids, Dresden).

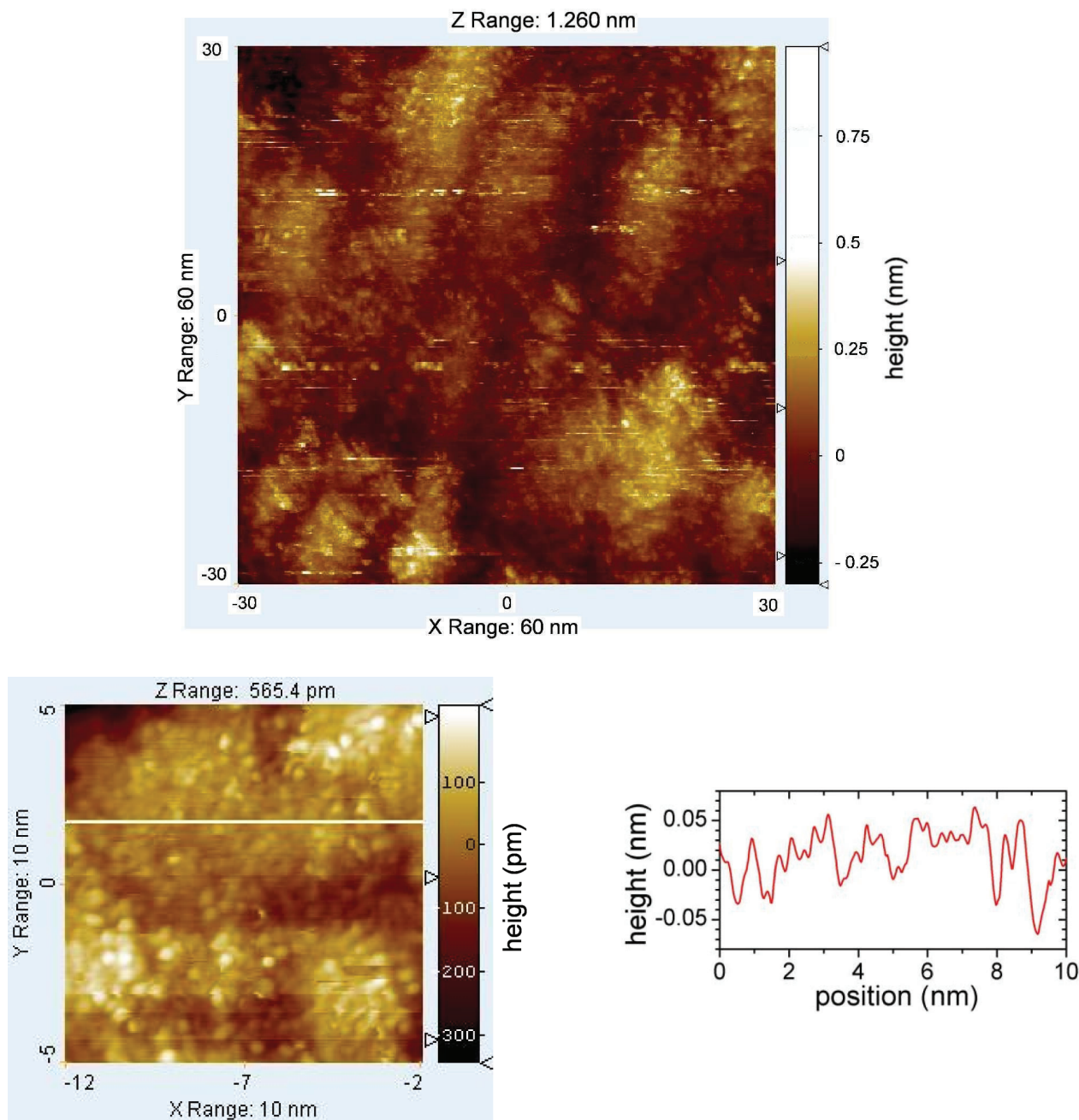


Figure 6.62: STM image of a 60 nm x 60 nm surface of  $\text{CeRu}_4\text{Sn}_6$  cleaved at 20 K (top) and a 10 nm x 10 nm close up (bottom, left) across which a line scan (bottom, right) was measured. The in-situ cleaving process and the STM investigations were performed by S. Wirth (Max Planck Institute for Chemical Physics of Solids, Dresden).

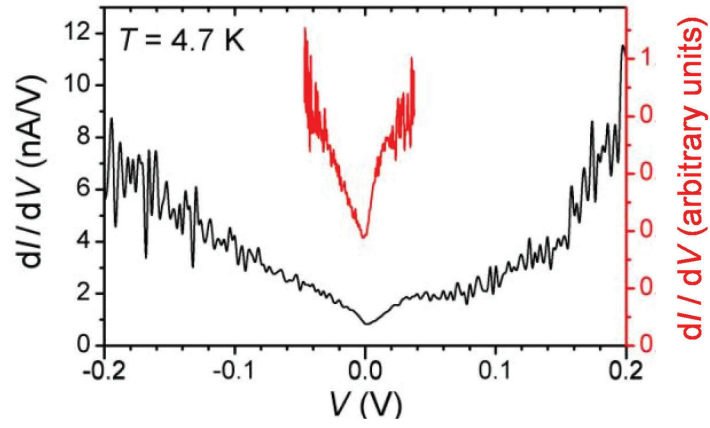


Figure 6.63: Preliminary scanning tunneling spectroscopy measurements on  $\text{CeRu}_4\text{Sn}_6$  performed by S. Wirth at 4.7 K. The red curve was measured with higher resolution than the black curve. In agreement to other investigations on  $\text{CeRu}_4\text{Sn}_6$ , an indication for a pseudogap is detected.



# Chapter 7

## Summary and outlook

Within this work, several  $\text{CeRu}_4\text{Sn}_6$  single crystals were grown using the floating zone technique (Sect. 4.2, Tab. 4.2). The growth procedure was performed based on the work of T. Nezu and A. Prokofiev [10]. Energy dispersive X-ray spectroscopy and X-ray powder diffraction measurements revealed that the crystals were single phase and of high crystalline and stoichiometric perfection. All batches were oriented by the Laue technique and subsequently by magnetization measurements. The additional magnetization measurements were necessary because the particular crystallographic structure of  $\text{CeRu}_4\text{Sn}_6$  did not allow to distinguish the two directions [001] and [110] with the used Laue device. The magnetization measurements confirmed the high quality of the single crystals.

All physical properties investigated within this thesis are highly anisotropic between the [001] axis and the tetragonal basal (001) plane. Within the (001) plane, only small anisotropy is found between the [100] and [110] direction. Optical reflectivity measurements by V. Guritanu, J. Sichelschmidt, T. Weig and M. Scheffler, together with local density approximation + dynamic mean-field theory calculations performed by P. Wissgott [9] revealed indications of an energy gap opening within the (001) plane, while the [001] direction remained essentially metallic (Sect. 6.6.2 and Chap. 5). The existence of a pseudo gap in  $\text{CeRu}_4\text{Sn}_6$  was confirmed by preliminary scanning tunneling spectroscopy measurements by S. Wirth (Sect. 6.6.3).

Electrical transport measurements performed within this thesis (Sects. 6.2 to 6.5) are in good agreement with this picture of an anisotropic gap opening in the electronic band structure. The temperature-dependent electrical resistivity cannot be described with a simple semiconductor model but is instead dominated by Kondo physics (Sect. 6.2). The Hall coefficient and Hall mobility display a logarithmic increase with decreasing temperature at low temperatures, similar to the Kondo insulators  $\text{CeRhSb}$  and  $\text{CeNiSn}$  [11] (Sect. 6.3). Surprising results were obtained by magnetoresistance measurements (Sect. 6.4): the direction of the magnetic field along [100] or within the (001) plane has a much stronger influence on the sign and magnitude of the magnetoresistance than the direction of the current or the angle ( $0^\circ$  or  $90^\circ$ ) between the current and the magnetic field (longitudinal or transverse magnetoresistance). This behaviour is best revealed by the field derivatives of the magnetoresistivity curves (Figs. 6.49 and 6.50).

These features in the magnetoresistance point to a strongly anisotropic field dependence of the electronic density of states.

Another important aim within this thesis was the determination of the crystalline electric field level scheme of the Ce  $4f$  electron. This information is important to understand the anisotropic hybridization and to provide the correct starting point for the ongoing theoretical calculations. Direct magnetization (DM) and torque magnetometry (TM) measurements revealed a large magnetic anisotropy with a hard  $c$  axis and an easy (001) plane character (Sect. 6.1). TM measurements show a stronger anisotropy than DM measurements. At low temperatures, the combination of DM and TM measurements yields a large negative magnetization along the  $c$  axis; further investigations are needed to confirm this result. The temperature dependence of the magnetic susceptibility curves obtained from DM measurements was fitted with different crystalline electric field level schemes. Best agreement above 300 K was found for a ground state doublet of pure ( $J=5/2$ ,  $m_j=\pm 1/2$ ) states. Resonant X-ray absorption spectroscopy (XAS) measurements performed by F. Strigari (Sect. 6.6.1) on the other hand, observed an almost pure doublet of ( $J=5/2$ ,  $m_j=\pm 3/2$ ) states as ground state. This discrepancy might be due to surface and/or self absorption effects in XAS. Bulk sensitive non-resonant inelastic X-ray absorption spectroscopy (NIXS) measurements will be carried out shortly to resolve this conflict.

Various further measurements on the CeRu<sub>4</sub>Sn<sub>6</sub> single crystals grown during this PhD work are ongoing or planned. Firstly, thermoelectric properties are of great interest because both the cage-like crystal structure and the flat bands in the vicinity of the pseudo gap might lead to enhanced  $ZT$  values. Secondly, the electronic band structure is planned to be investigated with angle-resolved photoemission spectroscopy (ARPES). This measurement could directly determine the  $k$ -dependent electronic band structure and thus test the picture that has emerged from this work. Muon spin rotation ( $\mu$ SR) and neutron scattering measurements are only available on polycrystalline CeRu<sub>4</sub>Sn<sub>6</sub> samples yet. Thus, measurements on CeRu<sub>4</sub>Sn<sub>6</sub> single crystals are planned to enhance the accuracy of the measurements and open various additional possibilities of investigations. Finally, the ground state of the Ce  $4f$  electron is of great interest and we hope to clarify this by NIXS measurements.

In addition to the investigations on CeRu<sub>4</sub>Sn<sub>6</sub>, service measurements on Ce<sub>3- $x$</sub> La <sub>$x$</sub> Pd<sub>20</sub>Si<sub>6</sub> and on the type-I clathrate Ba<sub>8</sub>Au<sub>6</sub>Si<sub>40</sub> substituted with Ce and La were performed within other projects. These measurements are shown and briefly discussed in the appendix.

In summary, with the CeRu<sub>4</sub>Sn<sub>6</sub> single crystals synthesized and studied within this thesis near insight into strongly correlated systems at the border between metallic and insulating behaviour was gained. Single crystalline CeRu<sub>4</sub>Sn<sub>6</sub> turned out to be a potential candidate for improving the understanding of the anisotropic hybridization gap formation in Kondo insulators.

# Appendix A

## Contributions to other projects

Apart from the investigations on  $\text{CeRu}_4\text{Sn}_6$ , physical property measurements on other compounds were performed which are briefly discussed below.

### A.1 $\text{Ce}_{3-x}\text{La}_x\text{Pd}_{20}\text{Si}_6$

$\text{Ce}_3\text{Pd}_{20}\text{Si}_6$  is a cubic heavy-fermion compound which exhibits a field-induced quantum critical point at about 1 T. In zero magnetic field, two phase transitions at about  $T_l = 0.31$  K and  $T_u = 0.5$  K were observed [111]. Within the author's master thesis, the effect of substituting the Ce ions by La and Lu ions was investigated [49]. These substitutions yield a positive (Lu) or negative (La) chemical pressure. The Ce atoms occupy two different crystallographic sites, namely  $4a$  and  $8c$  with a ratio of 1 to 2. Therefore, a preferential site occupation of the La or Lu atoms was additionally investigated (formation of a sublattice of Lu or La ions) which would lead to the possibility of a site-selective determination of physical properties. Indeed, an indication of a site-selective occupation was found in the electrical resistivity measurements for  $\text{Ce}_2\text{LaPd}_{20}\text{Si}_6$  which show the typical  $-\ln T$  behaviour of incoherent Kondo scattering [112]. Within the author's master thesis, electrical resistivity measurements on  $\text{Ce}_{3-x}\text{La}_x\text{Pd}_{20}\text{Si}_6$  samples ( $x = 0.33, 0.67$ ) at  $T > 2$  K revealed similar incoherent Kondo scattering behaviour as found for  $x = 0$  and  $x = 1$  (Fig. A.1) [49].

In parallel to the this PhD thesis, the low temperature behaviour ( $T < 2$  K) of the  $\text{Ce}_{3-x}\text{La}_x\text{Pd}_{20}\text{Si}_6$  samples ( $x = 0.33, 0.67$ ) was investigated in collaboration with K.-A. Lorenzer (Fig. A.1) [113]. The derivative of the electrical resistivity  $\partial\rho(T)/\partial T$  exhibits a maximum at about 180 mK (190 mK) for  $x = 0.67$  ( $x = 0.33$ ) indicating a magnetic ordering. Due to these promising results for a site-selective occupation of the  $4a$  and  $8c$  site by Ce atoms, three additional polycrystalline  $\text{Ce}_{3-x}\text{La}_x\text{Pd}_{20}\text{Si}_6$  ( $x = 0.78, 0.89$  and  $1.5$ ) samples were grown and characterized within this project. Detailed analysis of the low temperature behaviour was performed by K.-A. Lorenzer within his PhD thesis [78]. Here, the relative resistivity  $\bar{\rho}(T) = \rho(T) / \rho(300 \text{ K})$  of the  $\text{Ce}_{3-x}\text{La}_x\text{Pd}_{20}\text{Si}_6$  samples measured by the author at  $T > 2$  K with



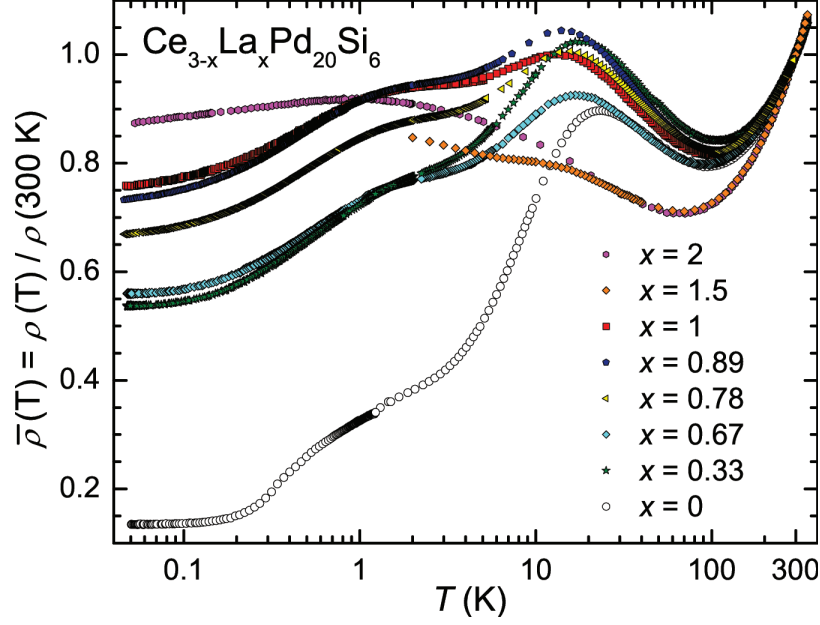


Figure A.1: Relative electrical resistivity  $\bar{\rho}(T) = \rho(T) / \rho(300 \text{ K})$  measured on  $\text{Ce}_{3-x}\text{La}_x\text{Pd}_{20}\text{Si}_6$  samples as a function of temperature  $T$  on a semilogarithmic plot.

their low temperature data ( $T < 2 \text{ K}$ ) measured by K.-A. Lorenzer are shown on a semilogarithmic plot (Fig. A.1). As already mentioned above,  $\text{Ce}_{3-x}\text{La}_x\text{Pd}_{20}\text{Si}_6$  ( $x \leq 1$ ) revealed similar behaviour as found in samples with  $x = 0$  and  $x = 1$ . These results are in agreement with a preferential occupation of the  $8c$  site by Ce atoms and suggested a dominance of Kondo physics in the  $8c$  sublattice compared to the  $4a$  sublattice [113]. Therefore, a remarkable change in the physical properties, which are dominated by the Kondo effect, was expected for  $x > 1$ . This characteristic change of the incoherent Kondo regime was observed for  $\bar{\rho}(T)$  with  $x = 1.5$ . At  $T > 20 \text{ K}$ ,  $\bar{\rho}(T)$  of  $x = 1$  and  $x = 1.5$  show similar behaviour with a remarkable lower minimum in  $\bar{\rho}(T)$  than the compounds with  $x \leq 1$ . For a detailed investigation of the site-selective occupation, heat capacity  $C_p$  measurements were performed with the horizontal  $^3\text{He}$  heat capacity set-up in a physical property measurement system (PPMS) from Quantum Design (Fig. A.2, left panel).

The  $C_p$  measurements were analyzed at the lowest temperatures with an  $s$ - $d$  Kondo resonance model by Schotte and Schotte [114]. This procedure is similar to the analysis in the PhD thesis by K.-A. Lorenzer. Detailed informations about this model in combination with non-substituted  $\text{Ce}_3\text{Pd}_{20}\text{Si}_6$  can be found in that work [78]. The fit parameters for the investigations within this thesis were chosen in accordance to the results obtained for  $\text{Ce}_3\text{Pd}_{20}\text{Si}_6$  by K.-A. Lorenzer. The site-selective occupation is shown in Fig. A.2 (right panel). For compounds with  $x \leq 1$ , a value of 2 for the  $8c$  site occupation with Ce ( $x$ -axis) is expected if a strongly preferred  $8c$  occupation exists. At least an attendance in the yellow area in Fig. A.2 (right panel) of the relations is expected for a preferential occupation of the  $8c$  site. Agreement with a strongly enhanced  $8c$  occupation is only found for  $x = 0.33$ . By contrast, no site-selective occupation



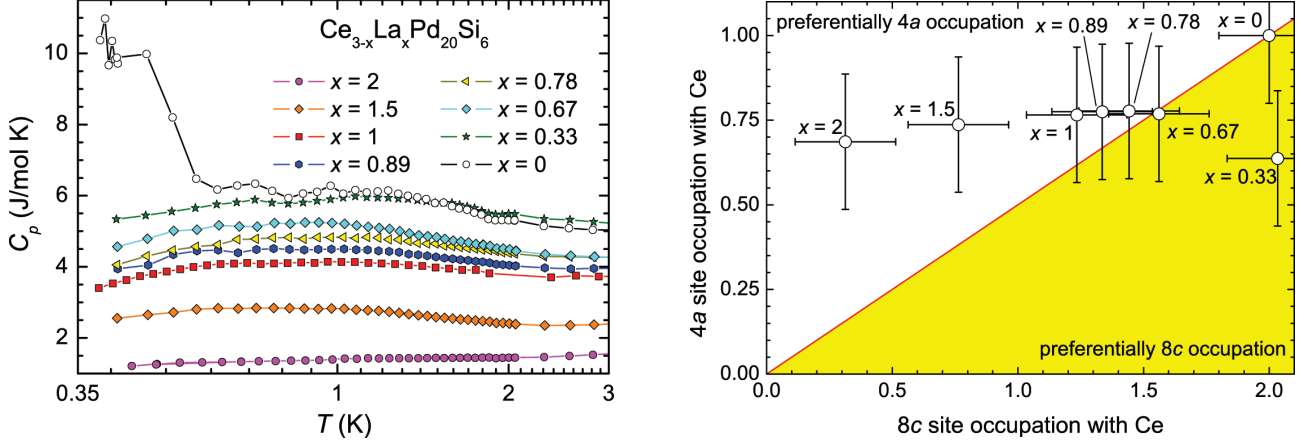


Figure A.2: Left: Heat capacity  $C_p$  measured on  $\text{Ce}_{3-x}\text{La}_x\text{Pd}_{20}\text{Si}_6$  samples as a function of temperature  $T$ . Right: Site occupation of the Ce atoms in  $\text{Ce}_{3-x}\text{La}_x\text{Pd}_{20}\text{Si}_6$  samples derived by analyzing the  $C_p$  data with a theoretical model by Schotte and Schotte [114]. This analysis is described in detailed by K.-A. Lorenzer in his PhD thesis [78].

was observed within this analysis for  $x \geq 0.67$ .

## A.2 Physical properties measurements on type-I clathrates including La and Ce

Thermoelectric materials are promising candidates to enhance the efficiency of prospective energy systems which is of great interest due to the worldwide increasing energy consumption. The wasted thermal energy could be used by converting a temperature gradient into an electrical current via thermoelectric elements. Beside the technical and economical requirements (long-term stability, costs of production, usage of non-toxic elements, etc.), a high electrical conductivity and thermopower in combination with a low thermal conductivity are needed for high efficiency. The type-I clathrates are promising candidates for thermoelectric applications due to their extraordinarily low lattice thermal conductivities [115]. Within our project, an enhancement of the thermopower of the type-I clathrate  $\text{Ba}_8\text{Au}_6\text{Si}_{40}$  due to the Kondo effect was realized by including the rare-earth element Ce [116]. So,  $\text{Ba}_{6.91 \pm 0.17}\text{Ce}_{1.06 \pm 0.12}\text{Au}_{5.56 \pm 0.25}\text{Si}_{40.47 \pm 0.43}$  (BCAS),  $\text{Ba}_{6.99 \pm 0.17}\text{La}_{1.23 \pm 0.12}\text{Au}_{5.91 \pm 0.25}\text{Si}_{39.87 \pm 0.43}$  (BLAS, reference compound) and  $\text{Ba}_8\text{Au}_6\text{Si}_{40}$  were grown and characterized by collaborators. Magnetic susceptibility  $\chi(T)$  at  $T \geq 300$  K (BCAS, BLAS), heat capacity  $C_p(T)$  at  $T \geq 2$  K (BAS) and electrical resistivity  $\rho(T)$  at  $T \geq 300$  K (BCAS, BLAS) was measured by the author within this project. Figure A.3 shows  $\rho(T)$  (top) and  $\chi(T)$  (bottom) at  $T > 300$  K. Further measurements and analysis revealed an enhancement of the thermopower at high temperatures. We suggest that a rattling-enhanced Kondo interaction [117] causes this enhancement.

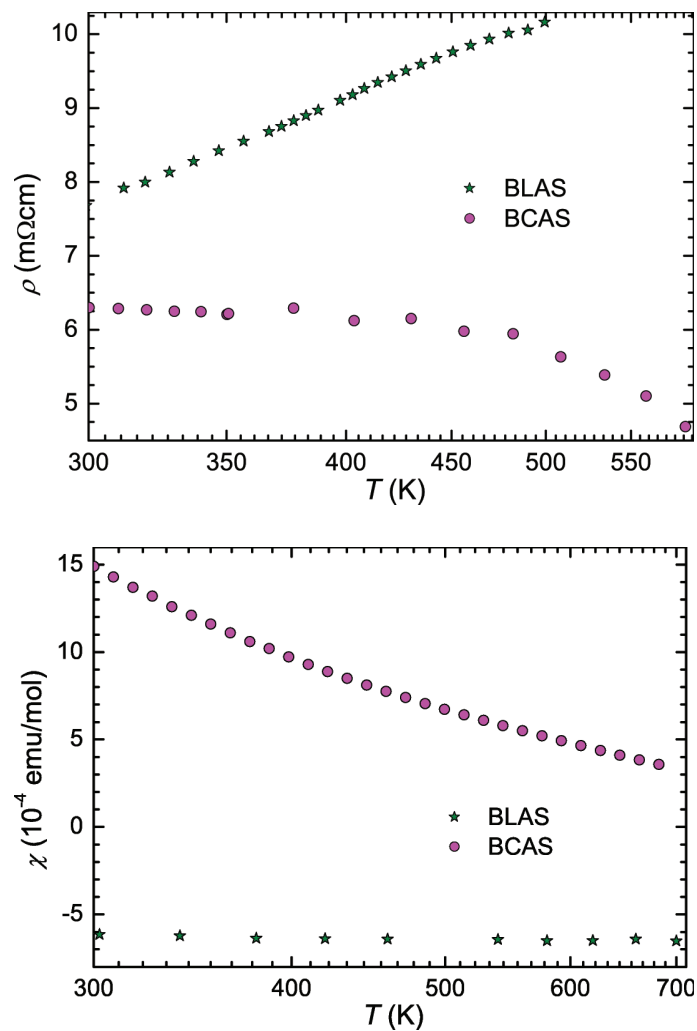


Figure A.3: Electrical resistivity  $\rho$  (top) and magnetic susceptibility  $\chi$  (bottom) measured on type-I clathrate  $\text{Ba}_8\text{Au}_6\text{Si}_{40}$  substituted with La (BLAS) and Ce (BCAS) as a function of temperature  $T$  on a semilogarithmic plot.

# Publications

- H. Winkler, K.-A. Lorenzer, S. Laumann, J. Custers, A. Prokofiev and S. Paschen;  
“Chemical pressure, dilution and disorder in the heavy fermion compounds  $\text{Ce}_{3-x}\text{La}_x\text{Pd}_{20}\text{Si}_6$  ( $x = \frac{1}{3}, \frac{2}{3}$ )”;  
*J. Phys.: Condens. Matter* **23**, 094208 (2011).
- J. Custers, K.-A. Lorenzer, M. Müller, A. Prokofiev, A. Sidorenko, H. Winkler, A. M. Strydom, Y. Shimura, T. Sakakibara, R. Yu, Q. Si and S. Paschen;  
“Destruction of the Kondo effect in the cubic heavy-fermion compound  $\text{Ce}_3\text{Pd}_{20}\text{Si}_6$ ”;  
*Nature Mater.* **11**, 189-194 (2012).
- H. Winkler, K.-A. Lorenzer, A. Prokofiev and S. Paschen;  
“Anisotropic electrical resistivity of the Kondo insulator  $\text{CeRu}_4\text{Sn}_6$ ”;  
*J. Phys.: Conf. Ser.* **391**, 012077 (2012).
- V. Guritanu, P. Wissgott, T. Weig, H. Winkler, J. Sichelschmidt, M. Scheffler, A. Prokofiev, S. Kimura, T. Iizuka, A. M. Strydom, M. Dressel, F. Steglich, K. Held and S. Paschen;  
“Anisotropic optical conductivity of the putative Kondo insulator  $\text{CeRu}_4\text{Sn}_6$ ”;  
*Phys. Rev. B* **87**, 115129 (2013).
- A. Prokofiev, A. Sidorenko, K. Hradil, M. Ikeda, R. Svagera, M. Waas, H. Winkler, K. Neumaier and S. Paschen;  
“Thermopower enhancement by encapsulating cerium in clathrate cages”;  
Accepted for publication in *Nature Mater.* (2013).



# Bibliography

- [1] I. Das, E. V. Sampathkumaran, *Phys. Rev. B* **46**, 4250 (1992).
- [2] A. Strydom, Z. Guo, S. Paschen, R. Viennois, F. Steglich, *Physica B: Condens. Matter* **359-361**, 293 (2005).
- [3] P. S. Riseborough, *Adv. Phys.* **49**, 257 (2000).
- [4] U. Köhler, *Thermoelectric transport in rare-earth compounds*, Ph.D. thesis, Fakultät Mathematik und Naturwissenschaften der Technischen Universität Dresden (2007).
- [5] H. Ikeda, K. Miyake, *J. Phys. Soc. Jpn.* **65**, 1769 (1996).
- [6] J. Moreno, P. Coleman, *Phys. Rev. Lett.* **84**, 342 (2000).
- [7] B. Cornut, B. Coqblin, *Phys. Rev. B* **5**, 4541 (1972).
- [8] Zlatić, V. and Monnier, R., *Phys. Rev. B* **71**, 165109 (2005).
- [9] P. Wissgott, *Transport Properties of Correlated Materials from First Principles*, Ph.D. thesis, Technischen Universität Wien Fakultät für Physik (2012).
- [10] T. Nezu, *Herstellung und Charakterisierung von  $CeRu_4Sn_6$  Einkristallen*, Master's thesis, Technischen Universität Wien Fakultät für Physik (2008).
- [11] T. Takabatake, *et al.*, *J. Magn. Magn. Mater.* **177-181**, **Part 1**, 277 (1998).
- [12] Y. Inada, *et al.*, *Physica B* **230-232**, 690 (1997).
- [13] G. Nakamoto, *et al.*, *J. Phys. Soc. Jpn.* **64**, 4834 (1995).
- [14] G. Boebinger, A. Passner, P. Canfield, Z. Fisk, *Physica B: Condens. Matter* **211**, 227 (1995).
- [15] F. Strigari, *et al.*, *Work in progress: 4f ground-state wave functions of  $CeRu_4Sn_6$  and  $YbAlB_4$  with X-ray absorption spectroscopy*, Poster session, Conference "Quantum Criticality & Novel Phases" Dresden (2012).
- [16] V. Guritanu, *et al.*, *Phys. Rev. B* **87**, 115129 (2013).
- [17] J. Kondo, *Prog. Theor. Phys.* **32**, 37 (1964).

- [18] W. J. de Haas, J. H. de Boer, G. J. van de Berg, *Physica (Utrecht)* **1**, 1115 (1934).
- [19] K. Andres, J. E. Graebner, H. R. Ott, *Phys. Rev. Lett.* **35**, 1779 (1975).
- [20] Q. Si, F. Steglich, *Science* **329**, 1161 (2010).
- [21] P. Gegenwart, S. Qimiao, S. Steglich, *Nature Phys.* **4**, 186 (2008).
- [22] Q. Si, S. Paschen, *Phys. Status Solidi (b)* **250**, 425 (2013).
- [23] A. Menth, E. Buehler, T. H. Geballe, *Phys. Rev. Lett.* **22**, 295 (1969).
- [24] J. W. Allen, B. Batlogg, P. Wachter, *Phys. Rev. B* **20**, 4807 (1979).
- [25] M. Kasaya, F. Iga, K. Negishi, S. Nakai, T. Kasuya, *J. Magn. Magn. Mater.* **31-34**, 437 (1983).
- [26] M. Kasaya, K. Katoh, K. Takegahara, *Solid State Commun.* **78**, 797 (1991).
- [27] G. P. Meisner, M. S. Torikachvili, K. N. Yang, M. B. Maple, R. P. Guertin, *J. Appl. Phys.* **57**, 3073 (1985).
- [28] G. B. Martins, M. A. Pires, G. E. Barberis, C. Rettori, M. S. Torikachvili, *Phys. Rev. B* **50**, 14822 (1994).
- [29] E. D. Bauer, A. Slebarski, E. J. Freeman, C. Sirvent, M. B. Maple, *J. Phys.: Condens. Matter* **13**, 4495 (2001).
- [30] V. Jaccarino, G. K. Wertheim, J. H. Wernick, L. R. Walker, S. Aarj, *Phys. Rev.* **160**, 476 (1967).
- [31] T. Palstra, G. Nieuwenhuys, J. Mydosh, K. Buschow, *J. Magn. Magn. Mater.* **54-57**, Part 1, 549 (1986).
- [32] T. Takabatake, *et al.*, *J. Phys. Soc. Jpn.* **59**, 4412 (1990).
- [33] T. Takabatake, *et al.*, *Phys. Rev. B* **41**, 9607 (1990).
- [34] S. K. Malik, D. T. Adroja, *Phys. Rev. B* **43**, 6277 (1991).
- [35] S. Yoshii, M. Kasaya, H. Takahashi, N. Mori, *Physica B: Condens. Matter* **223-224**, 421 (1996).
- [36] K. Sengupta, *et al.*, *Phys. Rev. B* **70**, 064406 (2004).
- [37] L. Menon, P. de V. du Plessis, A. M. Strydom, *Solid State Commun.* **106**, 519 (1998).
- [38] V. Tran, *et al.*, *Physica B: Condens. Matter* **312-313**, 215 (2002).
- [39] K. Sugiyama, *et al.*, *Physica B: Condens. Matter* **230-232**, 683 (1997).
- [40] R. Pöttgen, *et al.*, *J. Solid State Chem.* **134**, 326 (1997).

- 
- [41] Z. Guo, *Electrtransport studies of the anomalous semimetal ground state in CeRu<sub>4</sub>Sn<sub>6</sub>*, Master's thesis, University of Johannesburg Department of Physics (2005).
- [42] A. Strydom, A. Hillier, D. Adroja, S. Paschen, F. Steglich, *J. Magn. Magn. Mater.* **310**, 377 (2007).
- [43] E. Brüning, *et al.*, *J. Magn. Magn. Mater.* **310**, 393 (2007).
- [44] E. Brüning, *et al.*, *Physica B: Condens. Matter* **378-380**, 839 (2006).
- [45] A. M. Strydom, D. Adroja, Private communication (2011).
- [46] E. M. Brüning, *et al.*, *Phys. Rev. B* **82**, 125115 (2010).
- [47] K. Sengupta, K. K. Iyer, R. Ranganathan, E. V. Sampathkumaran, *J. Phys.: Conf. Ser.* **377**, 012029 (2012).
- [48] Y. Uwatoko, *et al.*, *J. Phys. Soc. Jpn.* **65**, 27 (1996).
- [49] H. Winkler, *Untersuchung physikalischer Eigenschaften von korrelierten Käfigverbindungen*, Master's thesis, Technischen Universität Wien Fakultät für Physik (2008).
- [50] S. Paschen, *et al.*, *J. Phys.: Conf. Ser.* **200**, 012156 (2010).
- [51] M. F. Hundley, P. C. Canfield, J. D. Thompson, Z. Fisk, J. M. Lawrence, *Phys. Rev. B* **42**, 6842 (1990).
- [52] C. Zener, *Phys. Rev.* **16**, 440 (1951).
- [53] T. Kasuya, *Prog. Theor. Phys.* **16**, 45 (1956).
- [54] S. Doniach, *Physica B+C* **91**, 231 (1977).
- [55] E. Bauer, S. Paschen, Lecture notes: Strongly Correlated Electron Systems (2010).
- [56] R. Martin, *Phys. Rev. Lett.* **48**, 362 (1982).
- [57] D. Adroja, *et al.*, *J. Optoelectron. Adv. Mater.* **10**, 1719 (2008).
- [58] N. Nagaosa, J. Sinova, S. Onoda, A. H. MacDonald, N. P. Ong, *Rev. Mod. Phys.* **82**, 1539 (2010).
- [59] A. C. Hewson, *The Kondo problem to heavy fermions* (Cambridge University Press, Cambridge; New York, 1997).
- [60] N. S. Vidhyadhiraja, V. E. Smith, D. E. Logan, H. R. Krishnamurthy, *J. Phys.: Condens. Matter* **15**, 4045 (2003).
- [61] L. D. Landau, *J. Exptl. Theoret. Phys.* **30**, 1058 (1956).
-

- [62] J. Custers, *Quantum Critical Behavior in the Heavy Fermion Compounds  $\text{YbRh}_2\text{Si}_2$  and  $\text{CeIn}_{3-x}\text{Sn}_x$* , Ph.D. thesis, Fakultät Mathematik und Naturwissenschaften der Technischen Universität Dresden (2004).
- [63] B. Coqblin, J. R. Schrieffer, *Phys. Rev.* **185**, 847 (1969).
- [64] B. Cornut, B. Coqblin, *Solid State Commun.* **13**, 1171 (1973).
- [65] D. Huo, J. Sakurai, O. Maruyama, T. Kuwai, Y. Isikawa, *J. Magn. Magn. Mater.* **226-230, Part 1**, 202 (2001).
- [66] M. R. Lees, B. R. Coles, E. Bauer, N. Pillmayr, *J. Phys.: Condens. Matter* **2**, 6403 (1990).
- [67] V. Zlatić, *et al.*, *Phys. Rev. B* **68**, 104432 (2003).
- [68] A. K. Bhattacharjee, B. Coqblin, *Phys. Rev. B* **13**, 3441 (1976).
- [69] N. E. Bickers, D. L. Cox, J. W. Wilkins, *Phys. Rev. B* **36**, 2036 (1987).
- [70] S. Maekawa, S. Kashiba, M. Tachiki, S. Takahashi, *J. Phys. Soc. Jpn.* **55**, 3194 (1986).
- [71] S. Hartmann, *Thermoelectric transport in correlated electron systems*, Ph.D. thesis, Fakultät Mathematik und Naturwissenschaften der Technischen Universität Dresden (2010).
- [72] B. Stroka, *et al.*, *Zeitschrift für Phys. B Condens. Matter* **90**, 155 (1993).
- [73] E. Hall, *Am. J. Math.* **2**, 287 (1879).
- [74] A. Fert, P. M. Levy, *Phys. Rev. B* **36**, 1907 (1987).
- [75] W. R. Datars, K. Kadowaki, N. Ali, S. B. Woods, *J. Phys. F: Metal Phys.* **16**, L63 (1986).
- [76] E. Cattaneo, *J. Magn. Magn. Mater.* **47-48**, 529 (1985).
- [77] K. W. H. Stevens, *Proc. Phys. Soc. London, Sec. A* **65**, 209 (1952).
- [78] K.-A. Lorenzer, *Quantum critical behaviour in cubic heavy-fermion compounds*, Ph.D. thesis, Technischen Universität Wien Fakultät für Physik (2013).
- [79] Quantum Design, Inc., <http://www.qdusa.com/sitedocs/appNotes/ppms/1096-306-Rev-B0.pdf>.
- [80] Quantum Design, Inc., <http://www.qdusa.com/products/ppms.html>.
- [81] R. Resel, *et al.*, *Rev. Sci. Instrum.* **67**, 1970 (1996).
- [82] P. Hansmann, *et al.*, *Phys. Rev. Lett.* **100**, 066405 (2008).
- [83] T. Willers, *et al.*, *Phys. Rev. B* **80**, 115106 (2009).



- 
- [84] G. Venturini, B. E. Idrissi, J. Marêché, B. Malaman, *Mater. Res. Bull.* **25**, 1541 (1990).
- [85] T. C. Ozawa, S. J., *J. Appl. Cryst.* **37**, 679 (2004).
- [86] Z. Schlesinger, *et al.*, *Phys. Rev. Lett.* **71**, 1748 (1993).
- [87] M. Kasaya, F. Iga, K. Negishi, S. Nakai, T. Kasuya, *J. Magn. Magn. Mater.* **31-34**, 437 (1983).
- [88] T. T. M. Palstra, *et al.*, *J. Magn. Magn. Mater.* **67**, 331 (1987).
- [89] M. Rotter, *J. Magn. Magn. Mater.* **481**, 272 (2004).
- [90] D. Schmitt, *J. Phys. F: Metal Phys.* **9**, 1759 (1979).
- [91] R. Coehoorn, *Supermagnets, Hard Magnetic Materials* (Kluwer Academic publishers; Dordrecht, 1991).
- [92] J. C. Duthie, V. Heine, *J. Phys. F: Metal Phys.* **9**, 1349 (1979).
- [93] Y. Hashimoto, H. Fujii, H. Fujiwara, T. Okamoto, *J. Phys. Soc. Jpn.* **47**, 67 (1979).
- [94] Y. L. Wang, *Phys. Lett. A* **35**, 383 (1971).
- [95] P. Boutron, *Phys. Rev. B* **7**, 3226 (1973).
- [96] R. J. Elliott, *Magnetism* (Academic Press; Waltham, 1965).
- [97] T. Takeuchi, *et al.*, *J. Phys. Soc. Jpn.* **70**, 877 (2001).
- [98] E. Holland-Moritz, *et al.*, *Phys. Rev. B* **39**, 6409 (1989).
- [99] I. Aviani, *et al.*, *Phys. Rev. B* **64**, 184438 (2001).
- [100] H. Xiao, T. Hu, C. C. Almasan, T. A. Sayles, M. B. Maple, *Phys. Rev. B* **73**, 184511 (2006).
- [101] M. D. Kuz'min, *J. Magn. Magn. Mater.* **154**, 333 (1996).
- [102] H. Winkler, K.-A. Lorenzer, A. Prokofiev, S. Paschen, *J. Phys.: Conf. Ser.* **391**, 012077 (2012).
- [103] J. D. Thompson, *et al.*, *Proceedings of the Hiroshima Workshop on f-Electron Systems*, edited by H. Fujii, T. Fujita and G. Oomi (New York: Plenum), p. 35 (1993).
- [104] A. Lacerda, *et al.*, *Physica B: Condens. Matter* **199**, 469 (1994).
- [105] J. Cooley, *et al.*, *J. Supercon.* **12**, 171 (1999).
- [106] S. Wolgast, *et al.*, arXiv 1211.5104 (2012).
- [107] T. Takabatake, *et al.*, *Physica B: Condens. Matter* **328**, 53 (2003).

- [108] J. Hänel, *et al.*, *Thermoelectric properties of the Kondo insulator CeRu<sub>4</sub>Sn<sub>6</sub>*, Poster session, Workshop "New materials for thermoelectric applications: theory and experiment" Hvar (2011).
- [109] H. Okamura, *et al.*, *Physica B: Condens. Matter* **259-261**, 317 (1999).
- [110] A. B. Kuzmenko, *Rev. Sci. Instrum.* **76**, 083108 (2005).
- [111] S. Paschen, *et al.*, *J. Magn. Magn. Mater.* **316**, 90 (2007).
- [112] H. Winkler, S. Laumann, J. Custers, A. Prokofiev, S. Paschen, *Phys. Status Solidi (b)* **247**, 516 (2010).
- [113] H. Winkler, *et al.*, *J. Phys.: Condens. Matter* **23**, 094208 (2011).
- [114] K. Schotte, U. Schotte, *Phys. Lett.* **55**, 38 (1975).
- [115] E. S. Toberer, M. Christensen, B. B. Iversen, G. J. Snyder, *Phys. Rev. B* **77**, 075203 (2008).
- [116] A. Prokofiev, *et al.*, Accepted for publication in *Nature Materials* (2013) .
- [117] T. Hotta, *J. Phys. Soc. Jpn.* **76**, 084702 (2007).

# Acknowledgments

I thank my thesis supervisor Professor Silke Bühler-Paschen for her support during this thesis, giving me the chance to work in a fascinating field of physics and the fruitful discussions about the compounds investigated.

Within this thesis, a lot of measurements with different devices were performed at the Institute of Solid State Physics at the Vienna University of Technology and by collaborators at their Universities or external facilities. Many thanks are addressed to:

- A. Prokofiev for the support concerning the single crystal growth of  $\text{CeRu}_4\text{Sn}_6$ .
- A. Sidorenko for performing direct magnetization measurements and fruitful discussions about the magnetic properties in general.
- V. Guritanu, J. Sichelschmidt, T. Weig and M. Scheffler for performing optical reflectivity measurements.
- S. Wirth for the first cleaving tests, scanning tunneling microscopy and preliminary scanning tunneling spectroscopy measurements.
- F. Strigari and A. Severing for performing X-ray absorption spectroscopy and various discussions about the origin of the discrepancies observed using different measurement techniques.
- M. Ikeda for the support regarding thermopower measurements and fruitful discussions.
- K.-A. Lorenzer for performing low temperature measurements in the dilution refrigerator and fruitful discussions.
- M. Waas and R. Svagera for analyzing the  $\text{CeRu}_4\text{Sn}_6$  single crystals by energy dispersive X-ray spectroscopy and scanning electron microscopy.
- E. Bauer for the support and usage of his homemade high temperature resistivity and thermopower device set-ups.
- M. Reissner for the support on measurements in the physical properties measurement system (PPMS).
- V. Peter for the support on single crystal preparation.

---

Fortunately, living is not only work. Hence, I want to thank a lot of colleagues for a very good time at the Institute of Solid State Physics. Here, I want to mention especially my colleagues M. Ikeda, J. Hänel and K.-A. Lorenzer, who shared the office with me. Additionally, I want to thank the group of D. Süss for very great lunchtimes and fascinating discussions about and apart physics.

Many thanks to my family, my friends and especially my girlfriend Eva for the strong support during this thesis especially within the last months.

Finally, I acknowledge the financial support from the European Research Council/ERC Advanced Grant No. 227378.

Many thanks to all of you,  
Winkler Hannes H.

# Versicherung

Hiermit versichere ich, dass ich die vorliegende Arbeit ohne unzulässige Hilfe Dritter und ohne Benutzung anderer als der angegebenen Hilfsmittel angefertigt habe. Die aus fremden Quellen direkt oder indirekt übernommenen Gedanken sind als solche kenntlich gemacht. Die Arbeit wurde bisher weder im Inland noch im Ausland in gleicher oder ähnlicher Form einer anderen Prüfungsbehörde vorgelegt.

Die vorliegende Dissertation wurde am Institut für Festkörperphysik der Technischen Universität Wien unter der wissenschaftlichen Betreuung von Univ. Prof. Dr.rer.nat. Silke Bühler-Paschen angefertigt.

Ich erkenne die Promotionsordnung der Technischen Universität Wien an.

Villach, 09. September 2013

---

# Curriculum Vitae

**Dipl.-Ing. Hannes Heinrich Winkler**

Hermesberg 1  
9531 Nötsch im Gailtal

## Persönliche Informationen:

Staatsbürgerschaft	Österreich
Geburtstag	26.10.1983
Geburtsort	Villach, Österreich

## Ausbildung/Titel:

09/1990 - 07/1994	Volksschule Obere Fellach, Villach
09/1994 - 07/1998	Peraugymnasium Villach
09/1998 - 06/2003	Höhere technische Bundes-, Lehr- und Versuchsanstalt Villach, Bautechnik/Tiefbau
06/2003	Matura
09/2003 - 04/2004	Präsenzdienst
10/2004 - 01/2010	Studium der Technischen Physik an der Technischen Universität Wien
01/2010	Verleihung des Titels „Dipl.-Ing.“
seit 03/2010	Doktoratsstudium der technischen Wissenschaften Technischen Physik an der Technischen Universität Wien
03/2010 - 04/2013	Beschäftigung als Projektassistent an der Technischen Universität Wien